Design and development of multifunctional inorganic pigments for cool coating applications

by

THEJUS P K

Registration No: 10CC18A39003

A thesis submitted to the

Academy of Scientific & Innovative Research

for the award of the degree of

DOCTOR OF PHILOSOPHY

in

SCIENCE

Under the supervision of

Dr. K. G. NISHANTH

सीएसआईआर का अंतर्विषयी आयाम
Interdisciplinary face of CSIR

CSIR-National Institute for Interdisciplinary Science and Technology (CSIR-NIIST)

Thiruvananthapuram-695019

Academy of Scientific and Innovative Research

AcSIR Headquarters, CSIR-HRDC campus

Sector 19, Kamla Nehru Nagar,

Ghaziabad, U.P. – 201 002, India

September-2023

Thesis is dedicated to

my beloved family...

Dr. K. G. Nishanth   **Email: nishanthkg@niist.res.in**

Senior Scientist   **Mob: 9656728857**

Centre for Sustainable Energy Technologies

CERTIFICATE

This is to certify that the work incorporated in this Ph.D. thesis entitled, "*Design and development of multifunctional inorganic pigments for cool coating applications*", submitted by **Mr. Thejus P K** to the Academy of Scientific and Innovative Research (AcSIR), in partial fulfillment of the requirements for the award of the Degree of *Doctor of Philosophy in Science*, embodies original research work carried-out by the student. We, further certify that this work has not been submitted to any other University or Institution in part or full for the award of any degree or diploma. Research materials obtained from other sources and used in this research work have been duly acknowledged in the thesis. Images, illustrations, figures, tables etc., used in the thesis from other sources, have also been duly cited and acknowledged.

Thejus P K   Dr. K G Nishanth

                                                                                (Research supervisor)

Thiruvananthapuram

September 2023

STATEMENTS OF ACADEMIC INTEGRITY

I, **Thejus P K**, a Ph.D. student of the Academy of Scientific and Innovative Research (AcSIR) with Registration No. 10CC18A39003 hereby undertake that, the thesis entitled "***Design and development of multifunctional inorganic pigments for cool coating applications***" has been prepared by me and that the document reports original work carried out by me and is free of any plagiarism in compliance with the UGC Regulations on "Promotion of Academic Integrity and Prevention of Plagiarism in Higher Educational Institutions (2018)" and the CSIR Guidelines for "Ethics in Research and in Governance (2020)".

18/09/2023

Thejus P K

September 2023

Thiruvananthapuram

___

It is hereby certified that the work done by the student, under my supervision, is plagiarism free in accordance with the UGC Regulations on "Promotion of Academic Integrity and Prevention of Plagiarism in Higher Educational Institutions (2018)" and the CSIR Guidelines for "Ethics in Research and in Governance (2020)".

18/09/2023

Dr. K G Nishanth

September 2023

Thiruvananthapuram

DECLARATION

I, Thejus P K, bearing AcSIR Registration No. 10CC18A39003 declare: that my thesis entitled, "*Design and development of multifunctional inorganic pigments for cool coating applications*" is plagiarism free in accordance with the UGC Regulations on "Promotion of Academic Integrity and Prevention of Plagiarism in Higher Educational Institutions (2018)" and the CSIR Guidelines for "Ethics in Research and in Governance (2020)".

I would be solely held responsible if any plagiarized content in my thesis is detected, which is violative of the UGC regulations 2018.

18/09/2023

Thejus P K

September 2023

Thiruvananthapuram

ACKNOWLEDGEMENTS

Table of contents

List of Abbreviations

IR   - Infrared radiation

NOAA   - National Oceanic and Atmospheric Administration

GDP   - Gross Domestic Product

IPCC   - Intergovernmental Panel on Climate Change

CFC   - chlorofluorocarbon

UHI   - Urban Heat Island

AC   - Air Conditioner

HAM   - High Albedo Materials

NIR   - Near Infrared reflective

PXRD   - Powder X-ray Diffraction

JCPDS   - Joint committee on Powder Diffraction Standards

DRS   - Diffuse Reflectance Spectroscopy

K-M   - Kubelka–Munk

CIE   - Commission Internationale del'Eclairage

PTFE   - Polytetrafluoroethylene

ASTM   - American Society for Testing and Materials

SEM   - Scanning Electron Microscope

EDS   - Energy Dispersive X-ray Spectroscopy

DLS   - Dynamic Light Scattering

TGA   - Thermogravimetric Analysis

EIS   - Electrochemical Impedance Spectroscopy

EEC   - Electrochemical Equivalent Circuit

SCE   - Saturated Calomel Electrode

XPS   - X-ray Photoelectron Spectroscopy

WP   - White Pigment

EDXRF   - Energy Dispersive X-ray Fluorescence spectrometer

HRTEM   - High-Resolution Transmission Electron Micrographs

SAED   - Selected Area Electron Diffraction

List of Figures

List of Tables

PREFACE

Average global temperature on the earth's surface has increased by 1 °C since 1981. Global warming, depleting forests, atmospheric pollution and most importantly the Urban Heat Island effect (UHI) are regarded as the primary reasons for this heat rise. Though intensive activities are followed to reduce global warming, pollution and deforestation, no serious attempts were made to address UHI. It is a condition where an urban or metropolitan area becomes warmer than its surrounding rural areas by virtue of heat energy dissipation to the atmosphere from buildings, pavements and roads. Moreover, population growth and inflating urbanization further worsen the scenario. Urban warming seriously impacts the buildings' energy consumption by increasing the peak electricity demand for cooling needs in summer. In this context, there is an aggregating requirement for the development of cool coatings to mitigate UHI and consequent environmental impacts.

The infrared (IR) rays (700-2500 nm) from the sunlight are responsible for the heat generation on material surface. Hence, coatings of passive radiative cooling materials with high IR reflectance that reduce heat build-up and control UHI became the choice of interest. In this aspect, the search for IR reflective inorganic pigments has seriously accelerated in the last two decades. ZnO and TiO_2 are examples of excellent IR reflective white pigments. Meanwhile, the fascination for aesthetics also introduced a few coloured cool pigments in the market, like $PbCrO_4$, $BiVO_4$, YInMn blue etc. Unfortunately, many of these pigments are highly toxic and expensive, hence, the necessity is still growing for better alternatives. In addition, since metals are subjected to corrosion, developing a sustainable cool metal roof coating necessitates an additional anticorrosive base coat. Although anticorrosive pigments such as $Zn_3(PO_4)_2$, Cr_2O_3 etc can sort out the issue, pigment toxicity is the main concern. Moreover, the traditional duplex coating practice leads to huge material consumption, enormous labour work and high expense. Hence, integrating the features of colour, reflectance and corrosion resistance on a single material can resolve all these allegations, which will have a massive impact on the industrial sector and will be highly beneficial for society and the environment. But, inorganic pigment that works in multiple aspects, especially IR reflective and anticorrosive, has not been reported. Further, it demands an in-depth understanding of the structural and spectral characteristics to combine multiple properties in a single material. Therefore, the present work concentrates on the design and development of cost-effective, intense colour multifunctional inorganic pigments with excellent IR reflectance and promising anticorrosive properties.

The thesis is organized into five chapters. Chapter 1 discusses the issue of global temperature rise, emphasizing the Urban Heat Island effect (UHI), its consequences and the need for energy efficient buildings. Further, it proposes cool coatings as an efficient solution, describing the role of IR reflective inorganic pigments. In addition, it mentions the significance of crystal structure and chromophore geometry behind the origin of colour. Moreover, the chapter deals with the challenges of bringing the concept of multifunctionality, including corrosion resistance property and IR reflectivity in a single pigment, to achieve a durable cool coat. Considering all the challenges working chapters were successfully constructed.

Chapter 2A, deals with new inorganic phosphate pigment series with general formula $ABPO_4$ (A - monovalent and B - divalent cations). The chromophore Co^{2+} substitution at B site brought three different colours, blue, purple and magenta for $NaZn_{1-x}Co_xPO_4$, $LiZn_{1-x}Co_xPO_4$ and $LiMg_{1-x}Co_xPO_4$, respectively. The spectroscopic analysis identified the d-d electronic transitions responsible for this colour change along with chromophore geometry. Tetrahedral coordination of Co^{2+} with O ligands resulted in blue and purple colour, whereas its octahedral arrangement led to magenta. Rietveld refinement analysis revealed structural distortion of the chromophore in $NaZn_{1-x}Co_xPO_4$ and $LiZn_{1-x}Co_xPO_4$ pigment series with respect to $CoAl_2O_4$ blue. Eventually, it was confirmed that distortions from the ideal structure brought variations in ligand and metal ion positions, which modified the band gap consequently, the colour. Multifunctional aspects of the pigments $NaZn_{0.9}Co_{0.1}PO_4$ blue and $LiMg_{0.8}Co_{0.2}PO_4$ magenta were investigated in Chapter 2B. The pigments exhibited R^* 64 and 57%, respectively, which is superior than the commercial Co pigment. Pigment powder successfully retained its colour tone and reflectance properties after coating on concrete and aluminium sheet. Thermal shielding experiments conducted for blue and magenta coatings displayed temperature reductions of ~ 4 and ~ 7 ℃ in the interior and exterior of the prepared model foam box, compared to $CoAl_2O_4$ blue. Both the pigments were active against the corrosion of steel in the marine medium through a phosphatization mechanism. Among these, magenta showcased relatively higher corrosion resistance over commercial $CoAl_2O_4$ blue. The ability of these phosphate pigments to work in multiple dimensions makes them unique over commercial pigments.

Bismuth vanadate ($BiVO_4$) gathered great attraction as a replacement for conventional toxic chrome and cadmium yellow, though it contains highly expensive Bi. Therefore, a considerable demand exists to develop cost-effective $BiVO_4$ inorganic pigment without compromising its optical properties. Chapter 3 demonstrates an effective strategy to develop

low-cost $BiVO_4$ complex pigments by the citrate-gel method. Nanoparticles of $BiVO_4$ decorated on ZnO achieved 75 wt% reduction in $BiVO_4$ content. The developed complex inorganic pigment exhibited an excellent greenish-yellow colour, similar to pure $BiVO_4$. An exceptional IR reflectance of 90%, displayed ~ 7 °C interior and coating surface temperature reduction compared to commercial yellow pigment. Hence, the developed complex pigment could be a better alternative for $BiVO_4$ yellow pigment.

Chapter 4 illustrates a multifunctional brown inorganic ferrite pigment series, free of toxic elements, via the solid-state ceramic method. Partial replacement of chromophore Fe^{3+} by Al^{3+} in the pigment composition ($ZnFe_{1.9}Al_{0.1}O_4$) brought structural distortion in its octahedral geometry. The introduction of Al^{3+} ions in place of Fe^{3+} promoted the pigment reflectance from 34 to 58%, along with significant colour improvement. The pigment coatings on Al substrate were equally well in displaying good colour strength and temperature shielding ability (~2.5 °C) with respect to $ZnFe_2O_4$. The pigment epoxy coating stands out with its promising anticorrosive performance over the toxic commercial candidates, chromates and phosphates, exhibiting excellent $R_{ct} = 4.1 \times 10^9$ Ωcm^2 with good stability. Therefore, the new high-performance multifunctional brown ferrite pigment can potentially replace the present commercial pigment.

Chapter 5 highlights solid-state synthesized new orange pigment series Si-doped $Bi_4V_2O_{11}$. Incorporating Si^{4+} at the Bi^{3+} site of $Bi_4V_2O_{11}$ brought a remarkable transformation in its colour tone from dark brownish-red to bright orange. The pigment powder $Bi_{3.8}Si_{0.2}V_2O_{11+\delta}$ exhibited an outstanding reflectance profile 86%, which was further enhanced to 93% in coatings. Thermal shielding analysis yielded a ~2 °C reduction in temperature with respect to commercial orange pigment. Corrosion resistance property of the pigment loaded epoxy coating showed an outstanding $R_{ct} = 1.9 \times 10^{10}$ Ωcm^2 with exceptional stability. Most importantly, the developed pigment exhibited a superlative performance over most of the commercial toxic anticorrosive pigments. Thus, with good colour, reflectance and impressive anticorrosive properties, the new pigment can be an asset for the existing pigment market. Overall, the present work is accomplished to design and deliver highly efficient, non-toxic, cost-effective, coloured inorganic pigments with multifunctional properties.

Chapter 1

Introduction

1.1. Abstract

The average global surface temperature rise has accelerated in the 21st century due to increasing global warming. Although strict regulations have been implemented at various stages to reduce greenhouse gas emissions, the problem is still not under control; it appears to cross the irreversible temperature threshold of 1.5 °C shortly. The developing industrial and transportation sectors across the world have made a significant contribution to global temperature rise. The expanding urban area further hastened this scenario by creating Urban Heat Islands. The consequent summer peak electricity demand and heat-related health issues are efficiently controlled by introducing cool coatings. The special inorganic pigments incorporated in the cool coatings were highly efficient in reflecting the IR radiations from the sunlight, thus reducing the heat convection and dissipation. Traditional white pigments TiO_2 and ZnO were the initial choice of interest, and later it was replaced by coloured IR reflective pigments. However, the presence of highly toxic (Cr, Pb, Cd, As, Se) and expensive (Y, La, In, Co) elements in their composition led the researchers to develop an alternative for the existing commercial pigments. The majority of the reports in this aspect were unsuccessful in introducing a low-cost, non-toxic pigment with good colour strength and IR reflectivity. It is also highly challenging to maintain the stability of a metal cool roof coating, which is prone to corrosion under variable climate conditions. Moreover, the traditional duplex coating approach is unreliable regarding cost, material, and time. Therefore, developing a single multifunctional inorganic pigment with intense colour, high IR reflectivity and good corrosion resistance would be ideal. In this context, the present thesis made an effort to develop a low-cost, non-toxic, multifunctional inorganic pigment for cool coating application.

1.2. Global temperature rise

Solar energy is the primary source of energy for life on earth. Half of the light energy that falls on the earth's surface is absorbed in the atmosphere by greenhouse gases such as CO_2, NO_x, and CH_4 and emitted as infrared (IR) radiation. The heat from the IR rays keeps the earth's atmosphere warm and makes life possible. This phenomenon is known as the 'greenhouse' effect[1-3]. However, continuous human activities in the modern world have generated significant disturbances in this process. Rapid industrialization, urbanization and growing transportation facilities have enormously increased energy production and consumption[4-6]. In the process, the earth's surface temperature began to slowly escalate, causing a long-term change in average weather patterns at the local, regional, and global levels[7].
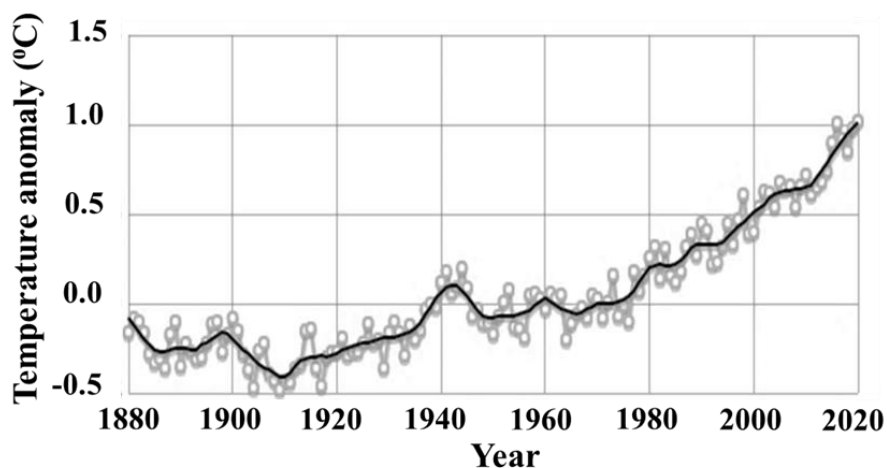
Fig. 1.1. Variation in surface air temperature of earth[8]

According to the National Oceanic and Atmospheric Administration's (NOAA) 2021 annual climate report, the earth's surface temperature increased at an average rate of 0.14 °C per decade from 1880 to 1980. But, since 1981, it has increased to 0.18 °C per decade. Between 1900 and 2020, the average surface air temperature of the earth has increased by about 1 °C, **Fig. 1.1**. The years 2016 and 2020 were regarded as the warmest years during this period[8].
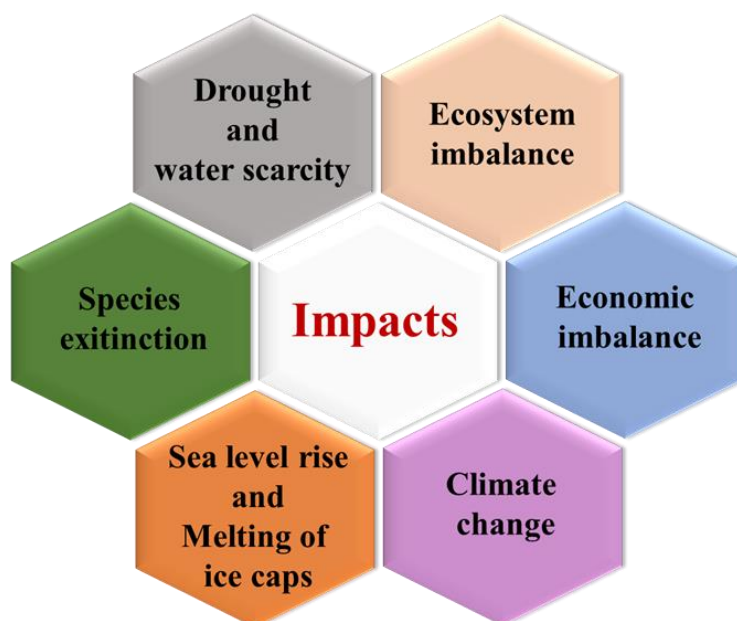
Fig. 1.2. Impacts of global temperature rise

Since temperature rise and extent of climate-related risks vary with geography, level of development, magnitude and duration of warming, its impacts are uneven around the planet, **Fig. 1.2**. The equatorial region will be the warmest in the summer, while the polar region will be the most affected in the winter. During the summer, approximately 14% of the population

was subjected to extreme heatwaves. Such a heatwave struck India and Pakistan in 2015, which is anticipated to persist in the following years. Drought and water scarcity have thus become a common problem in South Asia, North and South Africa, Australia, Southern Europe and Southern America. As a result, rainforests are disappearing, arid vegetation and deserts are increasing. This endangers the existence of several terrestrial species, some of which are on the verge of extinction and others are already extinct. The consequent ecosystem imbalance will be a major concern for the human species in the long run. Observations have already shown a few indications of this disaster. Diminishing pollinating insects such as bees, hoverflies and blowflies had an indirect impact on humanity by lowering agricultural productivity. Similarly, the external temperature environment significantly changed the period of sprouting, growth, flowering and several other mechanisms of the plants, eventually affecting food security. Extreme precipitation and flooding devastate different regions of the planet while people are under water stress in specific locations. It is also worth noting that the current global environment has significantly impacted on economic growth. United States loses approximately 2.3% (worth of 446 billion USD) of their Gross Domestic Product (GDP) for each degree Celsius increase in temperature[9-13].

Because of temperature rise, the aquatic environment and life have undergone substantial changes. The rise in ocean temperature, acidity and the fall in O_2 level risks the marine diversity and fisheries. It causes coral reef collapse and the disruption of ocean food webs, etc. Furthermore, the sea level is constantly rising due to the melting of glaciers in the Arctic region. As a result, coastal areas and island settlements are destroyed with time[14, 15].

According to the Intergovernmental Panel on Climate Change (IPCC), a United Nations body established to assess climate change science, modern humans have never seen the observed changes in our global climate before, and some of these changes will be irreversible over the next hundreds to thousands of years. Unfortunately, the situation is deteriorating, necessitating immediate action to tackle the issue and potentially avoid some of the worst outcomes[16].

1.3. Major reasons

1.3.1. Global warming

The degree of warming experienced by the earth in future is determined by how much carbon dioxide and other greenhouse gases we emit in the following decades. Rapid industrialization, growing transportation rates and innovative technologies have enormously

increased energy production and consumption. Since fossil fuels are the primary energy source, subsequent CO_2 emissions increased. Human activities add around 11 billion metric tonnes of carbon to the atmosphere each year, which is more than natural processes can remove, resulting in annual increases in atmospheric CO_2. It is estimated that industrial activities alone elevated CO_2 levels by nearly 50%[17]. Livestock digestion, manure and fertilizers used in agricultural practices, all led to an increase in the concentration of NO_x and CH_4 emissions in the air. Furthermore, the consumption of refrigerants has resulted in a massive discharge of chlorofluorocarbon (CFC) gases. The tremendous rise in greenhouse gas levels in the atmosphere facilitated long-term heating of the earth's atmosphere, known as global warming[7, 18, 19]. Countermeasures to make life easier in hotter climates, such as air conditioning and refrigeration, will unfortunately require more electricity from coal-burning power plants, generating CO_2. This will further exacerbate global warming and have major consequences for human health and the environment.

1.3.2. Deforestation

The rising population prompted the expansion of habitation and agricultural fields. Massive area of forests has been razed in this regard, mostly tropical rainforests. This disturbed the CO_2 to O_2 conversion rate and therefore, increased the CO_2 level in the atmosphere, thereby accelerated global warming and temperature rise[20]. In addition, since tropical forests reside many animal and plant species, deforestation is also a severe threat to biodiversity[21]. Losing trees and plants can cause soil to loosen up, making it prone to erosion[22]. Thereby, deforestation both directly and indirectly becomes a concern for the human race.

1.3.3. Pollution

Pollution of different kinds has triggered excessive levels of greenhouse gas emissions. To be precise, air pollution from vehicle exhaust, factory and power plant discharges, emissions from agriculture and other sources are mainly CO_2 and NO_x gases[23]. The increase in greenhouse gas levels in the atmosphere directly influences the atmospheric temperature.

1.3.4. Urban Heat Island (UHI) effect

The phenomenon of UHI was discovered in the 1810s by a British scientist, Luke Howard, who noticed that the City of London was warmer than the surrounding rural area. Later, a detailed understanding of the concept was given by Oke in 1982[24-26]. It is the phenomenon in which an urban sector suffers a warmer temperature compared to the surrounding rural area, **Fig. 1.3**,[27, 28]. Cities are densely populated with concrete constructions,

roadways and pavements. They are often made of asphalt concrete, which absorbs a large amount of infrared (IR) radiation from the sunlight. The solar spectrum contains 52% IR radiations (700-2500 nm), **Fig. 1.4**, and heat is the consequence of IR rays[29]. As a result, buildings, roads and pavements will gradually heat up over the day and the heat generated will be slowly released into the environment. However, this heat will be trapped in between the tall multistore buildings in the area, generating a local temperature rise. The lack of vegetation and wind flow aggravated this problem. Since the process occurs across a large area of land, it considerably raises the atmospheric temperature in that region.
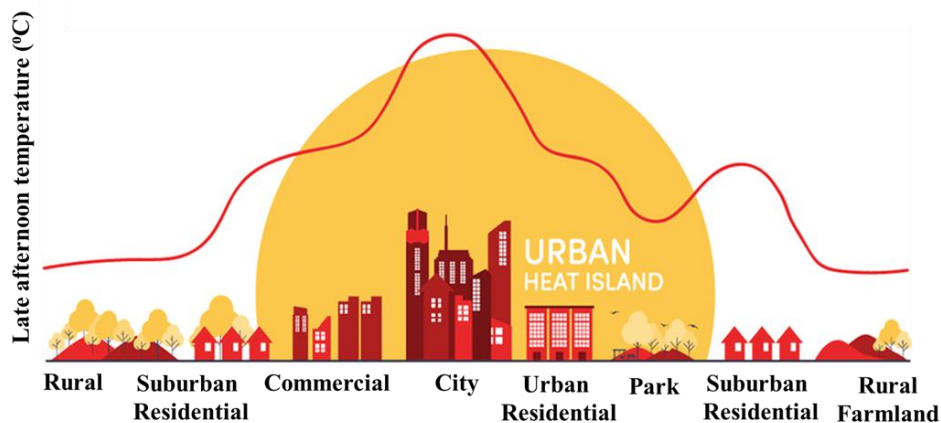
Fig. 1.3. Urban heat island effect[30]

The situation will be different in suburban and rural locations, where there are fewer buildings and roads, relatively denser green patch. The reports suggest that the daytime average annual temperature of certain metropolitan cities are 3 ℃ higher than that of the nearby rural region. However, it will rise to an average of 12 ℃ during the night[31]. Whether in urban or rural place, the environment is always hot during the day because of continuous sunshine. As a result, the influence of UHI will only result in a few degrees of temperature increase. Whereas, since the night is often cooler, the effect of UHI is more evident and results in a substantially higher temperature, making city life vulnerable.
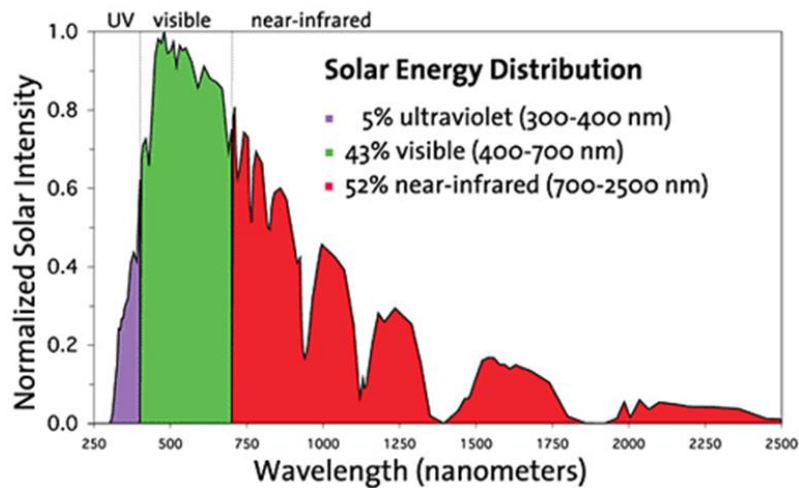
Fig. 1.4. Solar power distribution curve[32]

The UHI is more prominent in the summer season. As this phenomenon may affect the quality of life in the cities, various scientific studies have been carried out. The intensity of UHI phenomena depends on the factors such as,

- Local weather conditions
- Replacement of natural soil cause heat accumulation, generally, heat drain occurs through evapotranspiration in a rural area
- Use of asphalt, concrete and highly IR absorbing metal sheets for construction
- Geometry of buildings and extent of dark surfaces with low albedo
- Heat produced by combustion and by animal metabolism
- Excessive greenhouse gas release from factories and vehicles
- Reduction in water bodies like lakes, ponds, etc
- Urban vegetation design
- Extreme atmospheric pollution[33]

1.4. Consequences of UHI effect

The surveys reveal that more than half of the world's population resides in cities, which is expected to surpass 70% by 2050[34]. In the background of rising urbanization and technological advancement, the prevalence of hotter cities is increasing because of UHI. The major consequences of UHI are

- Seriously affects the living environment in the city
- Deteriorates urban ecosystem
- Huge release of pollutants from refrigerants and formation of smog

- Degradation of quality of fresh air

- High thermal stress on residents and public

- Heat-related illness and increase in risk of mortality

- Increase in peak electricity demand

- Significant rise in consumption of cooling appliances thereby cost[31, 35-38]
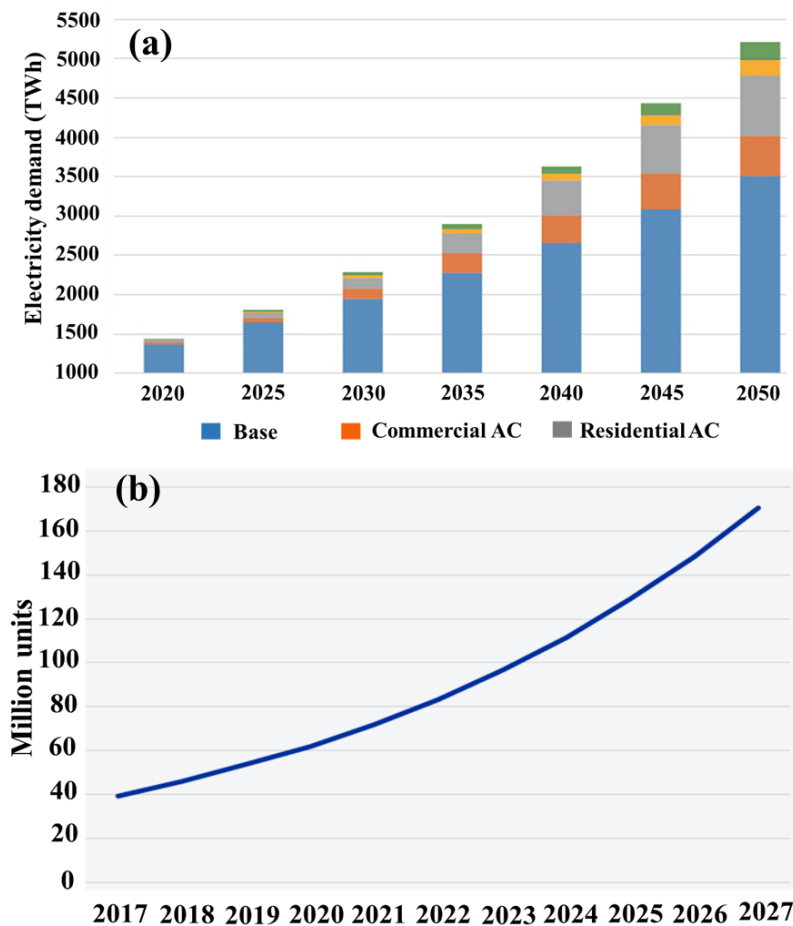
Fig. 1.5. (a) Electricity demand for cooling[39] and (b) consumption rate of air conditioners[40]

UHI profoundly impacted building energy consumption by increasing space cooling demand and decreasing space heating demand. Considering different climatic (humidity, solar radiation, wind speed, heating and cooling degree days) and economic (local GDP, energy price) parameters, extensive studies have been carried out to estimate the electricity demand in different parts of the world. It concluded that ambient temperature in the city plays a critical role in determining the variation in electricity demand. Because of UHI, the winter appeared to be at a higher ambient temperature, which subsequently reduced the need for heating inside buildings. At the same time, higher ambient temperature in the summer increases the need for cooling, **Fig. 1.5a**. Therefore, a huge hike is observed in the consumption rate of air

conditioners (AC) and other cooling appliances in proportion to the temperature rise. **Fig. 1.5b** shows the exponential increase in AC usage from 2020 onwards, which is expected to further enhance in the following years. Though AC temporarily helps to keep the building temperature optimum, the exhaust heat and gas pollutants discharged from the machines can create a local heating. It significantly contributes to elevate the ambient temperature of a metropolitan city, which eventually accelerates the temperature rise in the area[31, 35-40].
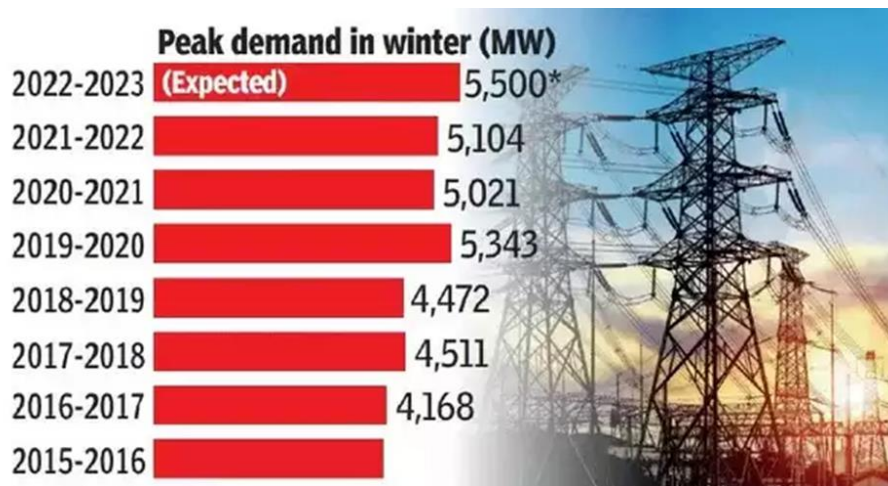
Fig. 1.6. Peak electricity demand chart in Delhi (Google images[1])

It was also reported that the temperature elasticity for the warm countries are 1.7% and cold countries are 0.51%. The potential increase in the peak electricity demand triggered by ambient warming is also high. According to recent studies, peak electricity demand rises from 0.45 to 4.6% for every degree of ambient temperature rise. This is equivalent to an additional charge of around 21 ± 10.4 W per degree of temperature rise per person[41]. Overall, the statistics indicate that the issue of rising electricity demand has a greater impact in hotter countries. **Fig. 1.6** gives an overview of the peak electricity demand in New Delhi for 8 years from 2015 to 2023. Electricity consumption has steadily increased over time and is likely to rise further in the upcoming years.

The UHI crisis also threatens present global health progress and causes health disparities between and within populations. Severe dehydration, heat-related illness, heat stress and in extreme cases, death are some of the direct consequences of UHI. Meanwhile, the indirect hurdles to overcome are the lack of clean air, safe drinking water, sufficient food, secure shelter and ecological imbalance. The IPCC suggested that the world must limit the temperature rise to 1.5 ºC. Every additional one-tenth degree of temperature rise will seriously impact on the environment and existence of the human species[42]. Unfortunately, in the contemporary world,

there has been a large population movement from rural to urban areas in quest of more work opportunities and better living standards. As a result, the population density is increasing and urban sectors are expanding, which worsens the repercussions.

1.5. Mitigation of UHI

The UHI mitigation measures focus on creating balance in the thermal budgets of the city by lowering heat intake and boosting thermal loss so that it can bring down the cooling energy consumption in buildings, minimize the heat-related health issues and improve the city life. The imperative strategy put forward by the scientific community is customise the city construction in a more scientific manner. That is, include inland water bodies, encourage rooftop farming, use of high albedo materials (HAM) and cool coatings, **Fig. 1.7**.

Urban inland waterbodies

Green roofs

High albedo materials

Cool coatings
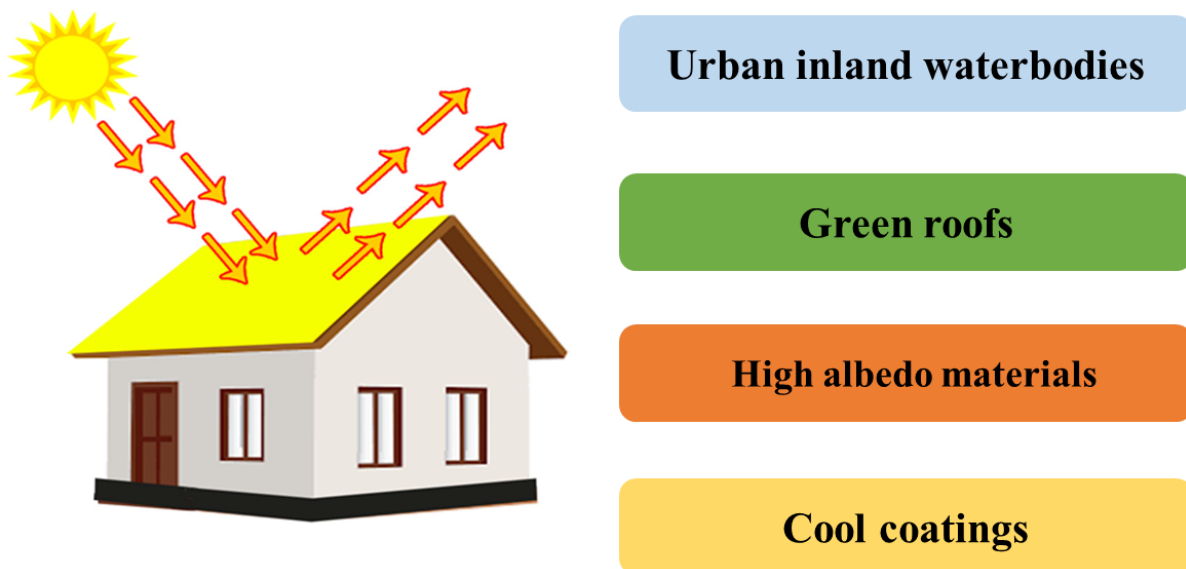
Fig. 1.7. Solutions to mitigate UHI

i) Urban inland water bodies: It helps to improve the evapotranspiration process, thus maintaining humidity in the inhabited area and controlling local surface temperature.

ii) Green roofs: It exclusively focuses the vegetation on rooftops and wall sides, which effectively reduces indoor temperature and air quality. However, it demands prior appropriate planning and specific design in the construction, which could be expensive. Lack of adequate design can adversely affect the building's strength and life by developing cracks and leaks on the roofs and walls. Most importantly, daily maintenance is essential to have the desired results in reducing UHI in the long run[43].

iii) High albedo materials: Materials like white marble and mosaic, metal, clay tile and sand can effectively reflect the solar rays to a great extent. Hence, utilizing these materials can

bring down the surface temperature of roofs and pavements. However, depending on the structure and purpose, the material must be chosen irrespective of its reflectivity[44].

iv) Cool coatings: Utilizing high albedo coatings for urban paving and building has evolved as the most efficient and economically viable strategy in reducing urban warming. High albedo coatings are known as 'cool' coatings, which can be applied on rooftops, exterior walls, roads and pavements. The area of roof surfaces in a city is 20-40% and roads/ pavements 29-44% of the total exposed area of solar radiation[45]. Therefore, implementing cool coatings that reflects solar rays was highly successful in reducing the indoor and outdoor temperature in summer thereby the energy consumption for cooling. According to statistics, replacing conventional roofs with cool roofs can result in direct energy savings of 20-70%[46].
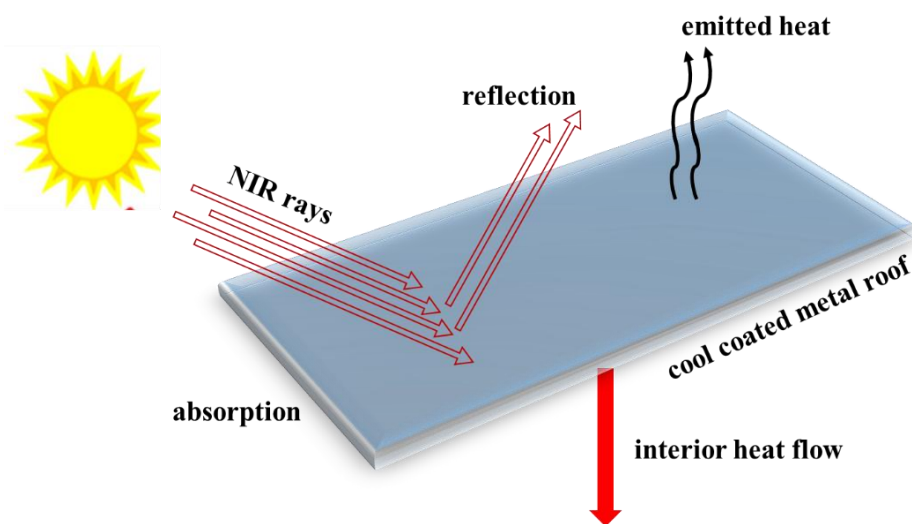
Fig. 1.8. Mechanism of cool coating

'Cool' coatings work through the mechanism of IR reflectance. On reflecting the heat producing IR rays in the solar spectrum, **Fig. 1.4**, the coating reduces the heat build-up on the surface. Therefore, the heat transfer from the surface to the interior of the building will be low, consequently, the interior temperature. Similarly, it will minimise the heat convection to the atmosphere and decelerate UHI, **Fig. 1.8,**[6, 44, 47, 48]. The photograph of a typical cool roof coating is shown in **Fig. 1.9a** and high reflective blue roads developed in Qatar is shown in **Fig. 1.9b**. Major benefits of cool coatings are,

- Mitigation of UHI
- Reduction of indoor and outdoor temperature
- Eliminate the threat of heat-related health issues

- Brings down the cooling load in summer

- Improve the life span of the coating substrate

- Avoid frequent maintenance

- Cost benefits[6, 44, 47, 48]

It implies that using cool coatings is extremely beneficial to society in dealing with the current global scenario of rising temperatures and increasing cooling energy demand.
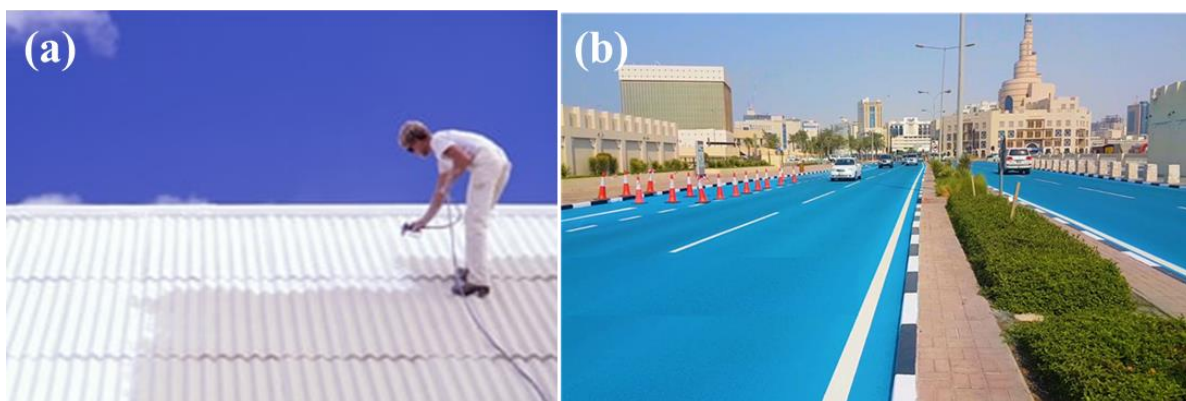
Fig. 1.9. (a) Cool roof coating and (b) cool road in Qatar (Image courtesy: Google images[2, 3])

1.6. IR reflective inorganic pigment

One of the most effective cool coating strategies for building roofs and walls is paints containing special inorganic pigments that reflect IR rays. Generally, inorganic pigments are insoluble solid materials that are utilized as dispersions to colour the medium or surface on which they are to be used. However, IR reflective pigments can be coloured or white, depending on whether it absorb the visible spectrum or not. The IR rays are too low in energy to induce any electronic transition in these pigments due to their peculiar chemical structure. Therefore, instead of absorbing, the IR rays will get reflected, refracted and scattered off from the pigment particle surface at different angles, known as diffused reflectance. Since IR reflectivity is an inherent characteristic property, predicting IR reflectivity of a pigment is almost impossible. Nevertheless, there are two important factors which influence the IR reflectivity of an inorganic pigment[29, 49, 50].

i)   Particle size: It is an important parameter of inorganic pigment powder for achieving high IR reflectance. The IR rays that fall on the pigment sample are reflected from the particle surface, while the rays that penetrate into the particle are reflected from the grain boundaries. Therefore, as particle size reduces, surface area and grain boundary increases, which increases the number of reflections. Consequently, the penetration depth of the

incident rays reduces, hence the extent of absorption decreases. The highest reflectance was recorded when the particle size is more than half of the wavelength of the incident radiation. Therefore, the particle size should be maintained between 0.35-0.55 μm to achieve the maximum reflectance in the 700-1100 nm region[29, 49, 50].

ii) Refractive index: The refraction of incident IR rays is enhanced as the refractive index increases. Consequently, IR reflectivity of the pigment enhances[29, 49, 50].

Apart from this, for an IR reflective pigment incorporated coating, concentration of pigment particles, particle dispersion, binder concentration and wavelength of the incident light are also important in determining the overall IR reflectance.

Inorganic pigments include metal oxides, chromates, sulfates, silicates, borates, molybdates, phosphates, vanadates, hydroxides and sulfides. Good opacity, dispersibility, excellent light fastness, weatherability, high chemical and temperature stability and low-cost manufacturing processes make inorganic pigment preferred over organic pigments in paint industries[51, 52]. Initially, white pigments like TiO_2, ZnO have been extensively used for cool coating applications because they had a high NIR solar reflectance R^* around 80%[53, 54]. Later, for aesthetic reasons, white pigments were replaced in the market by intense coloured pigments such as $PbCrO_4$ yellow, Cr_2O_3 green, $CdSe_{1-x}S_x$ red etc, **Fig. 1.10** [55, 56]. Though such pigments are highly IR reflective and come in various colour shades, the presence of acute and chronic toxic metals like Pb, Cr, Cd and Se has hindered its utilization[57, 58]. Many of these harmful inorganic pigments have already been banned in European countries[57]. In addition, cost of the pigment is also a matter of concern. $YIn_{0.9}Mn_{0.1}O_3$ blue is a very recent addition to the pigment market[59]. However, In and the rare earth metal Y are couple of expensive metals in this compound. Therefore, researchers have always been interested in developing novel low-cost, non-toxic pigments that show intense colour and high IR reflectivity. A few of the recently reported IR reflective inorganic pigments are summarized in **Table 1.1**.

$PbCrO_4$　　　**Cr_2O_3**　　　**$CdSe_{1-x}S_x$**　　　**$YIn_{0.9}Mn_{0.1}O_3$**
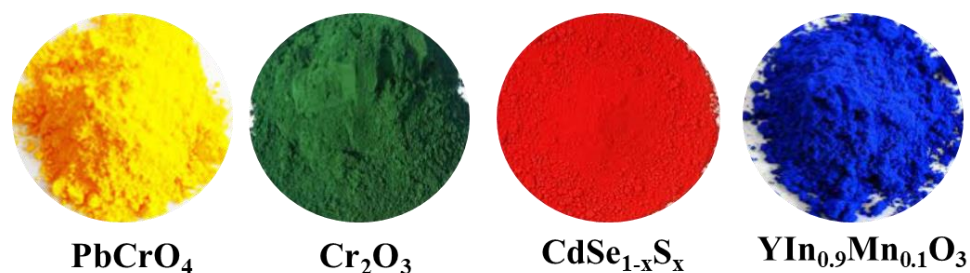
Fig. 1.10. Commercial IR reflective inorganic pigments

Table 1.1. CIE 1976 $L^*a^*b^*$ colour coordinates and R^* of reported pigments

Colour	Sample	L^*	a^*	b^*	R^*	Ref
Blue	$Ca_{0.9}La_{0.1}Al_{11.9}Co_{0.1}O_{19}$	73.3	-2.6	-34.1	70.7	[60]
	$Ca_{0.5}La_{0.5}Al_{11.5}Ni_{0.5}O_{19}$	75.6	-11.6	-28.3	67.1	[61]
	$Zn_{0.9}Co_{0.1}Al_2O_4$	64.5	-1.7	-45.3	63	[62]
	$ZnAl_2O_4:M = Co^{2+}/Nd^{3+}$	45.36	8.12	-36.9	63	[63]
	$YIn_{0.9-x}Mn_{0.1}Zn_{0.4}O_{3-\delta}$	46.58	3.01	-42.5	72.1	[64]
	$Sr_{0.6}Nd_{0.4}CuSi_4O_{10+\delta}$	68.7	-6.6	-24	68.6	[65]
	$Yin_{0.9}Mn_{0.1}O_3\text{-}ZnO$	49.94	-0.88	-40.5	70	[66]
	$CaAl_{11.7}Co_{0.1}Ti_{0.2}O_{19}$	64.89	3.88	-40.3	69.2	[67]
	$K_{0.3}WO_3$	32.5	-1.82	-10.23	66	[68]
	$Sr_{0.7}La_{0.3}Cu_{0.7}Li_{0.3}Si_4O_{10}$	49.6	10.4	-51.7	66	[69]
	$LaGa_{0.8}Mn_{0.2}Ge_2O_7$	45.77	14.92	-35.12	29	[70]
	$CoCr_{1.5}Al_{0.5}O_4$	51.6	-20.3	-11.4	43.5	[71]
	$YIn_{0.8}Mn_{0.2}O_3$	34.6	9.6	-38.9	41	[72]
	Al:Cu:Co:Ce:Nd 2:0.2:0.2:0.15:0.05	42.69	-8.9	-21.29	39	[73]
	$YB_{0.97}Mn_{0.03}O_3$	69.75	-5.46	-6.36	66.2	[74]
	$Mg_{0.8}Co_{0.2}WO_4$	46.28	6.33	-46.97	38	[75]
Green	$YInO_3\text{-}ZnO$	77.3	-15.7	9.3	41.3	[76]
	Y_2BaCuO_5	67.08	-33.33	21.59	50	[77]
	$Y_3Fe_4AlO_{12}$	79.55	-4.54	40.93	87.66	[78]
	$Bi_{0.6}Cr_{0.4}PO_4$	83.6	-7.91	0.14	84.63	[79]
	$Co_{0.1}Zn_{0.9}O$	62	-30.4	2.2	39.58	[80]
	$Y_{5.2}Nd_{0.8}MoO_{12}$	90.2	-8.0	17.9	89.9	[81]
	$Y_3Al_{4.7}Cr_{0.3}O_{12}$	73.48	-9.89	6.25	75.96	[82]
	$In_{1.9}Sc_{0.1}Cu_2O_5$	39.03	-25.16	13.17	68	[83]
	$La_2Cu_{0.8}Li_{0.2}Ge_{1.8}P_{0.2}O_8$	70.01	-37.72	-13.55	51	[84]
	$Bi_{12}Mn_{0.2}Ti_{0.8}O_{20}$	45.9	-9.86	25.8	> 50	[85]

Color	Material					Ref
Red	$0.1Fe_2O_3@SiO_2$	28.07	25.63	16.21	62.7	[86]
	$Li_2Mn_{0.9}Ti_{0.1}O_3$	38.28	34.82	29.8	86.52	[87]
	HGM/BiOI	62.21	25.97	29.51	92.64	[88]
	$Y_2Ce_{1.8}Tb_{0.2}O_7$	49.57	26.01	33.4	67.5	[89]
	Cr doped $YAlO_3$	45.26	34.24	22.89	43.1	[90]
	$0.1Ti^{4+}$ doped Li_3AlMnO_5	51.98	40.05	38.61	45	[91]
	Mica/$Ce_{1.6}Y_{0.4}S_3$ hybrid	58.82	33.15	15.94	93.66	[92]
	$KZn_{0.9}Fe_{0.1}PO_4$	36.39	26.34	16.28	46.1	[93]
	$Ce_{25}Pr_{0.8}MoO_y$	54.3	22.1	24.1	> 65	[94]
	Cu-/In-co-doped 2% ZnS_xSe_{1-x}	40.06	47.65	37.65	69.45	[95]
	$Y_{1.75}Tb_{0.25}Zr_{1.65}Fe_{0.35}O_{6.925}$	70	23	38	> 80	[96]
Yellow	$Sr_2Zr_{0.6}Tb_{0.4}O_4$	88.91	-6.35	53.36	90.49	[97]
	$Bi_{1.75}Y_{0.25}Ce_2O_7$	83.36	3.52	51.36	90.2	[98]
	$(BiV)_{0.6}(CaMo)_{0.4}O_4$	81.82	1.09	75.77	87	[99]
	$Bi_{1.7}Y_{0.3}W_{0.7}Mo_{0.3}O_6$	83.44	10.42	71.8	95.74	[100]
	$Li_{0.1}La_{0.1}Bi_{0.8}Mo_{0.2}V_{0.8}O_4$	83.3	6.04	81.86	90	[101]
	Fe^{3+}: Ti^{4+} = 1:3 molar ratio	74.31	10.67	29.09	80.3	[102]
	$La_2Mo_{1.95}Fe_{0.05}O_9$	85.5	1.33	23	75	[103]
	$GdCe_{0.65}Mo_{0.35}O_{3.5+Y}$	90.88	3.38	39.07	91	[104]
	$Yb_{4.8}Bi_{1.2}Mo_2O_{15}$	82.9	3.2	60.5	89.4	[105]
	$Y_{3.8}Zr_{0.2}MoO_{9+\delta}$	93.1	-4.8	57.5	90.1	[106]
	Bi_3YO_6	68.39	20.77	59.48	92.29	[107]
	5% Ni-doped $BaTi_5O_{11}$	95.13	-8.99	65.6	66.59	[108]
	$Bi_4Ti_3O_{12}$	90.72	-2.11	22.66	95	[109]
	$BiVO_4$	82.43	4.25	76.26	73.51	[110]
Orange	$Sr_4Mn_2(Cu_{0.5}Zn_{0.5})O_9$	64	19.8	52.3	83	[111]
	$BiFe_{0.8}Al_{0.2}O_3$/mica-titania	62.27	15.16	37.88	53	[112]
	$Bi_{2.6}Fe_{0.4}YO_6$	54	20	32	65	[107]
	$Al_{0.92}Fe_{0.08}PO_4$	56.54	16.89	29.79	73	[113]
	$Bi_{0.6}La_{0.4}FeO_3$	61.92	23.52	21.04	72	[114]
	N-doped $Mg_{0.7}Fe_{0.3}TiO_{3+\delta}$	55.02	20.89	23.51	54	[115]

$Bi_2Ce_{1.5}Ti_{0.5}O_7$	72.36	13.38	34.49	65	[116]
Bayferrox orange	53.9	23.4	42.3	57	[111]
Fe doped $MgTiO_3$	52.02	23.94	39.37	80.1	[117]
$La_{0.3}Bi_{0.7}YO_3$	80.56	7.74	34.88	95.57	[118]
$Ho_6Mo_2O_{15}$	77.2	0.1	56.1	98.1	[119]
$Li_2Mn_{0.95}Zr_{0.05}O_3$	41.96	36.78	33.61	89.14	[87]

Black	$YIn_{0.5}Mn_{0.1}Fe_{0.4}O_3$	30.82	-0.3	2.91	53.44	[120]
	$Ce_{0.8}Gd_{0.2}VO_4$	22.2	5.71	2.77	66.3	[121]
	30.1 wt% Co doped $ZnFe_2O_4$	26.8	0.3	-0.8	38.4	[122]
	$(CoO)_{0.5}(MgO:CaO)_{0.25}(Fe_2O_3)$	23.09	0.66	-0.88	24.5	[123]
	$NiFe_2O_4$	28.7	3.31	-0.59	52	[124]
	$Fe_{1.4}Cr_{0.5}Ti_{0.1}O_{3+\delta}$	25.5	2.01	0.1	50.9	[125]
	$Ca_2Mn_{0.85}Ti_{0.15}O_4$	23.8	4.45	2.83	66.2	[126]
	$((Al_2O_3)_{0.5}(Fe_2O_3)_{0.5})$ $(CoO)_{0.5}(MgO)_{0.5}\cdot$	24.4	1.4	1.2	23.9	[127]
	$CuCr_{1.93}Fe_{0.07}O_4$	18.35	1.15	-1.8	27.7	[128]

Brown	$SrSn_{0.9}Mn_{0.1}O_3$	38	6.1	11.4	42	[129]
	$Fe_2O_3: Sb_2O_3: SiO_2: Al_2O_3:$ $TiO_2 = 70: 10: 12: 2: 6$ wt%	35.57	15.92	11.23	46.7	[130]
	$MgAlFeO_4$	65.49	14.1	24.84	80	[131]
	$Y_3Al_3Fe_2O_{12}$	78.73	1.98	20.69	74.64	[132]
	$Zn_{0.9}Mg_{0.1}Fe_2O_4$	48.06	14.16	9.91	51	[133]
	$Zn_{0.9}Ni_{0.1}Fe_2O_4$	31.75	18.43	12.18	61	[124]
	5 wt% Pr doped $ZnFe_2O_4$	39.7	26.1	25.9	60.1	[122]
	$BiFeO_3$/mica titania	53.42	15.87	21.06	57.3	[112]
	$La_{0.3}Bi_{0.35}Tb_{0.35}YO_3$	55.34	14.92	23.14	78.7	[118]
	$La_2Ce_{1.8}Pr_{0.2}O_7$	54.29	16.16	19.18	84	[134]
	Ce: Pr: Fe - 2: 0.2: 0.1	41.03	18.89	17.13	82.7	[135]
	$Mg_{0.8}Mn_{0.2}Fe_2O_4$	39.51	3.73	5.39	56.7	[136]
	$Bi_{3.75}Ce_{0.25}Ti_3O_{12}$	51.66	17.8	24.4	71.8	[137]

The listed pigments have displayed impressive colour strength and good reflectance properties. Unfortunately, only a few succeeded in breaking into the pigment industry. It emphasizes the fact that there is still room for improvement and scientific inputs are necessary to overcome these shortcomings. Meanwhile, the rising energy cost also drives the need for advances in the field of inorganic pigments.

1.7. Multifunctional inorganic pigment

Roofs contributed roughly 60% of the total cooling demand of the building in different temperature zones[6]. Roof coatings, whether on concrete or metallic sheets, have thus become critical when constructing a potentially cool structure. At the same time, the roof's endurance is much more important in order to receive a long-term output from their top cool coatings. Unfortunately, it is inadequate for metallic roofs, particularly iron-rich alloys, which are prone to corrosion when exposed to harsh external conditions. Therefore, IR reflective coatings alone will not be sufficient to achieve long-lasting temperature regulation in cool coatings. In this connection corrosion resistant inorganic pigments are essential to protect the roof from rusting. $PbCrO_4$, Cr_2O_3, $Zn_3(PO)_4$, etc, are the widely used anticorrosive pigments in the market[138-140]. Since chromates are categorized as a hazardous material and zinc phosphate requires high material concentration, implementing these pigment coatings under cool coat will be inappropriate[58, 140]. Furthermore, the present multilayer coating protocol for managing a stable cool roof surface, which is cool paint coating over anticorrosive primer, has issues such as high cost, massive material consumption and enormous workload. Hence, integrating the features colour, reflectance and corrosion resistance on a single material would be ideal to resolve all these allegations.

Beyond the traditional source of colour, inorganic pigments have been utilized for different applications.

- Luminescent pigments: Absorbs radiations and emit in the longer wavelength. eg: $SrAl_2O_4$: Eu^{2+}, Dy^{3+} [141]
- Camouflage pigments: Regulate the reflectance of the substrate to match with its surroundings. eg: Cr_2O_3 green[142]
- Anticorrosive pigments: Prevent metal corrosion by passive or active mechanism. eg: $Zn_3(PO_4)_2$, Cr_2O_3 etc[140]
- Thermochromic pigments: Change its colour in response to the temperature gradient. eg: Tb doped Cr doped Al_2O_3 [143]

- Security pigments: Used for counterfeit identification.eg: La doped $SrAl_2O_4$ [144]

Unfortunately, relatively few investigations have been carried out to develop multifunctional pigments that works simultaneously in the dimensions of colour, IR reflectance and corrosion resistance[145]. Developing the kind of multifunctional inorganic pigment would be extremely challenging. However, it has the potential to have a significant impact on the industrial sector while also being extremely helpful to society and the environment. In this scenario, the present thesis made an effort to design a new inorganic pigment composition having intense colour, high IR reflectivity and good corrosion resistance properties, **Fig. 1.11**. Further, the works were also extended to address the issue of a couple of commercial inorganic pigments using rational synthetic strategies.
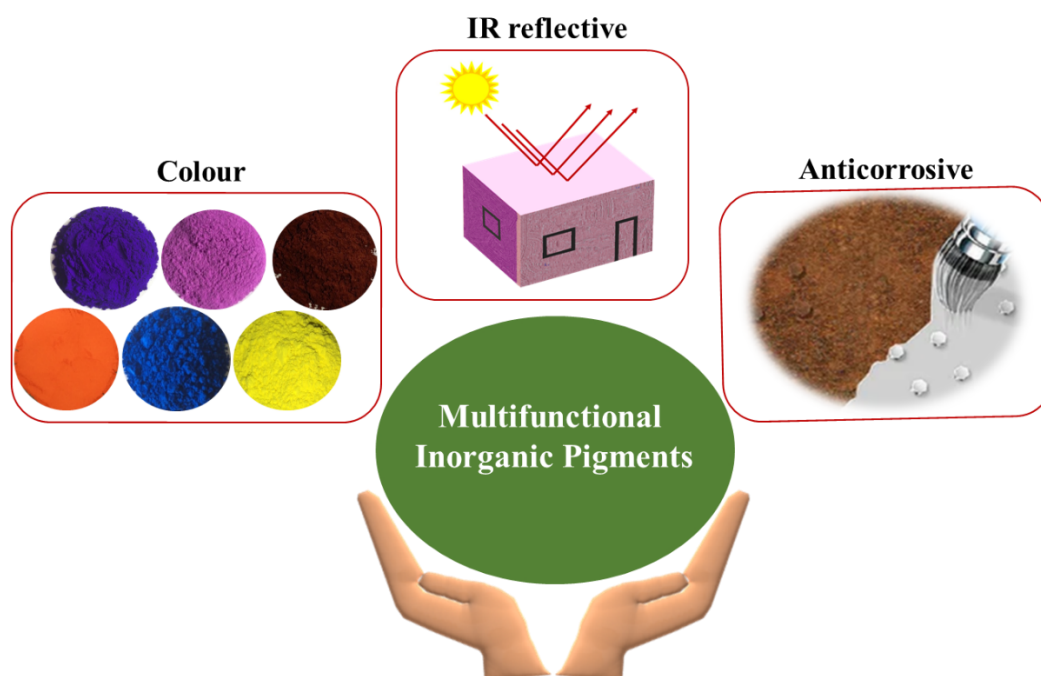
Fig. 1.11. Multifunctional inorganic pigments (Google images[4])

1.8. Objectives of the thesis

- Design and development of cost-effective Pb, Cr, Se and Cd free inorganic pigments
- Fine tuning the synthetic strategies
- Investigation on origin of colour and its structural correlation
- Study of reflectance property of the pigment and coatings
- Evaluation of temperature shielding ability of the coatings
- Exploration of anticorrosive property and its protection mechanism

Taking into account the challenges and focusing on the objectives, the current thesis provided four working chapters, which are organized as follows,

Design and development of multifunctional inorganic pigments for cool coating applications

Chapter 2A — **Synthesis of phosphate pigments and study of its colour: $NaZn_{0.9}Co_{0.1}PO_4$ blue, $LiZn_{0.9}Co_{0.1}PO_4$ purple and $LiMg_{0.8}Co_{0.2}PO_4$ magenta**

Chapter 2B — **Investigation on NIR reflectance and anticorrosive properties of $NaZn_{0.9}Co_{0.1}PO_4$ blue and $LiMg_{0.8}Co_{0.2}PO_4$ magenta**

Chapter 3 — **Cost reduction of $BiVO_4$ yellow through complex pigment strategy using ZnO without colour deterioration**

Chapter 4 — **Synthesis of high reflective $ZnFe_2O_4$ brown by Al^{3+} doping and investigation of NIR reflectance and anticorrosive properties**

Chapter 5 — **Colour tuning of $Bi_4V_2O_{11}$ from brownish red to intense orange by Si^{4+} doping and investigation of NIR reflectance and anticorrosive properties**

1.9. References

1. Oertel, C.; Matschullat, J. r.; Zurba, K.; Zimmermann, F.; Erasmi, S. J. G., Greenhouse gas emissions from soils-A review. **2016,** *76* (3), 327-352.

2. Kweku, D. W.; Bismark, O.; Maxwell, A.; Desmond, K. A.; Danso, K. B.; Oti-Mensah, E. A.; Quachie, A. T.; Adormaa, B. B. J. J. o. S. r.; reports, Greenhouse effect: greenhouse gases and their impact on global warming. **2018,** *17* (6), 1-9.

3. Shakoor, A.; Shakoor, S.; Rehman, A.; Ashraf, F.; Abdullah, M.; Shahzad, S. M.; Farooq, T. H.; Ashraf, M.; Manzoor, M. A.; Altaf, M. M. J. J. o. C. P., Effect of animal manure, crop type, climate zone, and soil attributes on greenhouse gas emissions from agricultural soils-A global meta-analysis. **2021,** *278*, 124019.

4. Sumaira; Siddique, H. M. A. J. E. S.; Research, P., Industrialization, energy consumption, and environmental pollution: evidence from South Asia. **2023,** *30* (2), 4094-4102.

5. Liu, H.; Wong, W.-K.; Cong, P. T.; Nassani, A. A.; Haffar, M.; Abu-Rumman, A. J. F., Linkage among Urbanization, energy Consumption, economic growth and carbon Emissions. Panel data analysis for China using ARDL model. **2023,** *332*, 126122.

6. Rawat, M.; Singh, R. J. E.; Environment, B., A study on the comparative review of cool roof thermal performance in various regions. **2022,** *3* (3), 327-347.

7. Helbling, M.; Meierrieks, D. J. J. o. P. E., Global warming and urbanization. **2023,** *36* (3), 1187-1223.

8. Lenssen, N. J.; Schmidt, G. A.; Hansen, J. E.; Menne, M. J.; Persin, A.; Ruedy, R.; Zyss, D. J. J. o. G. R. A., Improvements in the GISTEMP uncertainty model. **2019,** *124* (12), 6307-6326.

9. Houghton, J. T.; Ding, Y.; Griggs, D. J.; Noguer, M.; van der Linden, P. J.; Dai, X.; Maskell, K.; Johnson, C., *Climate chage 2001*. 2001.

10. Luterbacher, J.; Dietrich, D.; Xoplaki, E.; Grosjean, M.; Wanner, H. J. S., European seasonal and annual temperature variability, trends, and extremes since 1500. **2004,** *303* (5663), 1499-1503.

11. Karmalkar, A. V.; Bradley, R. S. J. P. o., Consequences of global warming of 1.5 ºC and 2 ºC for regional temperature and precipitation changes in the contiguous United States. **2017,** *12* (1), e0168697.

12. Rowlinson, P.; Steele, M.; Nefzaoui, A. In *Livestock and global climate change*, Proceedings of the International Conferences in Hammamet, May, 2008; pp 17-20.

13. Goel, A.; Bhatt, R. J. I. J. o. L. S. B.; Research, P., Causes and consequences of Global Warming. **2012,** *1* (1), 27-31.

14. Carlson, A. E.; LeGrande, A. N.; Oppo, D. W.; Came, R. E.; Schmidt, G. A.; Anslow, F. S.; Licciardi, J. M.; Obbink, E. A. J. N. G., Rapid early Holocene deglaciation of the Laurentide ice sheet. **2008,** *1* (9), 620-624.

15. Newson, S. E.; Mendes, S.; Crick, H. Q.; Dulvy, N. K.; Houghton, J. D.; Hays, G. C.; Hutson, A. M.; MacLeod, C. D.; Pierce, G. J.; Robinson, R. A. J. E. S. R., Indicators of the impact of climate change on migratory species. **2009,** *7* (2), 101-113.

16. Jain, A. K. J. E. S. S. D., Global Carbon Budget 2022. **2022,** *14* (11), 4811-4900.

17. Hashimoto, K.; Hashimoto, K. J. G. C. D. R. F. G. S. D. b. R. E., Global temperature and atmospheric carbon dioxide concentration. **2019**, 5-17.

18. Deb, N. C.; Basak, J. K.; Paudel, B.; Kim, N. E.; Moon, B. E.; Kim, H. T. J. A. Q., Atmosphere; Health, Emission of CO_2 in a livestock barn based on diurnal activities and various growing stages of pigs. **2023**, 1-12.

19. Venkataiah, S.; Sthithapragna, G. J. M. T. P., Comprehensive evaluation of nano refrigerants: A review. **2023,** *72*, 937-942.

20. Fearnside, P. M.; Laurance, W. F. J. E. A., Tropical deforestation and greenhouseﻕÄêgas emissions. **2004,** *14* (4), 982-986.

21. Stuart, B. L.; Rhodin, A. G.; Grismer, L. L.; Hansel, T. J. S., Scientific description can imperil species. **2006,** *312* (5777), 1137-1137.

22. Das, T. K.; Haldar, S. K.; Gupta, I. D.; Sen, S. J. L. R. i. L. R., River bank erosion induced human displacement and its consequences. **2014,** *8* (3), 1-35.

23. Ebi, K. L.; McGregor, G. J. E. h. p., Climate change, tropospheric ozone and particulate matter, and health impacts. **2008,** *116* (11), 1449-1455.

24. Oke, T. R. J. Q. j. o. t. r. m. s., The energetic basis of the urban heat island. **1982,** *108* (455), 1-24.

25. Jabbar, H. K.; Hamoodi, M. N.; Al-Hameedawi, A. N. In *Urban heat islands: a review of contributing factors, effects and data*, IOP Conference Series: Earth and Environmental Science, IOP Publishing: 2023; p 012038.

26. Mohajerani, A.; Bakaric, J.; Jeffrey-Bailey, T. J. J. o. e. m., The urban heat island effect, its causes, and mitigation, with reference to the thermal properties of asphalt concrete. **2017,** *197*, 522-538.

27. Luber, G.; McGeehin, M. J. A. j. o. p. m., Climate change and extreme heat events. **2008,** *35* (5), 429-435.

28. Chapman, S.; Watson, J. E.; Salazar, A.; Thatcher, M.; McAlpine, C. A. J. L. E., The impact of urbanization and climate change on urban temperatures: a systematic review. **2017,** *32*, 1921-1935.

29. Malshe, V. C.; Bendiganavale, A. K. J. R. P. o. C. E., Infrared reflective inorganic pigments. **2008,** *1* (1), 67-79.

30. FULADLU, K.; RIZA, M. g.; ILKAN, M., The effect of rapid urbanization on the physical modification of urban area. **2018**.

31. Santamouris, M. J. S. o. t. T. E., Analyzing the heat island magnitude and characteristics in one hundred Asian and Australian cities and regions. **2015,** *512*, 582-598.

32. Cambie, D.; Noel, T. J. A. o. S. F. C., Solar photochemistry in flow. **2018**, 1-27.

33. Stone, B.; Hess, J. J.; Frumkin, H. J. E. h. p., Urban form and extreme heat events: are sprawling cities more vulnerable to climate change than compact cities? **2010,** *118* (10), 1425-1428.

34. Organization, W. H., Health as the pulse of the new urban agenda: United Nations conference on housing and sustainable urban development, Quito, October 2016. **2016**.

35. Lai, L.-W.; Cheng, W.-L. J. S. o. t. t. e., Air quality influenced by urban heat island coupled with synoptic weather patterns. **2009,** *407* (8), 2724-2733.

36. Roth, M., -Urban Heat Islands. In *Handbook of environmental fluid dynamics, volume two*, CRC Press: 2012; pp 162-181.

37. Piracha, A.; Chaudhary, M. T. J. S., Urban air pollution, urban heat island and human health: a review of the literature. **2022,** *14* (15), 9234.

38. Leal Filho, W.; Echevarria Icaza, L.; Emanche, V. O.; Al-Amin, A. Q. J. I. j. o. e. r.; IJERPH, p. h., An evidence-based review of impacts, strategies and tools to mitigate urban heat islands. **2017,** *14* (12).

39. Barbar, M.; Mallapragada, D. S.; Alsup, M.; Stoner, R. J. S. D., Scenarios of future Indian electricity demand accounting for space cooling and electric vehicle adoption. **2021,** *8* (1), 178.

40. Kumar, S.; Kachhawa, S., *Demand analysis for cooling by sector in India in 2027*. Allaince for an Energy Efficient Economy: 2018.

41. Santamouris, M.; Cartalis, C.; Synnefa, A.; Kolokotsa, D. J. E.; buildings, On the impact of urban heat island and global warming on the power demand and electricity consumption of buildings-A review. **2015,** *98*, 119-124.

42. Arias, P. A.; Bellouin, N.; Coppola, E.; Jones, R. G.; Krinner, G.; Marotzke, J.; Naik, V.; Palmer, M. D.; Plattner, G.-K.; Rogelj, J. J. C. c., Technical summary. **2021,** *51*, 221-227.

43. Jamei, E.; Chau, H. W.; Seyedmahmoudian, M.; Stojcevski, A. J. S. o. t. T. E., Review on the cooling potential of green roofs in different climates. **2021,** *791*, 148407.

44. Santamouris, M.; Synnefa, A.; Karlessi, T. J. S. e., Using advanced cool materials in the urban built environment to mitigate heat islands and improve thermal comfort conditions. **2011,** *85* (12), 3085-3102.

45. Akbari, H.; Matthews, H. D. J. E.; Buildings, Global cooling updates: Reflective roofs and pavements. **2012,** *55*, 2-6.

46. Macintyre, H.; Heaviside, C. J. E. i., Potential benefits of cool roofs in reducing heat-related mortality during heatwaves in a European city. **2019,** *127*, 430-441.

47. Ashtari, B.; Yeganeh, M.; Bemanian, M.; Vojdani Fakhr, B. J. F. i. E. R., A conceptual review of the potential of cool roofs as an effective passive solar technique: elaboration of benefits and drawbacks. **2021,** *9*, 738182.

48. Pisello, A. L. J. S. E., State of the art on the development of cool coatings for buildings and cities. **2017,** *144*, 660-680.

49. Jeevanandam, P.; Mulukutla, R.; Phillips, M.; Chaudhuri, S.; Erickson, L.; Klabunde, K. J. T. J. o. P. C. C., Near infrared reflectance properties of metal oxide nanoparticles. **2007,** *111* (5), 1912-1918.

50. Fang, V.; Kennedy, J. V.; Futter, J.; Manning, J., *A review of near infrared reflectance properties of metal oxide nanostructures*. GNS Science: 2013.

51. Rosati, A.; Fedel, M.; Rossi, S. J. J. o. C. P., NIR reflective pigments for cool roof applications: A comprehensive review. **2021,** *313*, 127826.

52. Jose, S.; Joshy, D.; Narendranath, S. B.; Periyat, P. J. S. E. M.; Cells, S., Recent advances in infrared reflective inorganic pigments. **2019,** *194*, 7-27.

53. Fang, F.; Kennedy, J.; Carder, D.; Futter, J.; Rubanov, S. J. O. M., Investigations of near infrared reflective behaviour of TiO_2 nanopowders synthesized by arc discharge. **2014,** *36* (7), 1260-1265.

54. Kiomarsipour, N.; Razavi, R. S.; Ghani, K.; Kioumarsipour, M. J. A. S. S., Evaluation of shape and size effects on optical properties of ZnO pigment. **2013,** *270*, 33-38.

55. Sheffet, A.; Thind, I.; Miller, A. M.; Louria, D. B. J. A. o. E. H. A. I. J., Cancer mortality in a pigment plant utilizing lead and zinc chromates. **1982,** *37* (1), 44-52.

56. Kim, S. W.; Hasegawa, T.; Watanabe, M.; Sugimoto, K.; Saito, Y.; Uematsu, K.; Toda, K.; Sato, M. J. D.; Pigments, Environmentally friendly $Rb_3V_5O_{14}$ fluorescent red pigment. **2017,** *136*, 219-223.

57. Turner, A.; Filella, M. J. E. P., Lead and chromium in European road paints. **2023,** *316*, 120492.

58. Haney Jr, J. T.; Erraguntla, N.; Sielken Jr, R. L.; Valdez-Flores, C. J. R. T.; Pharmacology, Development of an inhalation unit risk factor for hexavalent chromium. **2014,** *68* (2), 201-211.

59. Smith, A. E.; Mizoguchi, H.; Delaney, K.; Spaldin, N. A.; Sleight, A. W.; Subramanian, M. A. J. J. o. t. A. C. S., Mn^{3+} in trigonal bipyramidal coordination: a new blue chromophore. **2009,** *131* (47), 17084-17086.

60. Rus, I.; Ianos, R.; Lazau, R.; Pacurariu, C. J. M. T. C., New blue pigments based on Col plus and Las plus doped hibonite for NIR-reflective coatings. **2023,** *28*.

61. Ianos, R.; Rus, I.; Lazau, R.; Pacurariu, C. J. C. I., Near-infrared reflective Ni, La-doped hibonite pigments for cool blue coatings. **2022,** *48* (23), 34428-34436.

62. Ianos, R.; Muntean, E.; Pacurariu, C.; Lazau, R.; Bandas, C.; Delinescu, G. J. D.; Pigments, Combustion synthesis of a blue Co-doped zinc aluminate near-infrared reflective pigment. **2017,** *142*, 24-31.

63. Primo, J. d. O.; Horsth, D. F.; Balaba, N.; Umek, P.; Anaissi, F. J.; Bittencourt, C. J. M., Synthesis of Blue Gahnite ($ZnAl_2O_4$: Co, Nd): A Cost-Effective Method for Producing Solar-Reflective Pigments for Cool Coatings. **2023,** *16* (4), 1696.

64. Zhang, M.; Feng, L.; Zeng, Z.; Yang, Y.; Sun, X. J. A. S. C.; Engineering, Environmentally Friendly High-Near-Infrared Reflectance Blue Pigment $YIn_{0.9-x}Mn_{0.1}M_xO_{3-\delta}$ Based on Li/Zn Doping. **2022,** *10* (41), 13877-13886.

65. Jing, J.; Zhang, Y.; Sun, J.; Zhao, X.; Gao, D.; Zhang, Y. J. D.; Pigments, A comparative study on different RE-doped (RE = Pr, Nd, Sm) $SrCuSi_4O_{10}$ blue pigments with high near-infrared reflectance. **2018,** *150*, 9-15.

66. Jose, S.; Jayaprakash, A.; Laha, S.; Natarajan, S.; Nishanth, K.; Reddy, M. J. D.; Pigments, $YIn_{0.9}Mn_{0.1}O_3$-ZnO nano-pigment exhibiting intense blue color with impressive solar reflectance. **2016,** *124*, 120-129.

67. Lv, K.; Zhu, Y.; Wang, L.; Chen, Z.; Zhang, Z.; Gao, Y. J. C. I., Codoping Ti in low Co-containing hibonite achieving excellent optical properties for near-infrared reflective pigment applications. **2023,** *49* (5), 7387-7395.

68. Cai, L.; Wu, X.; Gao, Q.; Fan, Y. J. D.; Pigments, Effect of morphology on the near infrared shielding property and thermal performance of $K_{0.3}WO_3$ blue pigments for smart window applications. **2018,** *156*, 33-38.

69. Jose, S.; Reddy, M. L. J. D.; Pigments, Lanthanum-strontium copper silicates as intense blue inorganic pigments with high near-infrared reflectance. **2013,** *98* (3), 540-546.

70. Saraswathy, D.; Rao, P. P.; Sameera, S.; James, V.; Raj, A. K. J. R. A., Monoclinic $LaGa_{1-x}Mn_xGe_2O_7$: a new blue chromophore based on Mn^{3+} in the trigonal bipyramidal coordination with longer apical bond lengths. **2015,** *5* (35), 27278-27281.

71. Hedayati, H.; Alvani, A. S.; Sameie, H.; Salimi, R.; Moosakhani, S.; Tabatabaee, F.; Zarandi, A. A. J. D.; pigments, Synthesis and characterization of $Co_{1-x}Zn_xCr_{2-y}Al_yO_4$ as a near-infrared reflective color tunable nano-pigment. **2015,** *113*, 588-595.

72. Smith, A. E.; Comstock, M. C.; Subramanian, M. J. D.; Pigments, Spectral properties of the UV absorbing and near-IR reflecting blue pigment, $YIn_{1-x}Mn_xO_3$. **2016,** *133*, 214-221.

73. Radhika, S. P.; Sreeram, K. J.; Nair, B. U. J. J. o. A. C., Rare earth doped cobalt aluminate blue as an environmentally benign colorant. **2012,** *1*, 301-309.

74. Fang, P.; Zhou, S.; Liu, Y.; Ye, J.; Wang, L.; Li, C.; Zhuo, S.; Chen, W. J. C. I., Solution combustion synthesis of gray-blue Mn-doped YBO_3 pigments with high NIR reflectance for energy-saving buildings. **2022,** *48* (24), 37203-37211.

75. Saraswathy, D.; Rao, P. P.; Raj, A. K.; Thara, T. A. J. C., Intense Blue Colors in Wolframite-Type Co^{2+}:$MgWO_4$ Oxides Through Distortion in Co^{2+} Octahedra. **2018,** *3* (2), 410-417.

76. Fedel, M.; Rosati, A.; Bertasini, M.; Rossi, S. J. P. i. O. C., Cu doped $YInO_3$-ZnO green colored NIR reflective pigments: Synthesis and application in PMMA based cool-roof coatings. **2023,** *182*, 107708.

77. Jose, S.; Prakash, A.; Laha, S.; Natarajan, S.; Reddy, M. L. J. D.; Pigments, Green colored nano-pigments derived from Y_2BaCuO_5: NIR reflective coatings. **2014,** *107*, 118-126.

78. Zhou, W.; Ye, J.; Zhuo, S.; Yu, D.; Fang, P.; Peng, R.; Liu, Y.; Chen, W. J. J. o. A.; Compounds, Synthesis and characterization of novel yellow-green Al-doped $Y_3Fe_5O_{12}$ nano-pigments with high NIR reflectance. **2022,** *896*, 162883.

79. Ding, C.; Han, A.; Ye, M.; Zhang, Y.; Yao, L.; Yang, J. J. S. E. M.; Cells, S., Synthesis and characterization of a series of new green solar heat-reflective pigments: Cr-doped $BiPO_4$ and its effect on the aging resistance of PMMA (Poly (methyl methacrylate)). **2019,** *191*, 427-436.

80. de Oliveira Primo, J.; Borth, K. W.; Peron, D. C.; de Carvalho Teixeira, V. n.; Galante, D.; Bittencourt, C.; Anaissi, F. J. J. o. A.; Compounds, Synthesis of green cool pigments ($Co_xZn_{1-x}O$) for application in NIR radiation reflectance. **2019,** *780*, 17-24.

81. Zhao, X.; Zhang, Y.; Huang, Y.; Gong, H.; Zhao, J. J. D.; Pigments, Synthesis and characterization of neodymium doped yttrium molybdate high NIR reflective nano pigments. **2015,** *116*, 119-123.

82. Chen, C.; Han, A.; Ye, M.; Chen, X.; Wang, J. J. J. o. S. S. C., Near-infrared solar reflectance and chromaticity properties of novel green ceramic pigment Cr-doped $Y_3Al_5O_{12}$. **2022,** *307*, 122873.

83. Divya, S.; Rao, P. P.; Sameera, S.; Raj, A. K. J. D.; Pigments, Influence of aliovalent cation substitutions on the optical properties of $In_2Cu_2O_5$ system. **2016,** *134*, 506-515.

84. Saraswathy, D.; Rao, P. P.; Raj, A. K.; Ajuthara, T. J. D.; Pigments, Enhanced pigmentary properties of rare earth germanates of the type $La_2CuGe_2O_8$ through CuO_6 octahedron distortion. **2017,** *142*, 472-480.

85. Medina, E.; Pathirana, V. H.; Li, J.; Ramirez, A.; Subramanian, M. J. J. o. S. S. C., Tetrahedral Mn^{4+} as chromophore in sillenite-type compounds. **2020,** *289*, 121463.

86. Soranakom, P.; Vittayakorn, N.; Rakkwamsuk, P.; Supothina, S.; Seeharaj, P. J. C. I., Effect of surfactant concentration on the formation of $Fe_2O_3@SiO_2$ NIR-reflective red pigments. **2021,** *47* (9), 13147-13155.

87. Gramm, G.; Fuhrmann, G.; Zimmerhofer, F.; Wieser, M.; Huppertz, H. J. Z. f. r. a. u. a. C., Development of High NIR-Reflective Red Li_2MnO_3 Pigments. **2020,** *646* (21), 1722-1729.

88. Gao, Q.; Wu, X.; Lu, D.; Fan, Y. J. D.; Pigments, Optical property and thermal performance of hollow glass microsphere/$BiOBr_{1-x}I_x$ composites as a novel colored near infrared reflective pigment. **2018,** *154*, 21-29.

89. Raj, A. K.; Rao, P. P.; Sameera, S.; Divya, S. J. D.; Pigments, Pigments based on terbium-doped yttrium cerate with high NIR reflectance for cool roof and surface coating applications. **2015,** *122*, 116-125.

90. Chen, Y.; Zou, J.; Lin, H.; Zhang, P. J. J. o. A.; Compounds, Enhancing colour and solar reflective performances for Cr-doped $YAlO_3$ red pigment by tailoring chemical defects with the aid of $CaCO_3$ and $Na_2B_4O_7$ mineralizers. **2023,** *932*, 167652.

91. Divya, S.; Das, S. J. C. I., New red pigments based on Li_3AlMnO_5 for NIR reflective cool coatings. **2021,** *47* (21), 30381-30390.

92. Zhang, S.; Ye, M.; Chen, S.; Han, A.; Zang, Y. J. C. I., Synthesis and characterization of mica/γ-$Ce_{2-x}Y_xS_3$ composite red pigments with UV absorption and high NIR reflectance. **2016,** *42* (14), 16023-16030.

93. Wang, D.; Su, D.; Zhong, M. J. S. e., Chromatic and near-infrared reflective properties of Fe^{3+} doped $KZnPO_4$. **2014,** *110*, 1-6.

94. Sreeram, K. J.; Aby, C. P.; Nair, B. U.; Ramasami, T. J. S. e. m.; cells, s., Colored cool colorants based on rare earth metal ions. **2008,** *92* (11), 1462-1467.

95. Zhang, T.; Wang, Y.; Pan, Z. J. C. I., Synthesis and characterization of Cu-/In-co-doped ZnS_xSe_{1-x} with tunable band-gaps as high near-infrared reflective color pigments. **2018,** *44* (15), 18851-18862.

96. Jovani, M.; Sanz, A.; Beltran-Mir, H. c.; Cordoncillo, E. J. D.; Pigments, New red-shade environmental-friendly multifunctional pigment based on Tb and Fe doped $Y_2Zr_2O_7$ for ceramic applications and cool roof coatings. **2016,** *133*, 33-40.

97. Raj, A. K.; Rao, P. P.; Divya, S.; Ajuthara, T. J. P. t., Terbium doped Sr_2MO_4 [M= Sn and Zr] yellow pigments with high infrared reflectance for energy saving applications. **2017,** *311*, 52-58.

98. Raj, A. K.; Rao, P. P.; Sreena, T.; Thara, T. A. J. D.; Pigments, Pigmentary colors from yellow to red in $Bi_2Ce_2O_7$ by rare earth ion substitutions as possible high NIR reflecting pigments. **2019,** *160*, 177-187.

99. Sameera, S.; Rao, P. P.; Divya, S.; Raj, A. K.; Thara, T. A. J. E.; buildings, High IR reflecting $BiVO_4$-$CaMoO_4$ based yellow pigments for cool roof applications. **2017,** *154*, 491-498.

100. Huang, B.; Xiao, Y.; Zhou, H.; Chen, J.; Sun, X. J. A. S. C.; Engineering, Synthesis and characterization of yellow pigments of $Bi_{1.7}RE_{0.3}W_{0.7}Mo_{0.3}O_6$ (RE = Y, Yb, Gd, Lu) with high NIR reflectance. **2018,** *6* (8), 10735-10741.

101. Sameera, S.; Rao, P. P.; Divya, S.; Raj, A. K. J. A. S. C.; Engineering, Brilliant IR reflecting yellow colorants in rare earth double molybdate substituted $BiVO_4$ solid solutions for energy saving applications. **2015,** *3* (6), 1227-1233.

102. Gao, Q.; Wu, X.; Fan, Y.; Meng, Q. J. D.; Pigments, Color performance and near infrared reflectance property of novel yellow pigment based on Fe_2TiO_5 nanorods decorated mica composites. **2017,** *146*, 537-542.

103. Han, A.; Ye, M.; Liu, L.; Feng, W.; Zhao, M. J. E.; buildings, Estimating thermal performance of cool coatings colored with high near-infrared reflective inorganic pigments: Iron doped $La_2Mo_2O_7$ compounds. **2014,** *84*, 698-703.

104. Radhika, S. P.; Sreeram, K. J.; Unni Nair, B. J. A. S. C.; Engineering, Mo-doped cerium gadolinium oxide as environmentally sustainable yellow pigments. **2014,** *2* (5), 1251-1256.

105. Schildhammer, D.; Fuhrmann, G.; Petschnig, L.; Weinberger, N.; Schottenberger, H.; Huppertz, H. J. D.; Pigments, Synthesis and characterization of a new high NIR reflective ytterbium molybdenum oxide and related doped pigments. **2017,** *138*, 90-99.

106. Chen, S.; Cai, M.; Ma, X. J. J. o. A.; Compounds, Environmental-friendly yellow pigments based on Zr doped Y_4MoO_9. **2016,** *689*, 36-40.

107. Chen, J.; Xie, W.; Guo, X.; Huang, B.; Xiao, Y.; Sun, X. J. C. I., Near infrared reflective pigments based on Bi_3YO_6 for heat insulation. **2020,** *46* (15), 24575-24584.

108. Zou, J.; Zhang, P. J. C. I., Ni-doped $BaTi_5O_{11}$: New brilliant yellow pigment with high NIR reflectance as solar reflective fillers. **2020,** *46* (3), 3490-3497.

109. Meenakshi, P.; Selvaraj, M. J. S. E. M.; Cells, S., Bismuth titanate as an infrared reflective pigment for cool roof coating. **2018,** *174*, 530-537.

110. Thejus, P.; Nishanth, K. J. S. E. M.; Cells, S., Rational approach to synthesis low-cost $BiVO_4$-ZnO complex inorganic pigment for energy efficient buildings. **2019,** *200*, 109999.

111. Bae, B.; Takeuchi, N.; Tamura, S.; Imanaka, N. J. D.; Pigments, Environmentally friendly orange pigments based on hexagonal perovskite-type compounds and their high NIR reflectivity. **2017,** *147*, 523-528.

112. Yuan, L.; Han, A.; Ye, M.; Chen, X.; Ding, C.; Yao, L. J. C. I., Synthesis and characterization of novel nontoxic $BiFe_{1-x}Al_xO_3$/mica-titania pigments with high NIR reflectance. **2017,** *43* (18), 16488-16494.

113. Shi, Y.; Zhong, M.; Zhang, Z.; Wang, D. J. C. I., Crystal structure and near-infrared reflective properties of Fe^{3+} doped $AlPO_4$ pigments. **2017,** *43* (8), 5979-5983.

114. Yuan, L.; Han, A.; Ye, M.; Chen, X.; Yao, L.; Ding, C. J. D.; Pigments, Synthesis and characterization of environmentally benign inorganic pigments with high NIR reflectance: lanthanum-doped $BiFeO_3$. **2018,** *148*, 137-146.

115. Yang, R.; Han, A.; Ye, M.; Chen, X.; Yuan, L. J. S. E. M.; Cells, S., Synthesis, characterization and thermal performance of Fe/N co-doped $MgTiO_3$ as a novel high near-infrared reflective pigment. **2017,** *160*, 307-318.

116. Kavitha, K.; Sivakumar, A. J. I. C. C., Impact of titanium concentration in structural and optical behaviour of nano $Bi_2Ce_{2-x}Ti_xO_7$ (x = 0-1) high NIR reflective and UV shielding yellow and orange pigments. **2020,** *120*, 108163.

117. Sangwong, N.; Suwan, M.; Supothina, S. J. I. F., Synthesis of NIR-Reflective Oxide Ceramic Orange Pigment from MgO and Leucoxene. **2022,** *222* (1), 283-292.

118. Xiao, Y.; Huang, B.; Chen, J.; Sun, X. J. J. o. A.; Compounds, Novel Bi^{3+} doped and Bi^{3+}/Tb^{3+} co-doped $LaYO_3$ pigments with high near-infrared reflectances. **2018,** *762*, 873-880.

119. Schildhammer, D.; Fuhrmann, G.; Petschnig, L.; Schottenberger, H.; Huppertz, H. J. D.; Pigments, Synthesis and optical properties of new highly NIR reflective inorganic pigments $RE_6Mo_2O_{15}$ (RE= Tb, Dy, Ho, Er). **2017,** *140*, 22-28.

120. Zhang, M.; Yang, Y.; Feng, L.; Sun, X. J. C. I., Synthesis and characterization of Fe^{3+} doped $YIn_{1-y}Mn_yO_3$ black pigment with high near-infrared reflectance. **2023,** *49* (11), 19290-19300.

121. Moriomoto, T.; Oka, R.; Minagawa, K.; Masui, T. J. R. a., Novel near-infrared reflective black inorganic pigment based on cerium vanadate. **2022,** *12* (26), 16570-16575.

122. Suwan, M.; Sangwong, N.; Supothina, S. In *Effect of Co and Pr doping on the properties of solar-reflective $ZnFe_2O_4$ dark pigment*, IOP Conference Series: Materials Science and Engineering, IOP Publishing: 2017; p 012003.

123. Sangwong, N.; Suwan, M.; Supothina, S. J. M. T. P., Effect of calcination temperature and dolomite or Al_2O_3 doping on properties of NIR-reflective $CoFe_2O_4$ black pigment. **2019,** *17*, 1595-1601.

124. Suwan, M.; Sangwong, N.; Supothina, S. J. C. S. t., Effect of Ni doping and synthesis temperature on the properties of NIR-reflective $ZnFe_2O_4$ black pigments. **2020,** *64* (2), 172-179.

125. Hwang, J. S.; Jung, K. Y. J. R. a., Effect of calcination temperature and Ti substitution on optical properties of $(Fe, Cr)_2O_3$ cool black pigment prepared by spray pyrolysis. **2022,** *12* (1), 72-77.

126. Oka, R.; Masui, T. J. R. a., Synthesis and characterization of black pigments based on calcium manganese oxides for high near-infrared (NIR) reflectance. **2016,** *6* (93), 90952-90957.

127. Sanada, K.; Morisawa, Y.; Ozaki, Y. J. J. o. t. C. S. o. J., Environmentally friendly synthesis and physical and optical properties of highly reflective green-black pigments. **2014,** *122* (1425), 322-328.

128. Bai, M.; Li, W.; Hong, Y.; Wang, S.; Wang, Y.; Chang, Q. J. S. E., Synthesis and characterization of Fe/Mn co-doped $CuCr_2O_4$ black pigment with high near-infrared reflectance. **2022,** *234*, 240-250.

129. Hroch, J.; Dohnalova, Z.; Sulcova, P. J. C. I., Impact of synthesis method on the properties of near-infrared region-reflective $SrSn_{0.9}Mn_{0.1}O_3$ brown pigment. **2023,** *49* (15), 25246-25252.

130. Thongkanluang, T.; Chirakanphaisarn, N.; Limsuwan, P. J. P. E., Preparation of NIR reflective brown pigment. **2012,** *32*, 895-901.

131. Gopal, B.; Biswal, S.; Navami, K. J. S. E. M.; Cells, S., Solar reflective brick brown stable iron doped magnesium aluminate: Combustion synthesis, structure and chromatic properties. **2023,** *258*, 112400.

132. Chen, C.; Han, A.; Ye, M.; Wang, J. J. S. E. M.; Cells, S., Study on thermal insulation performance of ASA (acrylonitrile-styrene-acrylate) modified by Fe-doped $Y_3Al_5O_{12}$ NIR solar reflective pigment. **2022,** *239*, 111656.

133. Liu, L.; Han, A.; Ye, M.; Feng, W. J. S. E., The evaluation of thermal performance of cool coatings colored with high near-infrared reflective nano-brown inorganic pigments: Magnesium doped $ZnFe_2O_4$ compounds. **2015,** *113*, 48-56.

134. Huang, B.; Xiao, Y.; Huang, C.; Chen, J.; Sun, X. J. D.; Pigments, Environment-friendly pigments based on praseodymium and terbium doped $La_2Ce_2O_7$ with high near-infrared reflectance: synthesis and characterization. **2017,** *147*, 225-233.

135. Xiong, C.; Liu, P.; Chen, M.; Cao, X.; Wang, H. J. J. o. A.; Compounds, The far-infrared emissivity and near-infrared reflectance of $Mg_{1-x}Mn_xFe_2O_4$ synthesized by xerogel-microwave method. **2020,** *836*, 155516.

136. Radhika, S.; Sreeram, K. J.; Nair, B. U. J. J. o. C. S., Effective synthesis route for red-brown pigments based on Ce-Pr-Fe-O and their potential application for near infrared reflective surface coating. **2014,** *126*, 65-73.

137. Kavitha, K.; Sivakumar, A. J. I. C. C., Synthesis and characterization of cerium doped bismuth titanate proficient UV shielding and NIR reflective reddish brown pigment by citrate autocombustion synthesis. **2022,** *136*, 109162.

138. Zamani, A.; Eavani, S.; Rafiee, E. J. J. o. C. P., Synthesis and characterization of anticorrosion, low-lead leaching $PbCrO_4$/eggshell composites as the environmentally sustainable yellow pigments. **2021,** *304*, 127103.

139. Palimi, M.; Rostami, M.; Mahdavian, M.; Ramezanzadeh, B. J. P. i. O. C., Application of EIS and salt spray tests for investigation of the anticorrosion properties of polyurethane-based nanocomposites containing Cr_2O_3 nanoparticles modified with 3-amino propyl trimethoxy silane. **2014,** *77* (11), 1935-1945.

140. Shao, Y.; Jia, C.; Meng, G.; Zhang, T.; Wang, F. J. C. S., The role of a zinc phosphate pigment in the corrosion of scratched epoxy-coated steel. **2009,** *51* (2), 371-379.

141. Lazau, R.; Ianos, R.; Pacurariu, C.; Caprariu, D. A.; Racu, A.; Cornea, V. J. N., Combustion Synthesis of $SrAl_2O_4$: Eu^{2+}, Dy^{3+} Phosphorescent Pigments for Glow-in-the-Dark Safety Markings. **2023,** *13* (4), 687.

142. Zhou, Z.; Li, P.; Zhong, H.; Xu, H.; Zhang, Y. J. C. J., High infrared reflective chromic oxide green pigment prepared by thermal decomposition of CrO_3 doped with V_2O_5. **2012,** *63*, 3316-3323.

143. Nguyen, D. K.; Lee, H.; Kim, I.-T. J. M., Synthesis and thermochromic properties of Cr-doped Al_2O_3 for a reversible thermochromic sensor. **2017,** *10* (5), 476.

144. Abdelhameed, M. M.; Attia, Y. A.; Abdelrahman, M. S.; Khattab, T. A. J. L., Photochromic and fluorescent ink using photoluminescent strontium aluminate pigment and screen printing towards anticounterfeiting documents. **2021,** *36* (4), 865-874.

145. Aranzabe Basterrechea, E. b.; Arriortua Marcaida, M. a. I.; Larranaga Varga, A.; Aranzabe, A.; Villasante, P. M. a.; March, R., Designing multifunctional pigments for an improved energy efficiency in buildings. **2017**.

Google images

1. Delhi power supply and consumption:
2. Cool roof coating: https://www.thehansindia.com/posts/index/Environment/2015-08-20/Paint-your-rooftops-with-glass-paints-to-keep-house-cool-in-summers/171416
3. Cool road in Qatar: https://www.iloveqatar.net/guide/places/coloured-roads-in-qatar
4. Anti-corrosion paint: https://www.indiamart.com/proddetail/bulwark-anti-corrosion-paint-2850537378088.html

Design and development of intense coloured phosphate pigments, investigation on its origin of colour

2A.1. Abstract

Three inorganic phosphate pigment series, $NaZn_{1-x}Co_xPO_4$, $LiZn_{1-x}Co_xPO_4$ and $LiMg_{1-x}Co_xPO_4$, were prepared by solid-state method, exhibiting deep blue, intense purple and bright magenta colour, respectively. The physical characterizations PXRD, SEM and DLS analyses demonstrated the crystalline nature of pigments with broad particle size distribution. In terms of colour and cost, the composition $NaZn_{0.9}Co_{0.1}PO_4$ was found to be superior to the commercial blue pigment ($CoAl_2O_4$). The origin of the pigment colour was investigated by means of crystallographic and optical studies. The spectroscopic features indicated that the spin-allowed ligand field transitions from tetrahedral coordination of Co^{2+} is responsible for the blue colour, while octahedral geometry is responsible for the magenta shade. The unusual purple colour of CoO_4 tetrahedral coordination in $LiZn_{0.9}Co_{0.1}PO_4$ originated from the highly distorted geometry with significantly shorter Co-O bonds. The structural changes attributed strongly to the spectral features leading to the origin of excellent colours.

2A.2. Introduction

Inorganic pigments have been greatly admired throughout the history of mankind owing to their potential use as a colourant in paints, inks, glazes etc[1-3]. The blue colour has a long history of eternal fascination among different hues due to its unique dimension in the arts, science and culture. There were massive efforts in various directions to explore a stable blue colour in history. Azurite ($Cu_3(CO_3)_2(OH)_2$), Egyptian blue ($CaCuSi_4O_{10}$), Chinese blue ($BaCuSi_4O_{10}$), lapis lazuli ($(Na,Ca)_8[SiAlO_4]_6(S,SO_4)$), prussian blue ($Fe_4[Fe(CN)_6]_3$), ultramarine ($Na_7Al_6Si_6O_{24}S_3$) are the major landmarks in the quest. Unfortunately, most of these pigments were not used for long owing to the serious stability issue[4-6]. Currently, spinel $CoAl_2O_4$ (Pigment Blue 28) is the most widely known blue pigment in the market due to its excellent chemical and thermal stability[7]. However, the production cost of $CoAl_2O_4$ is considerably large due to high processing temparatures (~1200 ℃) and excess concentration of scarce and expensive Co metal (~33 wt%)[8-10]. Recently, Smith et al., reported a Co-free blue pigment Mn doped $YInO_3$ as an alternative, but the cost is still debatable due to the presence of expensive Y and In[11]. In this context, developing a low-cost blue pigment with reduced cobalt content is important without compromising its colour properties.

Phosphates are a class of low-cost inorganic compounds, having low synthesis temperature and high stability[12]. It has been extensively used in pigment applications, where $CoZr_4(PO_4)_6$, $Co_3V_4(PO_4)_6$, $Co_2P_2O_7$, $MgCo_{2-x}Mg_xP_2O_7$ and $SrZn_{1-x}Co_xP_2O_7$ are few

examples[10, 13-16]. $Co_3(PO_4)_2$ and NH_4MnPO_4 are commercial pigments in this category. This inspired to choose a monophosphate system with the general formula $ABPO_4$ as the base system for the present work, where A and B denote monovalent and divalent cations, respectively. Three different parent compounds, $NaZnPO_4$, $LiZnPO_4$ and $LiMgPO_4$, were synthesized by altering A or B site with Na/Li and Zn/Mg ions. The presence of mono, di and pentavalent sites in $ABPO_4$ allows for the introduction of various chromophores to develop colour. Herein, divalent chromophores such as Co^{2+}, Ni^{2+} and Cu^{2+} were substituted at the B site of the prepared phosphate compounds. The chromophores were selected based on the various literature reports available, as they have been extensively employed to generate blue colour[17-20] and subsequently carried out a detailed investigation on the science behind the origin of pigment colour.

2A.3. Experimental section

2A.3.1. Materials and methods

The pigment series $NaZn_{1-x}Co_xPO_4$, $LiZn_{1-x}Co_xPO_4$ and $LiMg_{1-x}Co_xPO_4$ were synthesized by conventional solid-state method. Extra pure Na_2CO_3 (99%), Li_2CO_3 (99.9%), $CoCO_3$ (99.99%), ZnO (99.9%), MgO (99.9%) and $NH_4H_2PO_4$ ($\geq$ 98%) were purchased from Merck, for the synthesis. A stoichiometric amount of precursors ground well in ethanol wetting medium and calcined. The calcining process involves a preliminary heating at 500 °C for 3 h, subsequently ground well to improve the homogeneity of the precursor mixture. Further, the preheated precursor powder of $NaZn_{1-x}Co_xPO_4$ was calcined at 800 °C for 5 h, whereas $LiZn_{1-x}Co_xPO_4$ and $LiMg_{1-x}Co_xPO_4$ calcined at 900 °C for 5 h. The obtained pigments were ground well and taken for characterization.

2A.3.2. Characterization techniques

2A.3.2a. Powder X-ray Diffraction (PXRD)

X-rays scattered from the periodic array of atoms/ molecules with long-range order can constructively interfere at specific angles. This phenomenon is called X-ray diffraction. It is commonly used for phase identification, quantitative phase analysis and structural parameter calculations such as lattice parameters, grain size, crystallinity, strain and crystal defects. It operates based on Bragg's law

$$n \lambda = 2 d \sin\theta \tag{2A.1}$$

where,

n – integral number

λ – wavelength of X-ray

d – distance between two parallel crystal planes

θ – angle of diffraction

According to Bragg's relationship, constructive interference of the X-ray beams scattered from horizontal parallel crystal planes will occur when the path difference is an integral multiple of the X-ray wavelength, **Fig. 2A.1** [21].
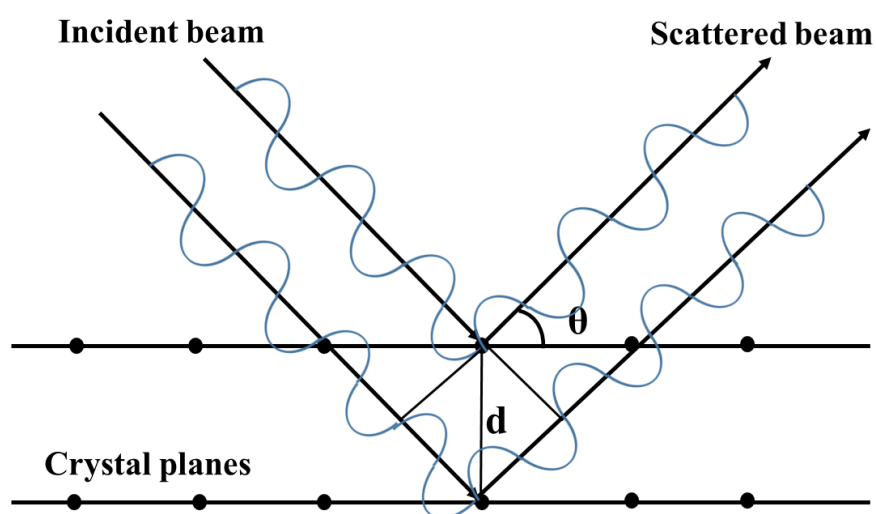
Fig. 2A.1. Principle of X-ray diffraction analysis

Phase purity and crystal structure of the prepared pigment series were analyzed by PXRD using Malvern PANalytical diffractometer, Ni-filtered Cu-Kα (λ = 0.154060 nm) radiation. Data were collected by step scanning over a 2θ range from 10-75° with a step size of 0.03° and 20 s counting time at each step. Rietveld refinement of the pigments was carried out using this PXRD data in GSAS-II software.

2A.3.2b. Diffuse Reflectance Spectroscopy (DRS)

The optical properties of the pigment were analyzed through diffuse reflectance spectroscopy (DRS). Light falls on the pigment powder and reflects in many directions due to the different shapes of the particles. The reflected rays were collected with the help of an integrating sphere to develop a diffuse reflectance spectrum of the material. The light absorption and scattering properties of a pigment can be explained by Kubelka–Munk (K-M) theory [22, 23]. According to K-M theory,

$$\frac{K}{S} = \frac{(1-R_\infty)^2}{2R_\infty} \tag{2A.2}$$

where,

K – coefficient of absorption

S – coefficient of scattering

R∞ - diffuse reflectance

The colour properties of the pigment was quantified from the same technique, using the CIE 1976 $L^*a^*b^*$ colourimetric method, as recommended by the Commission Internationale del'Eclairage (CIE), **Fig. 2A.2a**. The method describes L^* represents the colour lightness ($L^* = 0$ for black and $L^* = 100$ for white), a^* gives the green (−)/red (+) axis, and b^* gives the blue (−)/yellow (+) axis. The parameter C^* (chroma) denotes the saturation of the colour and is given by equation

$$C^* = \sqrt{(a*)^2 + (b*)^2} \tag{2A.3}$$

the hue angle, h° is expressed in degrees and ranges from 0 to 360°, **Fig. 2A.2b**, which is calculated by the formula

$$h^\circ = \tan^{-1}(b^*/a^*) \tag{2A.4}$$

Each colourimetric experiment was made in triplicate, and an average value was taken as the result. Typically, for a given sample, the standard deviation of the measured CIE-$L^*a^*b^*$ value is less than 0.10, and the relative standard deviation < 1%, indicating that the measurement error can be ignored[24, 25].

Shimadzu UV-3600 Spectrophotometer with an integrating sphere attachment, ISR-2200, was utilized for optical studies of pigment samples and coatings. Barium sulphate was used as the reference for the UV-Vis range (300-700 nm) and polytetrafluoroethylene (PTFE) for the NIR range (700–2500 nm). The NIR solar reflectance (R^*) between wavelength 700–2500 nm was calculated according to (American Society for Testing and Materials) ASTM standard number E891-87 as reported elsewhere[26-28]. The NIR solar reflectance or the fraction of solar radiation incident at wavelengths between 700 and 2500 nm that is reflected by a surface is the irradiance-weighted average of its spectral reflectance, $r(\lambda)$, and can be determined using the relation,

$$R^* = \frac{\int_{700}^{2500} r(\lambda)i(\lambda)d(\lambda)}{\int_{700}^{2500} i(\lambda)d(\lambda)} \tag{2A.5}$$

where,

$r(\lambda)$ - experimentally obtained spectral reflectance (Wm^{-2})

$i(\lambda)$ - solar spectral irradiance (Wm^{-2} nm^{-1}) obtained from ASTM standard E891-87
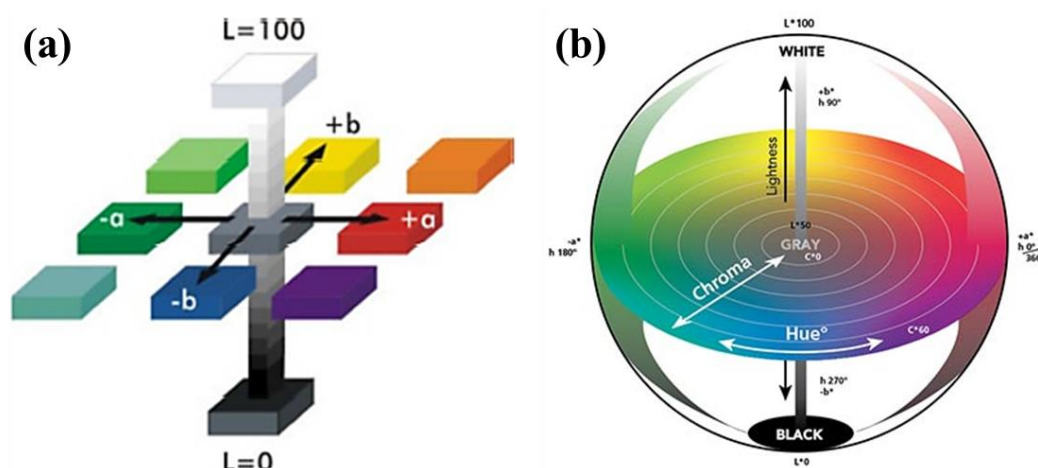
Fig. 2A.2. (a) CIE 1976 L*a*b* colour scales[24], (b) hue angle chart[29]

Thermal analysis was carried out in the temperature range 30-1000 °C using an SII Nanotechnology Inc., TG/DTA 6200 in air atmosphere at a heating rate of 10 °C/min. JEOL JSM-5600 model Scanning Electron Microscope (SEM) was employed to identify the pigment morphology. Energy Dispersive X-ray Spectroscopy (EDS) was conducted using a silicon drift detector X-MaxN attached with a Carl Zeiss EVO SEM apparatus to confirm the pigment composition. Particle size distribution was measured by Anton Paar Instrument LITESIZER 500 Dynamic Light Scattering analyser (DLS).

2A.4. Results and discussion

2A.4.1. Thermal analysis (TGA)

Thermogravimetric analysis of the precursor mixture was conducted and **Fig. 2A.3** displayed the corresponding graphs. All the TG curves exhibited nearly comparable weight loss patterns. The initial weight loss up to 160 °C indicates the evaporation of adsorbed water molecules[30], subsequently, the precursor decomposition was started. The possible overall reaction can be written as follows.

$$0.5\ Na_2CO_3 + ZnO + NH_4H_2PO_4 \rightarrow NaZnPO_4 + 0.5\ CO_2 + NH_3 + 1.5\ H_2O \quad (2A.6)$$
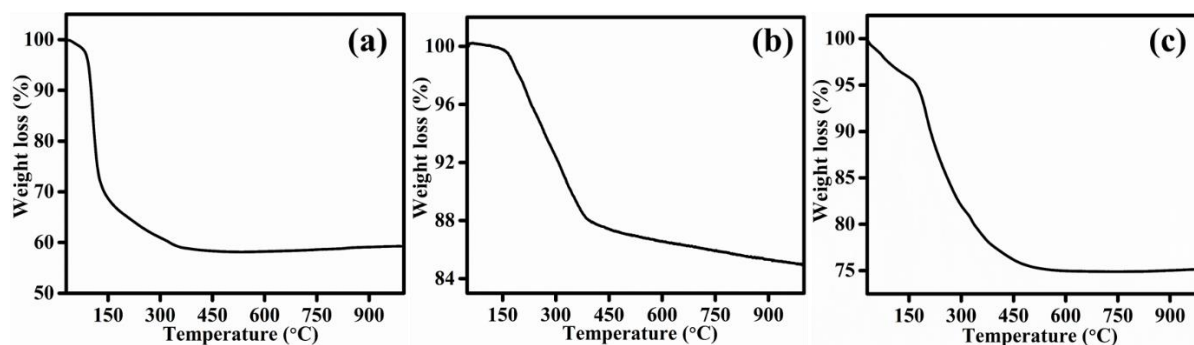
Fig. 2A.3. TGA curves of (a) $NaZnPO_4$, (b) $LiZnPO_4$, and (c) $LiMgPO_4$ precursor mixture

In the case of $NaZnPO_4$, the weight loss between 160-240 °C corresponds to NH_3 gas evolution from $NH_4H_2PO_4$[31]. Further, CO_2 and H_2O elimination was carried out in the temperature range of 240-500 °C. The H_2O molecules are generated by the reaction between $3H^+$ (coming from $NH_4H_2PO_4$ decomposition into $NH_3 + H_3PO_4$) and oxide anions $3/2O^{2-}$ (from ZnO). Similarly, carbonate decomposition ($\frac{1}{2}Li_2CO_3$) generated CO_2[32, 33]. After 500 °C, the TGA curve was found to be stable up to 1000 °C, during which the phase formation took place. The weight loss patterns in $LiZnPO_4$ and $LiMgPO_4$ were almost similar; however, the temperature range was expanded from 240 to 600 °C. Consequently, the phase formation was observed only after 600 °C. Therefore, the calcining temperature for $NaZnPO_4$ was fixed at 800 °C, whereas for $LiZnPO_4$ and $LiMgPO_4$, 900 °C.

2A.4.2. X-ray diffraction analysis

Divalent chromophores Co^{2+}, Ni^{2+} and Cu^{2+} were substituted at the B site of the three host systems $NaZnPO_4$, $LiZnPO_4$ and $LiMgPO_4$. Phase formation of the synthesized pigment was confirmed from PXRD results, shown in **Fig. 2A.4**. Since only Co^{2+} doping succeeded in delivering excellent colours, further investigation was conducted based on Co^{2+} substituted pigments. The PXRD patterns of $NaZn_{1-x}Co_xPO_4$ ($0 \leq x \leq 0.4$), $LiZn_{1-x}Co_xPO_4$ ($0 \leq x \leq 0.8$) and $LiMg_{1-x}Co_xPO_4$ ($0 \leq x \leq 0.8$) pigment series were illustrated in **Fig. 2A.5**. The sharp diffractions peaks observed in the patterns indicated that the prepared pigments are highly crystalline in nature. The phase purity of each series was analyzed by comparing the XRD patterns with its parent compound and corresponding JCPDS file. Following that, the phase purity was ensured for all the pigment series up to 40 mol% doping. Both $NaZn_{1-x}Co_xPO_4$ and $LiZn_{1-x}Co_xPO_4$ compounds were crystallized in monoclinic crystal structure, the former with a P21/n and the latter with a Cc space group. $LiMg_{1-x}Co_xPO_4$ series was crystallized in orthorhombic structure with Pmnb space group. The major peaks of each pigment series were indexed based on the JCPDS files 79-0217, 79-0804 and 32-0574 for $NaZn_{1-x}Co_xPO_4$, $LiZn_{1-}$

$_x$Co$_x$PO$_4$ and LiMg$_{1-x}$Co$_x$PO$_4$, respectively. Hence, it was confirmed that Co^{2+} ions are successfully incorporated into the Zn^{2+}/Mg^{2+} sites in the host lattice[34].
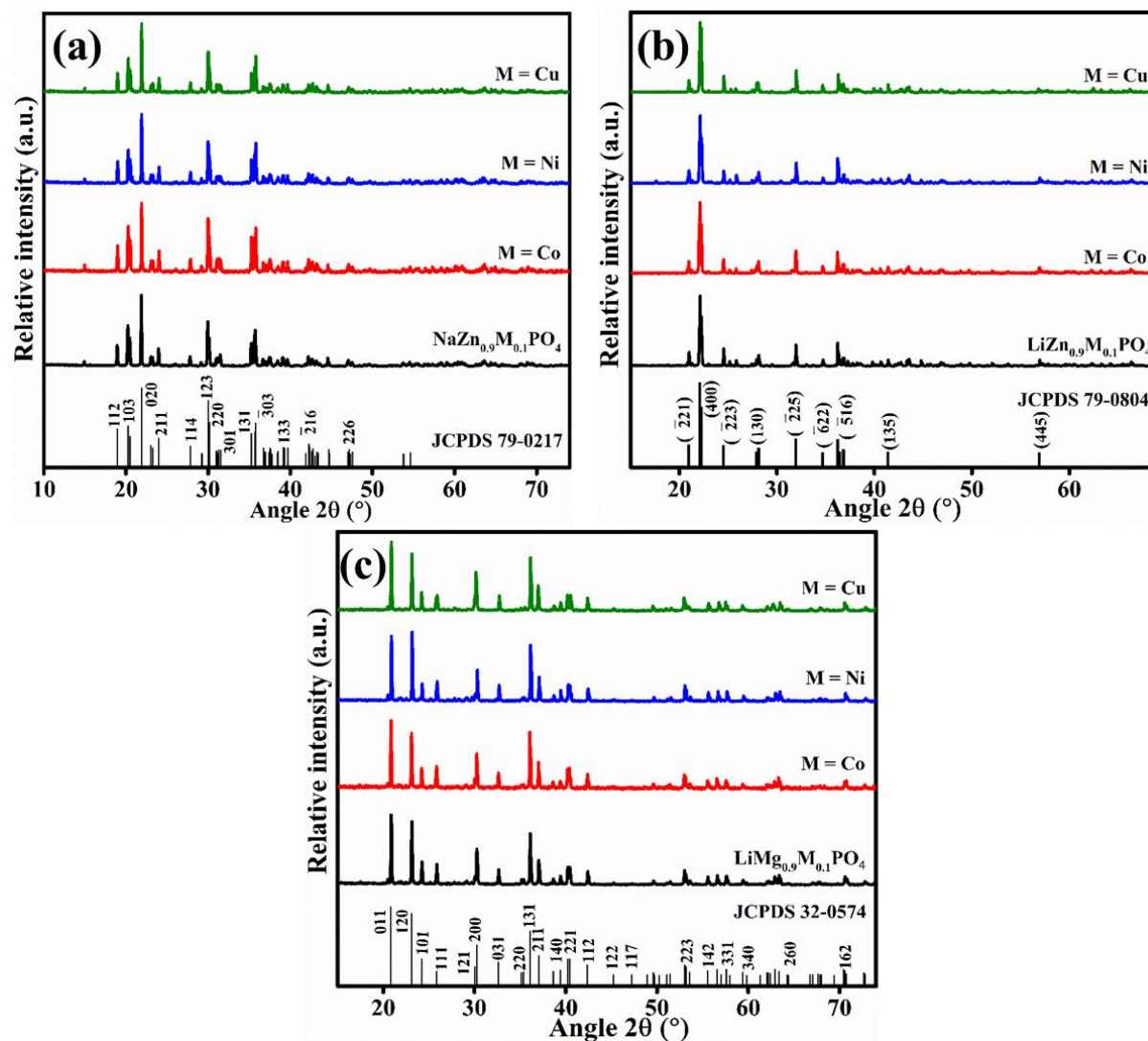
Fig. 2A.4. PXRD patterns of (a) NaZn$_{0.9}$M$_{0.1}$PO$_4$, (b) LiZn$_{0.9}$M$_{0.1}$PO$_4$ and (c) LiMg$_{0.9}$M$_{0.1}$PO$_4$; M = Co^{2+}, Ni^{2+}, Cu^{2+}

Additionally, the ionic radius of Co^{2+} (0.58 Å) is smaller than that of Zn^{2+} (0.60 Å) in a four co-ordination environment[35]. Therefore, when Co^{2+} substituted Zn^{2+} ions, the unit cell of the crystal structure experienced a shrinkage. It was reflected in the XRD patterns as a shift towards a higher diffraction angle, **Fig. 2A.5b, d**. Moreover, as the dopant concentration increased, the extend of shift was also increased. However, the ionic radius of Co^{2+} (0.745 Å) is larger than that of Mg^{2+} (0.72 Å) in a six co-ordination environment[35]. Thus, the unit cell slightly expanded after Co^{2+} doping and the corresponding PXRD patterns were shifted towards a lower diffraction angle, **Fig. 2A.5f**. In LiZn$_{1-x}$Co$_x$PO$_4$ and LiMg$_{1-x}$Co$_x$PO$_4$, secondary phase reflections were observed at 17.5°, 23.0° and 25.8° beyond 40 mol% doping,

marked * in the PXRD patterns. It was found to be LiCoPO$_4$ with orthorhombic crystal structure and Pnma space group ((Joint Committee on Powder Diffraction Standards) JCPDS 89-6192).
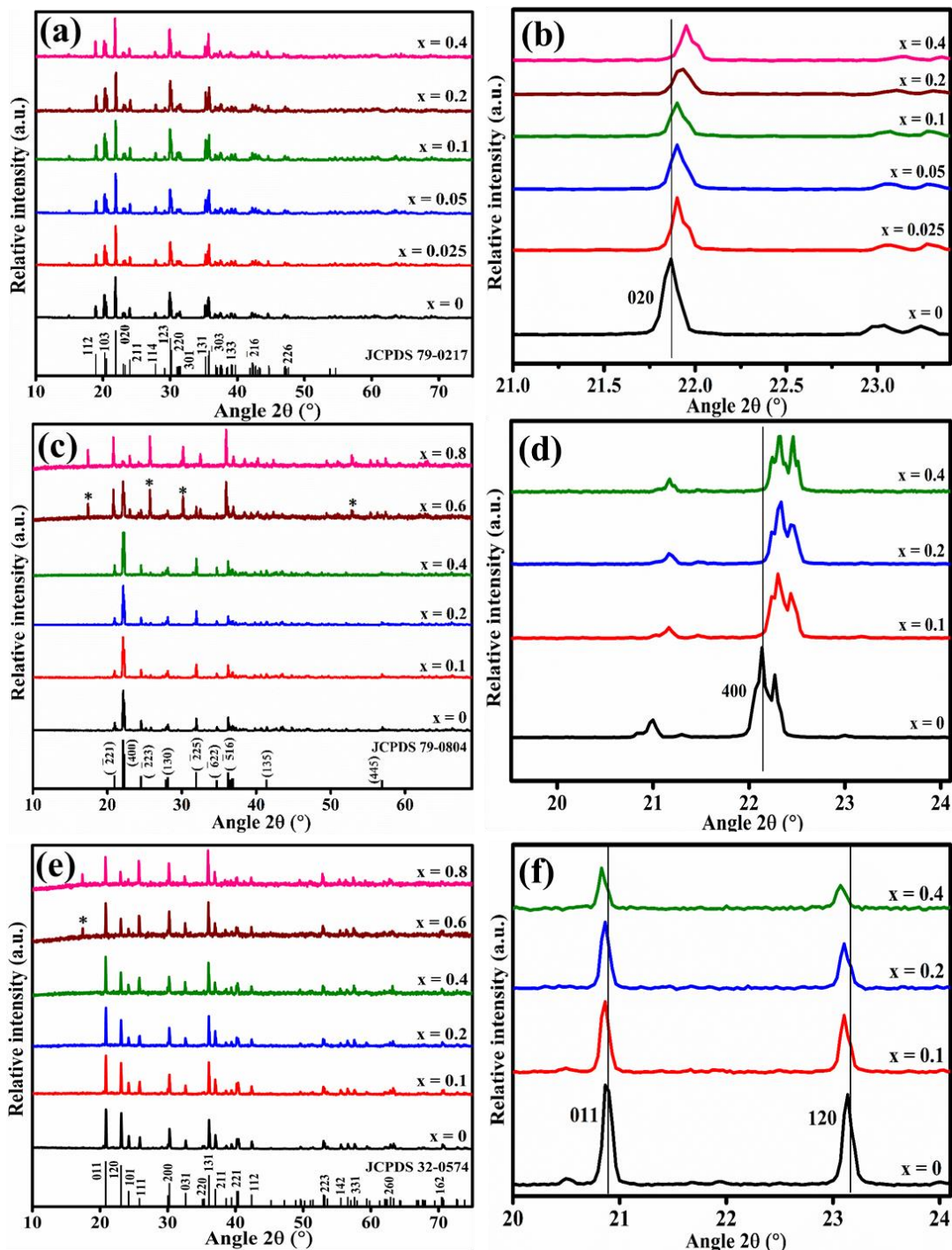
Fig. 2A.5. PXRD patterns of (a) NaZn$_{1-x}$Co$_x$PO$_4$ (0 ≤ x ≤ 0.4) (c) LiZn$_{1-x}$Co$_x$PO$_4$ (0 ≤ x ≤ 0.8), (e) LiMg$_{1-x}$Co$_x$PO$_4$ (0 ≤ x ≤ 0.8) and peak shift in PXRD patterns of (b) NaZn$_{1-x}$Co$_x$PO$_4$ (0 ≤ x ≤ 0.4) (d) LiZn$_{1-x}$Co$_x$PO$_4$ (0 ≤ x ≤ 0.4), (f) LiMg$_{1-x}$Co$_x$PO$_4$ (0 ≤ x ≤ 0.8)

2A.4.3. Morphology and particle size analysis

SEM images of representative samples from all the pigment series are given in **Fig. 2A.6**. Non-aggregate pigment particles were observed for $NaZn_{0.9}Co_{0.1}PO_4$ and $LiZn_{0.9}Co_{0.1}PO_4$, whereas a highly agglomerated mixed morphology of rods and flakes have seen in $LiMg_{0.8}Co_{0.2}PO_4$ micrographs. The EDS spectra detected the presence of constituent elements Na, Zn/Mg, Co, P, and O. Furthermore, the experimentally determined stoichiometric composition of the pigments were in close agreement with the theoretical value. The particle size distribution estimated from all the SEM images were very broad, certainly due to the high temperature synthesis process. The DLS analysis provided more details on particle size distribution. Consistent with SEM analysis, a broad size distribution curve was obtained in DLS measurements. It was found to be 3-10 and 1-8 μm for $LiZn_{0.9}Co_{0.1}PO_4$ and $LiMg_{0.8}Co_{0.2}PO_4$, respectively, **Fig. 2A.7**. The same time, $NaZn_{0.9}Co_{0.1}PO_4$ displayed relatively narrow size distribution, from 1-5 μm.
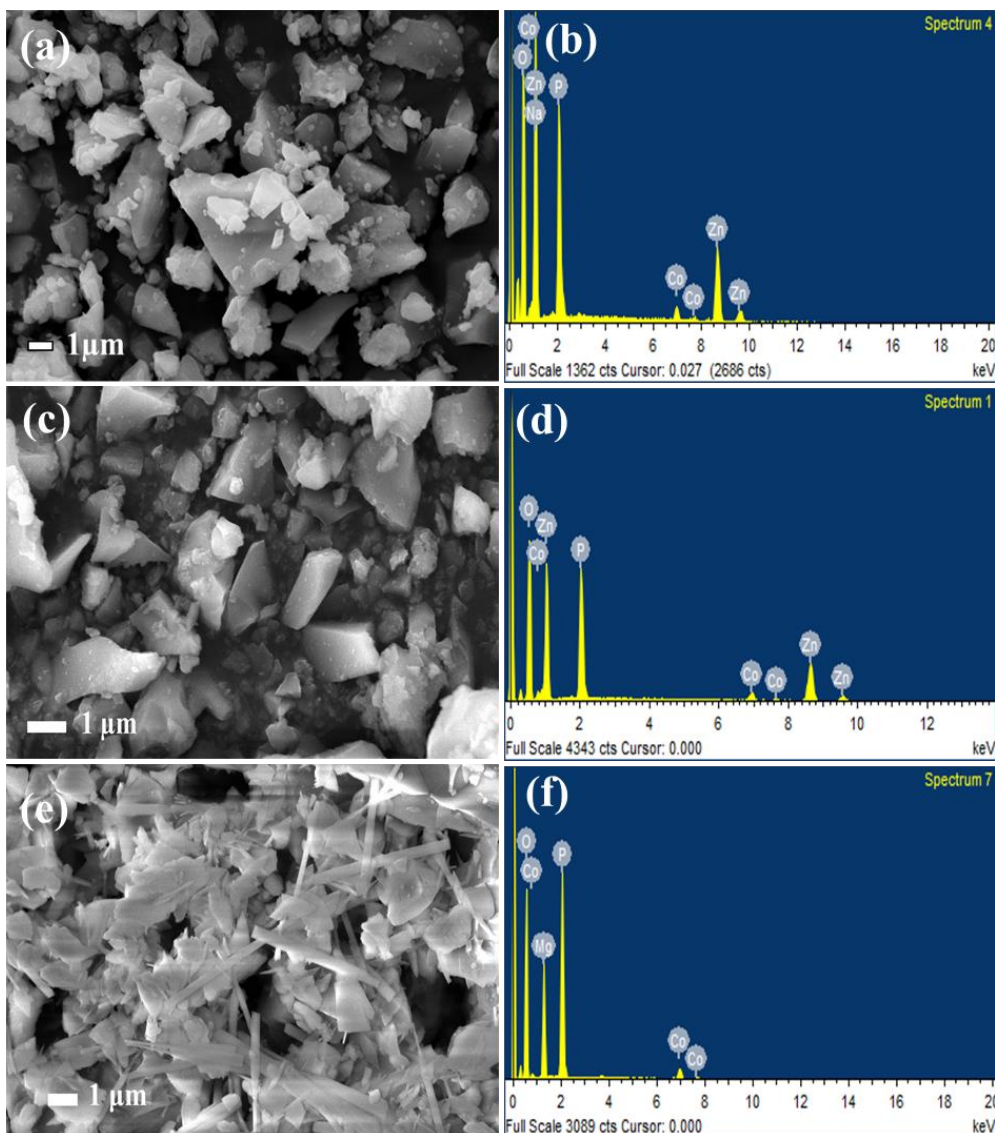
Fig. 2A.6. SEM images of (a) $NaZn_{0.9}Co_{0.1}PO_4$, (c) $LiZn_{0.9}Co_{0.1}PO_4$ (e) $LiMg_{0.8}Co_{0.2}PO_4$ and SEM-EDS spectra of (b) $NaZn_{0.9}Co_{0.1}PO_4$, (d) $LiZn_{0.9}Co_{0.1}PO_4$ (f) $LiMg_{0.8}Co_{0.2}PO_4$
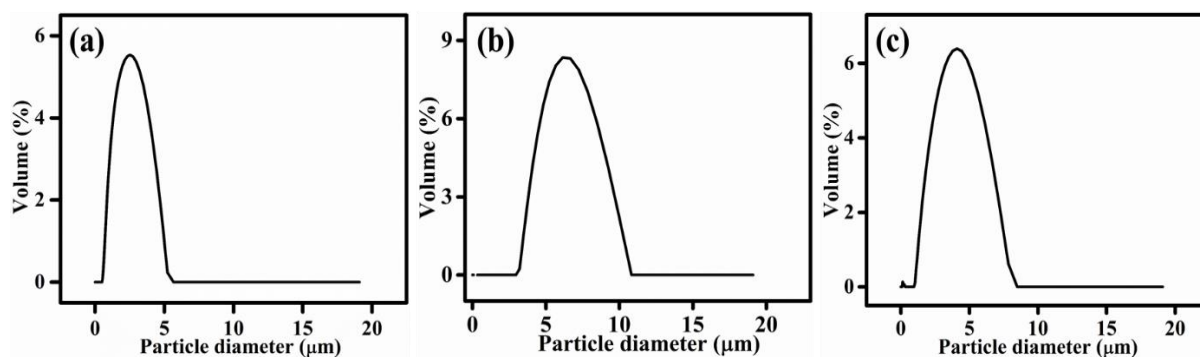
Fig. 2A.7. DLS curves of (a) $NaZn_{0.9}Co_{0.1}PO_4$, (b) $LiZn_{0.9}Co_{0.1}PO_4$ and (c) $LiMg_{0.8}Co_{0.2}PO_4$

42

2A.4.4. Chromatic properties

The pigment series $NaZn_{1-x}Co_xPO_4$ exhibited an intense blue colour; photographs were exhibited in **Fig. 2A.8a**. CIE 1976 $L^*a^*b^*$ colour system was utilized to quantify the pigment colour strength through hue, chroma and brightness. **Table 2A.1** provided an overview of the colour coordinates obtained for different pigment compositions. A deep blue colour resulted from the Co substitution at the Zn site, as indicated by negative b^* and 270-290° hue angle. The magnitude of b^* and colour saturation C^* rose in proportion to the rise in Co concentration. The maximum blue colour was recorded for 10 mol% of Co doping ($b^* = -59.21$), which is about 10 units higher than that of commercial $CoAl_2O_4$ ($b^* = -49.98$) [3, 36]. Additionally, $NaZn_{0.9}Co_{0.1}PO_4$ blue was synthesized at a relatively lower temperature, and the estimated Co concentration in the particular composition (3.22 wt%) is 10 times lower than that of $CoAl_2O_4$ (33.31 wt%). Processing temperature and chromophore concentration are critical parameters determining the pigment cost. Because of this, the new blue pigment becomes extremely important in the context of rising energy consumption and cobalt market price[8]. Further, higher doping concentration resulted in a slight colour change from blue to navy blue, as demonstrated by an increase in red component a^*. The brightness of the pigment was explicitly related to cobalt concentration that usually followed an inverse trend as in the current investigation[7]. Hence, the result provided a remarkable prospective for $NaZn_{0.9}Co_{0.1}PO_4$ pigment.

Fig. 2A.8. Photographs of pigment series (a) $NaZn_{1-x}Co_xPO_4$ ($0 \leq x \leq 0.4$), (b) $LiZn_{1-x}Co_xPO_4$ ($0 \leq x \leq 0.8$) and (c) $LiMg_{1-x}Co_xPO_4$ ($0 \leq x \leq 0.8$)

CIE 1976 colour co-ordinates of $LiZn_{1-x}Co_xPO_4$ ($0 \leq x \leq 0.8$) are summarized in **Table 2A.1**. The pigment series displayed a vivid purple colour, which is a combination of red and blue colours, **Fig. 2A.8b**. It conveyed that the colour parameter combination must be a^* and $-b^*$. The pigment series illustrated a^* and $-b^*$ in the ratio 1:2, which was almost maintained until it crossed the phase pure compositions. All the phase pure pigments showed a^* and $-b^*$ values above 25 and 52, respectively. Among these, $LiZn_{0.9}Co_{0.1}PO_4$ was chosen as the best pigment because it had an outstanding $a^* = +25.25$, $b^* = -52.32$ and $L^* = 49.74$ values despite having a low Co content. The C^* value, around 60, determined the richness of purple colour and hue angle lies in between blue and red region provided an additional support. There have been very few reports of purple pigments, among them $LiZn_{0.9}Co_{0.1}PO_4$ found to be a strong contender (**Table 2A.2**). Above 40 mol%, Co concentration did not have any significant impact in enhancing the purple colour. Instead, the colour was changed to a violet hue due to the secondary phase formation, as evident from the XRD data, **Fig. 2A.5c**. The sudden fall in b^* indicates this colour change, which is clearly visible in the pigment photographs, **Fig. 2A.8b**.

Table 2A.1. CIE 1976 $L^*a^*b^*$ colour coordinates of synthesized pigment series

Pigment	Composition	L^*	a^*	b^*	C^*	$h°$
$NaZn_{1-x}Co_xPO_4$	x = 0	92.13	0.15	-0.32	0.35	295
	x = 0.025	60.43	3.68	-41.66	41.82	275
	x = 0.05	52.05	8.99	-49.57	50.38	280
	x = 0.1	51.78	10.70	-59.21	60.17	280
	x = 0.2	44.31	17.31	-56.66	59.25	287
	x = 0.4	42.15	19.21	-53.55	56.89	289
$LiZn_{1-x}Co_xPO_4$	x = 0	96.00	0.18	-0.75	0.77	284
	x = 0.1	49.74	25.25	-52.32	58.10	296
	x = 0.2	39.47	28.11	-52.81	59.83	298
	x = 0.4	35.75	31.16	-52.29	60.87	301
	x = 0.6	41.40	20.65	-36.75	42.16	299
	x = 0.8	38.33	29.04	-31.89	43.14	312
$LiMg_{1-x}Co_xPO_4$	x = 0	94.80	0.26	-0.03	0.26	354
	x = 0.1	70.17	23.08	-22.53	32.25	316
	x = 0.2	65.19	26.45	-26.83	37.68	315
	x = 0.4	56.99	32.63	-31.66	45.47	316
	x = 0.6	53.88	36.20	-34.95	50.32	316
	x = 0.8	48.30	31.85	-30.69	44.23	316
$CoAl_2O_4$	-	40.42	1.95	-49.98	50.01	272

Colour coordinates of $LiMg_{1-x}Co_xPO_4$ pigment series was enumerated in **Table 2A.1**. The pigment demonstrated a bright magenta colour, **Fig. 2A.8c**, which is also a combination of a^* and $-b^*$, but in a different ratio. The colour analysis revealed that a^* and $-b^*$ in nearly equal proportion delivers a magenta tone. Respective hue angle 300-320° further substantiated the pigment colour. While increasing the dopant concentration, a slight improvement was noticed in the colour values and intensity up to the phase pure compositions. However, 60 mol% doping onwards, the presence of $LiCoPO_4$ secondary phase brought an apparent colour change from magenta to violet.

Table 2A.2. CIE 1976 $L^*a^*b^*$ colour coordinates comparison of reported purple pigments

Pigment	L^*	a^*	b^*
$YGa_{0.95}Mn_{0.05}O_3$	47.45	25.01	-30.01 [37]
$LiCoPO_4$	41.00	34.50	-49.50 [38]
$Ba(Zn_{0.85}Co_{0.15})_2Si_2O_7$	28.60	52.20	-65.50 [39]
$Zn_{0.9}Co_{0.1}MoO_4$	47.03	22.93	-62.72 [40]
$Co_{0.75}Mg_{0.25}Zr_4(PO_4)_6$	53.2	21.8	-39.60 [13]
$LiZn_{0.9}Co_{0.1}PO_4$	**49.74**	**25.25**	**-52.32 [Present study]**

2A.4.5. UV-Visible-NIR absorption

Fig. 2A.9. illustrated the UV-Vis-NIR absorption spectra of $NaZn_{1-x}Co_xPO_4$ ($0 \leq x \leq 0.4$) pigment series. As shown in **Fig. 2A.9a**, the Co substituted compounds exhibited a broad absorption band in the visible region 470-675 nm. The band consists of three peaks at 545, 581 and 620 nm, indicating a strong absorption in the green, yellow and orange regions, besides, the absorption valley is extended over to the red region as well. Therefore, the pigments reflected the entire blue-violet colours, resulting in an intense blue colour. The corresponding Tanabe-Sugano diagram established that the absorption is attributed to the spin allowed ligand field transition $^4A_2(F) \rightarrow {}^4T_1(P)$, from the tetrahedrally coordinated Co^{2+} [10, 41-45]. Further, the spin forbidden transitions $^4A_2(F) \rightarrow {}^2T_1(2P)$ and $^4A_2(F) \rightarrow {}^2T_1(2H)$ identified at 482 and 450 nm as weak absorptions, respectively, corroborated the tetrahedral chromophore geometry. The absorption peak splitting was originated from the spin-orbit (L-S Russell-Saunders) coupling effect and Jahn-Tellar distortion of the tetrahedral structure. Further increase in Co concentration amplified these effects resulting in an associated peak broadening [46, 47]. Meanwhile, relatively broader and weaker absorption was registered in the NIR region 940-2050 nm, **Fig. 2A.9b**. This triplet peak was accounted for the transitions $^4A_2(F) \rightarrow {}^4T_1(F)$ at 940-1310 nm and $^4A_2(F) \rightarrow {}^4T_2(F)$ at 1310-2050 nm[38].

UV-Vis-NIR absorption spectra of the synthesized phase pure $LiZn_{1-x}Co_xPO_4$ pigment series are displayed in **Fig. 2A.10a, b**. Similar to the blue pigment series, equally stronger and slightly broader absorption was recorded in a spectral range of 460-680 nm, with a triplet band of unequal intensities at 525, 575 and 615 nm. Except violet and a portion of red, the pigment absorbed the whole visible spectrum. Hence, the pigment exhibited an intense purple hue, a combination of blue-violet and red. As per Tanabe-Sugano diagram, this corresponds to a spin

allowed d-d transition $^4A_2(F) \rightarrow {}^4T_1(P)$ of tetrahedrally co-ordinated Co^{2+} ions[10, 41-44]. The spectra also showed low intensity absorptions of spin forbidden d-d transitions $^4A_2(F) \rightarrow {}^2T_1(^2H)$ and $^4A_2(F) \rightarrow {}^2T_1(^2P)$, at 405 and 445 nm, respectively[45, 48, 49]. The characteristic peak splitting and peak broadening of tetrahedral Co^{2+} was also noticed for $LiZn_{1-x}Co_xPO_4$ absorption spectra[42, 46, 47]. Moreover, increasing the Co doping from 10 to 40 mol% resulted in an enhancement in absorption intensity as the optical density increased. More insight on Co^{2+} geometry was obtained from the absorption profile in the NIR region. A broad absorption was observed in the 950-2100 nm range, associated with electronic transitions $^4A_2(F) \rightarrow {}^4T_2(F)$ and $^4A_2(F) \rightarrow {}^4T_1(F)$ [38].
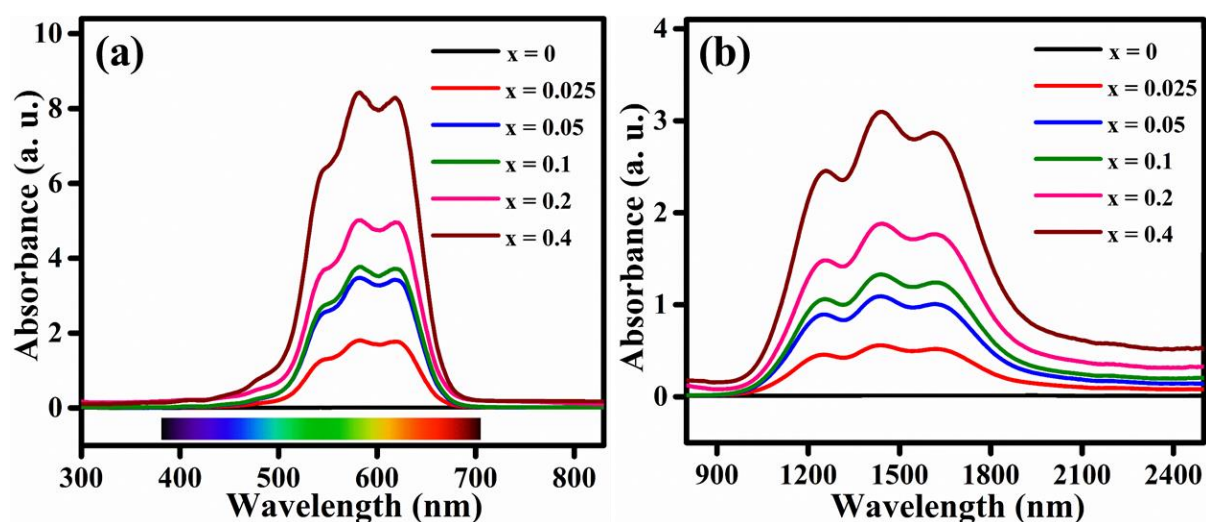
Fig. 2A.9. Absorption spectra of $NaZn_{1-x}Co_xPO_4$ ($0 \leq x \leq 0.4$) in (a) UV-visible and (b) NIR region

Once the Co doping increased over 40 mol%, a progressive blue shift was noticed in the absorption onset from 680 to 655 nm, **Fig. 2A.10c, d**. It absorbed blue, green, yellow and orange colours in the visible light and reflected the entire violet and red colours back. Since the pigment began to reflect more red region, a colour change from purple to violet was noticed in contrast to the previous case. When Co concentration increased from 40 to 60 mol%, the absorption shoulder at 615 nm began to fade, while a new shoulder peak appeared at 490 nm. Similarly, a new sharp absorption peak was observed in the NIR region 720-1010 nm, in addition to the broad peak located at 1560 nm. According to the electronic transitions ascribed to the three absorptions, $^4T_{1g}(F) \rightarrow {}^4T_{1g}(P)$ visible range, $^4T_{1g}(F) \rightarrow {}^4A_{2g}(F)$ at 788 nm and $^4T_{1g}(F) \rightarrow {}^4T_{2g}(F)$ at 1560 nm NIR region, it corresponds to octahedrally co-ordinated Co^{2+} ions. It indicates that after 40 mol% doping, the chromophore geometry switches from tetrahedral to octahedral, with both coexisting. Furthermore, at 80 mol% doping, the pigment

contains only Co^{2+} octahedra[38, 48]. The findings are compatible with PXRD data because the presence of $LiCoPO_4$ secondary phase was observed from 60 mol% doping that contains octahedrally co-ordinated Co^{2+} ions.
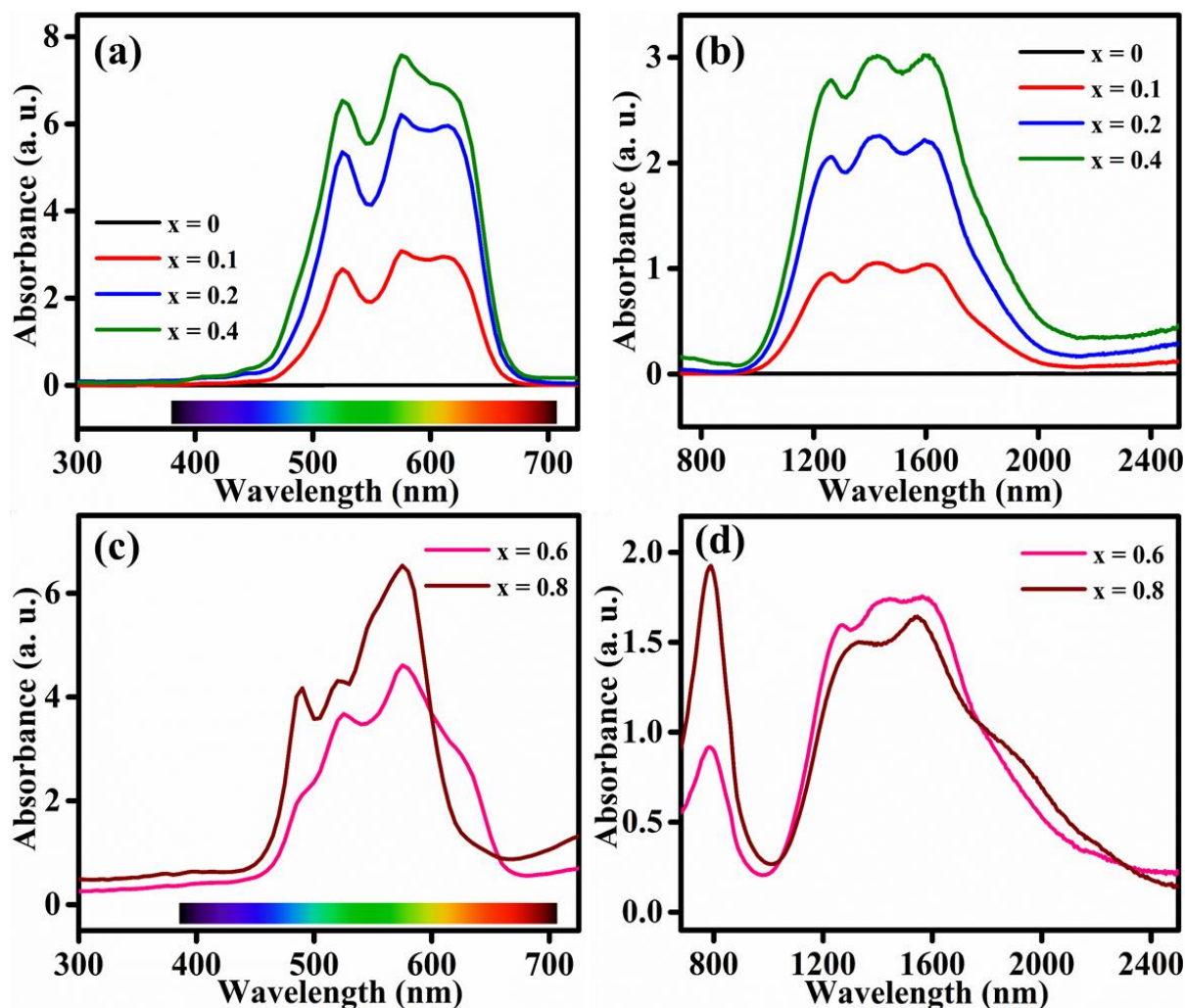
Fig. 2A.10. Absorption spectra of $LiZn_{1-x}Co_xPO_4$ ($0 \leq x \leq 0.4$) in (a) UV-visible, (b) NIR region and $LiZn_{1-x}Co_xPO_4$ ($0.6 \leq x \leq 0.8$) in (c) UV-visible and (d) NIR region

Fig. 2A.11a, b depicts the absorption spectra of $LiMg_{1-x}Co_xPO_4$ ($0 \leq x \leq 0.8$) pigment series. The spectra have three major absorptions spread across the visible and NIR regions. An intense broad absorption at 435-645 nm (visible region) having 3 peaks at 485, 520 and 575 nm. The pigment demonstrated a bright magenta colour because it covers the whole absorption spectrum except a portion of red and violet wavelengths. As seen in colour parameters, the combination of violet and red in equal portion produces the magenta colour. Additionally, a narrow band at 650-950 nm (visible-NIR region) and a broad band at 1010-2450 nm (NIR region) were observed. The electronic transitions that correspond to these absorptions in a d^7 system was described using the Tananbe-Sugano diagram. The spin allowed d-d transitions

$^4T_{1g}(F) \rightarrow {}^4T_{1g}(P)$, $^4T_{1g}(F) \rightarrow {}^4A_{2g}(F)$ and $^4T_{1g}(F) \rightarrow {}^4T_{2g}(F)$ correspond to absorptions at 435-645, 650-950 and 1010-2450 nm, respectively[38, 48]. The observed electronic transitions shed light on the typical octahedral geometry of the chromophore. The examination of peak splittings and peak broadening yielded further information on the chromophore structure. Similar to the previous cases, the triplet splitting of the high energy absorption was attributed to spin-orbit coupling effect and Jahn-Tellar distortion[46, 47]. Even for the multiple phase compositions (above 40 mol% doping), there was no substantial change in the absorption profile of magenta pigment series, **Fig. 2A.11c, d**. However, the absorption intensity increased with the addition of Co^{2+} concentration and turned violet in the presence of $LiCoPO_4$ secondary phase. It is unambiguous that all of the prepared compositions in $LiMg_{1-x}Co_xPO_4$ series have the same chromophore geometry.
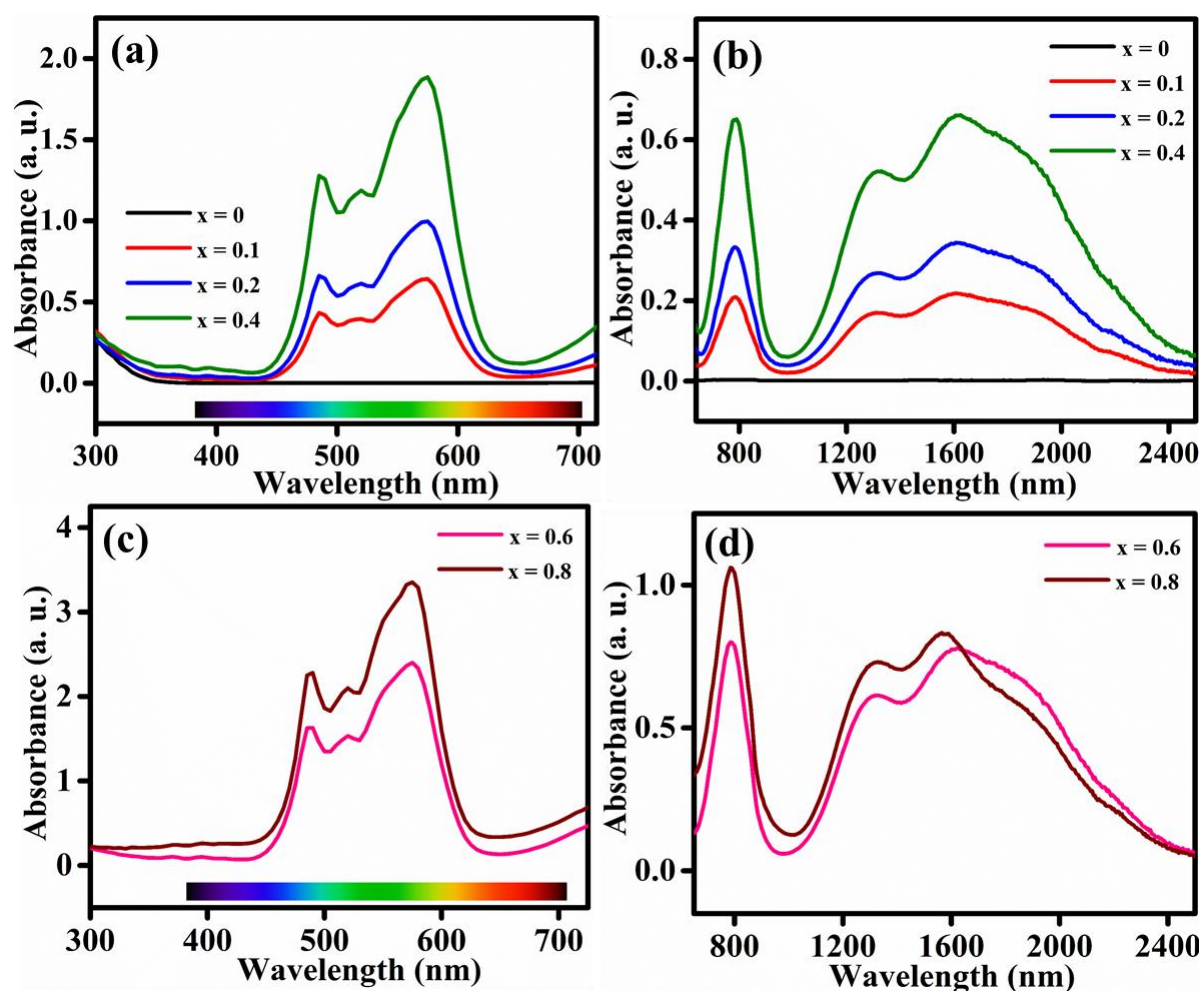
Fig. 2A.11. Absorption spectra of $LiMg_{1-x}Co_xPO_4$ ($0 \le x \le 0.4$) in (a) UV-visible, (b) NIR region and $LiMg_{1-x}Co_xPO_4$ ($0.6 \le x \le 0.8$) in (c) UV-visible and (d) NIR region

The spectral characteristics and colour analyses emphasized the importance of chromophore geometry in determining the pigment's colour tone. Because, when comparing

$NaZn_{0.9}Co_{0.1}PO_4$, $LiZn_{0.9}Co_{0.1}PO_4$ and $LiMg_{0.9}Co_{0.1}PO_4$ pigments, having the same chromophore in same concentration (10 mol%), give rise to three different colours; blue, purple and magenta. The magenta colour was produced by octahedral Co^{2+} geometry, while blue and purple were produced by tetrahedral geometry. According to previous reports, a tetrahedral CoO_4 geometry generally develops intense blue and green colours, typical examples are $CoAl_2O_4$ and Co^{2+} doped ZnO, respectively[50, 51]. Interestingly, with a tetrahedral geometry, Co^{2+} in $LiZn_{0.9}Co_{0.1}PO_4$ exhibited an intense purple colour. Therefore, absorption spectra of $CoAl_2O_4$, $NaZn_{0.9}Co_{0.1}PO_4$ and $LiZn_{0.9}Co_{0.1}PO_4$ pigments were compared to have more idea on this observation.
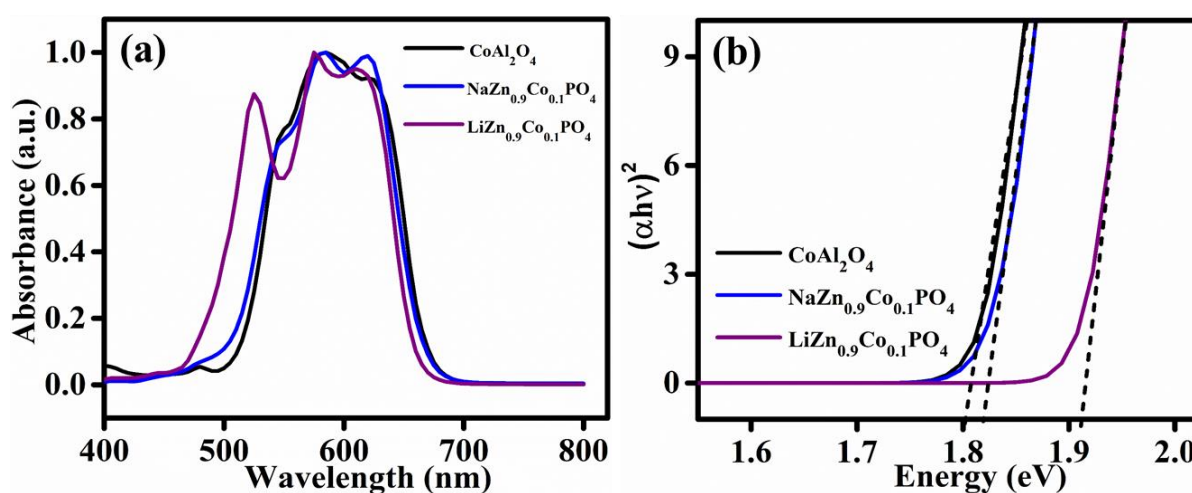
Fig. 2A.12. (a) Normalized absorption spectra and (b) Tauc plot of $CoAl_2O_4$, $NaZn_{0.9}Co_{0.1}PO_4$ and $LiZn_{0.9}Co_{0.1}PO_4$

Fig. 2A.12a, showed a comparison of the visible range absorption spectra of $CoAl_2O_4$, $NaZn_{0.9}Co_{0.1}PO_4$ and $LiZn_{0.9}Co_{0.1}PO_4$. It is noteworthy that there is a profound blue shift occurred for $NaZn_{0.9}Co_{0.1}PO_4$ and $LiZn_{0.9}Co_{0.1}PO_4$ systems compared to $CoAl_2O_4$. The band gap calculated from the Tauc plot, **Fig. 2A.12b**, was 1.80, 1.82 and 1.91 eV, for $CoAl_2O_4$, $NaZn_{0.9}Co_{0.1}PO_4$ and $LiZn_{0.9}Co_{0.1}PO_4$, respectively. Furthermore, the science behind this fascinating result was sorted out from the structural studies.

2A.4.6. Structural study

Structural details of the chromophore in $NaZn_{0.9}Co_{0.1}PO_4$ and $LiZn_{0.9}Co_{0.1}PO_4$ pigments were studied via Rietveld refinement analysis. The Rietveld refined XRD pattern of $NaZn_{0.9}Co_{0.1}PO_4$ was depicted in **Fig. 2A.13a**, and the corresponding crystallographic data were presented in **Table 2A.3**. The R_p factor of refined XRD pattern is 12.37%, which is acceptable for a monoclinic system[52]. The constituent ions Na^+, Zn^{2+} and P^{5+} were occupied in

three different co-ordination environments in the complex structure of $NaZn_{0.9}Co_{0.1}PO_4$. Na^+ in NaO_8 polyhedra (Na1) and NaO_6 distorted octahedra (Na2 and Na3), Zn^{2+} in ZnO_4 distorted tetrahedra (Zn1, Zn2 and Zn3), and P^{5+} in PO_4 tetrahedra (P1, P2 and P3). According to the refinement results, Co^{2+} ions are accommodated in the Zn(2) tetrahedral site of the $NaZn_{0.9}Co_{0.1}PO_4$ structure. **Table 2A.4** provides the bond length and bond angle of $Zn(2)/CoO_4$ in $NaZn_{0.9}Co_{0.1}PO_4$. Structural details of the base compound were taken from the report by Elammari et al., for comparison[53].
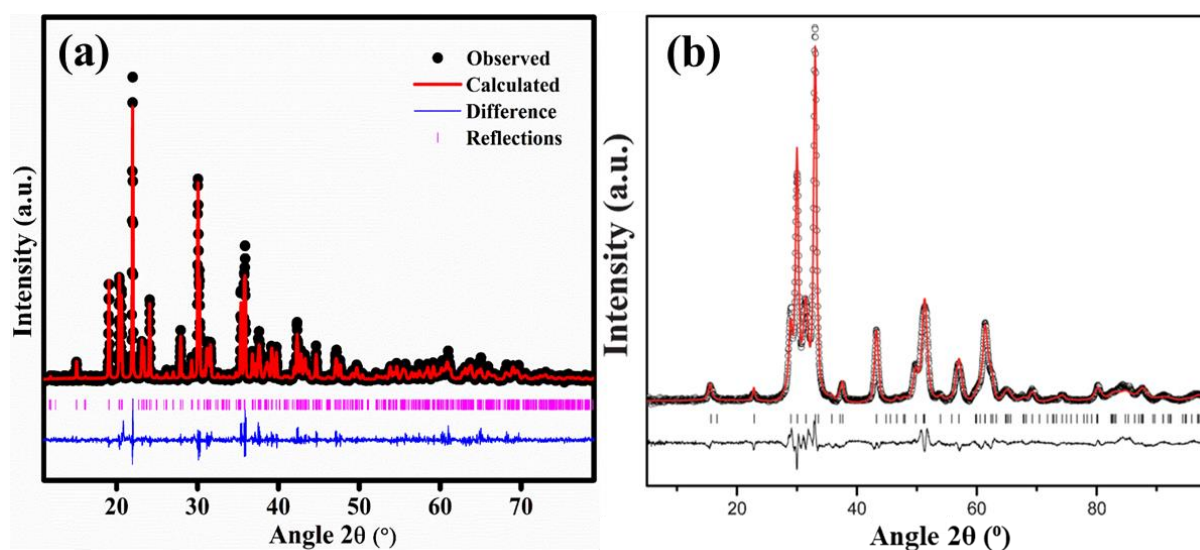
Fig. 2A.13. Rietveld refined PXRD pattern of (a) $NaZn_{0.9}Co_{0.1}PO_4$ and (b) $LiZn_{0.9}Co_{0.1}PO_4$

In comparison to the Zn-O bonds in $Zn(2)O_4$ structure, the Co doped tetrahedron carries three shorter and one longer Co-O bonds. The bond length decreased from 1.93-1.95 Å to 1.79-1.87 Å. Likewise, considerable variations were observed in the bond angles. The results demonstrated that the Co substitution induced significant distortion in the geometry of $Zn(2)O_4$, **Fig. 2A.14a**. Main parameter that controlled the bond length was variation in host and dopant ionic size. Even the slight difference in ionic size between Zn^{2+} (0.60 Å) and Co^{2+} (0.58 Å) brought the covalency factor into picture. Smaller the ionic size higher will be the covalency, in turn shorter will be the metal oxygen bond length[54]. Therefore, the decrease in Co-O bond length led to a shrinkage of $Zn(2)/CoO_4$ tetrahedra.
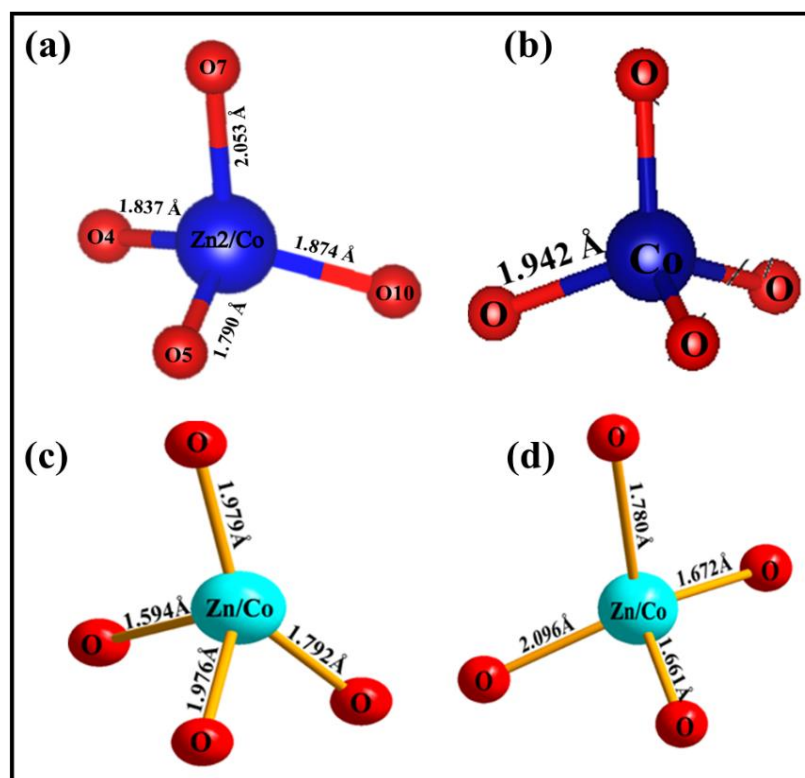
Fig. 2A.14. Co^{2+} coordination environment in (a) $NaZn_{0.9}Co_{0.1}PO_4$, (b) $CoAl_2O_4$, (c) $Zn2/CoO4$ and (d) $Zn2/CoO_4$ of $LiZn_{0.9}Co_{0.1}PO_4$

In fact, Co^{2+} in $CoAl_2O_4$ pigment possesses an ideal tetrahedral geometry, having a bond length of 1.942 Å, **Fig. 2A.14b**. But, the new blue pigment $NaZn_{0.9}Co_{0.1}PO_4$ comprises a distorted tetrahedral arrangement, with relatively shorter Co-O bonds. This indicates that the oxide ligands in $NaZn_{0.9}Co_{0.1}PO_4$, are closer to the metal ion. It enhances the interelectronic repulsion between ligand and metal orbitals, increasing the d orbital splitting in Co^{2+}. As a result, the band gap widens, and the absorption spectra shift to higher energy. Hence, distorted tetrahedral geometry of Co^{2+} brought 0.02 eV blue shift in the absorption spectrum of $NaZn_{0.9}Co_{0.1}PO_4$, compared to $CoAl_2O_4$. However, it was insufficient to cause a colour change in the pigment, therefore, the pigment remained blue.

Table 2A.3. Crystallographic data for $NaZn_{0.9}Co_{0.1}PO_4$

Atoms	x	y	z	Occupancy
Zn1	0.43650	0.22120	0.40790	1.000
Zn2/Co1	0.11010	0.71300	0.42010	0.900
Zn3	0.91519	0.21582	0.26519	1.000
Na1	0.24460	0.54700	0.25450	1.000
Na2	0.73351	0.53815	0.41150	1.000
Na3	0.72330	0.47100	0.06900	1.000
P1	0.44161	0.81623	0.40235	1.000
P2	0.11057	0.33077	0.42704	1.000
P3	0.92387	0.82590	0.26770	1.000
O1	-0.00200	0.47900	0.88670	1.000
O2	0.95700	0.24300	0.04090	1.000
O3	0.08600	0.23000	0.18480	1.000
O4	0.23331	0.33510	0.03191	1.000
O5	0.15040	0.50000	0.43980	1.000
O6	0.94915	0.33602	0.36189	1.000
O7	0.07300	0.20900	0.50500	1.000
O8	0.23000	0.22600	0.36870	1.000
O9	0.55300	0.50400	0.19840	1.000
O10	0.44400	0.20900	0.19850	1.000
O11	0.72400	0.23700	0.20310	1.000
O12	0.55656	0.34216	0.33097	1.000

Rietveld refined XRD pattern of $LiZn_{0.9}Co_{0.1}PO_4$ and respective crystallographic data were displayed in **Fig. 2A.13b** and **Table 2A.5**, respectively. The R_p fitting factor for the fitted graph is 7.38%. The result was in good agreement with its parent compound α-$LiZnPO_4$, which consists of three types of tetrahedra PO_4 (P1-P8), distorted LiO_4 (Li1-Li8) and ZnO_4 (Zn1-Zn8), one of each kind, share one corner. In the refined crystal structure, Zn^{2+}/Co^{2+} are associated with two different crystallographic sites Zn2 and Zn7, forming corner sharing tetrahedral geometry. Calculated bond lengths and bond angles of the $Zn2/CoO_4$ and $Zn7/CoO_4$ tetrahedra were tabulated in **Table 2A.4**. Structural details of $LiZnPO_4$ were taken from the report by Elammari et al., for comparison[55].

Table 2A.4. Bond length and bond angle of Co^{2+} tetrahedra

Pigment	Bond length (Å)		Bond angle (°)	
$NaZn_{0.9}Co_{0.1}PO_4$	$d_{Zn2/Co-O4}$	1.83656 (0)	$\theta_{O10-Zn2-O4}$	125.7 (11)
	$d_{Zn2/Co-O5}$	1.79 (4)	$\theta_{O10-Zn2-O5}$	101.3 (15)
	$d_{Zn2/Co-O7}$	2.05 (3)	$\theta_{O10-Zn2-O7}$	110.4 (14)
	$d_{Zn2/Co-O10}$	1.87 (4)	$\theta_{O4-Zn2-O7}$	100.5 (9)
			$\theta_{O7-Zn2-O5}$	110.8 (13)
			$\theta_{O5-Zn2-O4}$	108.1 (10)
$LiZn_{0.9}Co_{0.1}PO_4$	$d_{Zn2/Co-O84}$	1.98 (14)	$\theta_{O84-Zn2-O64}$	122.602
	$d_{Zn2/Co-O62}$	1.79 (19)	$\theta_{O84-Zn2-O52}$	88.319
	$d_{Zn2/Co-O52}$	1.59 (16)	$\theta_{O84-Zn2-O22}$	109.000
	$d_{Zn2/Co-O22}$	1.98 (18)	$\theta_{O64-Zn2-O52}$	143.595
			$\theta_{O64-Zn2-O22}$	102.328
			$\theta_{O52-Zn2-O22}$	82.254
	$d_{Zn7/Co-O63}$	1.67 (16)	$\theta_{O72-Zn7-O53}$	101.758
	$d_{Zn7/Co-O12}$	1.67 (14)	$\theta_{O72-Zn7-O63}$	115.385
	$d_{Zn7/Co-O72}$	1.78 (19)	$\theta_{O72-Zn7-O12}$	133.761
	$d_{Zn7/Co-O5}$	2.10 (19)	$\theta_{O63-Zn7-O12}$	85.310
			$\theta_{O63-Zn7-O53}$	111.600
			$\theta_{O53-Zn7-O12}$	108.153

The Co-O bond length was reduced in $LiZn_{0.9}Co_{0.1}PO_4$ due to the difference in bond covalence, as it was in $NaZn_{0.9}Co_{0.1}PO_4$. In the case of $Zn2/CoO_4$ tetrahedra, two of the four Co-O linkages were unusually small when compared to the $CoAl_2O_4$ system, **Fig. 2A.14c**. As a result, the geometry became significantly more strained, forcing the bond angle to deviate from the standard 109°28' so that the bond strain could be kept to a minimum, eventually forming highly distorted tetrahedra. $Zn7/CoO_4$ tetrahedra were also found in distorted geometry, where three shorter and one slightly longer Co-O bonds are observed, **Fig. 2A.14d**. Hence, the refinement data confirmed the formation of heavily distorted Zn/CoO_4 tetrahedra in $LiZn_{0.9}Co_{0.1}PO_4$. Subsequently, the interelectronic repulsion between ligand and metal orbitals increased, in turn d orbital splitting. This brought 0.09 eV blue shift in the absorption spectrum of $LiZn_{0.9}Co_{0.1}PO_4$ compared to $CoAl_2O_4$. Consequently, the pigment turns from blue to purple colour.

Table 2A.5. Crystallographic data for LiZn$_{0.9}$Co$_{0.1}$PO$_4$

Atom	x	y	z	Occupancy
Zn(1)	0.479(2)	0.210(4)	0.333(2)	1.000
Zn(2)/Co	0.232(3)	0.458(5)	0.328(2)	0.9/0.1
Zn(3)	-0.001(3)	0.176(4)	0.328(3)	1.000
Zn(4)	0.266(3)	0.204(4)	0.084(2)	1.000
Zn(5)	0.009(2)	0.050(4)	0.577(3)	1.000
Zn(6)	0.292(2)	0.285(4)	0.582(2)	1.000
Zn(7)/Co	0.264(2)	0.081(4)	0.834(3)	0.9/0.1
Zn(8)	0.040(2)	0.483(4)	0.071(2)	1.000
P(1)	0.567(5)	0.441(8)	0.263(6)	1.000
P(2)	0.037(4)	0.445(8)	0.270(5)	1.000
P(3)	0.080(5)	0.192(9)	0.022(6)	1.000
P(4)	0.098(5)	0.255(8)	0.520(5)	1.000
P(5)	0.287(5)	0.207(9)	0.269(6)	1.000
P(6)	0.328(6)	0.661(8)	0.263(5)	1.000
P(7)	0.353(5)	0.050(8)	0.519(5)	1.000
P(8)	0.320(5)	0.439(9)	0.010(5)	1.000
O(11)	0.101(10)	0.035(17)	0.352(11)	1.000
O(12)	0.693(8)	0.311(16)	0.273(8)	1.000
O(13)	0.063(8)	0.023(14)	0.190(11)	1.000
O(14)	0.516(9)	0.335(17)	0.278(10)	1.000
O(21)	0.468(9)	0.014(15)	0.315(11)	1.000
O(22)	0.128(9)	0.526(16)	0.338(10)	1.000
O(23)	0.029(9)	0.321(17)	0.244(10)	1.000
O(24)	0.058(10)	0.552(17)	0.192(10)	1.000
O(31)	0.041(10)	0.291(16)	0.105(10)	1.000
O(32)	0.579(9)	0.227(16)	0.433(11)	1.000
O(33)	0.149(10)	0.140(16)	0.040(9)	1.000
O(34)	0.010(11)	0.094(17)	0.003(10)	1.000
O(41)	0.038(8)	0.217(14)	0.457(10)	1.000
O(42)	0.122(9)	0.157(15)	0.606(9)	1.000
O(43)	0.170(8)	0.177(16)	0.502(10)	1.000
O(44)	0.123(9)	0.544(16)	0.028(9)	1.000
O(51)	0.288(9)	0.276(18)	0.185(10)	1.000
O(52)	0.200(9)	0.316(15)	0.351(8)	1.000
O(53)	0.279(10)	0.079(18)	0.259(10)	1.000
O(54)	0.380(11)	0.246(15)	0.344(10)	1.000
O(61)	0.305(10)	0.212(16)	0.694(11)	1.000
O(62)	0.239(9)	0.558(19)	0.243(10)	1.000
O(63)	0.331(9)	0.793(16)	0.342(11)	1.000
O(64)	0.401(10)	0.577(17)	0.296(11)	1.000
O(71)	0.391(10)	0.203(17)	0.552(11)	1.000
O(72)	0.276(10)	0.007(16)	0.430(10)	1.000
O(73)	0.409(9)	0.090(15)	-0.009(10)	1.000
O(74)	0.341(9)	0.031(15)	0.086(10)	1.000
O(81)	0.407(9)	0.373(15)	0.028(9)	1.000
O(82)	0.358(9)	0.515(13)	0.094(9)	1.000
O(83)	0.242(9)	0.328(16)	-0.003(9)	1.000

O(84)	0.320(9)	0.457(17)	0.440(10)	1.000
Li(1)	0.63(3)	0.14(4)	0.22(3)	1.000
Li(2)	0.12(2)	0.27(4)	0.23(2)	1.000
Li(3)	0.36(2)	0.16(4)	0.41(3)	1.000
Li(4)	0.46(4)	0.81(5)	0.64(4)	1.000
Li(5)	0.13(3)	0.53(5)	0.46(3)	1.000
Li(6)	0.15(3)	0.06(5)	0.41(3)	1.000
Li(7)	0.38(3)	0.36(4)	0.19(3)	1.000
Li(8)	0.38(3)	0.00(4)	0.70(3)	1.000

2A.5. Conclusions

Three novel inorganic pigment series were synthesized from white monophosphate compounds $NaZnPO_4$, $LiZnPO_4$ and $LiMgPO_4$, via solid-state method. Substitution of Co^{2+} chromophore at the host divalent site developed a deep blue colour in $NaZnPO_4$, an intense purple colour in $LiZnPO_4$ and a bright magenta colour in $LiMgPO_4$. The phase purity of the pigments was confirmed up to the doping concentration of 40 mol%. Representative SEM images from each pigment series indicated a broad particle size distribution, later verified by DLS analysis. The pigment colour strength was evaluated using CIE 1976 $L^*a^*b^*$ colour scale and determined the best composition. The composition $NaZn_{0.9}Co_{0.1}PO_4$ exhibited better colour parameters than that of commercial $CoAl_2O_4$ blue. Based on the Tanabe-Sugano diagram, ligand field electronic transitions responsible for the specific pigment colour were identfied from the spectral characteristics. The tetrahedral Co^{2+} was responsible for blue and purple colours, whereas octahedral Co^{2+} developed magenta hue. The structural comparison of the chromophore geometry through Rietveld refinement analysis revealed that compared to $CoAl_2O_4$, the tetrahedral geometry of Co^{2+} in $NaZn_{0.9}Co_{0.1}PO_4$ and $LiZn_{0.9}Co_{0.1}PO_4$ are distorted. However, the extent of distortion in $LiZn_{0.9}Co_{0.1}PO_4$ was very strong such that it enhanced the optical bandgap inducing a colour change from blue to purple.

2A.6. References

1. Pastoureau, M.; Cruse, M., *Blue: The History of a Color*. Princeton University Press: 2001.

2. Samain, L.; Grandjean, F.; Long, G. J.; Martinetto, P.; Bordet, P.; Strivay, D. J. T. J. o. P. C. C., Relationship between the synthesis of Prussian blue pigments, their color, physical properties, and their behavior in paint layers. **2013,** *117* (19), 9693-9712.

3. Ocana, M.; Espinos, J.; Carda, J. J. D.; Pigments, Synthesis, through pyrolysis of aerosols, of $YIn_{1-x}Mn_xO_3$ blue pigments and their efficiency for colouring glazes. **2011,** *91* (3), 501-507.

4. Berke, H. J. C. S. R., The invention of blue and purple pigments in ancient times. **2007,** *36* (1), 15-30.

5. Berke, H. J. A. C. I. E., Chemistry in ancient times: the development of blue and purple pigments. **2002,** *41* (14), 2483-2487.

6. Del Federico, E.; Shofberger, W.; Schelvis, J.; Kapetanaki, S.; Tyne, L.; Jerschow, A. J. I. c., Insight into framework destruction in ultramarine pigments. **2006,** *45* (3), 1270-1276.

7. Yoneda, M.; Gotoh, K.; Nakanishi, M.; Fujii, T.; Konishi, Y.; Nomura, T. J. J. o. t. A. C. S., Solid-state synthesis and characterization of cobalt blue core-shell pigment particles. **2019,** *102* (6), 3468-3476.

8. Zou, J.; Zheng, W. J. C. i., $TiO_2@CoTiO_3$ complex green pigments with low cobalt content and tunable color properties. **2016,** *42* (7), 8198-8205.

9. De Souza, L. K.; Zamian, J. R.; da Rocha Filho, G. N.; Soledade, L. E.; dos Santos, I. M.; Souza, A. G.; Scheller, T.; Angelica, R. m. S.; da Costa, C. E. J. D.; Pigments, Blue pigments based on $Co_xZn_{1-x}Al_2O_4$ spinels synthesized by the polymeric precursor method. **2009,** *81* (3), 187-192.

10. Llusar, M.; Fores, A.; Badenes, J.; Calbo, J.; Tena, M.; Monros, G. J. J. o. t. E. C. S., Colour analysis of some cobalt-based blue pigments. **2001,** *21* (8), 1121-1130.

11. Smith, A. E.; Mizoguchi, H.; Delaney, K.; Spaldin, N. A.; Sleight, A. W.; Subramanian, M. A. J. J. o. t. A. C. S., Mn^{3+} in trigonal bipyramidal coordination: a new blue chromophore. **2009,** *131* (47), 17084-17086.

12. Meseguer, S.; Tena, M.; Gargori, C.; Galindo, R.; Badenes, J.; Llusar, M.; Monros, G. J. C. I., Development of blue ceramic dyes from cobalt phosphates. **2008,** *34* (6), 1431-1438.

13. Gorodylova, N.; Kosinova, V.; Dohnalova, Z.; Sulcova, P.; Belina, P. J. D.; Pigments, A comparative study of the influence of mineralisers on the properties of $CoZr_4(PO_4)_6$-based pigments. **2014,** *111*, 156-161.

14. Porter, S. H.; Xiong, J.; Avdeev, M.; Merz, D.; Woodward, P. M.; Huang, Z. J. I. C., Structural, Magnetic, and Optical Properties of $A_3V_4(PO_4)_6$ (A = Mg, Mn, Fe, Co, Ni). **2016,** *55* (12), 5772-5779.

15. Hunault, M.; Robert, J.-L.; Newville, M.; Galoisy, L.; Calas, G. J. S. A. P. A. M.; Spectroscopy, B., Spectroscopic properties of five-coordinated Co^{2+} in phosphates. **2014,** *117*, 406-412.

16. Llusar, M.; Zielinska, A.; Tena, M.; Badenes, J.; Monros, G. J. J. o. t. E. C. S., Blue-violet ceramic pigments based on Co and Mg $Co_{2-x}Mg_xP_2O_7$ diphosphates. **2010,** *30* (9), 1887-1896.

17. Kusumoto, K. J. J. o. t. C. S. o. J., Synthesis of Co-free inorganic blue pigments based on turquoise blue glaze. **2018,** *126* (5), 408-411.

18. Costa, G.; Ribeiro, M.; Hajjaji, W.; Seabra, M.; Labrincha, J.; Dondi, M.; Cruciani, G. J. J. o. t. E. C. S., Ni-doped hibonite ($CaAl_{12}O_{19}$): a new turquoise blue ceramic pigment. **2009,** *29* (13), 2671-2678.

19. Chen, Y.; Zhang, Y.; Feng, S. J. D.; Pigments, Hydrothermal synthesis and properties of pigments Chinese purple $BaCuSi_2O_6$ and dark blue $BaCu_2Si_2O_7$. **2014,** *105*, 167-173.

20. El Jazouli, A.; Tbib, B.; Demourgues, A.; Gaudon, M. J. D.; Pigments, Structure and colour of diphosphate pigments with square pyramid environment around chromophore ions (Co^{2+}, Ni^{2+}, Cu^{2+}). **2014,** *104*, 67-74.

21. Stanjek, H.; Husler, W. J. H. i., Basics of X-ray Diffraction. **2004,** *154*, 107-119.

22. note, P. T. J. A., Diffuse Reflectance-Theory and Applications. 2011; p p. 2.

23. Pfaff, G. J. C., The world of inorganic pigments. **2022,** *8* (3), 15.

24. Andrade, S. n.; Goncalves, F.; Guine, R. In *Physical-chemical properties of Corema album (white crowberry or camarinha)*, ICEUBI2015-International Conference of Engineering: Engineering for Society, 2015.

25. Jose, S.; Reddy, M. L. J. D.; Pigments, Lanthanum-strontium copper silicates as intense blue inorganic pigments with high near-infrared reflectance. **2013,** *98* (3), 540-546.

26. Levinson, R.; Akbari, H.; Berdahl, P. J. S. E., Measuring solar reflectance-Part I: Defining a metric that accurately predicts solar heat gain. **2010,** *84* (9), 1717-1744.

27. Levinson, R.; Akbari, H.; Berdahl, P. J. S. E., Measuring solar reflectance-Part II: Review of practical methods. **2010,** *84* (9), 1745-1759.

28. Thongkanluang, T.; Kittiauchawal, T.; Limsuwan, P. J. C. I., Preparation and characterization of Cr_2O_3-TiO_2-Al_2O_3-V_2O_5 green pigment. **2011,** *37* (2), 543-548.

29. Rana, H. Evaluating Hue Shifts in Spot Color Tints in Flexographic Package Printing. Clemson University, 2020.

30. Gu, X. Y.; Luo, W. Q.; Chen, Y. X. J. A. M.; Materials, Study on Co-$KZr_2(PO_4)_3$-type crystalline purple ceramic pigments. **2010,** *34*, 790-794.

31. Pardo, A.; Romero, J.; Ortiz, E. In *High-temperature behaviour of ammonium dihydrogen phosphate*, Journal of Physics: Conference Series, IOP Publishing: 2017; p 012050.

32. Pasierb, P.; Gajerski, R.; Komornicki, S.; Rekas, M. J. J. o. t. a.; calorimetry, Structural properties and thermal behavior of Li_2CO_3-$BaCO_3$ system by DTA, TG and XRD measurements. **2001,** *65* (2), 457-466.

33. Bensalem, A. J. J. o. S. S. C., Synthesis and characterization of a new layered lithium zinc phosphate hydrate. **2001,** *162* (1), 29-33.

34. Liu, L.; Han, A.; Ye, M.; Feng, W. J. S. E., The evaluation of thermal performance of cool coatings colored with high near-infrared reflective nano-brown inorganic pigments: Magnesium doped $ZnFe_2O_4$ compounds. **2015,** *113*, 48-56.

35. Shannon, R. D. J. A. c. s. A. c. p., diffraction, theoretical; crystallography, g., Revised effective ionic radii and systematic studies of interatomic distances in halides and chalcogenides. **1976,** *32* (5), 751-767.

36. Jose, S.; Jayaprakash, A.; Laha, S.; Natarajan, S.; Nishanth, K.; Reddy, M. J. D.; Pigments, $YIn_{0.9}Mn_{0.1}O_3$-ZnO nano-pigment exhibiting intense blue color with impressive solar reflectance. **2016,** *124*, 120-129.

37. Tamilarasan, S.; Sarma, D.; Reddy, M.; Natarajan, S.; Gopalakrishnan, J. J. R. A., $YGa_{1-x}Mn_xO_3$: A novel purple inorganic pigment. **2013,** *3* (10), 3199-3202.

38. Gaudon, M.; Deniard, P.; Voisin, L.; Lacombe, G.; Darnat, F.; Demourgues, A.; Perillon, J.-L.; Jobic, S. J. D.; Pigments, How to mimic the thermo-induced red to green transition of ruby with control of the temperature via the use of an inorganic materials blend? **2012,** *95* (2), 344-350.

39. Tsukimori, T.; Shobu, Y.; Oka, R.; Masui, T. J. R. a., Synthesis and characterization of $Ba(Zn_{1-x}Co_x)_2Si_2O_7$ ($0 \leq x \leq 0.50$) for blue-violet inorganic pigments. **2018,** *8* (16), 9017-9022.

40. Cornu, L.; Jubera, V.; Demourgues, A.; Salek, G.; Gaudon, M. J. C. I., Luminescence properties and pigment properties of A-doped (Zn, Mg)MoO_4 triclinic oxides (with A = Co, Ni, Cu or Mn). **2017,** *43* (16), 13377-13387.

41. Mimani, T.; Ghosh, S. J. C. S., Combustion synthesis of cobalt pigments: Blue and pink. **2000**, 892-896.

42. Pozas, R.; Orera, V.; Ocana, M. J. J. o. t. E. C. S., Hydrothermal synthesis of Co-doped willemite powders with controlled particle size and shape. **2005,** *25* (13), 3165-3172.

43. Alvarez-Docio, C. M.; Reinosa, J.; Del Campo, A.; Fernandez, J. J. D.; Pigments, 2D particles forming a nanostructured shell: a step forward cool NIR reflectivity for $CoAl_2O_4$ pigments. **2017,** *137*, 1-11.

44. Weakliem, H. A. J. T. J. o. C. P., Optical spectra of Ni^{2+}, Co^{2+}, and Cu^{2+} in tetrahedral sites in crystals. **1962,** *36* (8), 2117-2140.

45. Ardit, M.; Cruciani, G.; Dondi, M. J. A. M., Structural relaxation in tetrahedrally coordinated Co^{2+} along the gahnite-Co-aluminate spinel solid solution. **2012,** *97* (8-9), 1394-1401.

46. Bamford, C. J. P. C. G., The application of the ligand field theory to coloured glasses. **1962,** *3* (6), 189-202.

47. Bates, T. J. M. a. o. t. v. s., Ligand field theory and absorption spectra of transition-metal ions in glasses. **1962,** *2*, 195-254.

48. Robertson, L.; Duttine, M.; Gaudon, M.; Demourgues, A. J. C. o. M., Cobalt-zinc molybdates as new blue pigments involving Co^{2+} in distorted trigonal bipyramids and octahedra. **2011,** *23* (9), 2419-2427.

49. Yang, S.; Aravindan, V.; Cho, W.; Chang, D.; Kim, H.; Lee, Y. J. J. o. t. E. S., Realizing the performance of $LiCoPO_4$ cathodes by Fe substitution with off-stoichiometry. **2012,** *159* (7), A1013.

50. Mokhtari, K.; Salem, S. J. R. a., A novel method for the clean synthesis of nano-sized cobalt based blue pigments. **2017,** *7* (47), 29899-29908.

51. Gaudon, M.; Toulemonde, O.; Demourgues, A. J. I. c., Green coloration of Co-doped ZnO explained from structural refinement and bond considerations. **2007,** *46* (26), 10996-11002.

52. Saraswathy, D.; Rao, P. P.; Raj, A. K.; Thara, T. A. J. C., Intense Blue Colors in Wolframite-Type Co^{2+}: $MgWO_4$ Oxides Through Distortion in Co^{2+} Octahedra. **2018,** *3* (2), 410-417.

53. Elammari, L.; Durand, J.; Cot, L.; Elouadi, B. J. Z. f. K.-C. M., The structure of $NaZnPO_4$. **1987,** *180* (1-4), 137-140.

54. Thejus, P.; Koley, B.; Nishanth, K. J. D.; Pigments, An intense purple chromophore based on Co^{2+} in distorted tetrahedral coordination. **2018,** *158*, 267-276.

55. Elammari, L.; Elouadi, B. J. A. C. S. C. C. S. C., Structure of α-LiZnPO$_4$. **1989,** *45* (12), 1864-1867.

Exploration of multifunctional properties of blue and magenta phosphate pigments

2B.1. Abstract

Beyond aesthetics, exploiting multifunctional capabilities of inorganic pigments for societal benefit is imperative. The NIR reflectance and anticorrosive properties of the new inorganic pigment series $NaZn_{1-x}Co_xPO_4$ blue and $LiMg_{1-x}Co_xPO_4$ magenta were investigated. Unlike conventional cobalt pigments, $NaZn_{0.9}Co_{0.1}PO_4$ and $LiMg_{0.8}Co_{0.2}PO_4$ demonstrated a superior NIR solar reflectance, 64 and 57%, respectively. Temperature shielding experiments employing pigment acrylic coatings successfully lowered the interior temperature of the foam box. The pigment incorporated epoxy coating on steel substrate was highly efficient in retarding the corrosion process in the marine medium. Precisely, 15 wt% $LiMg_{0.8}Co_{0.2}PO_4$ loaded epoxy coating exhibited the highest corrosion resistance, 9.3×10^9 Ωcm^2, which is four order higher than commercial blue and bare epoxy coatings. The XPS analysis established the anticorrosive mechanism that the phosphatized inhibitive film served as the corrosion barrier at the defective site. Therefore, the investigations concluded that the synthesized pigments can be employed as potential multifunctional inorganic pigments for developing anticorrosive 'cool' paint for energy-efficient buildings.

2B.2. Introduction

The new inorganic pigment series $NaZn_{1-x}Co_xPO_4$, $LiZn_{1-x}Co_xPO_4$ and $LiMg_{1-x}Co_xPO_4$ exhibited intense blue, purple and brilliant magenta colours, respectively. Geometry and structural distortion of Co chromophore played a crucial role in their origin of colour. Meanwhile, the research advancement has brought new dimensions for pigments apart from aesthetics. In this connection, the IR reflective inorganic pigments, known as 'cool' pigments, evolved as the latest development in pigment technology[1-4]. Because IR reflective pigments coated exterior walls and roofing sheets effectively mitigate the interior heat build-up, thereby reducing peak electricity demand in summer[5-10]. Therefore, the present chapter investigates the IR reflectance property of the synthesized inorganic pigments. Based on the colour demand $NaZn_{1-x}Co_xPO_4$ blue and $LiMg_{1-x}Co_xPO_4$ magenta pigment series were opted for the reflectance studies.

The most important part of constructing a potential cool building is the roof coatings, whether on concrete or metal sheet. In that case, the stability of the roof is crucial to get a sustainable output from their top 'cool' coatings. Unfortunately, it is inferior to metal roofs, which are subjected to corrosion under long-term exposure to harsh environmental conditions. In this regard corrosion resistant inorganic pigments are essential for developing anticorrosive

paints and primers. However, relying on many pigments for each distinct feature can significantly enhance the cost through a huge workload, excessive material and energy consumption, etc. In this scenario, a low-cost multifunctional inorganic pigment that simultaneously serves as a colourant, IR reflective and anticorrosive material would be ideal.

Cobalt pigments often exhibit poor NIR solar reflectance due to the fact that some of their d-d electronic transition falls in the IR region[11]. For example, the commercial Co pigment $CoAl_2O_4$ blue has only 29% NIR solar reflectance[12, 13]. In addition, there was also the challenge of incorporating anticorrosive property into the same pigment. Since $ABPO_4$ is a highly reflective compound, its reflectance profile can be maintained to a large extent even at high chromophore concentrations. Simultaneously, the phosphate moiety can introduce a phosphatization based corrosion protection mechanism as well[14]. Hence, the choice of $ABPO_4$ system as the base compound was well justified. In this rationale, the current chapter made an effort to explore the IR reflectance and anticorrosive properties of the pigment series $NaZn_{1-x}Co_xPO_4$ and $LiMg_{1-x}Co_xPO_4$.

2B.3. Experimental section

2B.3.1. Materials and methods

Acrylic emulsion of the pigment was prepared by dispersing pigment and acrylic binder in 1:4 ratio, by ultrasonication. The emulsion was brush coated on TiO_2 base coated concrete and Al sheet. IR reflectance studies were carried out on both pigment powder and coatings. Temperature shielding ability of the pigment coating was analyzed and compared to that of commercial $CoAl_2O_4$ coating using the experimental setup shown in **Fig. 2B.1**. Two identical foam model houses with dimensions $15 \times 15 \times 15$ cm were made and roofed with 19×19 cm pigment coated Al sheet. Two thermocouples T_1 (top) and T_2 (bottom) were inserted 2 cm below the roof and 3 cm above the base, respectively, to monitor the temperature buildup inside the box. The model houses were kept under IR lamp (Philips, 250 W), by maintaining the distance between rooftop and IR bulb at 40 cm. The experiment was carried out by continually exposing the IR lamp on the rooftop for one hour. Average of the temperatures measured at T_1 and T_2, gives the interior temperature of the box, was recorded at 10 min. intervals. FLIR C2 thermal imaging camera was used to capture thermal images of the coated surface from the level of the IR lamp at the same time intervals. Finally, a temperature against time plot was used to determine the interior and surface temperature trends.

Anticorrosive performance of the pigment was analyzed by using pigment loaded epoxy coatings on steel, having composition C = 0.24, Mn = 0.90, Al = 0.03, Si = 0.20, Cr = 0.04, V = 0.10, P = 0.08, Cu = 0.06 and remaining Fe. Steel coupons were cut into $4 \times 3 \times 0.2$ cm dimension and mechanically abraded with SiC paper grade 220 to 1000 subsequently, acetone degreased and dried. Different wt% (5, 10, 15, 20 and 25) pigment sample was dispersed in n-butanol-epoxy-polyamide (2:2:1) system by ultrasonication. The dispersion was dip coated on polished specimens at a dipping rate of 80 mm/min and allowed to cure for 24 h.
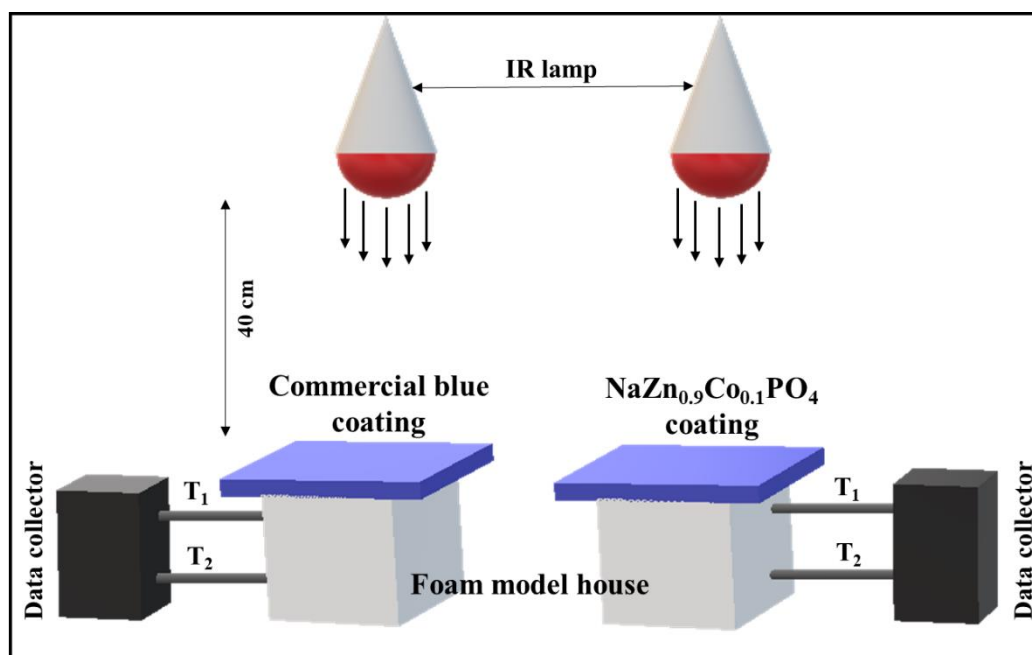
Fig. 2B.1. Schematic representation of thermal shielding experimental setup

2B.3.2. Characterization techniques

2B.3.2a. Electrochemical Impedance Spectroscopy (EIS)

Electrochemical impedance (Z) is the frequency-dependent resistance, measured by applying an alternating current to an electrochemical cell. Impedance is a complex number that has a real and an imaginary component. It can be represented via two plots, Nyquist and Bode. The Nyquist plot is a semi-circular plot with the real component (Z_{real}) on the X-axis and the imaginary part ($-Z_{img}$) on the Y-axis. Bode plot is expressed as log frequency on the X-axis, the impedance values and phase-shift on the Y, respectively (**Fig. 2B.2**).
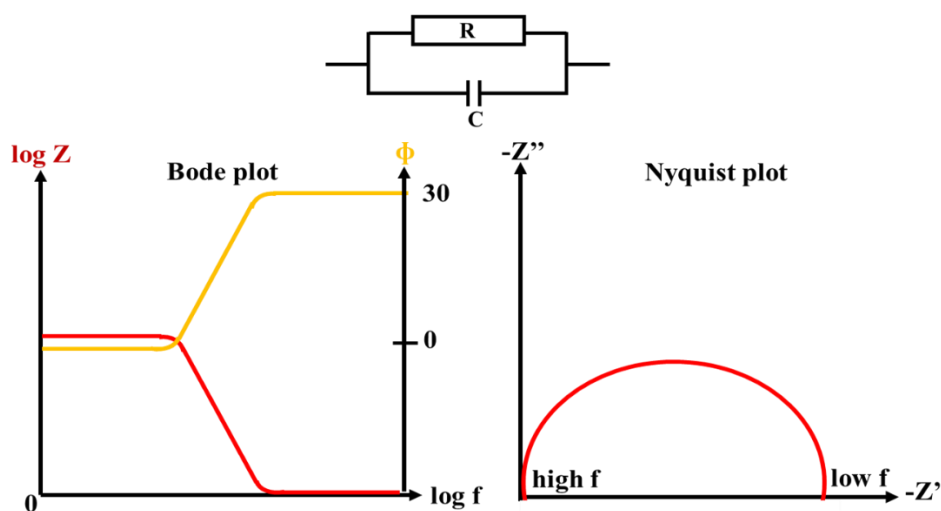
Fig. 2B.2. (a) Bode and (b) Nyquist plots from EIS

Generally, EIS data are analyzed by fitting to an electrochemical equivalent circuit (EEC) model[15]. The majority of the circuit elements in the model are common electrical elements such as resistors, capacitors etc. The elements in the model should have a basis in the physical electrochemistry of the system. When a coated working electrode is immersed in an electrolyte, an electrical double-layer formation will occur at the metal-electrolyte interface, which acts as a parallel plate capacitor. The resistance given by the electrolyte between the electrodes is represented by the solution/electrolyte resistance (R_s), while the resistance offered by the polymer coat is represented by the coating resistance (R_{coat}). Charge transfer resistance (R_{ct}) is generated at the metal electrolyte interphase via a kinetically regulated electrochemical reaction. The capacitor on real cells often shows a non-ideal behaviour owing to surface roughness, "leaky" capacitor, non-uniform current distribution, etc. The capacitance (C) is treated with an empirical constant (n) with no real physical basis and denoted as constant phase element (Q). Therefore, the capacitance of a polymer coat and double layer capacitor are represented as Q_{coat} and Q_{dl}, respectively[16, 17].

Herein, pigment ($CoAl_2O_4$ and $NaZn_{0.9}Co_{0.1}PO_4$/ $LiMg_{0.8}Co_{0.2}PO_4$) incorporated epoxy polymer coatings were developed on steel substrate. Further, corrosion resistance of the coatings was analyzed using a multichannel potentiostat (Autolab) having a three-electrode corrosion cell. The cell consists of 3.5 wt% NaCl solution as electrolyte, saturated calomel electrode (SCE), graphite and steel with surface area 1.2 cm^2, as reference, counter and working electrodes, respectively. Open circuit potential was stabilized for 30 min. Electrochemical impedance spectroscopy (EIS) experiment was performed in the frequency range of 10^5-10^{-2}

Hz at 5 mV amplitude AC signal. EIS plots were evaluated by Nova 2.1 software. The experiments were reiterated five times for each coated specimen.

2B.3.2b. X-ray Photoelectron Spectroscopy (XPS)

XPS is widely used to investigate the composition of a solid surface by irradiating monoenergetic soft X-rays in vacuum and subsequently analysing the energy of emitted electrons. Photons have limited penetrating power through a solid material in the order of 1-10 μm and they interact with atoms on the surface causing electrons to be emitted by the photoelectric effect (**Fig. 2B.3**). The emitted electrons have measured kinetic energies given by the equation,

$$KE = h\nu - BE - \varphi \qquad (2B.1)$$

Where,

$h\nu$ - energy of the photon

BE - binding energy of the atomic orbital from which electron originates

φ - spectrometer work function

The XPS spectrum is a plot of the number of detected electrons per energy interval (intensity) versus their kinetic/binding energy. Each element's unique spectrum provides quantitative data that can be obtained from peak heights or peak areas. Exact measurement of peak positions clearly identifies the oxidation state of the element. Further, the shifts in binding energy indicates bonding interaction with certain atoms, which confirms the formation of chemical compounds on the surfaces[18]. In the present thesis, in order to understand the corrosion inhibition mechanism of the pigment-loaded epoxy coatings, surface analysis of the steel specimen after continuous EIS analysis was performed via PHI 5000 Versa Probe II X-ray Photoelectron Spectroscopy (XPS) using CasaXPS software.

IR and NIR solar reflectance of the prepared pigments and coatings were analyzed by UV-Vis-NIR spectroscopic technique as described in Chapter 2A. Pigment acrylic coating thickness was measured using Leica DMRX Optical microscope and epoxy coating thickness was measured using Dektak XT stylus Profilometer.
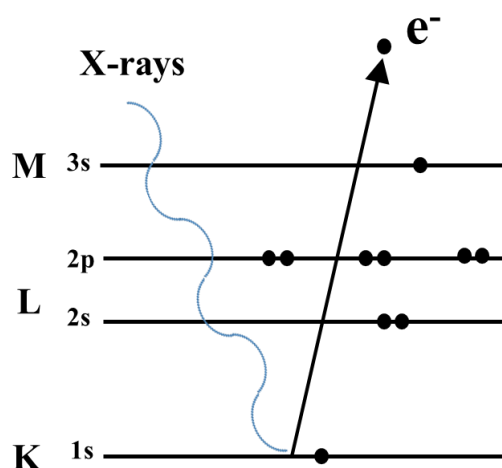
Fig. 2B.3. Principle of XPS technique

2B.4. Results and discussion

2B.4.1. Reflectance property of $NaZn_{1-x}Co_xPO_4$ and $LiMg_{1-x}Co_xPO_4$

As a result of the rising atmospheric temperature and accelerated UHI effect, the demand for heat shielding inorganic pigments has been gradually increasing. The NIR reflectance ability of the synthesized pigment series $NaZn_{1-x}Co_xPO_4$ (Blue) and $LiMg_{1-x}Co_xPO_4$ (Magenta) was estimated in this backdrop. The obtained NIR and NIR solar reflectance spectra were illustrated in **Fig. 2B.4**. Cobalt pigments, in general, are low reflective due to their characteristic absorption in the NIR range[12, 13, 19]. $CoAl_2O_4$ and $CoCr_2O_4$ are two well-known examples, with NIR solar reflectance R^* values of 29 and 30%, respectively[13, 20]. Unlike traditional colourants, the developed pigment series $NaZn_{1-x}Co_xPO_4$ and $LiMg_{1-x}Co_xPO_4$ displayed promising reflectivity, **Table 2B.1**. Despite the fact that the reflectance value decreased as Co concentration increased, both pigment series were able to attain NIR solar reflectance in the range of 40-70%. The findings confirmed that the developed inorganic pigments can be considered as potential 'cool' roof pigment. The selection of a high reflective base compound was vital in producing this excellent results. Since the present work was also emphasizes the colour strength, an optimum composition from each pigment series was decided based on reflectance (**Table 2B.1**) and colour parameters (**Table 2A.1**). It was found to be $NaZn_{0.9}Co_{0.1}PO_4$ and $LiMg_{0.8}Co_{0.2}PO_4$. The blue pigment has $b^* = -59.21$ and $R^* = 64\%$, while magenta pigment offers $a^* = 26.45$, $b^* = -26.83$ and $R^* = 57\%$.

Table 2B.1. Reflectance value of $NaZn_{1-x}Co_xPO_4$ and $LiMg_{1-x}Co_xPO_4$ pigment series

$NaZn_{1-x}Co_xPO_4$	NIR (%) at 1100 nm	R^* (%)	$LiMg_{1-x}Co_xPO_4$	NIR (%) at 1100 nm	R^* (%)
x = 0	87	87	x = 0	96	95
x = 0.025	56	67	x = 0.1	74	64
x = 0.05	50	65	x = 0.2	67	57
x = 0.1	49	64	x = 0.4	58	47
x = 0.2	32	52	x = 0.6	57	45
x = 0.4	37	40	x = 0.8	52	40
$CoAl_2O_4$	-	29	x = 1	36	27

Table 2B.2 summarises a comparison with literature reports, indicating the uniqueness of the novel pigment. Although certain reported pigments had better colour or reflectance, $NaZn_{0.9}Co_{0.1}PO_4$ was determined to be the best in terms of colour and R^* combined. Apart from a colourant, the developed blue and magenta inorganic pigments were able to handle different facet issues through their multiple capabilities. Further, the investigations were extended to ensure the property of pigment coatings on building materials.
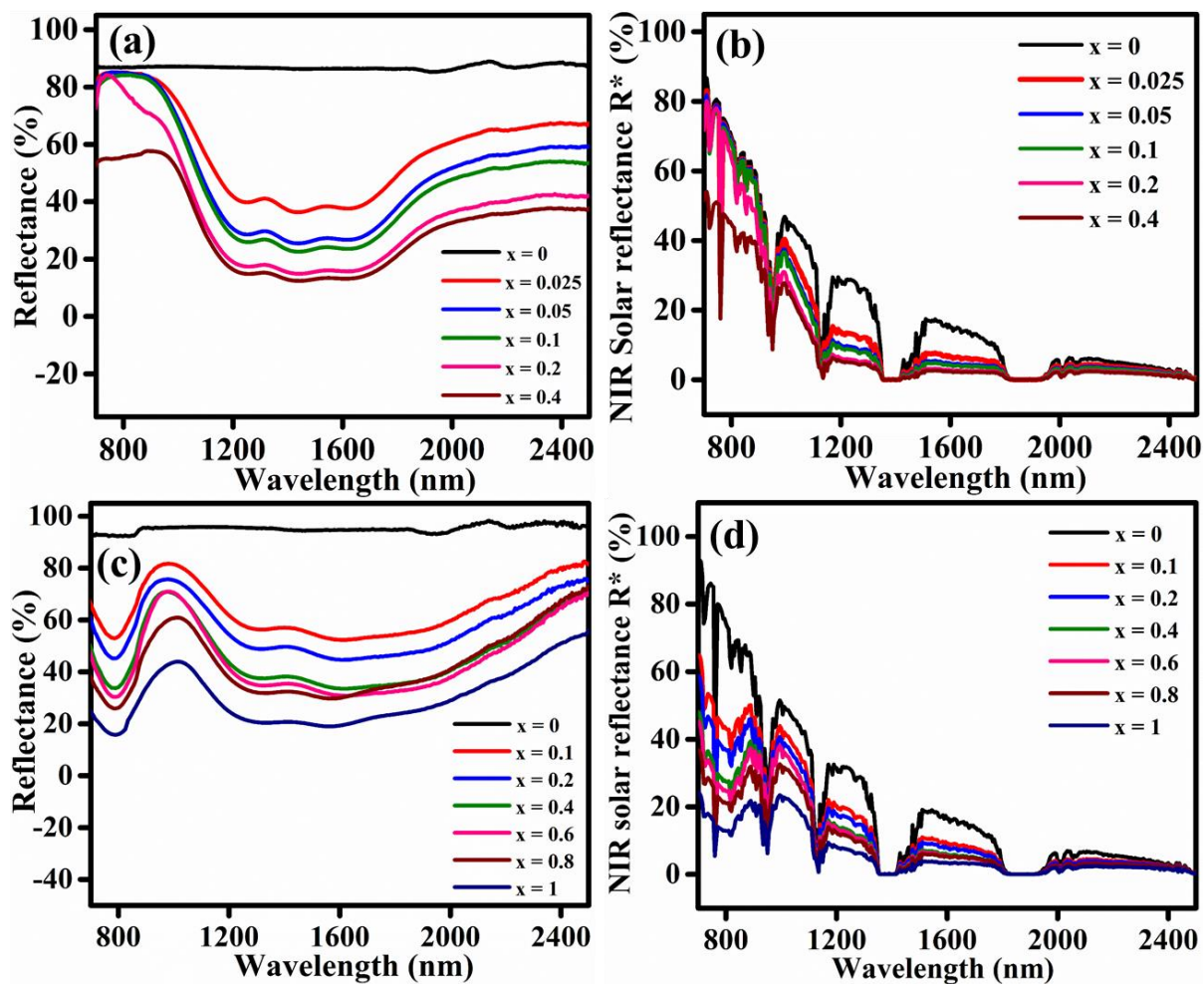
Fig. 2B.4. (a, c) NIR and (b, d) NIR solar reflectance spectra of $NaZn_{1-x}Co_xPO_4$ and $LiMg_{1-x}Co_xPO_4$ pigment series

Table 2B.2. Comparison of colour and solar reflectance with reported pigments

Sample	a^*	b^*	R^*
$YIn_{0.9}Mn_{0.1}O_3$-ZnO	-0.88	-40.55	70 [21]
$Sr_{0.8}Eu_{0.2}CuSi_4O_{10+\delta}$	-4.9	-27.5	72 [22]
$K_{0.3}WO_3$	-1.82	-10.23	66 [23]
$Sr_{0.7}La_{0.3}Cu_{0.7}Li_{0.3}Si_4O_{10}$	10.4	-51.7	66 [24]
$LaGa_{0.8}Mn_{0.2}Ge_2O_7$	14.92	-35.12	29 [25]
$CoCr_{1.5}Al_{0.5}O_4$	-20.3	-11.4	43 [20]
$YIn_{0.8}Mn_{0.2}O_3$	9.6	-38.9	41 [26]
Al:Cu:Co:Ce:Nd 2:0.2:0.2:0.15:0.05	-8.49	-21.29	39 [12]
$Zn_{0.9}Co_{0.1}Al_2O_4$	-3.7	-39.0	63 [27]
Kaolin-$CoAl_2O_4$ hybrid	-8.98	-39.06	60 [28]
$NaZn_{0.9}Co_{0.1}PO_4$	**10.70**	**-59.21**	**64 [Present study]**

2B.4.2. Chemical stability

The acid-base stability of the pigments was verified prior to coating preparation. The pigment samples were treated with acid, base and aqueous media for 1 h. Subsequently washed and dried, and measured the colour parameters, **Table 2B.3**. The difference in pigment colour coordinates before and after treatment, ΔE^*_{ab}, remained within the industrial limit, $\Delta E^*_{ab} \leq 1$ unit, hence confirmed the stability[21, 24].

Table 2B.3. Colour coordinates of $NaZn_{0.9}Co_{0.1}PO_4$ pigment after chemical treatment

Sample	pH	L^*	a^*	b^*	C^*	h^0	ΔE^*_{ab}
$NaZn_{0.9}Co_{0.1}PO_4$	-	51.78	10.70	-59.21	60.17	280.01	-
Water	6.6	51.65	10.04	-59.11	59.95	279.66	0.68
HNO_3	3.0	51.31	9.87	-58.66	59.48	279.56	1.10
NaOH	10.5	51.53	10.28	-58.91	59.80	279.9	0.57
$LiMg_{0.8}Co_{0.2}PO_4$	-	65.19	26.45	-26.83	37.68	314.60	-
Water	6.6	65.01	26.35	-26.61	37.45	314.71	0.30
HNO_3	3.0	64.55	26.10	-26.20	36.98	314.89	0.96
NaOH	10.5	64.71	26.12	-26.56	37.25	314.44	0.64

2B.4.3. Acrylic coatings

The pigment acrylic coatings were prepared on concrete and Al sheet, where coating thickness was determined from optical images to be 200-250 μm. Both the pigments successfully retained their colour strength in the coatings as well, **Table 2B.4**. Photographs of the coatings were shown alongside the bare substrate in **Fig. 2B.5** inset. Similarly, NIR and NIR solar reflectance property of the coatings were also remarkable. $NaZn_{0.9}Co_{0.1}PO_4$ and $LiMg_{0.8}Co_{0.2}PO_4$ exhibited R^* greater than 60 and 55%, respectively, **Fig. 2B.5**. Since bare concrete and Al sheet had only 44 and 45% reflectance, respectively, it is apparent that the new pigment coatings considerably enhanced the NIR reflectance ability of these surfaces. As a result, it can help to reduce the heat build up within buildings to some extent. Hence, the synthesized pigments can be established as potential coloured 'cool' pigments.
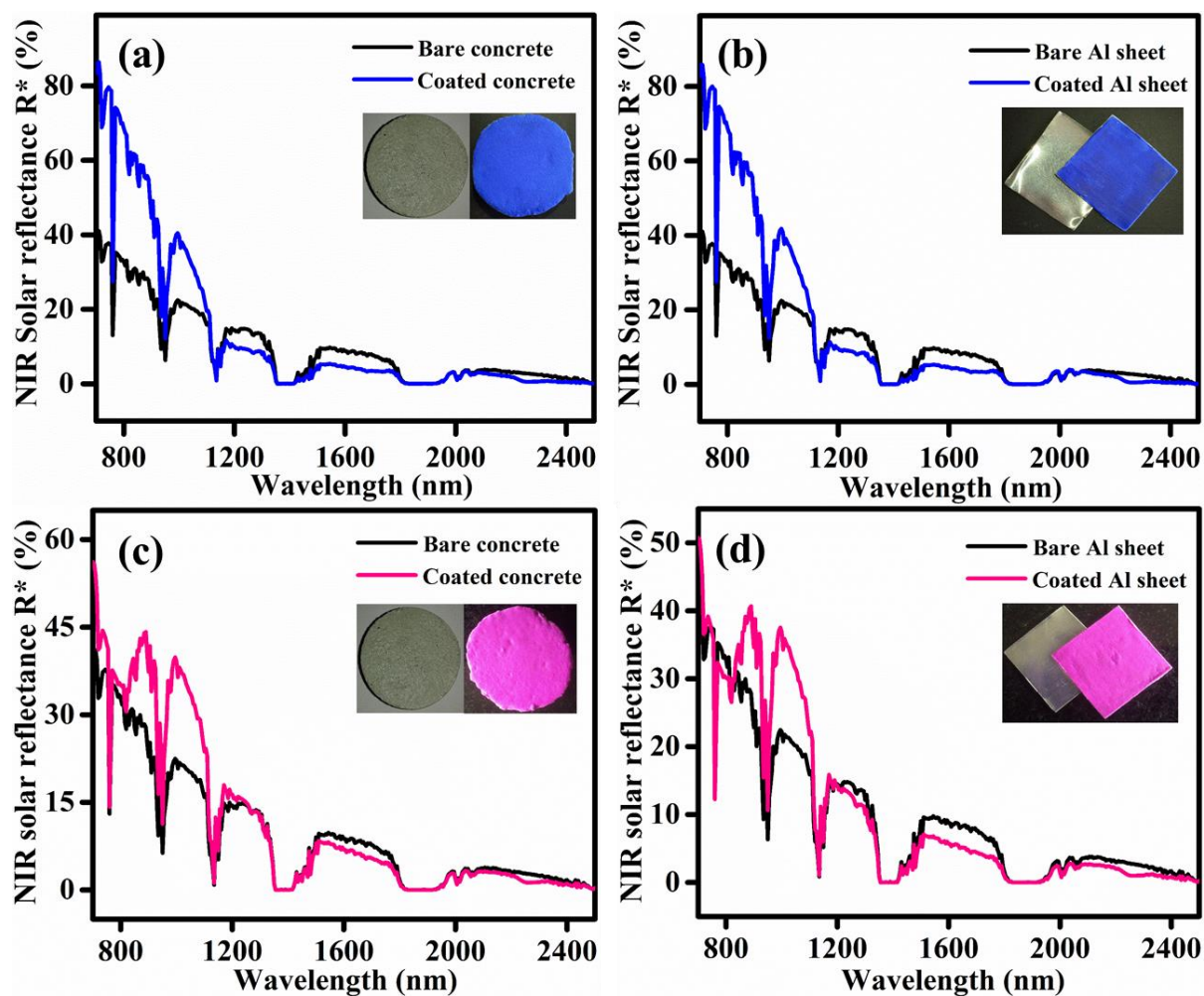
Fig. 2B.5. NIR solar reflectance spectra of NaZn$_{0.9}$Co$_{0.1}$PO$_4$ and LiMg$_{0.8}$Co$_{0.2}$PO$_4$

coatings on (a, c) concrete (b, d) Al sheet, respectively, with their bare surfaces (inset:

coating photos)

Table 2B.4. Colour coordinates and reflectance of pigment coatings

Pigment	Sample	L*	a*	b*	C*	h^o	NIR at 1100 nm (%)	R* (%)
NaZn$_{0.9}$Co$_{0.1}$PO$_4$	Powder	51.78	10.70	-59.21	60.17	280.25	49	64
	Concrete	49.90	1.61	-49.98	50.01	271.85	52	61
	Al sheet	47.46	6.01	-55.24	55.56	276.21	53	62
LiMg$_{0.8}$Co$_{0.2}$PO$_4$	Powder	65.19	26.45	-26.83	37.68	314.60	67	57
	Concrete	66.48	24.82	-21.65	32.93	318.91	65	53
	Al sheet	62.49	27.00	-23.36	35.71	319.14	68	47

2B.4.4. Temperature shielding study

High solar reflectance of pigment acrylic coatings triggered the investigation to determine the temperature shielding ability. The experiment was conducted for $NaZn_{0.9}Co_{0.1}PO_4$ and $LiMg_{0.8}Co_{0.2}PO_4$ coatings using the setup shown in **Fig. 2B.1**. It was also compared to commercial Co pigment ($CoAl_2O_4$) coatings. All of the prepared coatings utilized in the experiment had thicknesses in 200-250 μm range. The interior and coating surface temperature measurements were done using thermocouples and thermal imaging camera, respectively. The time versus temperature graph was plotted using these observations, **Fig. 2B.6**.

Interior temperature of the foam boxes rapidly increased during the first 10 minutes, which was attributed to the instantaneous IR absorption of the coatings and subsequent heat transfer. Further, the temperature attained an equilibrium, and no significant fluctuation detected after that, **Fig. 2B.6a**. In fact, it is entirely dependent on the IR reflectance of the pigment component in the coating. Because R^* of $NaZn_{0.9}Co_{0.1}PO_4$ and $LiMg_{0.8}Co_{0.2}PO_4$ is higher than that of $CoAl_2O_4$, both pigment coatings were able to reduce the heat transfer and interior heat build up. Specifically, the interior temperature of the blue and magenta roofed houses was around 4 and 7 °C lower than that of the $CoAl_2O_4$ roof, respectively. Since the $R*$ of blue pigment is greater than that of magenta, the blue coating was expected to perform better than the magenta coating. However, pigment brightness is also an important factor to be considered. L^* of $NaZn_{0.9}Co_{0.1}PO_4$, $LiMg_{0.8}Co_{0.2}PO_4$ and $CoAl_2O_4$ coatings are 47, 62 and 40, respectively. It demonstrates that the ΔL^* between $LiMg_{0.8}Co_{0.2}PO_4$ and $CoAl_2O_4$ coatings is higher than that of $NaZn_{0.9}Co_{0.1}PO_4$ and $CoAl_2O_4$. Therefore, the magenta coating was able to provide better temperature reduction than commercial blue.
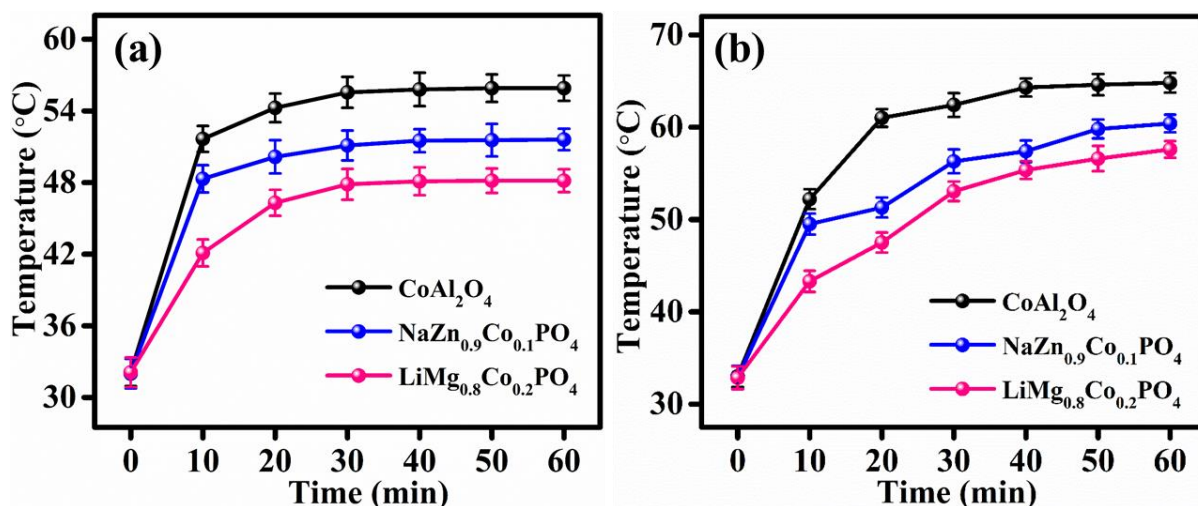
Fig. 2B.6. (a) Interior and (b) coating surface temperature comparison of $NaZn_{0.9}Co_{0.1}PO_4$ and $LiMg_{0.8}Co_{0.2}PO_4$ coatings with $CoAl_2O_4$ coatings

  Thermal imaging of the coating surfaces was used to further investigate the temperature shielding ability of pigment coatings. Surface temperature from the thermal images, **Fig. 2B.7**, was plotted against IR exposure time and shown in **Fig. 2B.6b**. The roof surface temperature followed a nearly similar trend to interior temperature. But unlike in the previous case, instead of an immediate temperature equilibration, a gradual decrease in temperature buildup rate was observed. Essentially, a significant temperature reduction of 4 and 7 ºC, respectively, was noticed on blue and magenta coatings compared to $CoAl_2O_4$. It confirms that both $NaZn_{0.9}Co_{0.1}PO_4$ and $LiMg_{0.8}Co_{0.2}PO_4$ are efficient IR reflective 'cool' pigments, which will be extremely beneficial in lowering the consumption of air conditioners during the summer season.
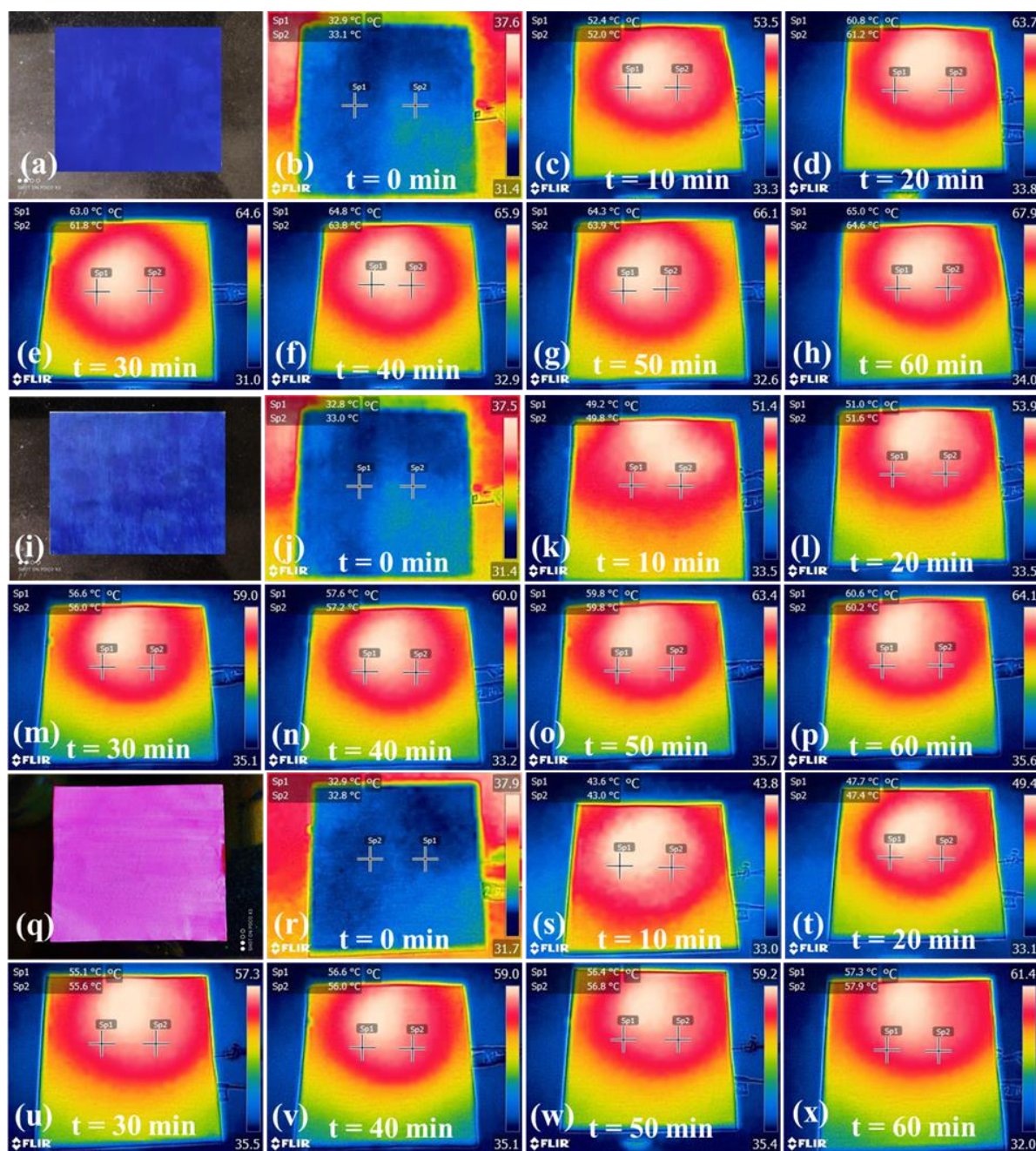
Fig. 2B.7. Photographs of (a) commercial blue, (i) $NaZn_{0.9}Co_{0.1}PO_4$ and (q) $LiMg_{0.8}Co_{0.2}PO_4$ coatings on Al sheet, thermal images of (b-h) commercial blue and (j-p) $NaZn_{0.9}Co_{0.1}PO_4$ and (r-x) $LiMg_{0.8}Co_{0.2}PO_4$ coatings

2B.4.5. Anticorrosive analysis

The corrosion resistant inorganic pigments play an important role in the development of stable protective coatings for metal substrates. Hence, a sustainable cool coat on metal roofs essentially requires an anticorrosive base coat support, which eventually makes the coating expensive. Therefore, it is highly appreciable for a coloured pigment to also function as an anticorrosive pigment in order to reduce cost. Herein, $NaZn_{0.9}Co_{0.1}PO_4$ and $LiMg_{0.8}Co_{0.2}PO_4$

pigments were examined to explore the anticorrosive property. Different wt% pigment loaded (5, 10, 15, 20 and 25 wt%) epoxy coatings of thickness ~12 μm were prepared on steel substrate. The EIS experiments have conducted on bare and pigment incorporated coatings in 3.5 wt% NaCl. Obtained Nyquist plots were displayed in **Fig. 2B.8**, and respective electrochemical parameters were tabulated in **Table 2B.5**.

The impedance spectrum of bare steel and bare epoxy coating on steel, **Fig. 2B.8a**, was fitted with Randles EEC. It is the basic EEC that consists of only two components, R_{ct} and Q_{dl}. R_{ct} of the bare metal substrate obtained from EIS experiment was 1.2×10^3 Ωcm^2. Further, an epoxy protective coating was provided on the metal surface to prevent electrolyte penetration. The respective EEC include two additional components, R_{coat} and Q_{coat}[17, 29]. Consequently, corrosion resistance recorded for the epoxy coating was 1.2×10^5 Ωcm^2.

Impedance spectra of $NaZn_{0.9}Co_{0.1}PO_4$ epoxy coatings (**Fig. 2B.8b, c**) were modeled with EEC $[Q_{coat}/(R_{coat}+Q_{dl}/R_{ct})]$, shown in the inset of **Fig. 2B.8c**. The solution resistance R_s is negligible thus excluded from the circuit. The impedance fitting data tabulated in **Table 2B.5** suggests that starting from 2.3×10^5 Ωcm^2, the corrosion resistance of $NaZn_{0.9}Co_{0.1}PO_4$ blue pigment was reached to a maximum of 8.8×10^6 Ωcm^2 at 20 wt% pigment loading, with minimum Q_{dl} 0.016 μFcm^{-2}. One order increase in R_{ct} over bare epoxy coating confirmed that the new blue pigment can be used for corrosion protection of steel in marine media. The findings suggest the possibility of a passive film formation at the metal electrolyte interface, similar to commercial $Zn_3(PO_4)_2$, that prevents rapid corrodent penetration[30, 31]. However, resistance drops dramatically over 20% wt% loading, indicating coat saturation. Because, above the saturation point, pigment particles deceive the coat by developing pores which facilitates the corrodent attack.
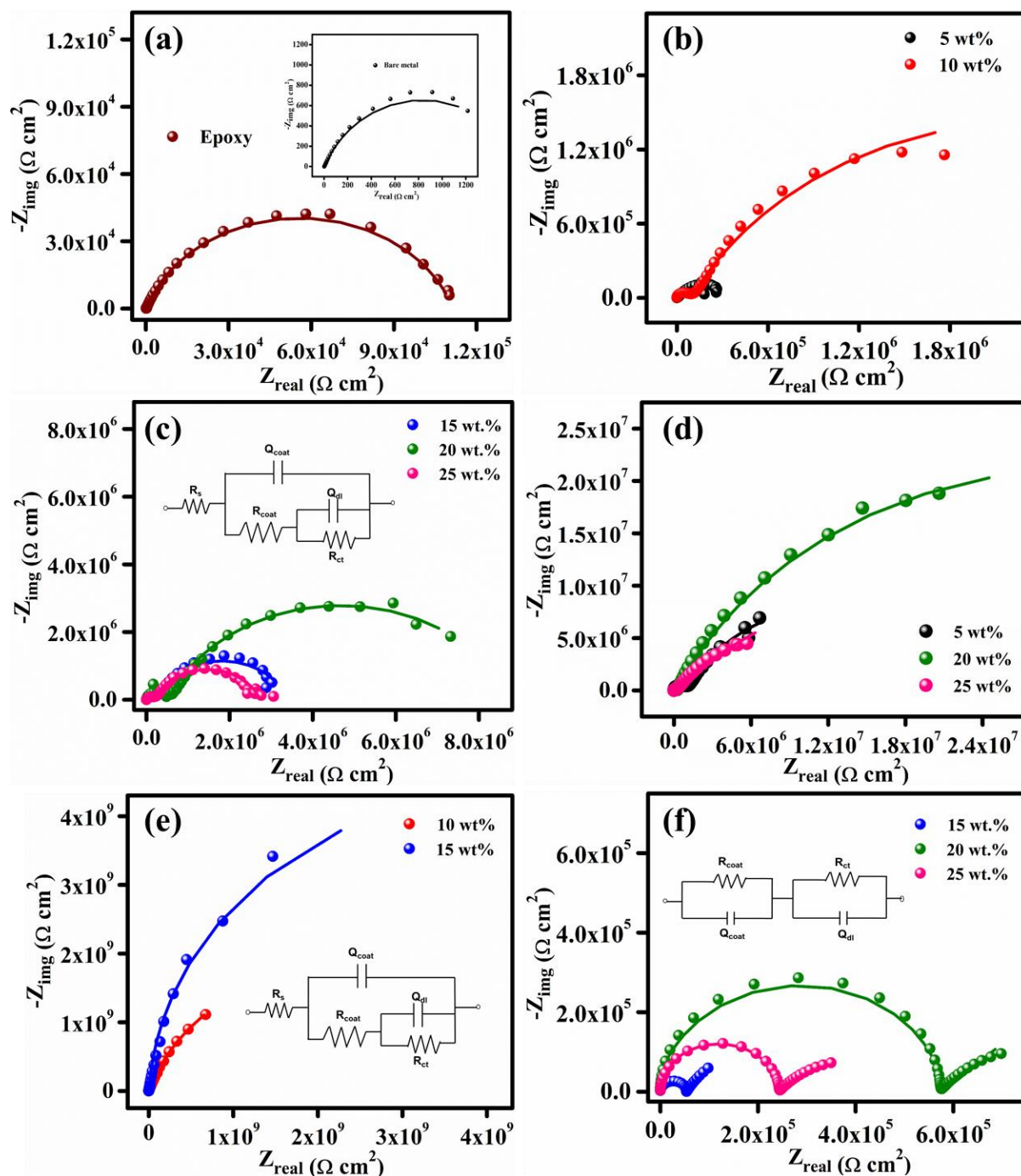
Fig. 2B.8. Nyquist plots of (a) bare epoxy and bare metal (inset), different wt% (b, c) NaZn$_{0.9}$Co$_{0.1}$PO$_4$, (d, e) LiMg$_{0.8}$Co$_{0.2}$PO$_4$ and (f) CoAl$_2$O$_4$, loaded epoxy coatings

The Nyquist diagram of LiMg$_{0.8}$Co$_{0.2}$PO$_4$ incorporated epoxy coatings (**Fig. 2B.8d, e**) were modeled with EEC [Q$_{coat}$/(R$_{coat}$+Q$_{dl}$/R$_{ct}$)]. Irrespective of the pigment concentration, magenta coatings exhibited a better performance in corrosion prevention than bare epoxy. The R$_{ct}$ found to increase from 5 to 15 wt% pigment loading and declined thereafter. The maximum R$_{ct}$ obtained at 15 wt%, was 9.3×10^9 Ωcm^2. The inverse trend in Q$_{dl}$ of the coatings, further substantiated these results. The four order hike in R$_{ct}$ compared to bare epoxy coat implies that

$LiMg_{0.8}Co_{0.2}PO_4$ is a promising anticorrosive pigment and 15 wt% is the optimum pigment volume concentration required to fabricate the best anticorrosive coating out of it. The subsequent increase in pigment content from 15 wt% initiated particle aggregation and pore formation in coatings, resulting in a decrease in R_{ct} value.

Table 2B.5. EIS parameters from Nyquist plot

Sample	Pigment loading (wt%)	EIS parameters			
		R_{coat} (Ωcm^2)	Q_{coat} (μFcm^{-2})	R_{ct} (Ωcm^2)	Q_{dl} (μFcm^{-2})
Bare metal	-	-	-	1.2×10^3	744
Epoxy	-	159.8	4.2	1.2×10^5	0.028
$CoAl_2O_4$	15	5.3×10^4	2.8	3.4×10^5	0.061
	20	5.4×10^5	0.53	8.7×10^5	0.026
	25	2.4×10^5	2.1	4.3×10^5	0.034
$NaZn_{0.9}Co_{0.1}PO_4$	5	6.9×10^4	2.9	2.3×10^5	0.032
	10	9.6×10^4	2.7	3.2×10^6	0.027
	15	2.3×10^5	1.6	3.4×10^6	0.017
	20	5.7×10^5	0.15	8.8×10^6	0.016
	25	1.9×10^5	0.35	2.8×10^6	0.021
$LiMg_{0.8}Co_{0.2}PO_4$	5	9.3×10^5	6.05	2.6×10^6	1.75
	10	4.0×10^6	5.82	5.3×10^9	0.93
	15	3.1×10^7	1.24	9.3×10^9	0.84
	20	1.9×10^5	3.86	6.4×10^7	2.15
	25	9.2×10^4	4.81	4.5×10^7	2.47

The anticorrosive analysis results of $NaZn_{0.9}Co_{0.1}PO_4$ and $LiMg_{0.8}Co_{0.2}PO_4$ were then compared with commercial $CoAl_2O_4$. The $CoAl_2O_4$ pigment loading in epoxy coating was varied from 15, 20 and 25 wt%. Corresponding impedance data were fitted with EEC [$Q_{coat}/R_{coat}+Q_{dl}/R_{ct}$] displayed in **Fig. 2B.8f** and electrochemical parameters were tabulated in **Table 2B.5**. None of the pigment concentrations was able to provide promising corrosion resistance in saline media. The maximum R_{ct} 8.7×10^5 Ωcm^2, was observed at 20 wt% loading, which is in the order of bare epoxy coating resistance. At the same time optimum concentration of $NaZn_{0.9}Co_{0.1}PO_4$ and $LiMg_{0.8}Co_{0.2}PO_4$ pigments displayed one order and four order hike, respectively, in its resistance value compared to $CoAl_2O_4$. Therefore, among the prepared

inorganic pigments, the 15 wt% $LiMg_{0.8}Co_{0.2}PO_4$ loaded epoxy coating proved to be the most corrosion resistant coating on steel in the marine environment.

Stability of the most efficient anticorrosive coating (15 wt% $LiMg_{0.8}Co_{0.2}PO_4$) was analyzed and compared with $CoAl_2O_4$ via one month continuous EIS analysis. **Fig. 2B.9a**, displayed the Bode plots of 15 wt% $LiMg_{0.8}Co_{0.2}PO_4$ and 20 wt% $CoAl_2O_4$ loaded epoxy coatings in accordance with Nyquist plots. Phase angle (-θ) above 90º at higher frequency range indicated the consistency of both the coatings. However, their phase angle curve behaviour was fairly different when they approached the low frequency end. $CoAl_2O_4$ possessed two time constants whereas one time constant for $LiMg_{0.8}Co_{0.2}PO_4$. The two time constants represents delamination of the epoxy coat, whereas the one time constant represents coat intactness[16]. It reveals that the incorporated pigment components operate entirely in different manner while in contact with a corrosive medium.

Additionally, one month continuous electrochemical analysis of 15 wt% $LiMg_{0.8}Co_{0.2}PO_4$ coating was performed to figure out a probable corrosion inhibitive mechanism, **Fig. 2B.9b**. Resistance of the anticorrosive coat was found to gradually decrease from 9.3×10^9 Ωcm^2 to 1.8×10^7 Ωcm^2 (10th day), then to 5.1×10^5 Ωcm^2 (15th day) and 2.3×10^5 Ωcm^2 (20th day), in 3.5 wt% NaCl solution. It implies that continuous electrolyte exposure may have caused the epoxy coating to develop pores, allowing corrossive medium to start penetrating. However, after 20 days, the resistance remained almost constant at 10^5 Ωcm^2 until the experiment was completed. Thus, the stability of magenta pigment incorporated epoxy coating against marine corrosion was established. This led to the hypothesis that there could be an active inhibitive mechanism at the metal electrolyte interface.
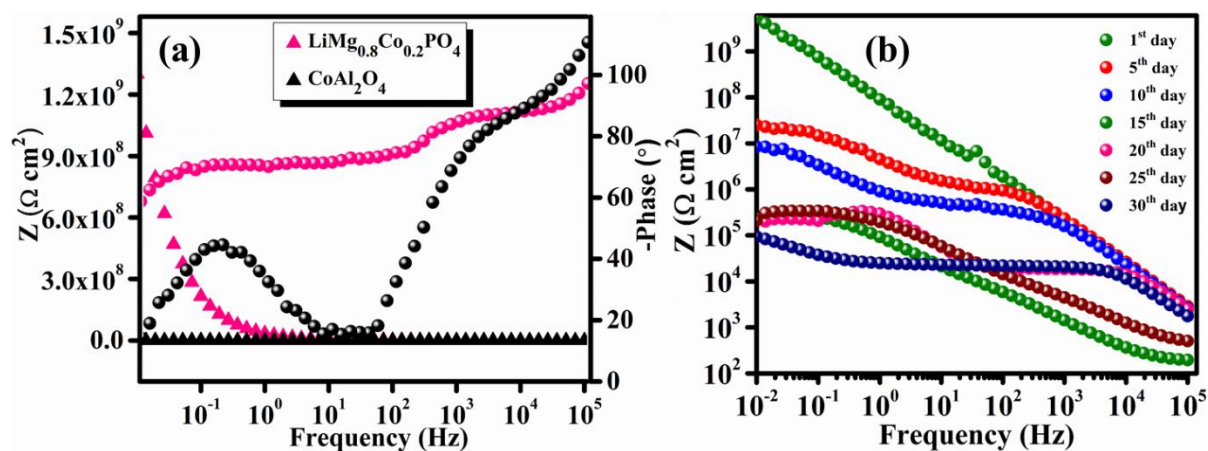
Fig. 2B.9. Bode plot of (a) 15 wt% $LiMg_{0.8}Co_{0.2}PO_4$ and 20 wt% $CoAl_2O_4$, (b) continuous study of $LiMg_{0.8}Co_{0.2}PO_4$ loaded epoxy coatings

2B.4.6. XPS surface analysis and anticorrosive mechanism

XPS surface analysis of the steel specimen after continuous EIS analysis revealed the hypothesised corrosion inhibition mechanism of the pigment-loaded epoxy coating. The presence of C, O, Mg, P, and Fe elements was confirmed by the survey spectrum shown in **Fig. 2B.10a**. In addition, deconvoluted XPS spectra of O1s, Fe2p and P2p were displayed in **Fig. 2B.10b-d**. Three major peaks at 529.4, 530.7 and 532.5 eV, were resolved in O1s spectrum, attributed to the corrosion products Fe_3O_4/ Fe_2O_3, corrosion intermediates $Fe(OH)_2$/$Fe(OH)_3$/$FeOOH$ and importantly $FePO_4$, respectively. The high resolution Fe2p spectrum contains binding energy peaks for corrosion products at 710.7 eV and $FePO_4$ at 712.9 eV. Similarly P2p spectrum also verified the presence of $FePO_4$ on steel surface from the binding energy peak at 133.3 ± 0.3 eV[32, 33]. Thus, comprehension of XPS findings validated the phosphatization assisted corrosion inhibition mechanism in 15 wt% $LiMg_{0.8}Co_{0.2}PO_4$ loaded epoxy coating. Explicitly, the polymer coat passivation was broken down during prolonged exposure to corrosive media. Simultaneously, the phosphate protective layer forms at the metal electrolyte interphase, refusing further corrodant penetration, **Fig. 2B.11**. The possible mechanism can be written as follows.

$$Fe \rightarrow Fe^{2+} + 2e^- \qquad (2B.2)$$

$$3Fe^{2+} + 2PO_4{}^{3-} + 8H_2O \rightarrow Fe_3(PO_4)_3.8H_2O + Fe_2O_3 + FeO \downarrow \qquad (2B.3)$$
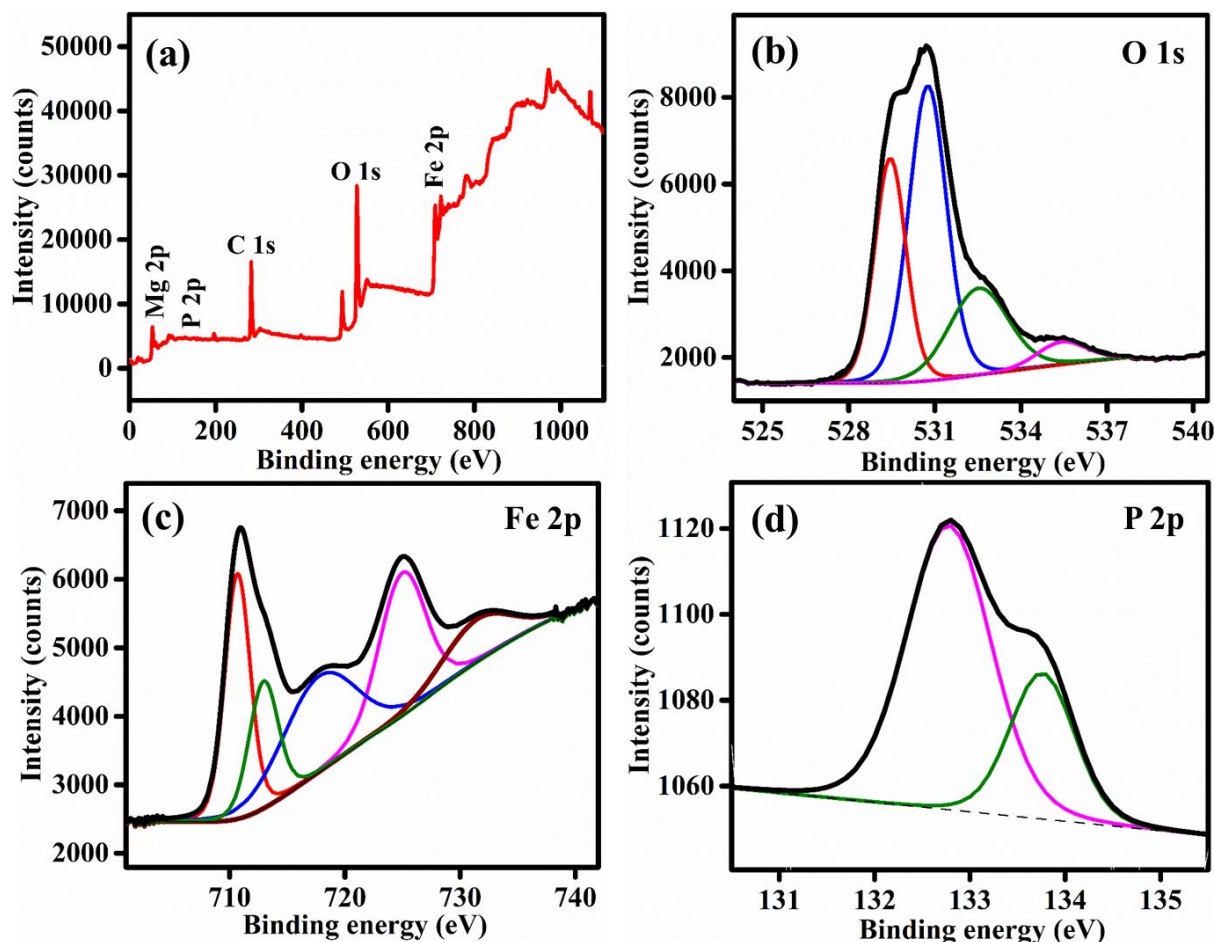
Fig. 2B.10. XPS (a) survey spectrum, fitted high resolution spectrum of (b) O1s, (c) Fe2p and (d) P2p of inhibitive film beneath the 15 wt% $LiMg_{0.8}Co_{0.2}PO_4$ loaded epoxy coat after continuous EIS analysis

Besides that, the passive nature of $LiMg_{0.8}Co_{0.2}PO_4$ pigment precluded NaCl penetration during the initial days of continuous electrochemical experiment. The active phosphatization inhibition comes into the picture only when the corrodent destroys this mechanism. The phosphatization barrier developed at the metal electrolyte interface provides stability to the coating under continuous exposure to aggressive media. Overall, the passive and active inhibitive mechanism collaborated in magenta pigment coating, resulting in an efficient and stable anticorrosive coat for metal roofs. By the virtue of which the necessity of duplex coatings for a sustainable 'cool' coat, which provide NIR reflectance and corrosion resistance separately, can be avoided.
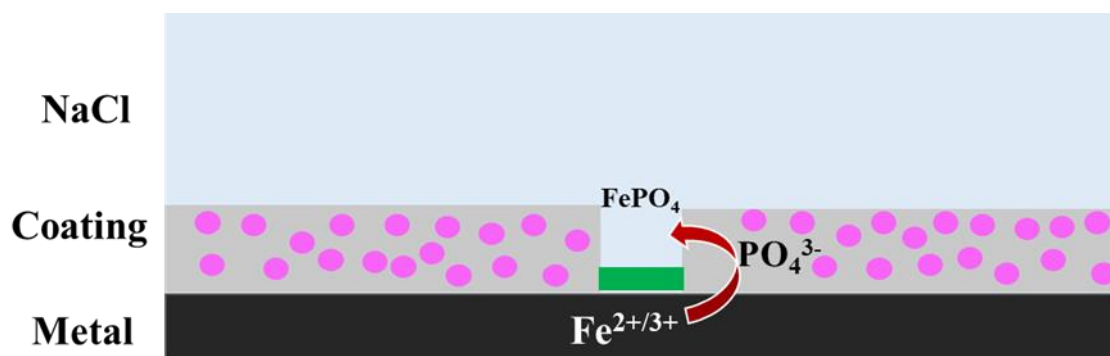
Fig. 2B.11. Anticorrosive mechanism in $LiMg_{0.8}Co_{0.2}PO_4$ epoxy coating

2B.5. Conclusions

The NIR reflectance property of inorganic pigment series $NaZn_{1-x}Co_xPO_4$ blue and $LiMg_{1-x}Co_xPO_4$ magenta was analyzed. In contrast to traditional Co pigments, both pigment series had an excellent reflectance profile with remarkable colour intensity. In terms of colour and reflectance properties, $NaZn_{0.9}Co_{0.1}PO_4$ and $LiMg_{0.8}Co_{0.2}PO_4$ were the best compositions in each pigment series, with 64 and 57% NIR solar reflectance, respectively. The pigment acrylic coatings on concrete and Al sheet successfully retained its colour and reflectance. Temperature shielding experiments using the pigment coatings yielded 4 and 7 ℃ reduction in interior temperature compared to $CoAl_2O_4$. Therefore, the new blue and magenta pigments can be employed as a potential 'cool' roof pigment for controlling UHI. Additionally, impressive corrosion resistance of the pigments furnished a multifunctional perspective for the colourants. Fifteen wt% magenta pigment loaded epoxy coating showed R_{ct} 9.3×10^9 Ωcm^2, which is four orders higher than bare epoxy and commercial $CoAl_2O_4$. One month continuous electrochemical analysis of the pigment coating, followed by surface analysis, revealed the formation of an iron phosphate layer at the metal electrolyte interphase, which is responsible for the corrosion protection mechanism. Thus, the synthesized inorganic pigments can be considered as promising candidates for developing multifunctional low-cost paints that could offer a primer-less anticorrosive cool exterior coat.

2B.6. References

1. Jeevanandam, P.; Mulukutla, R.; Phillips, M.; Chaudhuri, S.; Erickson, L.; Klabunde, K. J. T. J. o. P. C. C., Near infrared reflectance properties of metal oxide nanoparticles. **2007,** *111* (5), 1912-1918.

2. Malshe, V. C.; Bendiganavale, A. K. J. R. P. o. C. E., Infrared reflective inorganic pigments. **2008,** *1* (1), 67-79.

3. Berdahl, P., Pigments to reflect the infrared radiation from fire. **1995**.

4. Coser, E.; Moritz, V. F.; Krenzinger, A.; Ferreira, C. A. J. P., Development of paints with infrared radiation reflective properties. **2015,** *25*, 305-310.

5. Salvati, A.; Roura, H. C.; Cecere, C. J. E.; Buildings, Assessing the urban heat island and its energy impact on residential buildings in Mediterranean climate: Barcelona case study. **2017,** *146*, 38-54.

6. Skelhorn, C. P.; Levermore, G.; Lindley, S. J. J. E.; Buildings, Impacts on cooling energy consumption due to the UHI and vegetation changes in Manchester, UK. **2016,** *122*, 150-159.

7. Sun, Y.; Augenbroe, G. J. E.; Buildings, Urban heat island effect on energy application studies of office buildings. **2014,** *77*, 171-179.

8. Lowe, S. A. J. E. I. A. R., An energy and mortality impact assessment of the urban heat island in the US. **2016,** *56*, 139-144.

9. Li, X.; Zhou, Y.; Yu, S.; Jia, G.; Li, H.; Li, W. J. E., Urban heat island impacts on building energy consumption: A review of approaches and findings. **2019,** *174*, 407-419.

10. Santamouris, M.; Cartalis, C.; Synnefa, A.; Kolokotsa, D. J. E.; buildings, On the impact of urban heat island and global warming on the power demand and electricity consumption of buildings—A review. **2015,** *98*, 119-124.

11. Álvarez-Docio, C. M.; Reinosa, J.; Del Campo, A.; Fernández, J. J. D.; Pigments, 2D particles forming a nanostructured shell: a step forward cool NIR reflectivity for CoAl$_2$O$_4$ pigments. **2017,** *137*, 1-11.

12. Radhika, S. P.; Sreeram, K. J.; Nair, B. U. J. J. o. A. C., Rare earth doped cobalt aluminate blue as an environmentally benign colorant. **2012,** *1*, 301-309.

13. Ocaña, M.; Espinós, J.; Carda, J. J. D.; Pigments, Synthesis, through pyrolysis of aerosols, of YIn$_{1-x}$Mn$_x$O$_3$ blue pigments and their efficiency for colouring glazes. **2011,** *91* (3), 501-507.

14. Grundmeier, G.; Rossenbeck, B.; Roschmann, K.; Ebbinghaus, P.; Stratmann, M. J. C. s., Corrosion protection of Zn-phosphate containing water borne dispersion coatings: Part 2: Investigations of the corrosive de-adhesion of model latex coatings on iron. **2006,** *48* (11), 3716-3730.

15. Instruments, G. J. G. I., Complex impedance in Corrosion, Basics of electrochemical impedance spectroscopy. **2007**, 1-30.

16. Hao, Y.; Liu, F.; Han, E.-H.; Anjum, S.; Xu, G. J. C. S., The mechanism of inhibition by zinc phosphate in an epoxy coating. **2013,** *69*, 77-86.

17. Shao, Y.; Jia, C.; Meng, G.; Zhang, T.; Wang, F. J. C. S., The role of a zinc phosphate pigment in the corrosion of scratched epoxy-coated steel. **2009,** *51* (2), 371-379.

18. Stevie, F. A.; Donley, C. L. J. J. o. V. S.; A, T., Introduction to x-ray photoelectron spectroscopy. **2020,** *38* (6).

19. Saraswathy, D.; Rao, P. P.; Raj, A. K.; Thara, T. A. J. C., Intense Blue Colors in Wolframite-Type Co^{2+}: $MgWO_4$ Oxides Through Distortion in Co^{2+} Octahedra. **2018,** *3* (2), 410-417.

20. Hedayati, H.; Alvani, A. S.; Sameie, H.; Salimi, R.; Moosakhani, S.; Tabatabaee, F.; Zarandi, A. A. J. D.; pigments, Synthesis and characterization of $Co_{1-x}Zn_xCr_{2-y}Al_yO_4$ as a near-infrared reflective color tunable nano-pigment. **2015,** *113*, 588-595.

21. Jose, S.; Jayaprakash, A.; Laha, S.; Natarajan, S.; Nishanth, K.; Reddy, M. J. D.; Pigments, $YIn_{0.9}Mn_{0.1}O_3$–ZnO nano-pigment exhibiting intense blue color with impressive solar reflectance. **2016,** *124*, 120-129.

22. Zhang, Y.; Zhang, Y.; Zhao, X.; Zhang, Y. J. D.; Pigments, Sol–gel synthesis and properties of europium–strontium copper silicates blue pigments with high near-infrared reflectance. **2016,** *131*, 154-159.

23. Cai, L.; Wu, X.; Gao, Q.; Fan, Y. J. D.; Pigments, Effect of morphology on the near infrared shielding property and thermal performance of $K_{0.3}WO_3$ blue pigments for smart window applications. **2018,** *156*, 33-38.

24. Jose, S.; Reddy, M. L. J. D.; Pigments, Lanthanum-strontium copper silicates as intense blue inorganic pigments with high near-infrared reflectance. **2013,** *98* (3), 540-546.

25. Saraswathy, D.; Rao, P. P.; Sameera, S.; James, V.; Raj, A. K. J. R. A., Monoclinic $LaGa_{1-x}Mn_xGe_2O_7$: a new blue chromophore based on Mn^{3+} in the trigonal bipyramidal coordination with longer apical bond lengths. **2015,** *5* (35), 27278-27281.

26. Smith, A. E.; Comstock, M. C.; Subramanian, M. J. D.; Pigments, Spectral properties of the UV absorbing and near-IR reflecting blue pigment, $YIn_{1-x}Mn_xO_3$. **2016,** *133*, 214-221.

27. Ianoş, R.; Muntean, E.; Păcurariu, C.; Lazău, R.; Bandas, C.; Delinescu, G. J. D.; Pigments, Combustion synthesis of a blue Co-doped zinc aluminate near-infrared reflective pigment. **2017,** *142*, 24-31.

28. Liu, W.; Du, T.; Ru, Q.; Zuo, S.; Yang, X.; Yao, C.; Kong, Y. J. A. C. S., Facile synthesis and characterization of 2D kaolin/$CoAl_2O_4$: a novel inorganic pigment with high near-infrared reflectance for thermal insulation. **2018,** *153*, 239-245.

29. Zhao, X.; Qi, Y.; Zhang, Z.; Li, K.; Li, Z. J. C., Electrochemical impedance spectroscopy investigation on the corrosive behaviour of waterborne silicate micaceous iron oxide coatings in seawater. **2019,** *9* (7), 415.

30. Sørensen, P. A.; Kiil, S.; Dam-Johansen, K.; Weinell, C. E. J. J. o. c. t.; research, Anticorrosive coatings: a review. **2009,** *6*, 135-176.

31. Chastain, J.; King Jr, R. C. J. P.-E. C., Handbook of X-ray photoelectron spectroscopy. **1992,** *40*, 221.

32. Barbaux, Y.; Dekiouk, M.; Le Maguer, D.; Gengembre, L.; Huchette, D.; Grimblot, J. J. A. C. A. G., Bulk and surface analysis of a Fe-PO oxydehydrogenation catalyst. **1992,** *90* (1), 51-60.

33. Moulder, J. F.; Chastain, J., *Handbook of X-ray Photoelectron Spectroscopy: A Reference Book of Standard Spectra for Identification and Interpretation of XPS Data*. Physical Electronics Division, Perkin-Elmer Corporation: 1992.

Development of low-cost BiVO$_4$-ZnO yellow complex pigment

3.1. Abstract

Bismuth vanadate ($BiVO_4$) gathered great attraction as a yellow inorganic pigment which could replace the conventional chrome and cadmium yellow. However, its high cost over the other yellow pigments restricted its usage. Consequently, there exists a huge demand to develop cost-effective $BiVO_4$ inorganic pigment without compromising its optical properties. The present work demonstrates an effective strategy to develop low-cost $BiVO_4$ complex pigment. The citrate-gel synthesis method enabled a decoration of $BiVO_4$ nanoparticles on ZnO white pigment surface, resulting in an appreciable decrease in $BiVO_4$ content (75 wt%). The reduction in $BiVO_4$ had a remarkable impact on the economic viability of the new complex pigment. Similar to pure $BiVO_4$, the developed complex inorganic pigment exhibited excellent greenish-yellow colour ($a^* = -6.28$, $b^* = 76.45$). An exceptional near infrared reflectance has been recorded, which is estimated as high as 90%. High reflective coatings of the complex pigment displayed an outstanding performance in temperature shielding experiment, achieving a reduction of 8 °C in the interior temperature, compared to the commercial yellow pigment coating. Moreover, the findings demonstrate that the developed complex pigment could be a potential replacement for $BiVO_4$ yellow.

3.2. Introduction

Conventional yellow inorganic pigments $PbCrO_4$, CdS, $Pb_2Sb_2O_7$, As_2S_3 are outstanding candidates in terms of colour intensity and cost, despite the presence of highly toxic metal chromophores like Pb, Cr, Cd, Sb and As in their composition[1]. Among these, $BiVO_4$ yellow stands out due to its non-toxicity and high NIR reflectivity[2-5]. It has been used in coatings, ceramics, plastics and inks for the last two decades. However, owing to the presence of expensive Bi metal, the cost of $BiVO_4$ is really high, seriously limiting its widespread consumption. Therefore, a consistent demand is emerging to develop a cost-effective $BiVO_4$ pigment without compromising its excellent properties.

The routine way of approach towards achieving cost-effective pigment is, to reduce the expensive component in the material composition. It can be achieved either by developing substitution or hybrid pigments. Partial replacement of host by transition or lanthanide chromophores leads to substitution pigments and pigment particles supported by a relatively cheaper and readily available substrate material give rise to hybrid pigments. Among which hybrid pigment synthesis is essentially the more efficient strategy to reduce cost of expensive pigments without negotiating its properties. Hybrid materials are generally known for their

advantage to acquire the properties of its constituents, offering a broad range of applications. A good number of $BiVO_4$ hybrid pigments have already been reported that brought significant reduction in amount of costly component in the composition. Guan et al. synthesized the core-shell $BaSO_4$@$BiVO_4$ architecture, where they achieved 83 wt% reduction in $BiVO_4$ content maintaing good colour strength. But the preparation of core-shell morphology is very tedious, and thus the strategy will not be suited for bulk production[6]. Different research groups have introduced $BiVO_4$ nanoparticles decorated clay minerals such as attapulgite rods, sepiolite, montmorillonite, halloysite and kaolin sheets[7-11]. All the hybrid pigments exhibited an exceptional colour strength, particularly the attapulgite-$BiVO_4$ hybrid, with just 60 wt% $BiVO_4$. However, its processing temperature still remains high, increasing the pigment cost. Meanwhile, $BiVO_4$ coated mica-TiO_2 sheets, developed by Yuan et al., demonstrated good thermal shielding performance, achieving 4.5 °C decrease in inner surface temperature[12]. The SiO_2-$BiVO_4$ hybrid pigment saved 72 wt% $BiVO_4$ resource with good colour[13]. Márcia et al. published a similar report on $BiVO_4$-incorporated hollow ZnO particles, however they lack comprehensive information on chromaticity and reflectance properties[14]. Many substituted pigments have also been reported, including (Bi, Ca, Zn, La)VO_4 by Wendusu et al., (Bi, Ca, Zn)VO_4 by Masui et al., Ce doped $BiVO_4$ by Nevesa et al. with bright yellow hue[4, 15, 16]. However, the majority of such works have focused only on pigment properties rather than cost.

In this scenario, there is an excellent incentive for developing a profitable material combo for cost-effective $BiVO_4$ yellow pigment. Current work illustrates the synthetic strategy to prepare a $BiVO_4$ complex pigment employing cheaper and readily available white pigments (WP), ZnO/ TiO_2/ SiO_2/ Al_2O_3 as supporting material. $BiVO_4$ particles have grown on WP surface via citrate-gel method that followed a single step firing. The work also comprises an extensive study on morphology, chromatic and reflectance properties of the prepared complex pigment. Eventually, thermal shielding performance of the pigment coating was evaluated and compared with commercial yellow paint, to demonstrate its cool nature.

3.3. Experimental section

3.3.1. Materials and methods

$BiVO_4$-WP complex pigment was synthesized by citrate-gel method, **Scheme 3.1**. Analytical grade chemicals $Bi(NO_3)_3.5H_2O$ (99%), NH_4VO_3 (99%), ZnO (99.9%), Al_2O_3 (99%), SiO_2 (99.5%), TiO_2 (99%) and citric acid monohydrate (99%) were purchased from Merck and used as received without further purification.

Fifty ml Bi(NO$_3$)$_3$.5H$_2$O (3 mmol) and 20 ml citric acid monohydrate (6 mmol) solutions in distilled water was mixed by continuous stirring. Subsequently added 50 ml NH$_4$VO$_3$ solution dropwise under vigorous stirring. The resultant yellow solution was heated at 150 °C for 1 h after the slow addition of WP. Obtained solid xerogel ground well, afterwards calcined at 500 °C for 3 h under air atmosphere. Different compositions of BiVO$_4$-ZnO complex pigment was prepared by varying BiVO$_4$ wt% as 10, 15, 25 and 50. Weight of ZnO in complex pigment with respect to BiVO$_4$ was shown in parenthesis, 10%BiVO$_4$-ZnO (9 g), 15%BiVO$_4$-ZnO (5.6 g), 25%BiVO$_4$-ZnO (3 g) and 50%BiVO$_4$-ZnO (1 g), were denoted as 10%BVZ, 15%BVZ, 25%BVZ and 50%BVZ, respectively. Similarly varied the substrate from ZnO to Al$_2$O$_3$/ SiO$_2$/ TiO$_2$ in the composition 25% BiVO$_4$-ZnO and denoted as 25%BVA, 25%BVS, 25%BVT, respectively. In addition, 25%BVZ mixed pigment was prepared by mechanically mixing BiVO$_4$ and ZnO in 1:3 ratio and calcined at 500 °C. Further, acrylic coatings of 25%BVZ was developed on concrete and Al sheet. Thermal shielding ability of 25%BVZ coating was compared with commercial yellow coating, as described in Experimental section, Chapter 2B. The coating thickness was calculated from optical images.
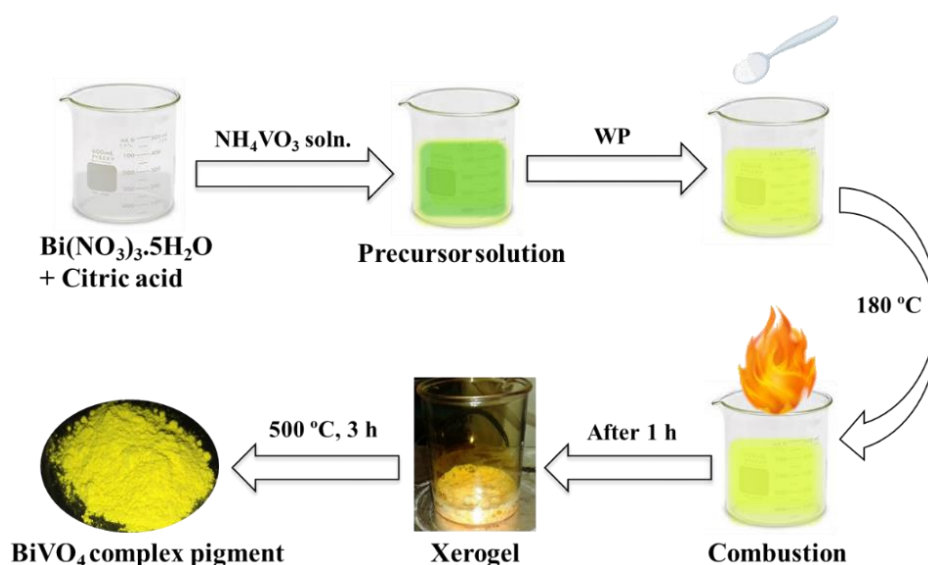
Scheme 3.1. Citrate-gel synthesis of BiVO$_4$ complex pigment

3.3.2. Characterization techniques

Thermal analysis of the precoursor mixture was carried out using TG/DTA in air atmosphere. Phase formation of the synthesized complex pigments were confirmed by PXRD analysis (details provided in Chapter 2A). The pigment composition was determined by PANalytical Epsilon 3 Energy Dispersive X-ray Fluorescence spectrometer (EDXRF) analysis.

Morphology studies and composition analysis were done using SEM and EDS analysis. The acrylic coating thickness was measured using Optical microscope and epoxy coating thickness was determined using Profilometer. High-Resolution Transmission Electron Micrographs (HRTEM) were recorded on JEOL JEM F-200 microscope operated at 200 kV. Particle size was measured by DLS technique. UV-vis-NIR Spectrophotometer was used to carry out the optical studies (details given in Chapter 2A). XPS analysis was performed to identify the electronic modifications in the material (details given in Chapter 2B).

3.4. Results and discussion

3.4.1. Thermal and X-ray diffraction analysis

Cost-effective $BiVO_4$ complex yellow pigments were developed by growing $BiVO_4$ nanoparticles on top of commercially available inexpensive WP via the citrate gel method. The obtained xerogel after the combustion reaction was initially subjected to TGA analysis. As shown in **Fig. 3.1a**, four weight losses were observed at 30-80, 80-140, 140-320 and 320-410 ºC. The water content in the sample was removed initially up to 80 ºC, followed by the elimination of absorbed water molecules between 80-140 ºC[17]. The nitrate and citrate functional group decomposition was observed till 320 ºC, subsequently the carbon skeleton oxidation[18, 19]. The major part of nitrate and citrate removal occurred during the combustion reaction itself. Then, rest of the decomposition was done in the calcining process as noted in the TGA plot. Based on which the xerogel was calcined at different temperatures 300, 400 and 500 ºC for 3 h duration and analyzed the corresponding PXRD patterns to confirm the temperature at which phase pure compound is achieved.

The formation temperature was optimized in order to obtain the monoclinic scheelite (m-s) phase of $BiVO_4$, which is responsible for the well-known vivid yellow colour[7]. The corresponding PXRD patterns in **Fig. 3.1b**, clearly displayed well-defined crystal plane reflections of ZnO and m-s $BiVO_4$ at each calcining temperature. However, when heated to 300 and 400 ºC, Bi_2O_3 impurity phase was observed at $2\theta = 24.40º$ (marked as *)[20]. Further, the impure phase was completely eliminated at 500 ºC, which set the formation temperature. The pigment compositions confirmed from EDXRF analysis, **Table 3.1**. It is worth noting that the citrate gel route was able to significantly reduced the synthesis temperature and time of $BiVO_4$ to 500 ºC for 3 h, which was instead prepared via solid state method at 800 ºC for 6 h prolonged heating with intermediate grinding[21, 22].
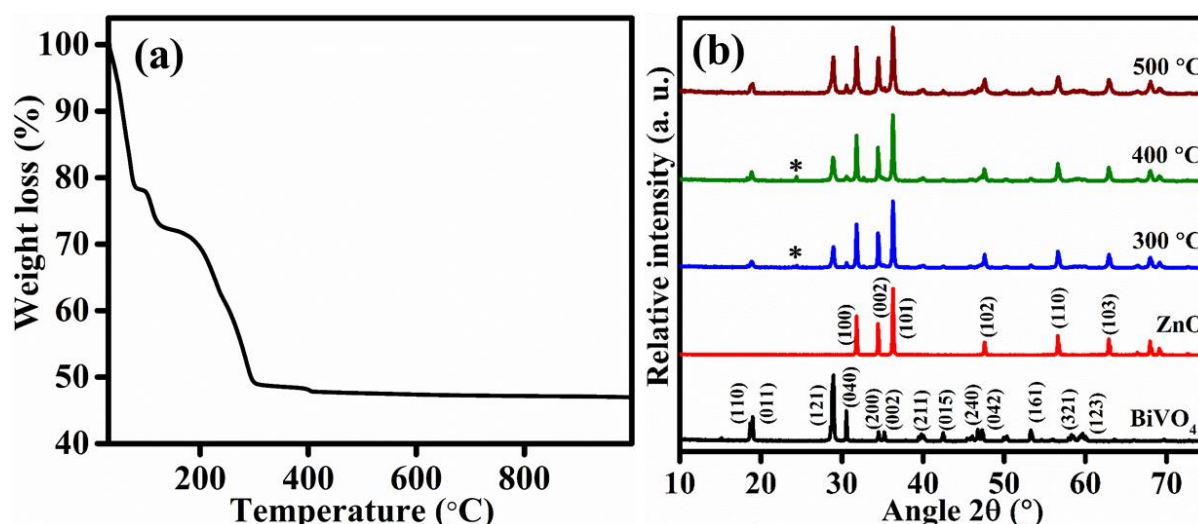
Fig. 3.1. (a) TGA curve and (b) PXRD pattern of 50%BVZ complex pigment at different calcining temperature along with its constituents

Fig. 3.2a presented the PXRD patterns of different BVZ complex pigment compositions. The m-s $BiVO_4$ phase (marked *) was indexed using JCPDS 14-0688, confirming the formation of BVZ complex pigment. Similarly, $BiVO_4$ phase formation was also ensured in the remaining pigment compositions 25%BVA, 25%BVS and 25%BVT, **Fig. 3.2b-d**. In contrast to ZnO, the $BiVO_4$ peak intensity was observed to rise when the composition was changed from 10%BVZ to 50%BVZ. The observation implies that $BiVO_4$ was successfully encapsulated on ZnO substrate to form BVZ complex pigment. Because typically precursors Bi^{3+} and $(VO_4)^{3-}$ are expected to deposit over pristine WP, allowing the free growth of yellow $BiVO_4$ at 500 ℃. Therefore, the extent of surface coverage on WP substrate was enhanced on increasing the concentration of $BiVO_4$. Consequently, X-ray exposure of ZnO became relatively lower than that of $BiVO_4$, resulting in reduced ZnO peak intensity and vice versa for $BiVO_4$.
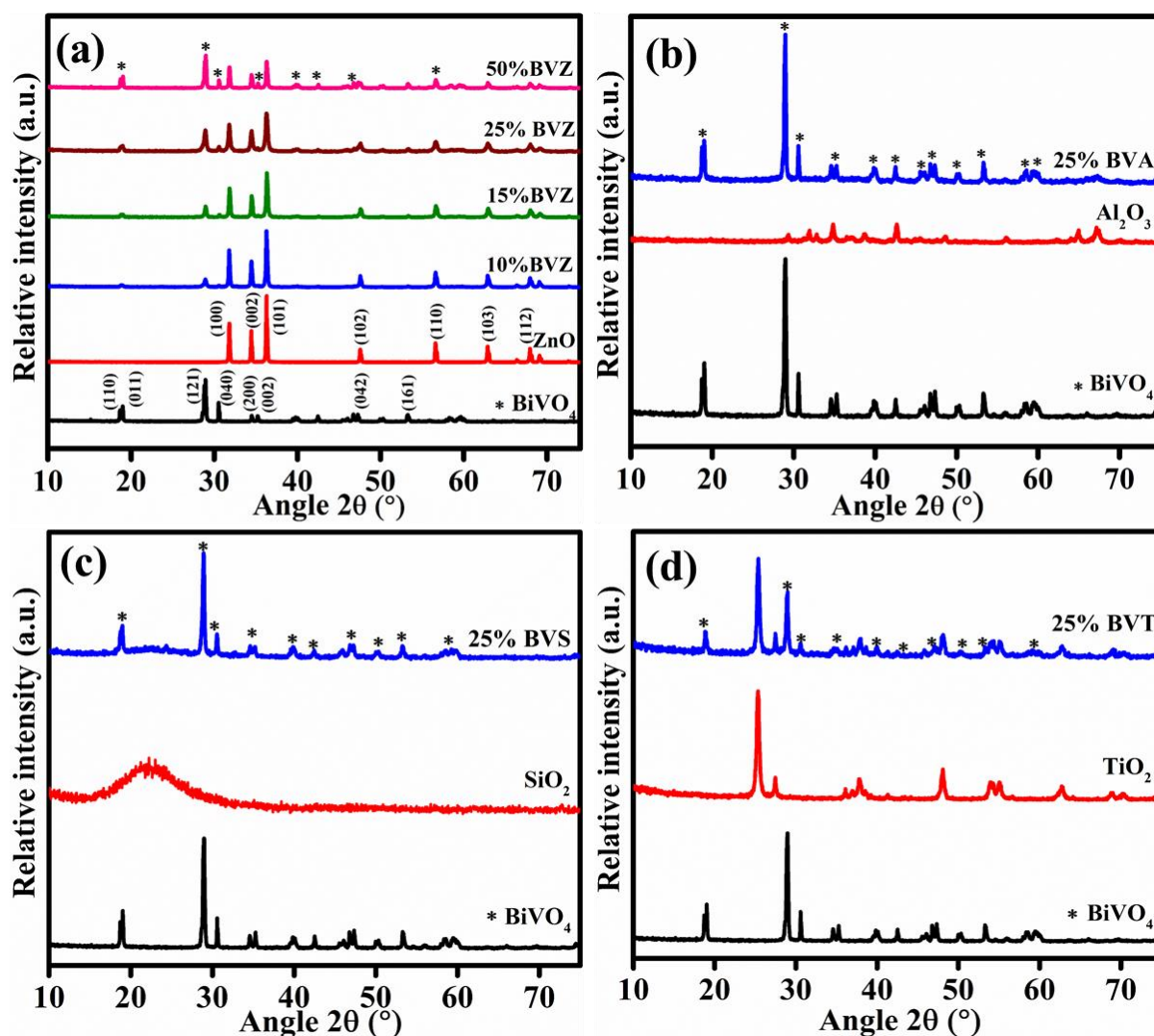
Fig. 3.2. PXRD patterns of (a) different compositions of BVZ complex pigments, (b) 25%BVA, (c) 25%BVS and (d) 25% BVT complex pigments along with its constituents

Table 3.1. EDXRF data of different BVZ complex pigments

Constituents	10%BVZ	15%BVZ	25%BVZ	50%BVZ
ZnO	86.60	84.32	75.57	51.12
Bi_2O_3	8.82	11.36	17.37	36.54
V_2O_5	3.07	3.08	5.85	12.06

3.4.2. Chromatic properties

CIE 1976 $L^*a^*b^*$ system was used to evaluate the prepared pigment colour and results were summarized in **Table 3.2**. The best colour values among BVZ complex pigments were identified in 25% and 50%BVZ compositions, which are equivalent to pure $BiVO_4$. The yellow colour parameter $b^* = 76$ with a slight negative a^* provided an exceptional greenish yellow hue

for both the 25% and 50%BVZ samples. Additionally, colour purity of the pigment was confirmed by its chroma $C^* > 75$ and hue angle 85-95°. Meanwhile, a small colour change from greenish yellow to orange yellow was visible in 10% and 15%BVZ samples, as seen in the photograph in **Fig. 3.3**. Therefore, the a^* parameter shifted towards the positive axis. Furthermore, b^* value of the pigments dropped significantly due to lower $BiVO_4$ content. Since, it demonstrated the best colour strength with the least amount of $BiVO_4$, 25%BVZ was chosen as the best composition in BVZ complex pigment series. Further, the supporting substrate in 25%BVZ was switched from ZnO to Al_2O_3/ SiO_2/ TiO_2, while maintaining the same $BiVO_4$ concentration. With nearly comparable colour tones to 25%BVZ ($b^* > 72$), 25%BVS and 25%BVT were stood out as excellent candidates. However, the estimated colour values confirmed that ZnO was indeed the best choice among the selected WP to develop $BiVO_4$ complex pigment through the citrate gel method. Finally, via 25%BVZ complex pigment, a substantial cost reduction was accomplished by minimizing the expensive $BiVO_4$ content (75 wt%), without compromising the colour strength. To highlight the importance of citrate-gel method 25%BVZ colour parameter was compared with equivalent mixed pigment. Because of the random distribution of $BiVO_4$ and ZnO, the yellow parameter b^* seems to be significantly smaller for mixed pigment than for complex pigment.

Fig. 3.3. Photos of (a) $BiVO_4$, (b) 25%BVZ, (c) 25%BVA, (d) 25%BVS and (e) 25%BVT

Table 3.2. Colour coordinates of synthesized complex pigments

Sample	L^*	a^*	b^*	C^*	$h^°$	NIR (%) at 1100nm	R^* (%)
BiVO$_4$	82.43	4.25	76.26	76.38	86.80	76	73
10%BVZ	90.87	2.88	41.81	41.91	86.05	98	91
15%BVZ	86.79	4.92	53.50	53.73	84.74	99	92
25%BVZ	91.53	-6.28	76.45	76.78	94.78	98	90
50%BVZ	89.06	-1.34	76.64	76.65	91.01	95	89
25%BVA	89.15	-3.83	72.90	73.00	93.02	88	85
25%BVS	89.84	-2.67	72.41	72.46	92.12	92	86
25%BVT	87.42	-3.88	62.42	62.54	93.56	91	86
Mixed pigment	92.73	-3.45	47.88	48.00	94.13	95	94

3.4.3. Morphology and particle size analysis

The morphology of 25%BVZ pigment sample was examined by SEM analysis, **Fig. 3.4a**. Highly agglomerated pigment particles were observed in the micrographs because of the free growth of BiVO$_4$ over the ZnO surface. Additionally, the SEM-EDS plot (**Fig. 3.4b**), estimated the weight percentage of BiVO$_4$ in the complex pigment to be 25%, which corroborated the pigment composition (**Fig. 3.4b inset**). The uniform distribution of constituent elements Bi, V, O and Zn in SEM elemental mapping further substantiated the pigment homogeneity, **Fig. 3.4c-f**.

Element	Weight %
O K	20.01
V K	4.39
Zn K	55.53
Bi M	20.07
Total	100.00
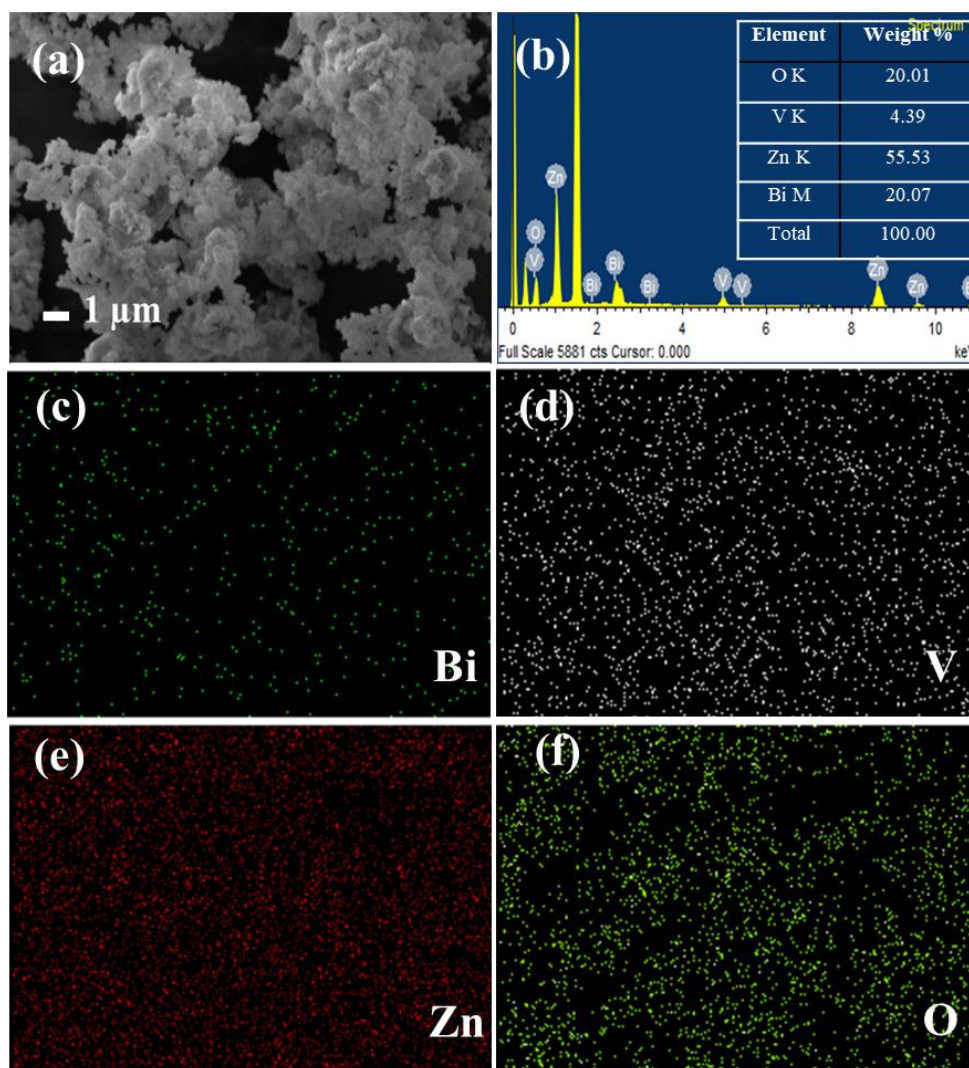
Fig. 3.4. (a) SEM image, (b) SEM-EDS and (c-f) SEM elemental mapping of 25%BVZ

TEM image in **Fig. 3.5a** shows well dispersed granular 25%BVZ nanoparticles of average particle size 25 nm. The high-resolution image revealed that 2 to 5 nm size $BiVO_4$ nanocrystals are decorated over ZnO nanoparticles, **Fig. 3.5b**, to form the complex pigment. The Selected Area Electron Diffraction (SAED) pattern and lattice fringes provided more information regarding the crystallinity of the pigment, **Fig. 3.5c-d.** The d spacing corresponding to ZnO (101) plane was marked in the lattice fringes obtained in HRTEM image, **Fig. 3.5d,** which is matching with the PXRD data. The pigment stoichiometry and particle size distribution were further analyzed via TEM-EDS and DLS measurements, respectively, **Fig. 3.6a, b**. A narrow size distribution curve with an average particle size of 204 nm, **Fig. 3.6b**, was noted for 25%BVZ. As seen in HRTEM image, it is attributed to the bulk pigment sample formed by the agglomeration of monodispersed primary particles.
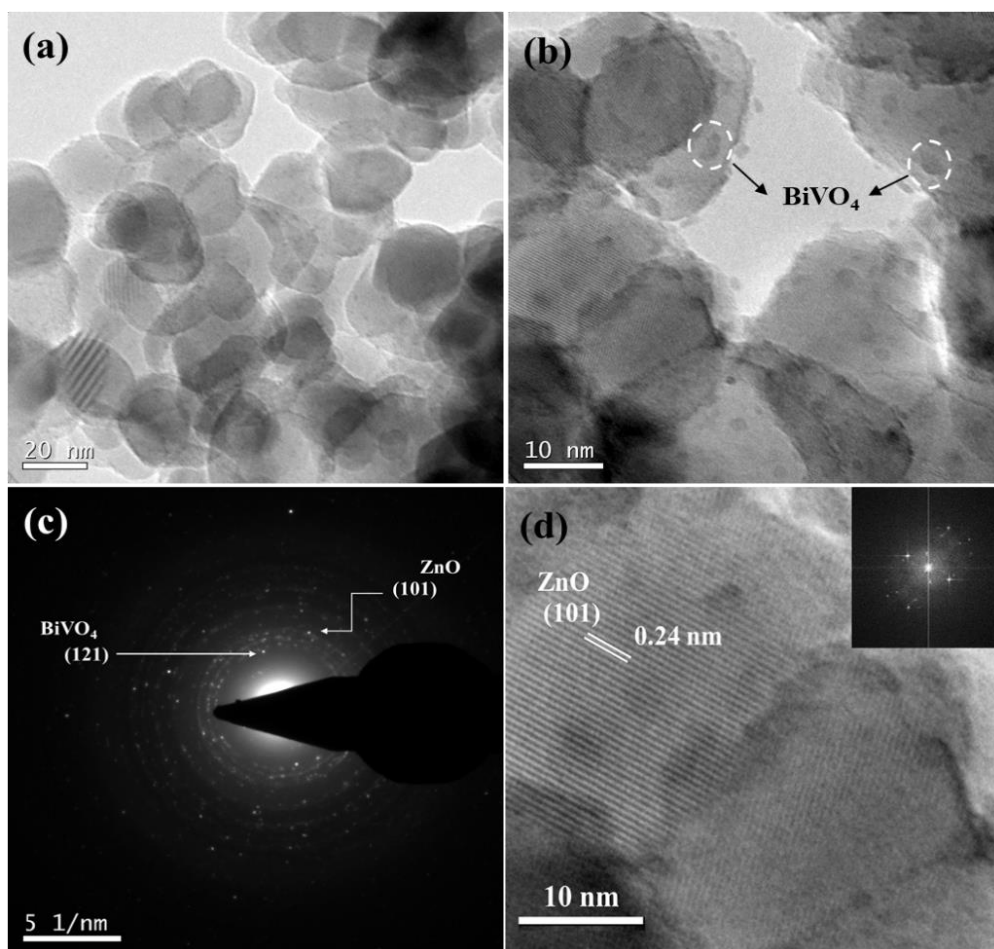
Fig. 3.5. (a, b) TEM images, (c) SAED pattern and (d) lattice fringes of 25%BVZ, diffraction pattern shown in the inset
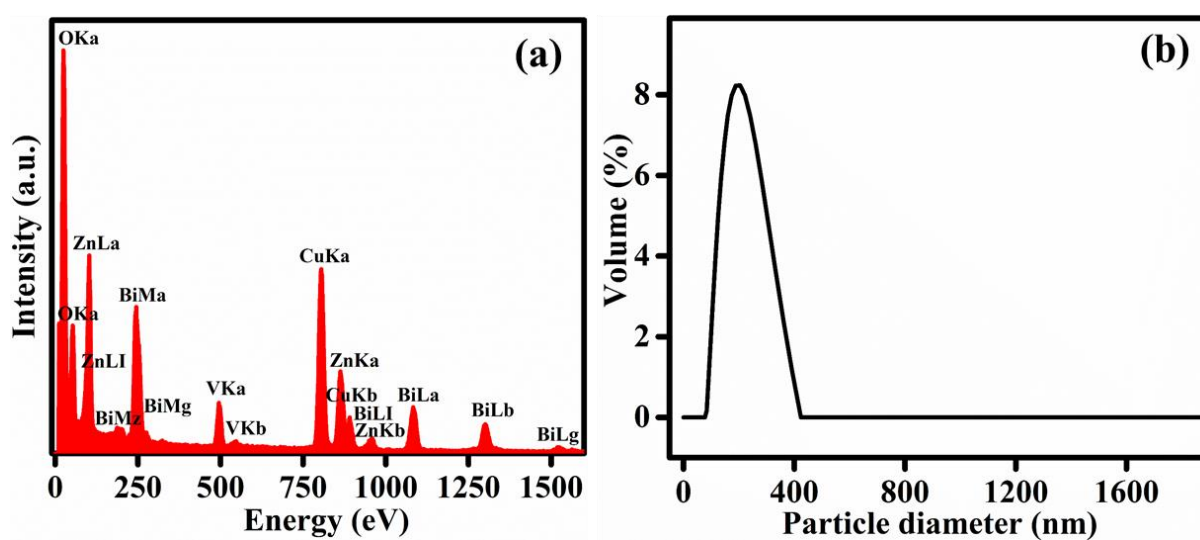
Fig. 3.6. (a) TEM-EDS and (b) DLS curve of 25%BVZ

3.4.4. UV-Vis-NIR spectral studies

The UV-Vis absorption spectrum of 25%BVZ in **Fig. 3.7a** illustrated an intense broad absorption band from 300-500 nm range. It is a combination spectrum of its constituent species $BiVO_4$ and ZnO, which supports that both the constituents were present without any chemical modifications in the synthesized complex pigment. The absorption at 395-500 nm is the characteristic absorption of $BiVO_4$ attributed to the charge transfer transition from valence band formed by the complex orbitals Bi_{6s} and O_{2p} to the conduction band V_{3d} orbital[23]. Similarly, the $\pi \rightarrow \pi^*$ electronic transitions in ZnO from the valence band to the conduction band ($O_{2p} \rightarrow Zn_{3d}$) is responsible for the absorption at 350 nm[14, 24-26]. The 25%BVZ exhibited a blue shift in the absorption spectrum when compared to pure $BiVO_4$. Consequently, the calculated bandgap using the Tauc plot was increased from 2.5 to 2.6 eV, **Fig. 3.7b**. Therefore, pigment began to reflect the green region in the visible spectrum and hence the a^* was shifted from positive to negative axis. It strictly confined the absorption spectrum within the violet-blue region, resulting in a pure and bright greenish yellow pigment.
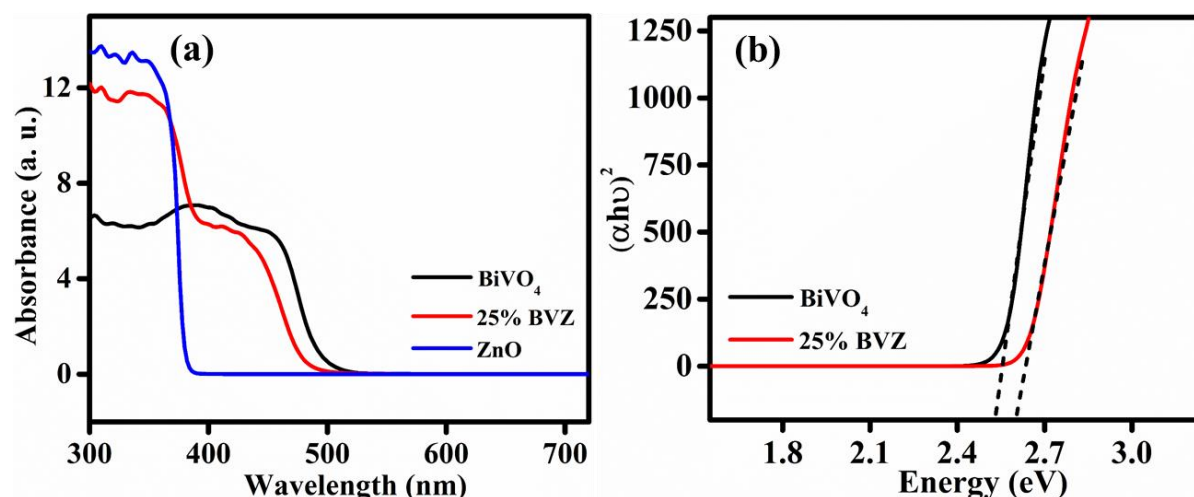
Fig. 3.7. (a) Absorption spectra and (b) Tauc plot of 25%BVZ

The blue shift in absorption spectrum was associated with the electronic modification in $BiVO_4$ moiety. It was confirmed from the XPS results shown in **Fig. 3.8**. Presence of constituent elements Bi, V, Zn and O were identified in the survey spectrum. The high resolution O1s, V2p spectra exhibited a positive shift in binding energy, whereas the Bi4f spectrum shown a negative shift[27]. The positive shift indicates the reduction in electron density, and vice versa. The change in electron density of valence and conduction band thus enhanced the bandgap, leading to the blue shift in absorption spectrum. In addition, the result also substantiated that the $BiVO_4$ nanocrystals are successfully anchored on top of ZnO substrate in the complex pigment.
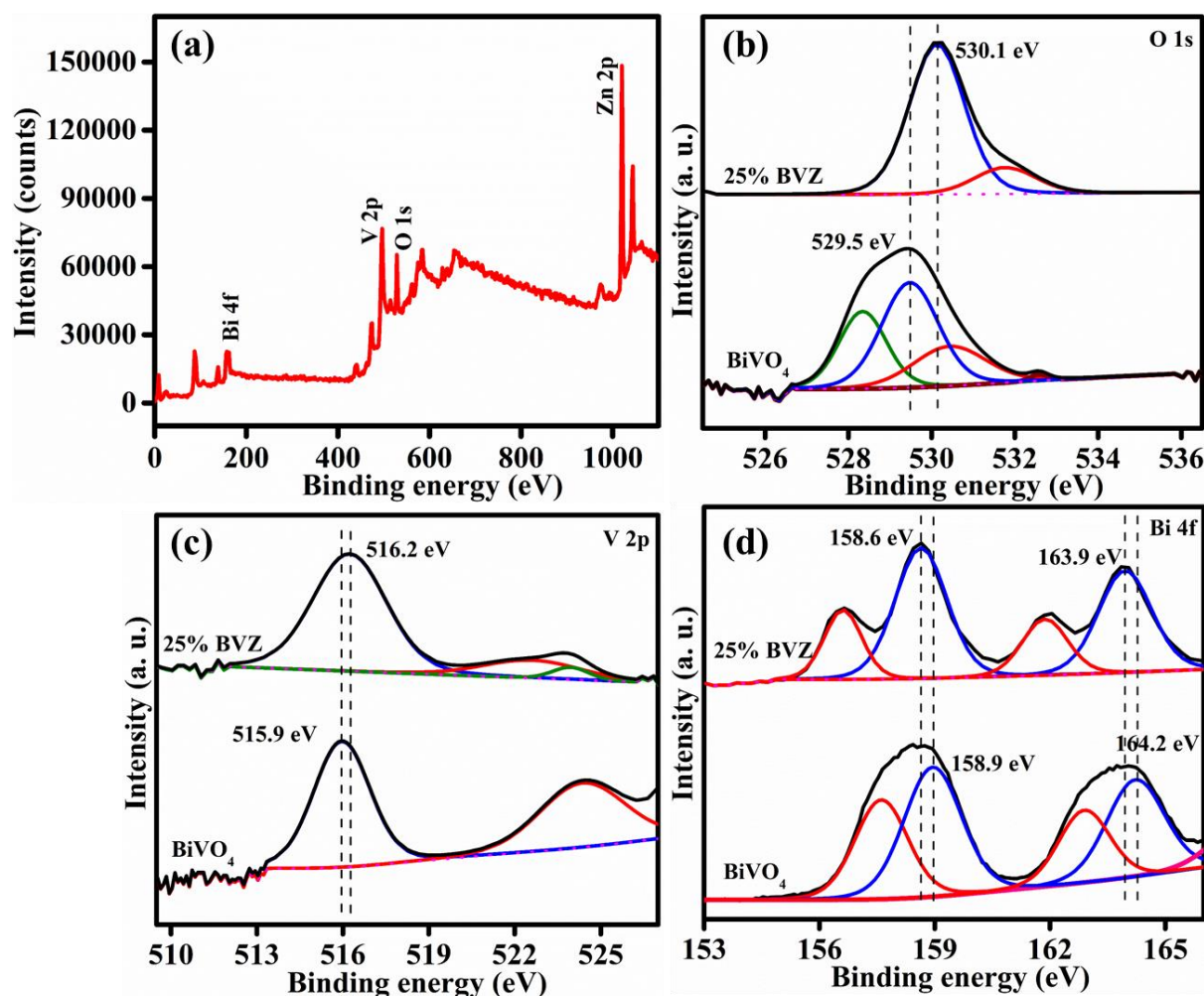
Fig. 3.8. (a) XPS survey spectrum of 25%BVZ, comparison in high resolution XPS spectra of (b) O1s, (c) V2p and (d) Bi4f of $BiVO_4$ and 25%BVZ

3.4.5. Reflectance analysis

The synthesized complex pigment exhibited a substantial enhancement in the reflectance profile compared to that of pure $BiVO_4$, **Fig. 3.9**. NIR reflectance and NIR solar reflectance (R^*) of 25%BVZ was found to be 98% and 90%, **Table 3.2**, respectively. The peculiar particle morphology allowed enough room for the infrared rays to get reflected from both $BiVO_4$ and ZnO surfaces. Therefore, the synergy of $BiVO_4$ and highly reflective ZnO brought considerable improvement in the NIR reflectance property of complex pigment, transforming it into an exciting 'cool' roof pigment. The mixed pigment also had an excellent reflectance profile because of the presence of $BiVO_4$ and ZnO in the composition. However, due to the lack of morphological benefit, its colour strength is relatively poor.
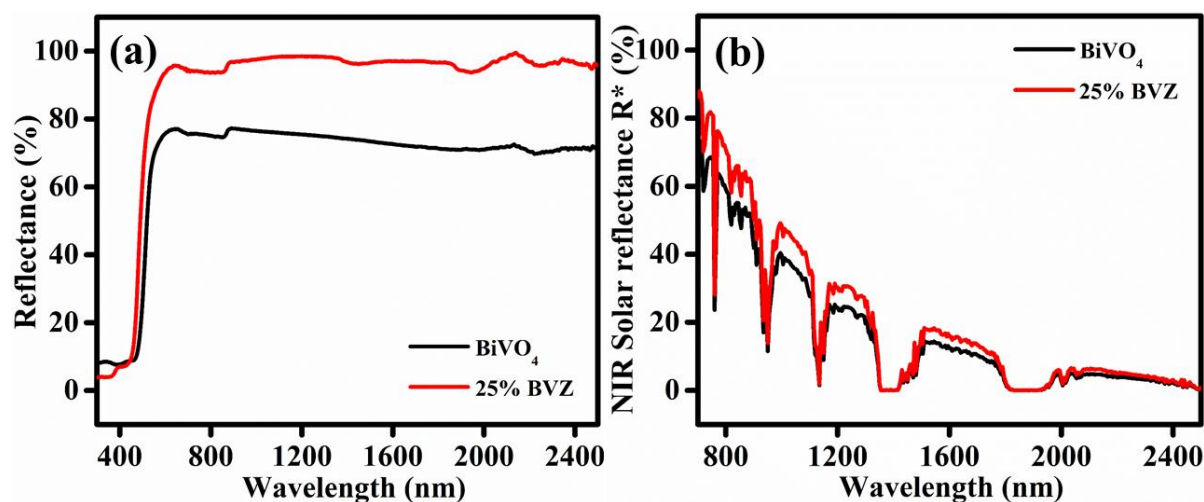
Fig. 3.9. (a) Reflectance and (b) NIR solar reflectance spectra of 25%BVZ

3.4.6. Chemical stability

Before application studies, stability of 25%BVZ complex pigment was ensured in aqueous, acid and base media[28]. The obtained colour parameters before and after the chemical treatment enumerated in **Table 3.3**. The difference in colour values between the treated and untreated sample stayed well within the industrial limit, $\Delta E^{*}_{ab} \leq 1$ unit[29-31]. Hence, it was confirmed that the $BiVO_4$ nanocrystals anchored ZnO is intact in aggressive media, thus chemically stable.

Table 3.3. CIE colour coordinates of 25%BVZ after chemical treatment

Sample	pH	L^{*}	a^{*}	b^{*}	C^{*}	h^{o}	ΔE^{*}_{ab}
25%BVZ	-	91.53	-6.28	76.45	76.78	94.78	-
Water	6.6	91.45	-5.99	76.22	76.45	95.01	0.38
HNO_3	3.0	91.10	-6.08	75.85	76.09	94.93	0.76
NaOH	10.5	90.96	-5.95	76.01	76.24	95.02	0.79

3.4.7. Coating studies

The complex pigment coatings were developed on concrete block and Al sheet. NIR solar reflectance spectra of the bare and pigment coated substrates were displayed in **Fig. 3.10**. Photographs of the coatings were shown in the inset of respective solar reflectance graphs. Results suggests that colour strength and saturation of both the coatings are excellent, almost overlaps with that of pigment powder. Moreover, the pigment coatings are highly NIR solar

reflective in nature even though the binder inclusion slightly reduced its reflectance, **Table 3.4**, which demonstrates the quality of the synthesized complex pigment.

Table 3.4. Colour coordinates and reflectance of pigment coatings

Sample	L^*	a^*	b^*	C^*	h^o	NIR at 1100 nm (%)	R^* (%)
25%BVZ	91.53	-6.28	76.45	76.78	94.78	98	90
Concrete	85.74	-3.97	76.97	77.07	96.62	77	75
Al sheet	81.93	-7.64	70.09	70.51	93.37	73	70
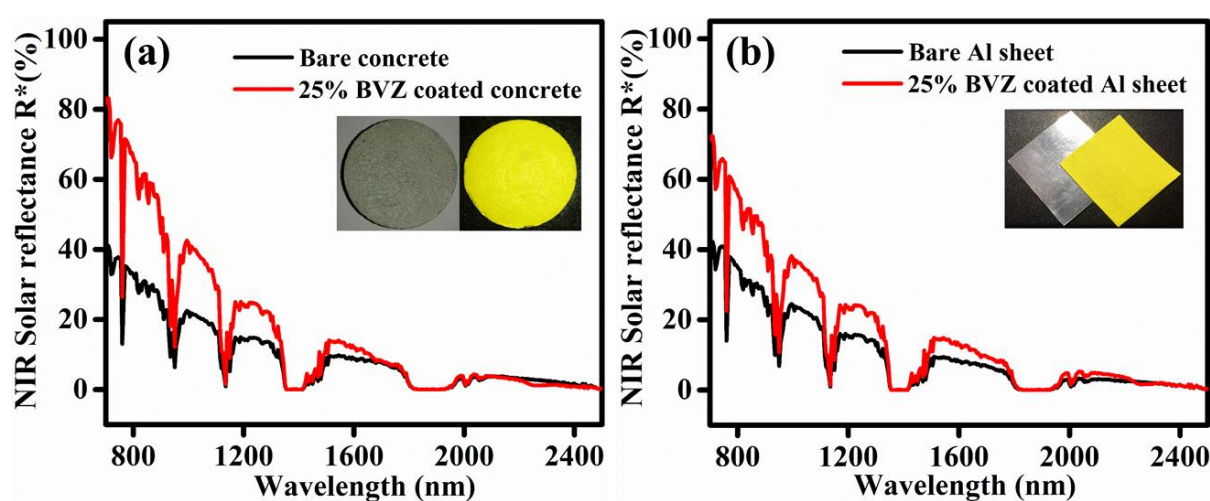
Fig. 3.10. NIR solar reflectance spectra of 25%BVZ coated (a) concrete block and (b) Al sheet, along with their bare surfaces (photographs of the coatings shown in inset)

3.4.8. Thermal shielding analysis

Thermal shielding performance of 25%BVZ coating was compared with commercial yellow coating via experimental setup shown in **Fig. 2B.1**. The coating thickness determined from the optical images was found to be 200-250 μm. The one-hour experiment reveals that the interior and coating surface temperatures rise dramatically during the first ten minutes. Then it was slowed and stabilized in the next 30 minutes, **Fig. 3.11**. A significant reduction was recorded in the temperature buildup of 25%BVZ coating with respect to commercial coating. The estimated interior temperature difference and the coated surface temperature determined from thermal images was ~ 7 °C, **Fig. 3.12**. Both the results establishes that 25%BVZ is an exceptional 'cool' pigment with a promising ability to reduce the heat buildup inside the buildings. The overall results confirmed that the new complex pigment 25%BVZ

can be an excellent alternative to $BiVO_4$ yellow pigment since it retained the general properties of the core pigment with a substantial reduction in material cost.
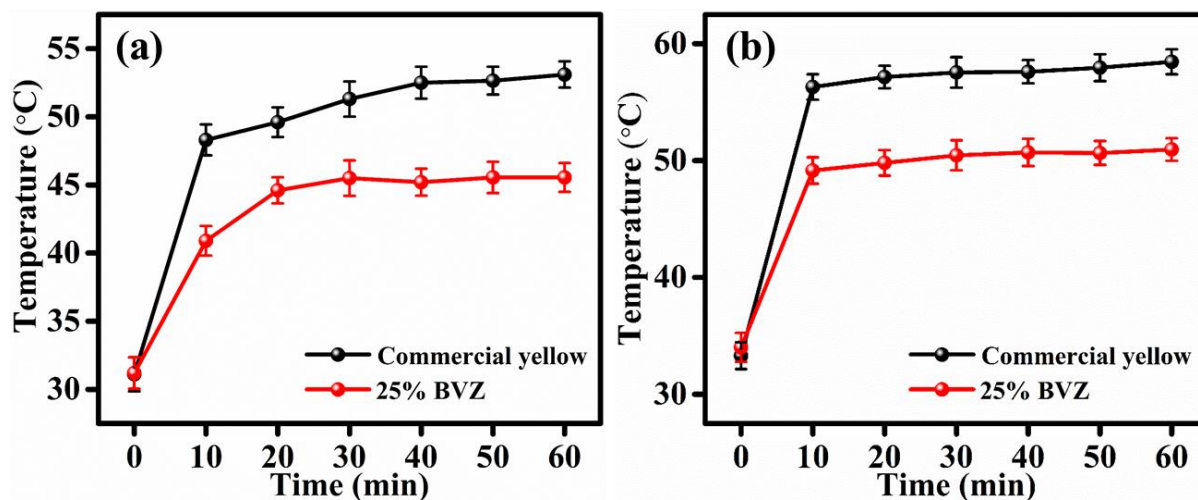
Fig. 3.11. (a) Interior and (b) coating surface temperature profile comparison of 25%BVZ and commercial yellow coatings
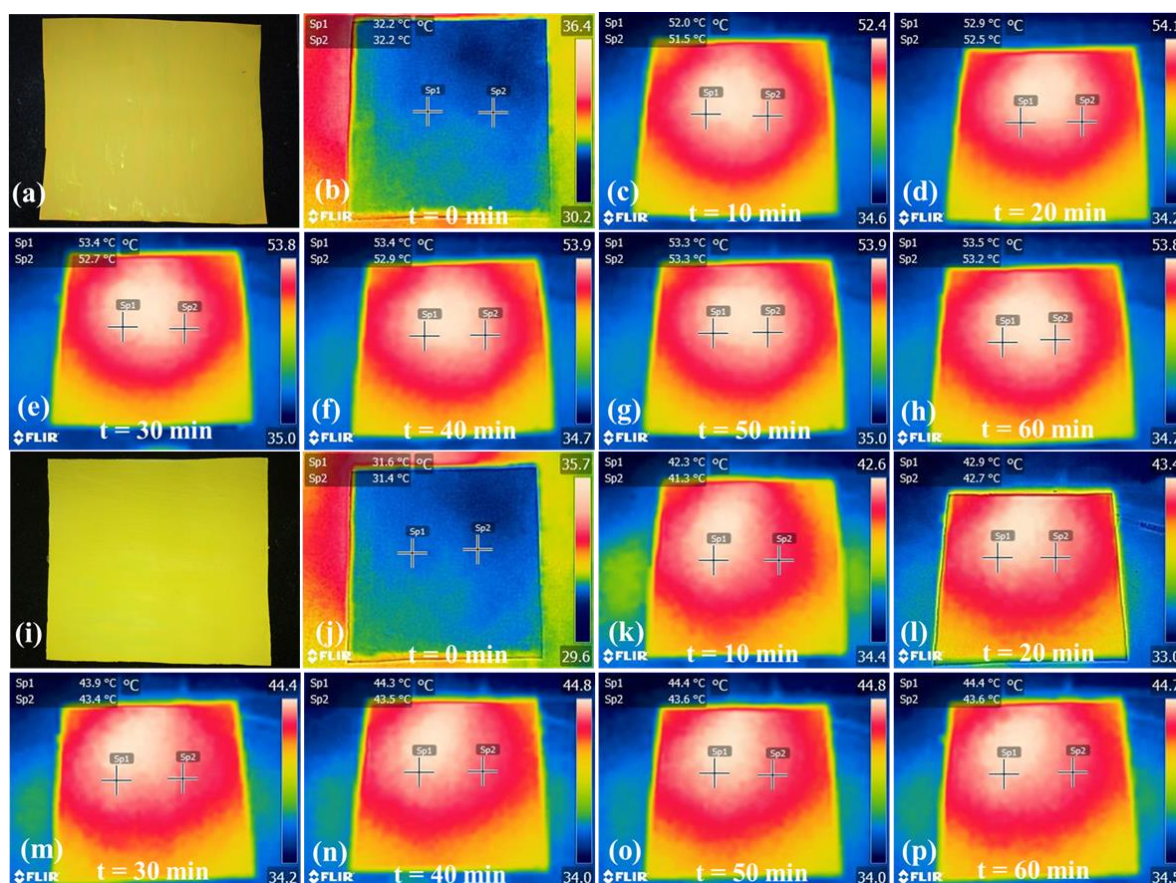
Fig. 3.12. Photographs of (a) commercial yellow and (i) 25%BVZ coatings on Al sheet, thermal images of (b-h) commercial yellow and (j-p) 25%BVZ coatings

3.5. Conclusions

BiVO$_4$ based complex pigment was successfully synthesized by using commercially available inexpensive WP, such as ZnO/ Al$_2$O$_3$/ SiO$_2$/ TiO$_2$ as a supporting substrate through the citrate-gel method. The X-ray diffraction analysis ensured the complex pigment formation, in which 25%BVZ was found to be the best composition with colour strength equivalent to pure BiVO$_4$. Morphological investigation of 25%BVZ via HRTEM revealed that 2-5 nm size BiVO$_4$ nanocrystals are decorated on ~25 nm ZnO particles to form the complex pigment. The unique morphology rendered excellent colour strength for the complex pigment even with 75 wt% reduction in BiVO$_4$ concentration. The synergy of ZnO with BiVO$_4$ was highly promising in enhancing the solar reflectance of the pigment from 76 to 90%. The thermal shielding experiment displayed 7 °C reduction in interior and surface temperature for 25%BVZ compared to commercial yellow paint coating. The results demonstrated the development of a new cost-effective complex pigment as an alternative to expensive BiVO$_4$ yellow.

3.6. References

1. Jeevanandam, P.; Mulukutla, R.; Phillips, M.; Chaudhuri, S.; Erickson, L.; Klabunde, K. J. T. J. o. P. C. C., Near infrared reflectance properties of metal oxide nanoparticles. **2007,** *111* (5), 1912-1918.

2. Telpande, D.; PARWATE, D. J. I. J. o. I. R. i. S., Engineering; Technology, Stability testing of non-toxic bismuth vanadate according to pharmaceutical criteria. **2015,** *4*, 5350.

3. Barata, M. A.; Neves, M. C.; Neto, C. P.; Trindade, T. J. D.; pigments, Growth of $BiVO_4$ particles in cellulosic fibres by in situ reaction. **2005,** *65* (2), 125-127.

4. Masui, T.; Honda, T.; Imanaka, N. J. D.; Pigments, Novel and environmentally friendly (Bi, Ca, Zn)VO_4 yellow pigments. **2013,** *99* (3), 636-641.

5. Sameera, S. F.; Rao, P. P.; Kumari, L. S.; James, V.; Divya, S. J. C. L., Potential NIR Reflecting Yellow Pigments in $(BiV)_{1-x}(YNb)_xO_4$ Solid Solutions. **2013,** *42* (5), 521-523.

6. Guan, L.; Fan, J.; Zhang, Y.; Guo, Y.; Duan, H.; Chen, Y.; Li, H.; Liu, H. J. D.; Pigments, Facile preparation of highly cost-effective $BaSO_4@BiVO_4$ core-shell structured brilliant yellow pigment. **2016,** *128*, 49-53.

7. Wang, X.; Mu, B.; Hui, A.; Wang, Q.; Wang, A. J. D.; pigments, Low-cost bismuth yellow hybrid pigments derived from attapulgite. **2018,** *149*, 521-530.

8. Wang, X.; Mu, B.; Zhang, Z.; Wang, A. J. C. P. B. E., Insights into halloysite or kaolin role of $BiVO_4$ hybrid pigments for applications in polymer matrix and surface coating. **2019,** *174*, 107035.

9. Wang, X.; Mu, B.; Wang, W.; Wang, Q.; Wang, A. J. A. C. S., A comparative study on color properties of different clay minerals/$BiVO_4$ hybrid pigments with excellent thermal stability. **2019,** *181*, 105221.

10. Wang, X.; Mu, B.; Xu, J.; Wang, A. J. A. A. M.; Interfaces, Reversible thermochromic superhydrophobic $BiVO_4$ hybrid pigments coatings with self-cleaning performance and environmental stability based on kaolinite. **2021,** *13* (2), 3228-3236.

11. Wu, L.; Mu, B.; Yang, H.; Wang, X.; Wang, A. J. J. o. A. P. S., Mechanochemical synthesis of multifunctional kaolin@ $BiVO_4$ hybrid pigments for coloring and reinforcing of acrylonitrile-butadiene-styrene. **2022,** *139* (22), 52266.

12. Yuan, L.; Han, A.; Ye, M.; Chen, X.; Ding, C.; Yao, L. J. S. E., Preparation, characterization and thermal performance evaluation of coating colored with NIR reflective pigments: $BiVO_4$ coated mica-titanium oxide. **2018,** *163*, 453-460.

13. He, X.; Wang, F.; Liu, H.; Wang, X.; Gao, J. J. N., Synthesis and coloration of highly dispersive $SiO_2/BiVO_4$ hybrid pigments with low cost and high NIR reflectance. **2019,** *30* (29), 295701.

14. Neves, M. C.; Trindade, T. J. M. r. b., Preparation of hollow shells of zinc oxide/bismuth (III) vanadate. **2003,** *38* (6), 1013-1020.

15. Honda, T.; Masui, T.; Imanaka, N. J. R. A., Novel environmentally friendly (Bi, Ca, Zn, La)VO_4 inorganic yellow pigments. **2013,** *3* (47), 24941-24945.

16. Neves, M. C.; Lehocky, M.; Soares, R.; Lapcik Jr, L.; Trindade, T. J. D.; pigments, Chemical bath deposition of cerium doped $BiVO_4$. **2003,** *59* (2), 181-184.

17. Vivekanandhan, S.; Venkateswarlu, M.; Satyanarayana, N. J. J. o. a.; compounds, Synthesis and characterization of nanocrystalline $LiNi_{0.5}Co_{0.5}VO_4$ powders by citric acid assisted sol-gel combustion process. **2008,** *462* (1-2), 328-334.

18. Ocaña, M.; Espinós, J.; Carda, J. J. D.; Pigments, Synthesis, through pyrolysis of aerosols, of $YIn_{1-x}Mn_xO_3$ blue pigments and their efficiency for colouring glazes. **2011,** *91* (3), 501-507.

19. Dos Anjos, P.; Pereira, E.; Gobato, Y. J. J. o. a.; compounds, Study of the structure and optical properties of rare-earth-doped aluminate particles prepared by an amorphous citrate sol-gel process. **2005,** *391* (1-2), 277-283.

20. Oudghiri-Hassani, H.; Rakass, S.; Al Wadaani, F. T.; Al-Ghamdi, K. J.; Omer, A.; Messali, M.; Abboudi, M. J. J. o. T. U. f. S., Synthesis, characterization and photocatalytic activity of α-Bi_2O_3 nanoparticles. **2015,** *9* (4), 508-512.

21. Sameera, S.; Rao, P. P.; Divya, S.; Raj, A. K.; Thara, T. A. J. E.; buildings, High IR reflecting $BiVO_4$-$CaMoO_4$ based yellow pigments for cool roof applications. **2017,** *154*, 491-498.

22. Sameera, S.; Rao, P. P.; James, V.; Divya, S.; Raj, A. K. J. D.; Pigments, Influence of $(LiLa)_{1/2}MoO_4$ substitution on the pigmentary properties of $BiVO_4$. **2014,** *104*, 41-47.

23. Tan, G.; Zhang, L.; Ren, H.; Wei, S.; Huang, J.; Xia, A. J. A. a. m.; interfaces, Effects of pH on the hierarchical structures and photocatalytic performance of $BiVO_4$ powders prepared via the microwave hydrothermal method. **2013,** *5* (11), 5186-5193.

24. Zak, A. K.; Abrishami, M. E.; Majid, W. A.; Yousefi, R.; Hosseini, S. J. C. I., Effects of annealing temperature on some structural and optical properties of ZnO nanoparticles prepared by a modified sol–gel combustion method. **2011,** *37* (1), 393-398.

25. Hongjun, L.; Zang, Z.; Tang, X. J. O. M. E., Synthesis mechanism and optical properties of well nanoflower-shaped ZnO fabricated by a facile method. **2014,** *4* (9), 1762-1769.

26. Achehboune, M.; Khenfouch, M.; Boukhoubza, I.; Mothudi, B.; Zorkani, I.; Jorio, A. In *Structural and optical characterization of Holmium coated ZnO nanorods*, Journal of Physics: Conference Series, IOP Publishing: 2018; p 012007.

27. Dimitrov, V.; Komatsu, T.; Sato, R. J. J. o. t. C. S. o. J., Polarizability, optical basicity and O1s binding energy of simple oxides. **1999,** *107* (1241), 21-26.

28. Yang, R.; Han, A.; Ye, M.; Chen, X.; Yuan, L. J. S. E. M.; Cells, S., Synthesis, characterization and thermal performance of Fe/N co-doped $MgTiO_3$ as a novel high near-infrared reflective pigment. **2017,** *160*, 307-318.

29. Levinson, R.; Akbari, H.; Berdahl, P. J. S. E., Measuring solar reflectance-Part I: Defining a metric that accurately predicts solar heat gain. **2010,** *84* (9), 1717-1744.

30. Levinson, R.; Akbari, H.; Berdahl, P. J. S. E., Measuring solar reflectance-Part II: Review of practical methods. **2010,** *84* (9), 1745-1759.

31. Thongkanluang, T.; Kittiauchawal, T.; Limsuwan, P. J. C. I., Preparation and characterization of Cr_2O_3-TiO_2-Al_2O_3-V_2O_5 green pigment. **2011,** *37* (2), 543-548.

Transformation of ZnFe$_2$O$_4$ brown towards a versatile pigment for energy efficient buildings

4.1. Abstract

The present work demonstrates a multifunctional brown inorganic ferrite pigment series that is free of highly toxic elements via the solid-state ceramic method. The partial replacement of chromophore Fe^{3+} by Al^{3+} in the pigment composition $ZnFe_{1.9}Al_{0.1}O_4$ induced structural distortion in its octahedral geometry, causing compressive stress inside the crystal unit cell. Even 5 mol% of Al^{3+} incorporation could promote the pigment reflectance profile 25 units higher than the parent system, especially with significant colour improvement. The acrylic coating of the pigment on Al sheet and concrete was equally well in displaying good colour strength and reflectance property. A significant temperature reduction (~2.5 ℃) was obtained for $ZnFe_{1.9}Al_{0.1}O_4$ coating compared to $ZnFe_2O_4$. The pigment outperformed commercial toxic anticorrosive pigments, chromates and phosphates with an outstanding $R_{ct} = 4.1 \times 10^9$ Ωcm^2. The stability of 20 wt% pigment loaded epoxy coating on steel activates through the combined action of $Zn(OH)_2$ and $FeOOH$ film mechanism. Since the pigment exhibits intense colour, high NIR solar reflectance and robust corrosion resistance properties, it is indispensable to employ it as a high-performance multifunctional pigment.

4.2. Introduction

Inorganic dark pigments are favoured over light pigments owing to their aesthetics and ease of maintenance. In fact, it is more beneficial because different colour shades can be achieved in convenience by dilution. Spinel ferrites are an exciting class of non-toxic dark inorganic colourants that exhibit high thermal and chemical stability[1]. Mostly, variations of black and brown colours are available in ferrite pigments[2, 3]. Charge transfer transition from O^{2-} to Fe^{3+} results in broad absorption in the visible spectrum, derived its attractive colour tones[4, 5]. However, subsequent ligand field transitions at NIR region made it a strong solar heat recipient, which brings the urban heat island effect into action[5, 6]. As a result, considerable effort has been made in the last few decades to enhance the NIR reflectivity of ferrite pigments[2, 7-9].

Brown is a customary colour choice for roofs and exterior wall coatings. In this regard, $ZnFe_2O_4$ is a highly recommended inexpensive ferrite pigment free of toxic elements. Several innovations have been tried on this ceramic pigment to address NIR reflectivity issues, with the majority of them compromising its colour intensity while achieving their target. Liu et al., attempted to incorporate Mg^{2+} at the Zn^{2+} site of $ZnFe_2O_4$, obtaining 58% R^* for the compound $Zn_{0.6}Mg_{0.4}Fe_2O_4$[10]. The report by Suwan et al., on Ni-doped $ZnFe_2O_4$, with the composition

$Zn_{0.9}Ni_{0.1}Fe_2O_4$, demonstrated significantly better R^* ~ 63%[11]. Unfortunately, the colour parameters for all of these compositions have deteriorated as compared to the parent ferrite. Elakkiya et al., made a similar effort synthesizing $ZnAl_{0.78}Fe_{0.2}Ce_{0.02}O_4$, with a very high R^* 80%, however the colour was found to be rather faint brown[12]. Surprisingly, the majority of these studies chose to partially replace the Zn^{2+} site of $ZnFe_2O_4$ with different metal ions. At the same time, it was evident from the spectral features that transitions in Fe^{3+} are responsible for the low reflectance of ferrites in the NIR region[5]. Hence, it would be perfect to modify the Fe^{3+} site of $ZnFe_2O_4$ to improve the NIR reflectance without affecting colour.

To develop a stable NIR reflective coating on a metallic roofing sheet under oscillating aggressive climatic conditions, the pigment must also be corrosion resistant. Fortunately, $ZnFe_2O_4$ is known for its outstanding anticorrosive property; however, beyond preliminary studies, comprehensive research on the pigment in coatings is limited[13-18]. Thus, it will be a massive transformation for $ZnFe_2O_4$ to enhance NIR reflectivity alongside exploiting its anticorrosive property to develop a sustainable cool coating.

Herein, by replacing the Fe^{3+} site of $ZnFe_2O_4$ with different metal ions, a rational approach was followed to improve the reflectance profile of $ZnFe_2O_4$ in the NIR region without losing colour strength. The best composition from the synthesized compounds was chosen and studied for structural and optical properties. Further, its corrosion resistance behaviour was evaluated. The colour, reflectance, stability and temperature shielding performance of the prepared acrylic coatings were commendable. Therefore, the present work provides a new insight to overcome the drawbacks of $ZnFe_2O_4$, simultaneously exploiting its multifunctional properties to escalate the market value.

4.3. Experimental section

4.3.1. Materials and methods

Solid-state method was used for $ZnFe_{1.9}M_{0.1}O_4$ (M = Al^{3+}, Si^{4+}, Ti^{4+}, La^{3+} and Y^{3+}) and $ZnFe_{1-x}Al_xO_4$ ($0 \leq x \leq 0.8$) pigment synthesis. Extra pure ZnO (99.9%), Fe_2O_3 (99%), Al_2O_3 (99%), SiO_2 (99.5%), TiO_2 (99%), La_2O_3 (99.9%) and Y_2O_3 (99.99%) were purchased from Merck. Stoichiometric amounts of precursors mixed homogeneously by 3 h grinding in ethanol medium and calcined at 1100 °C for 4 h in air atmosphere. An acrylic coating of $ZnFe_{1.9}Al_{0.1}O_4$ pigment was prepared on concrete and Al sheet. Thermal shielding ability of the coating was analyzed and compared with commercial brown pigment coating, as described in Experimental section, Chapter 2B[19, 20]. Thickness of all the prepared coatings were measured from optical

images. The pigment $ZnFe_{1.9}Al_{0.1}O_4$ was analyzed for anticorrosive property by developing epoxy coatings on steel, loaded with respective pigment powder, as described in Experimental section, Chapter 2B.

4.3.2. Characterization techniques

Phase purity and crystal structure determination of the prepared pigment series was done by PXRD analysis (details given in Chapter 2A). Morphology and particle size distribution were identified through SEM and HRTEM analysis. Composition analysis and particle size measurements were carried out using EDS and DLS techniques, respectively. Optical studies were performed using UV-Vis-NIR Spectrophotometer (details given in Chapter 2A). The pigment acrylic coating thickness was measured using Optical microscope and epoxy coating thickness was measured using Profilometer. The anticorrosive analysis of the pigments were done through a multichannel potentiostat (Autolab) and respective corrosion mechanism was identified from XPS analysis (details given in Chapter 2B).

4.4. Results and discussion

4.4.1. Synthesis of $ZnFe_{2-x}M_xO_4$ pigment series and structural studies

Metal ions such as Al^{3+}, Si^{4+}, Ti^{4+}, La^{3+} and Y^{3+} have been introduced at the Fe^{3+} site of $ZnFe_2O_4$, anticipating an improvement in NIR reflectance without colour deterioration. The criteria for selecting these metal ions as dopants were such that they were all excellent candidates for providing high NIR reflectance[21-24]. **Fig. 4.1a** illustrates the powder XRD results of all doped samples, including the base compound $ZnFe_2O_4$. Except for La^{3+} and Y^{3+} doped ferrites, PXRD patterns showed the formation of a highly crystalline single-phase compound that matched the parent system $ZnFe_2O_4$. Major peaks were well indexed to a cubic structure using JCPDS 022-1012. The ionic radii of Fe^{3+}, Si^{4+}, Al^{3+}, Ti^{4+}, Y^{3+} and La^{3+} are 0.645, 0.4, 0.535, 0.605, 0.9 and 1.032 Å, respectively[25]. Since, Si^{4+}, Al^{3+}, Ti^{4+} ions are smaller than Fe^{3+} ion, they have successfully replaced Fe^{3+} ion in the crystal lattice and developed phase pure compounds[26]. Because of the substantially greater ionic size of La^{3+} and Y^{3+}, the extent of doping was relatively low, leading to the formation of impurity phases $LaFeO_3$ (JCPDS 075-0541) and $YFeO_3$ (JCPDS 073-1345), respectively, (marked *). When smaller ions replace the larger ions, the unit cell experiences a reduction in dimensions and volume, resulting in a higher angle shift in X-ray diffraction patterns and vice versa[27]. As expected, Si^{4+}, Al^{3+}, Ti^{4+} doping resulted in a decrease in cell parameter, volume (**Table 4.1**) and a shift in XRD patterns (**Fig. 4.1b**) although no significant variations are observed for La^{3+} and Y^{3+} doping. This can also

substantiate the inconsistency of substitution due to ionic radii mismatch between host and guest ions.
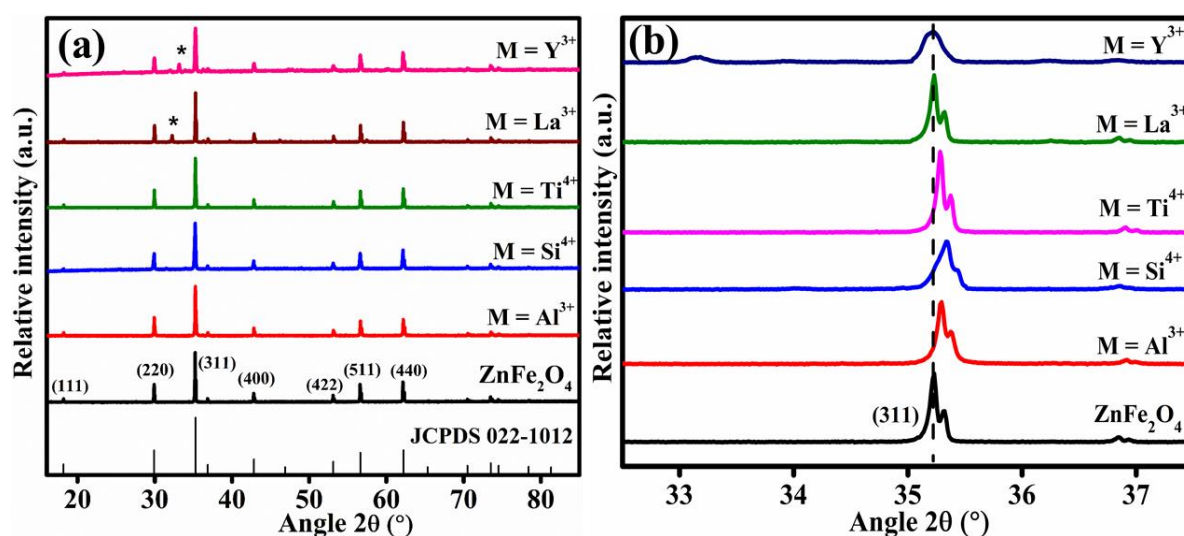
Fig. 4.1. (a) PXRD patterns and (b) peak shift in PXRD patterns of $ZnFe_{2-x}M_xO_4$ (M = Al^{3+}, Si^{4+}, Ti^{4+}, La^{3+} and Y^{3+})

Table 4.1. Cell parameters of synthesized ferrite pigments

Sample	Lattice parameter (Å)	Volume (Å³)	Crystallite size D (nm)	Strain (ε) $\times 10^2$	Dislocation density (δ) $\times 10^{13}$ lines/m²
$ZnFe_2O_4$	8.4430	601.8529	139.52	1.48	5.13
$ZnFe_{1.9}Al_{0.1}O_4$	8.4371	600.5920	139.51	1.48	5.13
$ZnFe_{1.9}Si_{0.1}O_4$	8.4366	600.4852	116.28	1.85	7.39
$ZnFe_{1.9}Ti_{0.1}O_4$	8.4405	601.3184	145.36	1.49	4.73
$ZnFe_{1.9}La_{0.1}O_4$	8.4436	601.9812	145.27	1.48	4.73
$ZnFe_{1.9}Y_{0.1}O_4$	8.4443	602.1309	96.83	2.22	10.66
$ZnFe_{1.8}Al_{0.2}O_4$	8.4330	599.7169	111.62	1.85	8.03
$ZnFe_{1.6}Al_{0.4}O_4$	8.4144	595.7574	93.04	2.23	11.55
$ZnFe_{1.4}Al_{0.6}O_4$	8.4052	593.8054	79.75	2.60	15.72
$ZnFe_{1.2}Al_{0.8}O_4$	8.3799	588.4594	62.05	3.34	25.97

NIR reflectance analysis of the prepared pigment samples were performed and the obtained spectra are displayed in **Fig. 4.2a**. All the compounds have exhibited a substantial enhancement in the reflectance profile, because of potential metal ion substituents in the host lattice. Simultaneously, it is essential to investigate the colour strength of the synthesized pigments, photographs exhibited in **Fig. 4.2b**. Because, introducing such metal ions can

seriously dilute brown colour of $ZnFe_2O_4$ pigment, which will be detrimental to its quality. In terms of colour and reflectance, Al^{3+} appeared to be the best choice among phase pure substituted pigments when compared to the other compounds (**Table 4.2**). The pigment $ZnFe_{1.9}Al_{0.1}O_4$ provided rich brown hue, a combination of strong red with feeble yellow, with colour parameters $a^* = 25$ and $b^* = 31$. Moreover, a hue angle closer to 45° falls in the reddish brown region with a superior colour saturation $C^* \sim 40$, further validating its selection. Subsequently, $ZnFe_{2-x}Al_xO_4$ pigment series was developed, emphasizing colour and reflectance properties, and an optimum composition was chosen.
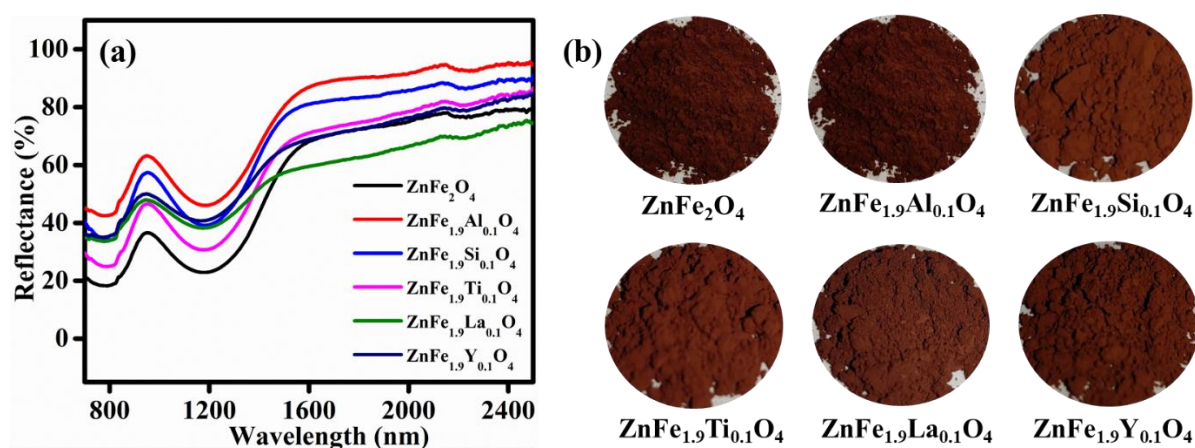
Fig. 4.2. (a) NIR reflectance spectra and (b) photographs of $ZnFe_{2-x}M_xO_4$ (M = Al^{3+}, Si^{4+}, Ti^{4+}, La^{3+} and Y^{3+})

The PXRD patterns of synthesized pigment series $ZnFe_{2-x}Al_xO_4$ ($0 \leq x \leq 0.8$) was shown in **Fig. 4.3a**. The diffraction peaks up to 60 mol% doping, are well matched to the parent cubic $ZnFe_2O_4$ with a spinel structure and indexed using JCPDS 022-1012. Beyond which, $AlFeO_3$ (JCPDS 08-2154) observed as an impurity phase (marked *).

Table 4.2. Colour and reflectance values of $ZnFe_{2-x}M_xO_4$ (M = Al^{3+}, Si^{4+}, Ti^{4+}, La^{3+} and Y^{3+})

Sample	L^*	a^*	b^*	c^*	$h^°$	NIR (%) at 1100 nm	R^* (%)
$ZnFe_2O_4$	38.93	22.46	25.05	33.64	48.11	25	34
$ZnFe_{1.9}Al_{0.1}O_4$	46.54	25.05	31.01	39.86	51.06	50	58
$ZnFe_{1.9}Si_{0.1}O_4$	45.14	25.34	34.24	42.60	53.49	43	51
$ZnFe_{1.9}Ti_{0.1}O_4$	39.54	22.23	20.98	30.57	43.33	34	41
$ZnFe_{1.9}La_{0.1}O_4$	37.72	21.59	19.37	29.00	41.89	40	44
$ZnFe_{1.9}Y_{0.1}O_4$	42.86	23.01	23.62	32.98	45.74	42	48
$ZnFe_{1.8}Al_{0.2}O_4$	46.82	24.28	30.08	38.66	51.09	48	56
$ZnFe_{1.6}Al_{0.4}O_4$	47.08	22.79	30.22	35.83	52.98	51	59
$ZnFe_{1.4}Al_{0.6}O_4$	51.21	22.65	31.96	39.17	54.67	53	61
$ZnFe_{1.2}Al_{0.8}O_4$	53.27	21.38	31.66	38.20	55.96	53	61

In comparison to the parent system, the addition of Al^{3+} ions generated a shift in diffraction peaks to higher diffraction angle. For example, **Fig. 4.3b** illustrates the shift of PXRD peaks corresponding to (220) and (311) Miller planes. It suggests that a larger fraction of Al^{3+} was able to successfully replace Fe^{3+} in $ZnFe_2O_4$ [26]. However, when smaller Al^{3+} (0.535 Å) incorporated at larger Fe^{3+} (0.645 Å) site of $ZnFe_2O_4$ crystal, a lattice strain was developed into the system[28]. As dopant concentration increased, so did the induced lattice distortion, the lattice periodicity and crystal symmetry tend to decrease. It was identified from the PXRD patterns, which exhibited a shift in Bragg reflections, depletion in peak intensity and peak broadening, **Fig. 4.3b**[5]. The calculated lattice parameter and unit cell volume from PXRD patterns also accounts for the developed compressive strain in the $ZnFe_2O_4$ unit cell. Both cell parameter and cell volume decreased steadily as Al^{3+} concentration increased, **Table 4.1**. The average crystallite size, calculated by Scherrer equation, $D = K\lambda/\beta \cos\theta$, was declined from 139.5 to 62 nm, because, Al^{3+} incorporation increases the nucleation rate which restricts the crystal growth[29]. Further, the induced lattice strain (ε) and dislocation density (δ) were calculated using the formula, $\varepsilon = \beta \cos\theta/4$ and $\delta = 1/D^2$, respectively[30, 31]. Both of these factors demonstrated the strain and defects exerted by the dopant ion on the parent crystal lattice, which began to increase with Al^{3+} content.
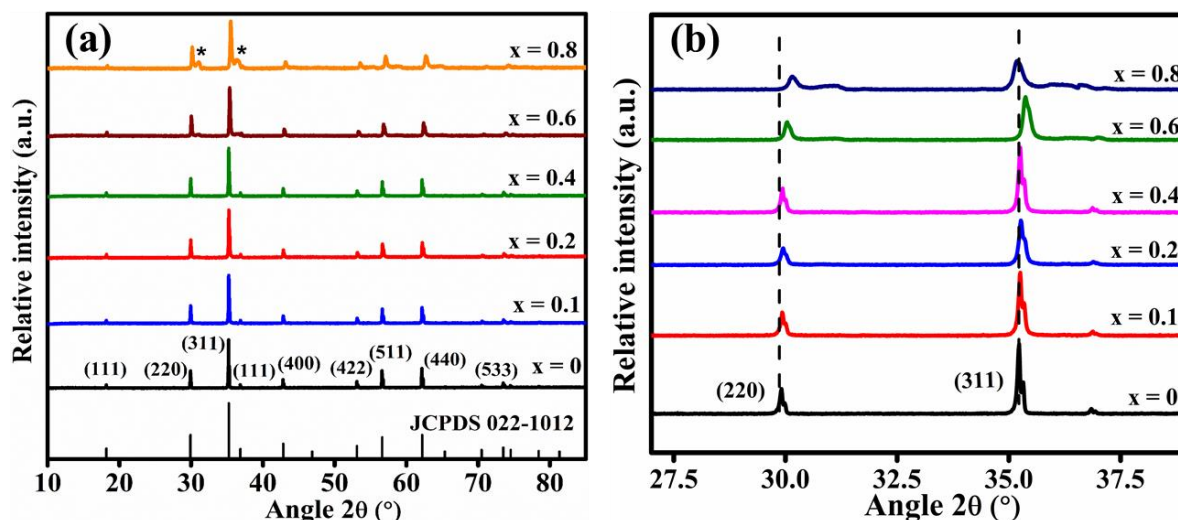
Fig. 4.3. (a) PXRD and (b) peak shift in PXRD of $ZnFe_{1-x}Al_xO_4$ ($0 \leq x \leq 0.8$)

The crystal structure modification due to Al^{3+} doping was understood through Rietveld refinement analysis of the composition $ZnFe_{1.9}Al_{0.1}O_4$. The refined XRD pattern with Rp factor 3.6%, and corresponding crystal structure were shown in **Fig. 4.4**, and the obtained crystallographic data was tabulated in **Table 4.3**. Calculated bond length and bond angle revealed that Zn^{2+} and Fe^{3+} exists in a nearly perfect tetrahedral and octahedral geometries, respectively, in the $ZnFe_2O_4$ structure. However, after Al^{3+} substitution, Fe-O bond length in FeO_6 structure was significantly reduced. This created a compression in the FeO_6 octahedra resulting in a structural distortion, **Fig. 4.4c**. This reduction in bond length eventually became the root cause of the compressive strain throughout the $ZnFe_{1.9}Al_{0.1}O_4$ crystal structure.
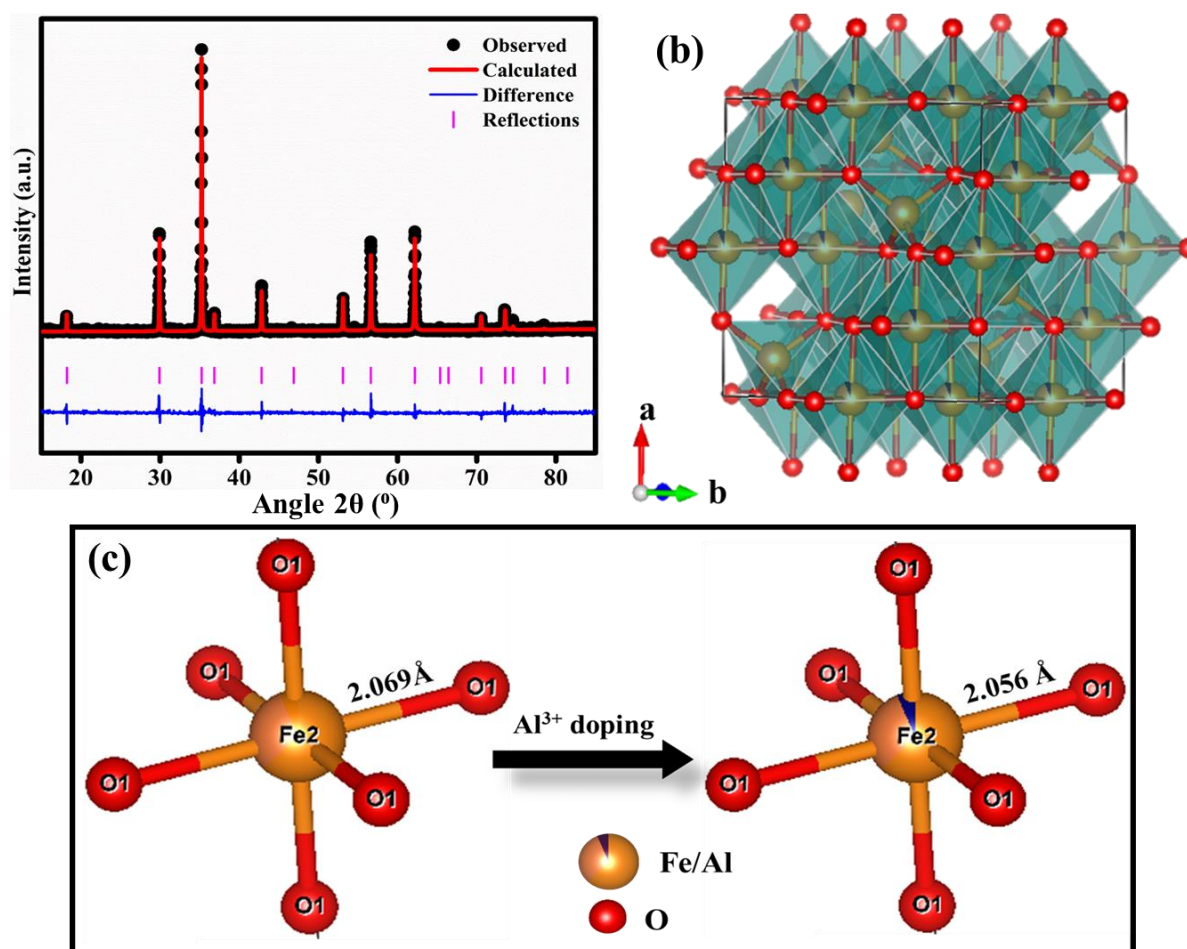
Fig. 4.4. (a) Rietveld refined XRD pattern and (b) crystal structure of $ZnFe_{1.9}Al_{0.1}O_4$, (c) bond length variation in FeO_6 octahedron after Al^{3+} doping

Table 4.3. Crystallographic data and structural parameters of $ZnFe_{1.9}Al_{0.1}O_4$

		x	y	z	Occupancy		
$ZnFe_2O_4$	Fe1	0.1250	0.1250	0.1250	0.621		O1-Zn2-O1 = 109.47(16)
	Zn1	0.1250	0.1250	0.1250	0.379	Zn-O = 1.868	
	Fe2	0.5000	0.5000	0.5000	0.689		O1-Fe2-O1 = 91.64(11)
	Zn2	0.5000	0.5000	0.5000	0.311	Fe-O = 2.069	O1-Fe2-O1 = 88.36(11)
	O1	0.2535	0.2535	0.2535	1.000		
$ZnFe_{1.9}Al_{0.1}O_4$	Fe1	0.1250	0.1250	0.1250	0.621		
	Zn1	0.1250	0.1250	0.1250	0.379		O1-Zn2-O1 = 109.4712(0)
	Fe2	0.5000	0.5000	0.5000	0.620	Zn-O = 1.89083	
	Zn2	0.5000	0.5000	0.5000	0.311		O1-Fe2-O1 = 92.4098(0)
	O1	0.2551	0.2551	0.2551	1.000	Fe-O = 2.05585	O1-Fe2-O1 = 87.5902(0)
	Al1	0.5000	0.5000	0.5000	0.069		

4.4.2. Morphology and particle size analysis

The SEM images of $ZnFe_2O_4$ and $ZnFe_{1.9}Al_{0.1}O_4$ pigment samples were illustrated in **Fig. 4.5a, d**. Both micrographs show particles of irregular morphology with little agglomeration. The $ZnFe_2O_4$ possess smooth surface particles, whereas Al^{3+} doping resulted in slightly rough surface particles. In addition, the observed microparticles were nearly uniform in size with relatively narrow size distribution. ZnF_2O_4 exhibited a size distribution of 0.9-1.8 μm, whereas, comparably smaller particles with narrower size distribution 0.2-1 μm, was noted for $ZnFe_{1.9}Al_{0.1}O_4$, **Fig. 4.5b, e**. The EDS analysis confirmed the presence of constituent elements Zn, Fe, Al and O. Further, the elemental compositions of $ZnFe_2O_4$ and $ZnFe_{1.9}Al_{0.1}O_4$ determined by EDS analysis showed close agreement with calculated values, **Fig. 4.5c, f** inset.
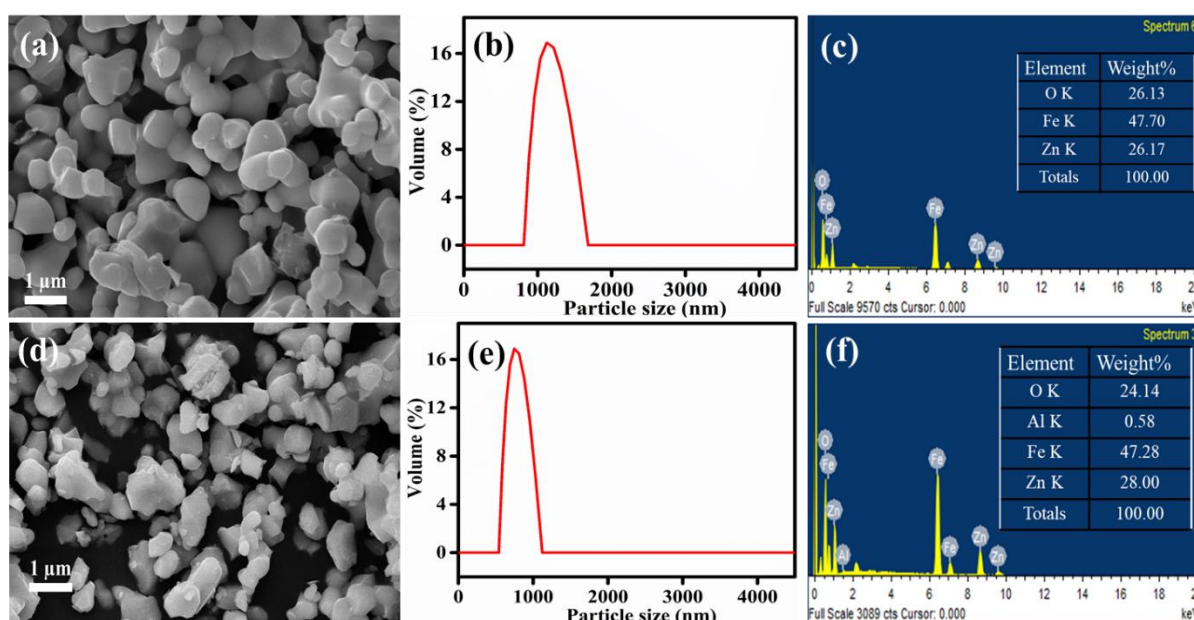
Fig. 4.5. (a, d) SEM images, (b, e) DLS curves, (c, f) SEM-EDS of $ZnFe_2O_4$ and $ZnFe_{1.9}Al_{0.1}O_4$, respectively

Morphology and size distribution from TEM images, shown in **Fig. 4.6a, d**, were consistent with SEM results. $ZnFe_2O_4$ displayed a broad particle size distribution, meanwhile it was narrowed down after Al^{3+} doping, **Fig. 4.6b, e**. In addition, average particle size was also reduced after the doping process, from ~1 to 0.5 μm. The HRTEM images in **Fig. 4.6c, f**, displayed the highly ordered lattice fringes. The d-spacing measured for the lattice planes (220), (311) and (400) of $ZnFe_{1.9}Al_{0.1}O_4$, was found to be smaller than that of $ZnFe_2O_4$. It validated the unit cell shrinkage observed in the $ZnFe_{1.9}Al_{0.1}O_4$ lattice as a result of Al^{3+} substitution. Because the dopant insertion disrupted the host crystal lattice, the particle growth was affected, giving rise to smaller particles.
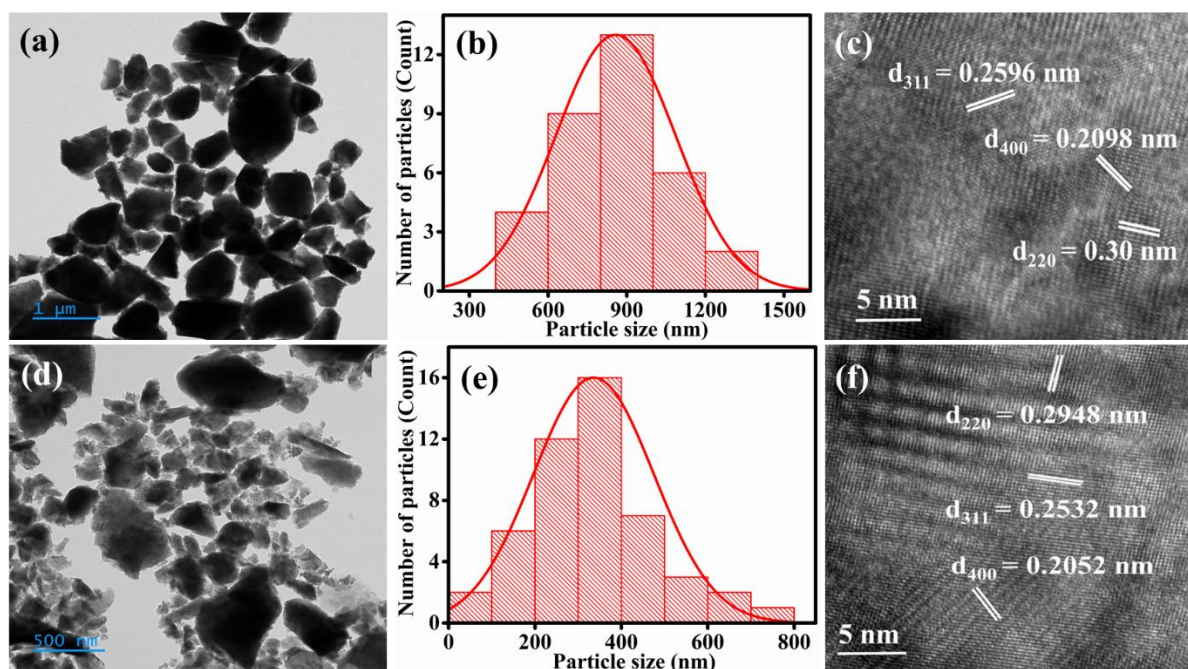
Fig. 4.6. (a, d) TEM images, (b, e) particle size distribution curves, and (c, f) HRTEM images of $ZnFe_2O_4$ and $ZnFe_{1.9}Al_{0.1}O_4$, respectively

4.4.3. Optical and chromatic properties

Optical properties of the pigment series $ZnFe_{2-x}Al_xO_4$ ($0 \leq x \leq 0.8$) were investigated by UV-Vis-NIR absorption spectroscopy. The resulting absorption spectra in **Fig. 4.7a**, displayed three major absorptions at 200-655 nm, 685-935 and 988-1417 nm region. The intense broad peak at 200-655 nm is a combination of two absorption bands having λ_{max} at 293 and 423 nm. The absorption lies in UV region correspond to the charge transfer transitions involving Zn^{2+} orbitals[5]. Further, strong absorption at high energy part of the visible spectrum was originated from $O_{2p} \rightarrow Fe_{3d}$ charge transfer transition, **Fig. 4.7b** [5, 32-34]. Starting from the UV region, the absorption edge extended to orange colour in the visible spectrum, leaving the entire low energy red rays to get reflected. The remaining absorptions at 785 and 1182 nm were attributed to intra-atomic d-d transitions in Fe^{3+}. However, according to Tanabe-Sugano diagram, all the d-d transitions from Fe^{3+} high-spin d^5 electronic configuration in an octahedral field are both spin and Laporte forbidden. Hence, intensity of these absorptions is found to be very low in comparison to the charge transfer transition. The forbidden transitions correspond to the peaks at 785 and 1182 nm are $^6A_{1g} \rightarrow {}^4T_{1g}$ and $^6A_{1g} \rightarrow {}^4T_{2g}$, respectively [5, 32-34].
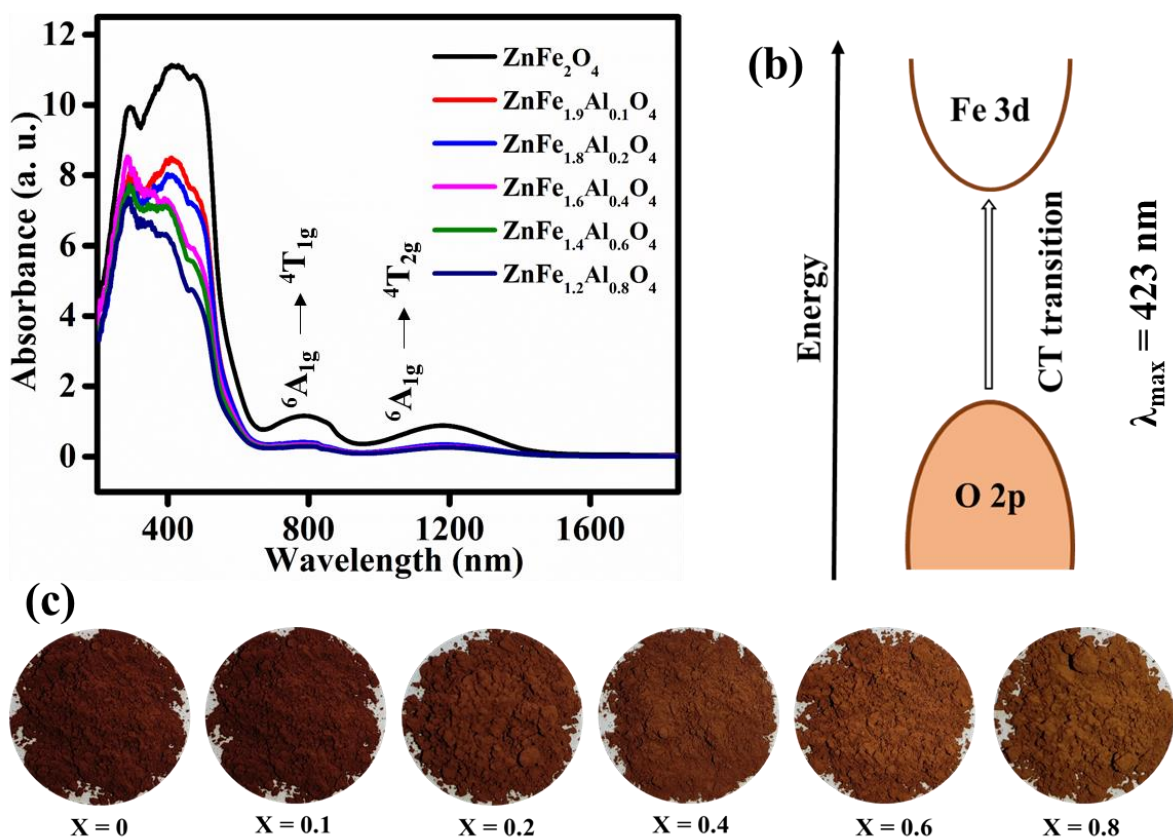
Fig. 4.7. (a) UV-Vis-NIR absorption spectra, (b) schematic representation of charge transfer transition and (c) photographs of $ZnFe_{2-x}Al_xO_4$ ($0 \leq x \leq 0.8$)

When Al^{3+} replaced Fe^{3+}, intensity of the absorption profile reduced due to a drop in chromophore concentration and the colour dilution effect caused by the dopant. Further detailed analysis revealed that compared to 293 nm peak, the absorption associated with Fe^{3+} (423, 785 and 1182 nm) exhibited a significant intensity drop. Apart from which, the absorption due to charge transfer transition in chromophore was slightly blue shifted with increase in Al substitution. It must be related to the structural strain imposed during the doping process.

Table 4.4. Colour comparison of $ZnFe_{1.9}Al_{0.1}O_4$ with literature reports

Sample	L^*	a^*	b^*	R^* (%)	Ref.
$LaFe_{0.9}Al_{0.1}O_3$	63.16	13.87	27.58	-	9
$Zn_{0.9}Mg_{0.1}Fe_2O_4$	48.06	14.16	9.91	51	10
$Zn_{0.9}Ni_{0.1}Fe_2O_4$	31.75	18.43	12.18	61	11
5 wt% Pr doped $ZnFe_2O_4$	39.7	26.1	25.9	60.1	34
$Zn_{0.7}Ni_{0.3}Fe_2O_4$	43	17	20	-	35
$MgFe_2O_4$	45.19	20.26	26.74	-	36
$ZnFe_2O_4$	37.34	15.04	11.67	-	36
$BiFeO_3$/mica titania	53.42	15.87	21.06	57.3	37
$Bi_{0.8}La_{0.2}FeO_3$	42.35	17.96	22.13	-	38
$La_{0.3}Bi_{0.35}Tb_{0.35}YO_3$	55.34	14.92	23.14	78.7	39
$Bi_{0.85}Sr_{0.15}FeO_3$	45.57	20.38	26.23	-	40
$Cu_{0.9}Mn_{0.1}Al_2O_4$	50.14	11.54	13.08	-	41
$La_2Ce_{1.8}Pr_{0.2}O_7$	54.29	16.16	19.18	84	42
Ce: Pr: Fe - 2: 0.2: 0.1	41.03	18.89	17.13	82.7	43
$SrY_{0.8}Ce_{1.2}O_4$	42.8	19.7	36.5	-	44
$Ba_4Zn_{0.5}Mn_{1.5}Fe_{36}O_{60}$	27.81	21.11	9.67	-	45
$ZnFe_{1.9}Al_{0.1}O_4$	**46.54**	**25.05**	**31.01**	**58**	**Present study**

The CIE 1976 $L^*a^*b^*$ colour parameters of the pigment series was summarized in **Table 4.2**. The combination of parameters a^* (red) and b^* (yellow) determined the intense brown colour of the pigment series, **Fig. 4.7c**. This observation was reinforced by hue angles closer to 45-50⁰ and high colour saturation. The brown colour intensity tend to decrease with increase in amount of Al^{3+} added, as indicated by the increase in L^* from 38 to 53. For $ZnFe_{1.9}Al_{0.1}O_4$, a^* and b^* increased in proportion to the base compound, resulting in improved colour strength. Later, a^* and b^* tend to decrease and increase, respectively, implying a drop in red tinge along with the rise in yellow. Fortunately, it did not end up in a colour change in the pigment series, rather than a gradual fading of brown tone.

4.4.4. Reflectance properties

Inorganic brown is a customary choice for buildings and roofs. But, being very dark shade, attaining a high NIR reflectance for brown pigment is always challenging. In an attempt to overcome this limitation, the new inorganic brown pigment series $ZnFe_{2-x}Al_xO_4$ ($0 \leq x \leq 0.8$)

was prepared. The NIR and NIR solar reflectance spectra of the pigment series was displayed in **Fig. 4.8a, b**. The base compound recorded 25 and 34%, NIR and NIR solar reflectance, respectively. When Al^{3+} replaced Fe^{3+}, a substantial improvement in the reflectance profile of the pigment series was monitored. It was able to increase the reflectance value R* up to 61% while maintaining the phase purity. The two forbidden transitions of Fe^{3+} in the NIR region are accountable for the low reflectance of $ZnFe_2O_4$. Intensity of these absorptions was marginally lowered by replacing Fe^{3+} with Al^{3+}, which resulted in an improvement in reflectance profile. Since colour strength is slightly fading with addition of Al^{3+}, $ZnFe_{1.9}Al_{0.1}O_4$ was chosen as the best composition in the pigment series. An enhancement in reflectance from 34 to 58% without losing the intense brown colour established the pigment $ZnFe_{1.9}Al_{0.1}O_4$ as an efficient 'cool' roof pigment for exterior coatings.
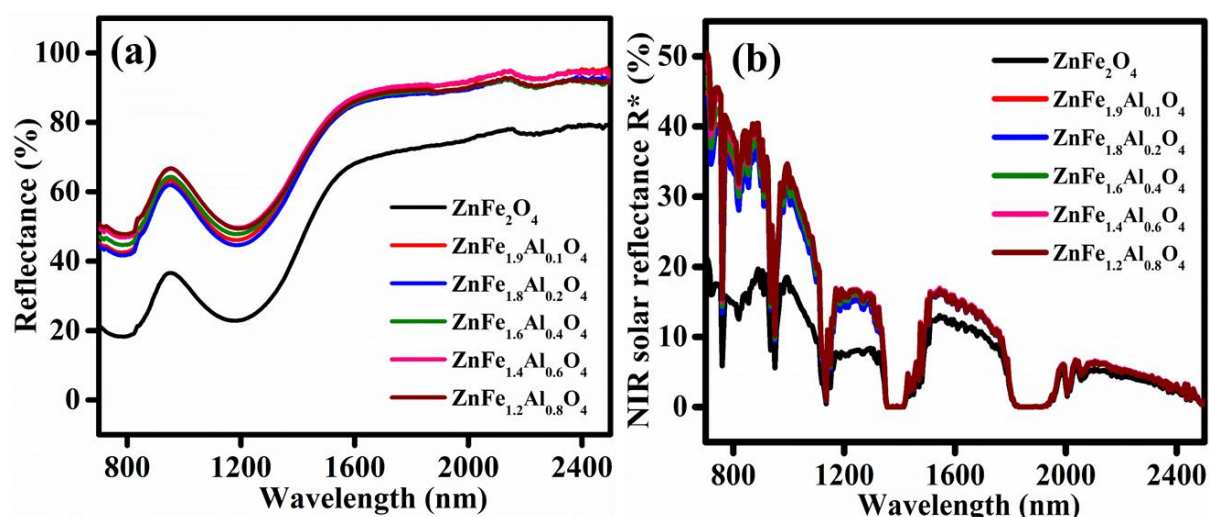
Fig. 4.8. (a) NIR reflectance, (b) NIR solar reflectance spectra of $ZnFe_{2-x}Al_xO_4$ ($0 \leq x \leq 0.8$)

Generally, a deep brown colour was defined as a^* and b^* nearly in 1:1 ratio with $L^* < 50$. However, too low or too high L^* will affect the reflectance or colour strength of the pigment, respectively. As a result, high magnitude a^* and b^*, L^* just below 50 will be ideal for an intense brown tone. Comparative colour analyses with some of the reported pigments were shown in **Table 4.4**,[9-11, 34-45]. Because of the high magnitude colour co-ordinates of suitably maintained proportion, $ZnFe_{1.9}Al_{0.1}O_4$ is undoubtedly the best candidate over the other compositions. Most of the pigments described in **Table 4.4** obtained high reflectance by sacrificing colour strength. Unlike others, $ZnFe_{1.9}Al_{0.1}O_4$ was able to achieve a comparatively high $R^* = 58\%$ with no colour fade.

4.4.5. Applications

The stability of the synthesized pigment was analyzed in different aggressive media, such as acid, base, and water. A pre-weighed pigment sample was vigorously stirred for 1 h in different media, subsequently dried, weighed and measured the colour property, **Table 4.5**. There was no significant colour difference between the pre-treated and treated samples, and the estimated ΔE^*_{ab} did not deviate from unity. Hence, the pigment stability has been validated [46, 47].

Table 4.5. Colour coordinates of $ZnFe_{1.9}Al_{0.1}O_4$ after acid/alkali treatment

Sample	pH	L^*	a^*	b^*	c^*	h^o	ΔE^*_{ab}
$ZnFe_{1.9}Al_{0.1}O_4$	-	46.54	25.05	31.01	39.86	51.06	-
Water	6.6	46.51	24.96	30.94	39.75	51.11	0.12
HNO_3	3.0	45.79	24.39	30.55	39.09	51.39	1.09
NaOH	10.5	45.92	24.21	30.71	39.11	51.74	1.08
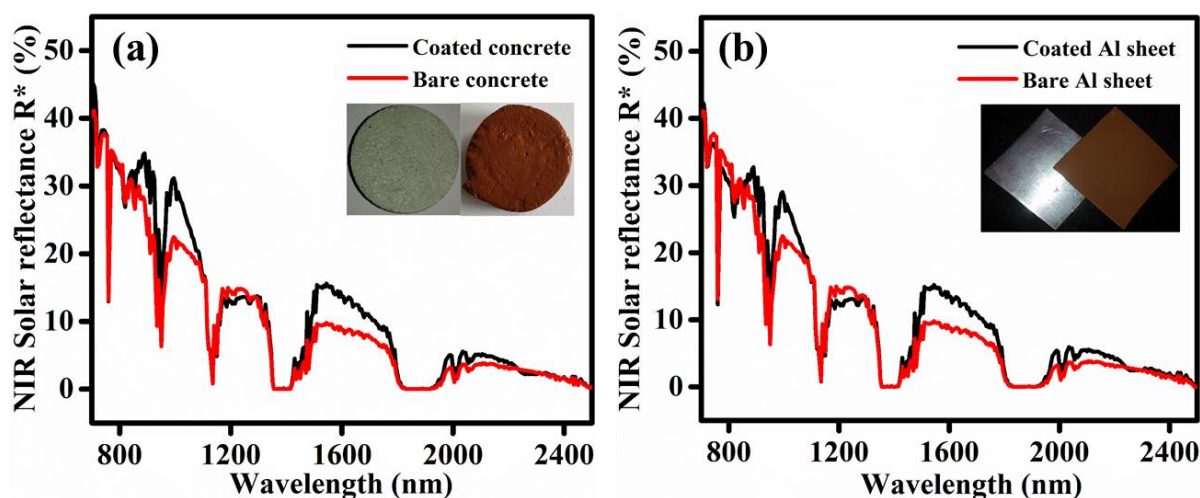
Fig. 4.9. Comparison in NIR solar reflectance spectra of $ZnFe_{1.9}Al_{0.1}O_4$ coatings on (a) concrete block and (b) Al sheet with their bare surfaces

Colour deliverability is another issue for most inorganic pigments, thus it was established through developing coatings on conventional building substrates. The pigment emulsion was brush coated over concrete block and Al sheet, which were then dried and analyzed for colour and reflectance properties. Obtained results were tabulated in **Table 4.6** and solar reflectance graphs were illustrated in **Fig. 4.9a, b**. Dark colours, in general, suffer from severe colour deterioration while coating. But, in the case of $ZnFe_{1.9}Al_{0.1}O_4$, the coatings seemed brighter than the pigment powder, as evidenced by an increase in L^*. Furthermore, calculated colour

parameters and solar reflectance revealed no substantial decline in colour strength or reflectance. Thus, it is unquestionably an outstanding choice as a replacement for the current brown pigment in the market.

Table 4.6. Colour coordinates and reflectance of pigment coatings

Sample	L^*	a^*	b^*	c^*	h^o	NIR (%) at 1100 nm	R^* (%)
$ZnFe_{1.9}Al_{0.1}O_4$	46.54	25.05	31.01	39.86	51.06	50	58
Concrete	57.75	20.50	32.67	38.56	57.89	44	50
Al sheet	49.71	21.41	31.79	38.33	56.04	42	52

4.4.6. Temperature shielding performance

The improved reflectance property of $ZnFe_{1.9}Al_{0.1}O_4$ over $ZnFe_2O_4$, enforced to carry out the temperature shielding experiment. The pigment coatings with thickness of 200-250 µm was employed for roofing foam boxes. The temperature against time plot for the experiment exhibited an abrupt rise in interior temperature during the initial 20 minutes followed by stabilization, **Fig 4.10a, b**. Apparently due to immediate IR absorption and heat transfer to the interior at the beginning and subsequent equilibration of the process. After 1 h of experiment it was delighted to observe nearly 2.5 ℃ drop in temperature beneath the $ZnFe_{1.9}Al_{0.1}O_4$ coated roof.
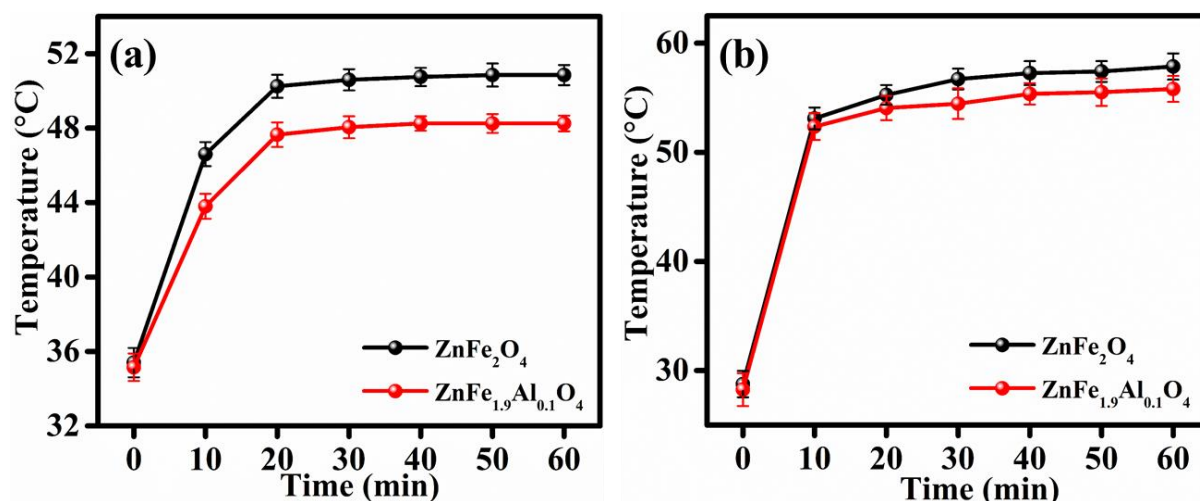
Fig. 4.10. Comparison in (a) interior temperature and (b) surface temperature build up between $ZnFe_2O_4$ and $ZnFe_{1.9}Al_{0.1}O_4$ coatings roofed foam box

A very similar trend was observed in the case of surface temperature build-up. Thermal images of the coating surfaces were illustrated in **Fig. 4.11**. The temperature versus time plot

in **Fig. 4.10b**, showed ~2.5 °C reduction in temperature on $ZnFe_{1.9}Al_{0.1}O_4$ coating surface when compared to $ZnFe_2O_4$. Overall, $ZnFe_{1.9}Al_{0.1}O_4$ coating is extremely beneficial in reducing the heat generation caused by NIR rays. Therefore, switching from traditional brown to new cool brown coating can have a great impact on energy conservation in large constructions.
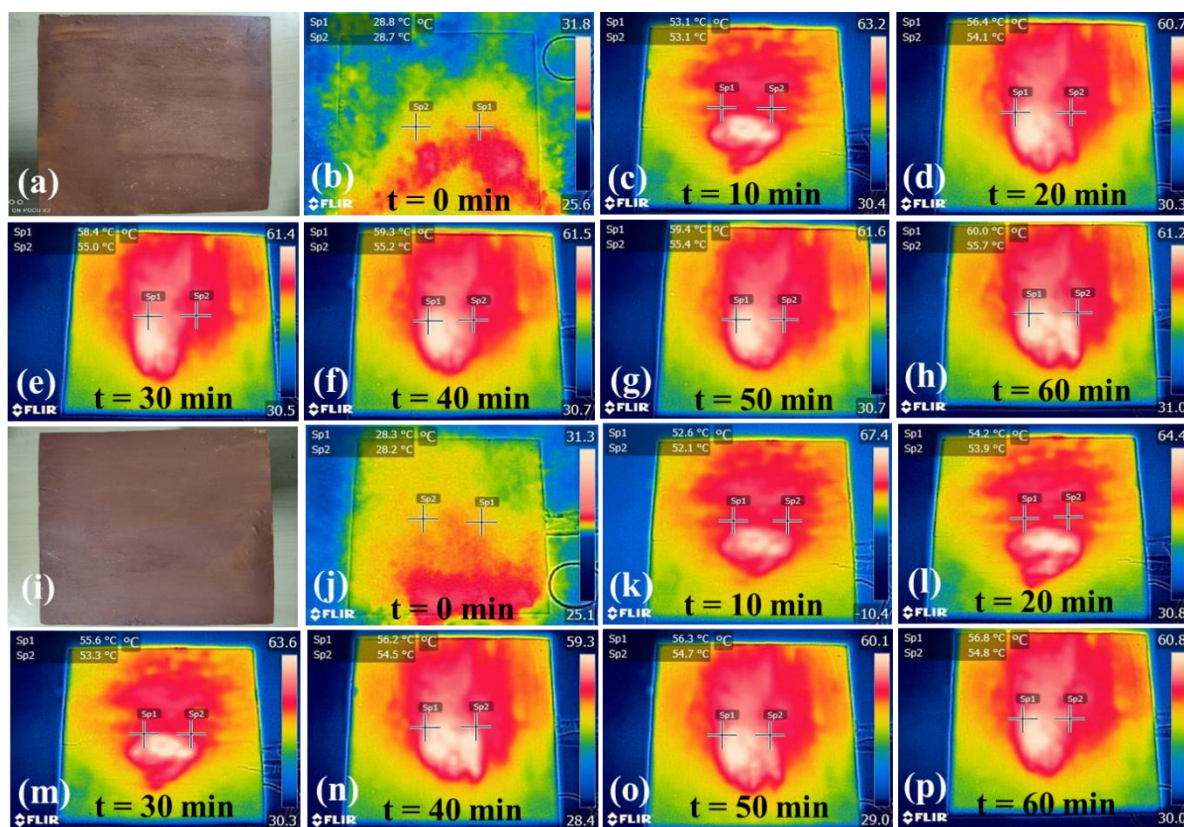
Fig. 4.11. Photographs of (a) commercial brown and (i) $ZnFe_{1.9}Al_{0.1}O_4$ coatings on Al sheet, thermal images of (b-h) commercial brown and (j-p) $ZnFe_{1.9}Al_{0.1}O_4$ coatings

4.4.7. Anticorrosive studies

The corrosion resistance feature of the coating material has a significant impact on the stability of metal coatings. Unlike traditional duplex coating, which uses a reflective layer over an anticorrosive base, a single layer anticorrosive cool coating can substantially conserve energy, money and time. This motivated a thorough investigation of the anticorrosive property of the developed $ZnFe_{1.9}Al_{0.1}O_4$ brown inorganic pigment. Herein, the corrosion resistance of $ZnFe_{1.9}Al_{0.1}O_4$ was investigated on steel in marine medium. Epoxy coatings of thickness ~12 µm have been prepared with different pigment loadings (5, 10, 15, 20 and 25 wt%). Further, EIS experiments have been performed and respective Nyquist plots of bare epoxy and pigment incorporated epoxy coatings on steel in 3.5 wt% NaCl were shown in **Fig. 4.12**.
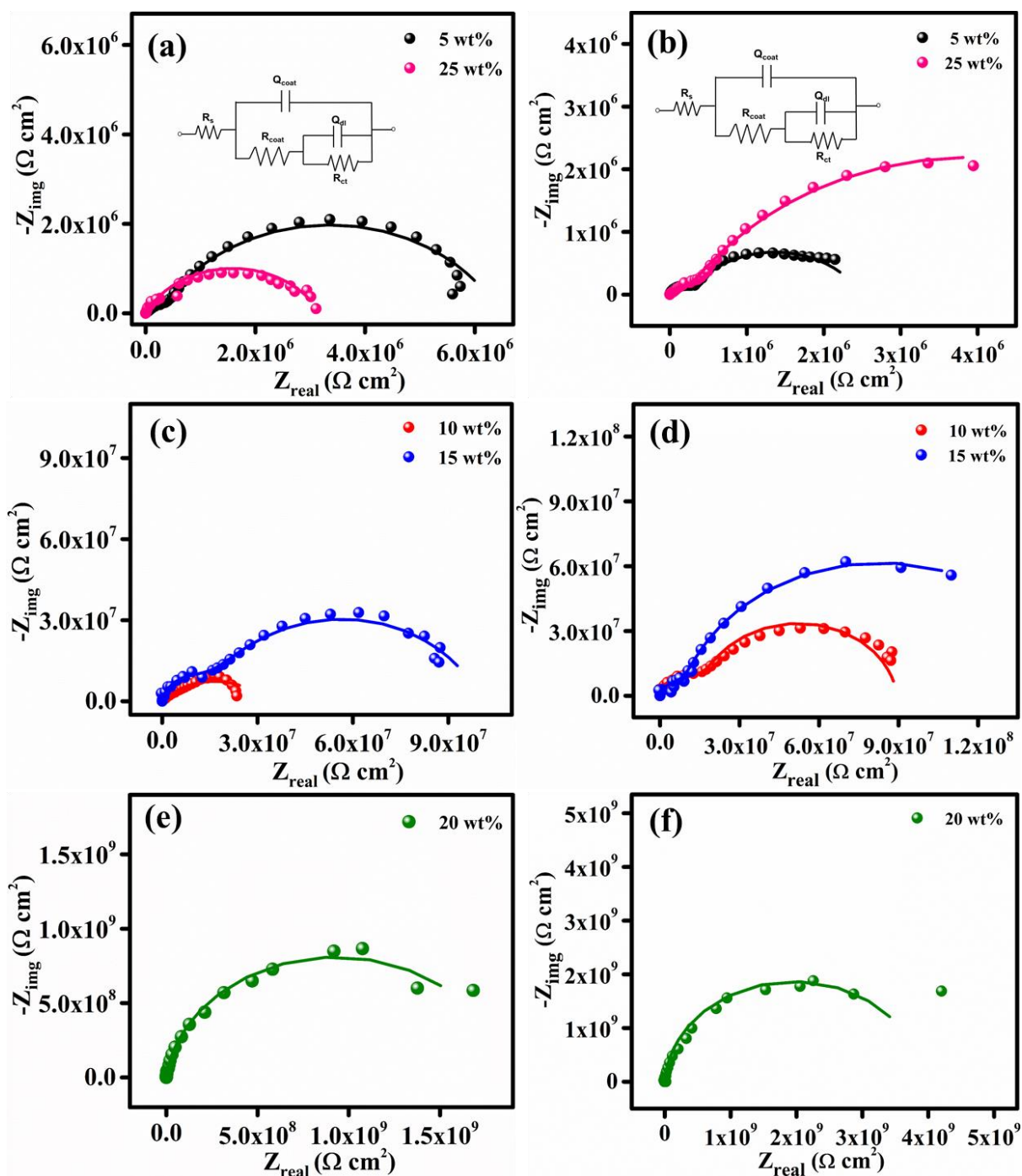
Fig. 4.12. Nyquist plots of (a, b) 5 and 25 wt% (EEC in inset), (c, d) 10 and 15 wt% and (e, f) 20 wt% $ZnFe_2O_4$ and $ZnFe_{1.9}Al_{0.1}O_4$ loaded epoxy coatings, respectively

The electrical equivalent circuit (EEC) used to fit all the impedance spectra of $ZnFe_2O_4$ and $ZnFe_{1.9}Al_{0.1}O_4$ epoxy coatings are [R_{coat}/ (Q_{coat} + Q_{dl}/ R_{ct})] shown inset of **Fig. 4.12a, b**. The electrochemical parameters from impedance fitting were tabulated in **Table 4.7**.

Table 4.7. EIS parameters from Nyquist plots

Sample	Pigment loading (wt%)	EIS parameters			
		R_{coat} (Ωcm^2)	Q_{coat} (μFcm^{-2})	R_{ct} (Ωcm^2)	Q_{dl} (μFcm^{-2})
$ZnFe_2O_4$	5	2.6×10^5	0.18	6.2×10^6	0.004
	10	1.3×10^6	0.34	3.1×10^7	0.002
	15	1.8×10^6	0.02	8.1×10^7	0.002
	20	6.7×10^4	0.008	1.9×10^9	0.008
	25	1.6×10^3	0.31	3.2×10^6	0.006
$ZnFe_{1.9}Al_{0.1}O_4$	5	2.8×10^5	0.14	2.8×10^6	0.03
	10	2.1×10^7	0.016	6.8×10^7	0.004
	15	1.3×10^7	0.06	1.4×10^8	0.011
	20	9.8×10^7	0.005	4.1×10^9	0.002
	25	2.2×10^5	0.23	7.4×10^6	0.03

The incorporation of pigment powder resulted in a substantial improvement in epoxy coat resistance on metal surface, of the order of 10^5 to 10^7 Ωcm^2. This suggests that the material has the potential to be used as an anticorrosive pigment. More information was gathered by evaluating the obtained R_{ct} values. Both the $ZnFe_2O_4$ and $ZnFe_{1.9}Al_{0.1}O_4$ pigments exhibited a similar trend in corrosion resistance, with the latter showing a slight improvement. The 5 wt% pigment loading gave rise to a one order increase in R_{ct} from 10^5 to 10^6 Ωcm^2. Further increase in loading up to 20 wt% demonstrated a consistent one order improvement in corrosion resistance. At 20 wt% loading, $ZnFe_2O_4$ and $ZnFe_{1.9}Al_{0.1}O_4$ had maximum $R_{ct} = 1.9 \times 10^9$ and 4.1×10^9 Ωcm^2, respectively, which dropped down to 10^6 Ωcm^2 at 25 wt%. The key conclusion from EIS results, is that synthesized ferrite pigments exhibit outstanding resistance against mild steel corrosion in marine medium. In addition, the trend in resistance value revealed a resistive mechanism that works best at 20 wt% loading.
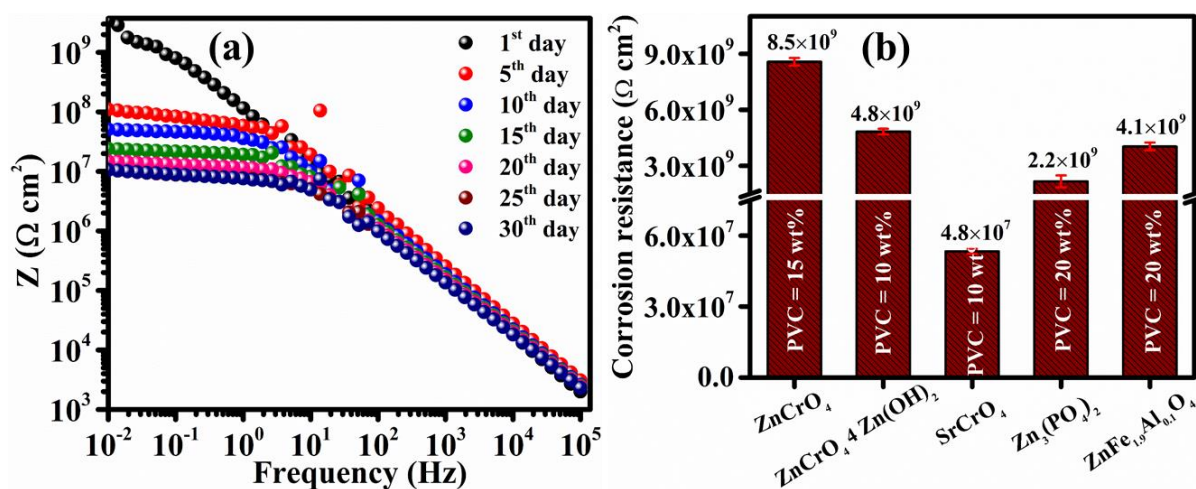
Fig. 4.13. (a) Bode plot of continuous one-month electrochemical study of 20 wt% $ZnFe_{1.9}Al_{0.1}O_4$ loaded epoxy coating, (b) comparison in corrosion resistance of $ZnFe_{1.9}Al_{0.1}O_4$ with commercial anticorrosive pigments

Table 4.8. EIS parameters from continuous electrochemical analysis

Sample	Corrosion resistance (Ωcm^2)						
	1st day	5th day	10th day	15th day	20th day	25th day	30th day
$ZnFe_{1.9}Al_{0.1}O_4$	4.1×10^9	1.1×10^8	5.1×10^7	2.4×10^7	1.4×10^7	1.1×10^7	1.1×10^7

A one-month continuous electrochemical investigation on steel in marine environment ensured the stability of 20 wt% pigment loaded coating. **Table 4.8** summarized the findings, while **Fig. 4.13a** depicted the Bode plot of the continuous analysis. From day 1 to day 10, the resistance value depleted in the order of one, 10^9 to 10^8 Ωcm^2, then 10^8 to 10^7 Ωcm^2. However, the resistance 10^7 Ωcm^2 remained persistent until the last day of the experiment, establishing stability of the anticorrosive coating. According to the literature, the stability of ferrite pigment coating is subjected to the production of a barely soluble passive hydroxide film on the metal surface during immersion in saline medium, which can operate as an inhibitive barrier and prevent corrosion[48]. Hence, XPS analysis was performed on the metal surface obtained after the continuous electrochemical analysis, to determine the presence of hydroxide inhibitive layer. Meanwhile, a comparative analysis in corrosion resistance of $ZnFe_{1.9}Al_{0.1}O_4$ with zinc and chromate based commercial anticorrosive pigments revealed to be quite promising, **Fig. 4.13b**. Though the critical pigment volume concentration is slightly on the higher side, replacing harmful chromium ions from the material composition while maintaining R_{ct} of the same order is invaluable, (**Table 4.9**).

Table 4.9. Corrosion resistance comparison with commercial pigments

Sample	CPVC (wt%)	EIS	
		R_{ct} (cm^2)	Q_{dl} (µFcm^{-2})
Zinc chromate (ZnCrO$_4$)	15	8.5×10^9	0.001
Zinc tetroxy chromate (ZnCrO$_4$. 4 Zn(OH)$_2$)	10	4.8×10^9	0.0015
Zinc phosphate (Zn$_3$(PO$_4$)$_2$)	20	2.2×10^9	0.002
ZnF$_{1.9}$Al$_{0.1}$O$_4$	20	4.1×10^9	0.002

4.4.8. XPS surface analysis

XPS surface analysis of coat removed steel strip provided a clear idea on the compounds formed beneath the pigment loaded epoxy coating. The presence of O, Zn, Fe, and Al elements were detected in the survey spectrum, **Fig. 4.14a**. High resolution deconvoluted XPS spectra of O1s, Zn2p and Fe2p were showed in **Fig. 4.14b-d**. In O1s spectrum, the binding energy peak at 531.1 eV belongs to iron oxyhydroxide (FeOOH) and 532.5 eV peak attributed to Zn(OH)$_2$ species. The Zn2p and Fe2p spectra, **Fig. 4.14c, d**, further confirmed the presence of Zn(OH)$_2$ and FeOOH with binding energy peaks at 1021.8 and 711.9 eV, respectively[49, 50].
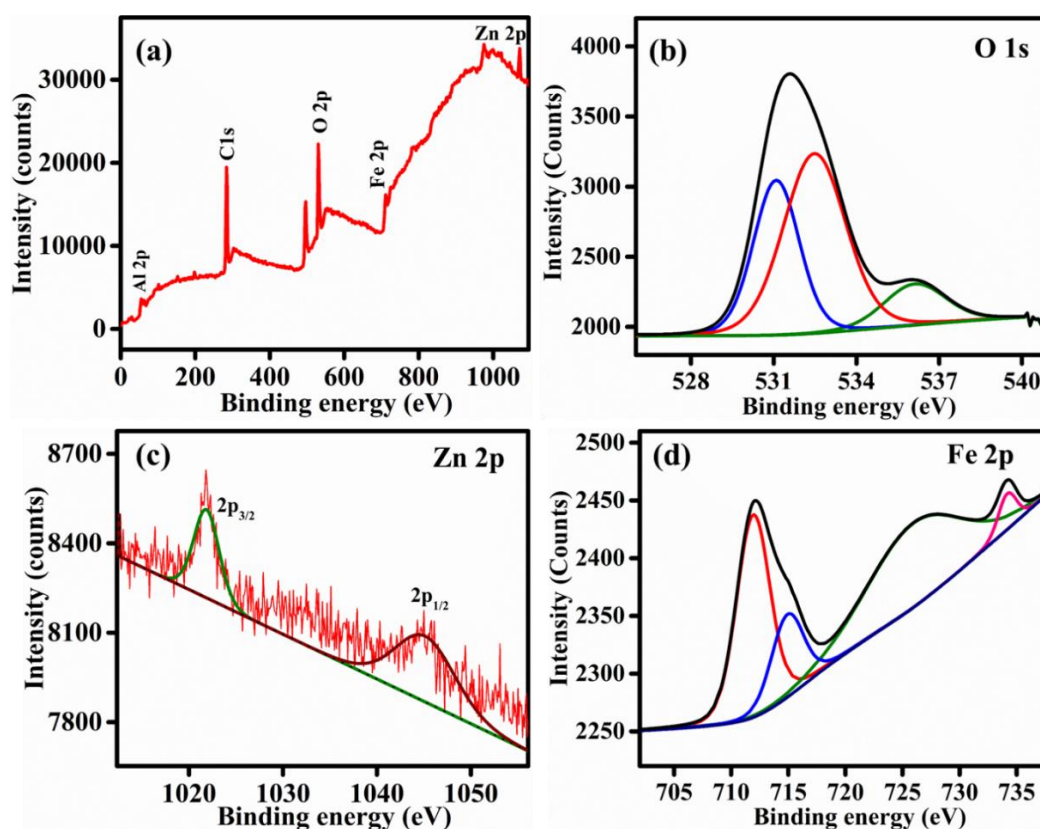
Fig. 4.14. XPS (a) survey spectrum, high resolution deconvoluted spectrum of (b) O1s, (c) Zn2p and (d) Fe2p of inhibitive film beneath the 20 wt% ZnFe$_{1.9}$Al$_{0.1}$O$_4$ loaded epoxy coat after continuous electrochemical analysis

Based on XPS results the corrosion inhibition mechanism involved in the prepared ferrite pigment loaded epoxy coating was explained as follows. The passive nature of the pigment buried in epoxy matrix initially serves to prevent the elecrolyte from reaching the metal surface. However, long-term interaction with NaCl solution triggers the resistive mechanism in the pigment by creating an alkaline environment at the metal-electrolyte interface. That is the hydroxyl ions generated at the cathode reacts with the metal ions in the ferrite pigment (Zn^{2+} and Fe^{3+}) to form corresponding metal hydroxides, (eq. 4.1-4.4).

$$\text{Anodic oxidation}: \mathbf{Fe \rightarrow Fe^{2+} + 2e^-} \tag{4.1}$$

$$\text{Cathodic reduction}: \mathbf{O_2 + 2H_2O + 4e^- \rightarrow 4OH^-} \tag{4.2}$$

$$\mathbf{Zn^{2+} + 2OH^- \rightarrow Zn(OH)_2} \quad \text{(slightly soluble)} \tag{4.3}$$

$$\mathbf{Fe^{3+} + 3OH^- \rightarrow Fe(OH)_3 \rightarrow FeOOH} \quad \text{(passive)} \tag{4.4}$$
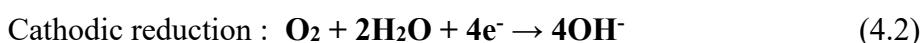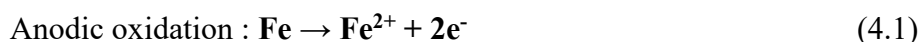
The sparingly soluble zinc hydroxide complex formed in between pigment coating and metal substrate inhibits corrosion reaction in chloride environment. This stable passivating barrier contributed to the remarkable corrosion resistance of $ZnFe_{1.9}Al_{0.1}O_4$. Furthermore, the synthesized ferrite pigment protects the steel surface by producing an amorphous passive FeOOH layer in combination with zinc hydroxide[48, 51, 52]. Therefore, both $Zn(OH)_2$ and FeOOH production subsidize to the anticorrosive mechanism of $ZnFe_{1.9}Al_{0.1}O_4$, **Fig. 4.15**. This qualifies it as an efficient candidate for protecting steel from marine corrosion.
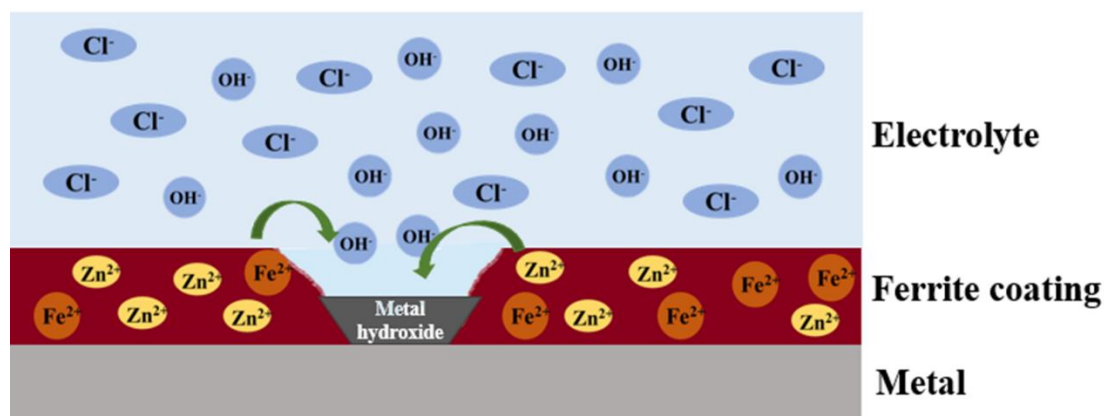
Fig. 4.15. Anticorrosive mechanism in $ZnFe_{1.9}Al_{0.1}O_4$ epoxy coating

4.5. Conclusions

A low-cost multifunctional brown inorganic pigment was synthesized based on Al^{3+} substituted $ZnFe_2O_4$. The best composition, $ZnFe_{1.9}Al_{0.1}O_4$, in the pigment series, $ZnFe_{2-x}Al_xO_4$ ($0 \leq x \leq 0.8$), exhibited colour co-ordinates, $a^* = 25.05$, $b^* = 31.01$ and NIR reflectance $R^* = 58\%$, which is higher than the reported brown pigments. Al^{3+} substitution at the Fe^{3+} site brought reduced Fe-O bonds in FeO_6 octahedra, resulting in unit cell shrinkage, thereby lattice distortion, and a decrease in crystallinity and crystal symmetry. The charge transfer transition $O_{2p} \rightarrow Fe_{3d}$ and d-d forbidden transitions in Fe^{3+} chromophore were responsible for the brown colour of the pigment. Temperature reduction of approximately 2.5 ℃ was achieved for $ZnFe_{1.9}Al_{0.1}O_4$ over $ZnFe_2O_4$ coating, confirming the potential of the pigment as a cool colourant. Under marine conditions, the anticorrosive performance ($R_{ct} = 4.1 \times 10^9$ Ωcm^2) of the pigment was appreciably higher than the toxic chrome pigments with respectable stability. The passivating $Zn(OH)_2$ and FeOOH layers formed at the metal electrolyte interface deploy the inhibitive mechanism involved in the pigment epoxy coating. Therefore, the new multifunctional pigment could be an efficient replacement for commercial brown pigment.

4.6. References

1. Chand, P.; Vaish, S.; Kumar, P. J. P. B. C. M., Structural, optical and dielectric properties of transition metal (MFe_2O_4; M = Co, Ni and Zn) nanoferrites. **2017,** *524*, 53-63.

2. Li, Y.; Ma, Y.; Wang, Z.; Liu, H.; Wang, X.; Wei, H.; Zeng, S.; Yi, N.; Cheng, G. J. J. S. E., A promising inorganic $YFeO_3$ pigments with high near-infrared reflectance and infrared emission. **2021,** *226*, 180-191.

3. Sangwong, N.; Suwan, M.; Supothina, S. J. M. T. P., Effect of calcination temperature and dolomite or Al_2O_3 doping on properties of NIR– reflective $CoFe_2O_4$ black pigment. **2019,** *17*, 1595-1601.

4. Elias, M.; Chartier, C.; Prévot, G.; Garay, H.; Vignaud, C. J. M. S.; B, E., The colour of ochres explained by their composition. **2006,** *127* (1), 70-80.

5. Pailhé, N.; Wattiaux, A.; Gaudon, M.; Demourgues, A. J. J. o. S. S. C., Correlation between structural features and vis – NIR spectra of α-Fe_2O_3 hematite and AFe_2O_4 spinel oxides (A= Mg, Zn). **2008,** *181* (5), 1040-1047.

6. Jeevanandam, P.; Mulukutla, R.; Phillips, M.; Chaudhuri, S.; Erickson, L.; Klabunde, K. J. T. J. o. P. C. C., Near infrared reflectance properties of metal oxide nanoparticles. **2007,** *111* (5), 1912-1918.

7. Balamurugan, S.; Brightlin, B.; Sherly Arputha Kiruba, V. J. J. o. N.; Nanotechnology, Synthesis of $BaFe_{12}O_{19}$ materials by mechano-thermal route: novel inorganic pigment with high near-infrared reflectance. **2015,** *15* (12), 9494-9499.

8. Sangwong, N.; Suwan, M.; Supothina, S., Synthesis and Optical Band Gap Study of NIR-Reflective $CoFe_2O_4$ Black Pigments Doped with MgO, CaO and Al_2O_3. **2020**.

9. Liu, L.; Han, A.; Ye, M.; Zhao, M. J. S. E. M.; Cells, S., Synthesis and characterization of Al^{3+} doped $LaFeO_3$ compounds: a novel inorganic pigments with high near-infrared reflectance. **2015,** *132*, 377-384.

10. Liu, L.; Han, A.; Ye, M.; Feng, W. J. S. E., The evaluation of thermal performance of cool coatings colored with high near-infrared reflective nano-brown inorganic pigments: Magnesium doped $ZnFe_2O_4$ compounds. **2015,** *113*, 48-56.

11. Suwan, M.; Sangwong, N.; Supothina, S. J. C. S., Effect of Ni doping and synthesis temperature on the properties of NIR-reflective $ZnFe_2O_4$ black pigments. **2020,** *64* (2), 172-179.

12. Elakkiya, V.; Sumathi, S. J. J. o. A.; Compounds, Ce and Fe doped gahnite: cost effective solar reflective pigment for cool coating applications. **2020,** *820*, 153174.

13. Kalendová, A.; Ryšánek, P.; Nechvílová, K. J. P. i. O. C., Investigation of the anticorrosion efficiency of ferrites $Mg_{1-x}Zn_xFe_2O_4$ with different particle morphology and chemical composition in epoxy-ester resin-based coatings. **2015,** *86*, 147-163.

14. Emira, H. J. A.-c. m.; materials, Effect of PVC/CPVC ratio of non-toxic, platy pigments on corrosion protection of acrylic-modified alkyd coatings. **2006,** *53* (4), 224-231.

15. Kalendova, A.; Veselý, D. J. A.-C. M.; Materials, Needle-shaped anticorrosion pigments based on the ferrites of zinc, calcium and magnesium. **2007,** *54* (1), 3-15.

16. Mahvidi, S.; Gharagozlou, M.; Mahdavian, M.; Naghibi, S. J. M. R., Potency of $ZnFe_2O_4$ nanoparticles as corrosion inhibitor for stainless steel; the pigment extract study. **2017,** *20*, 1492-1502.

17. Mahvidi, S.; Gharagozlou, M.; Mahdavian, M.; Naghibi, S. J. P. i. C., Colorants; Coatings, Anticorrosive Performance of polyester – melamine coating fortified with Zinc Ferrite nanoparticles. **2019,** *12* (1), 57-70.

18. Ahmed, N.; Fathi, A.; Mohamed, M.; Abd El-Gawad, W. J. P. i. O. C., Evaluation of new core-shell pigments on the anticorrosive performance of coated reinforced concrete steel. **2020,** *140*, 105530.

19. Thejus, P.; Krishnapriya, K.; Nishanth, K. J. S. E. M.; Cells, S., A cost-effective intense blue colour inorganic pigment for multifunctional cool roof and anticorrosive coatings. **2021,** *219*, 110778.

20. Thejus, P.; Krishnapriya, K.; Nishanth, K. J. S. E., NIR reflective, anticorrosive magenta pigment for energy saving sustainable building coatings. **2021,** *222*, 103-114.

21. Zhao, X.; Zhang, Y.; Huang, Y.; Gong, H.; Zhao, J. J. D.; Pigments, Synthesis and characterization of neodymium doped yttrium molybdate high NIR reflective nano pigments. **2015,** *116*, 119-123.

22. Yuan, L.; Han, A.; Ye, M.; Chen, X.; Yao, L.; Ding, C. J. D.; Pigments, Synthesis and characterization of environmentally benign inorganic pigments with high NIR reflectance: lanthanum-doped $BiFeO_3$. **2018,** *148*, 137-146.

23. Kavitha, K.; Sivakumar, A. J. I. C. C., Impact of titanium concentration in structural and optical behaviour of nano $Bi_2Ce_{2-x}Ti_xO_7$ (x = 0–1) high NIR reflective and UV shielding yellow and orange pigments. **2020,** *120*, 108163.

24. Zhou, W.; Ye, J.; Zhuo, S.; Yu, D.; Fang, P.; Peng, R.; Liu, Y.; Chen, W. J. J. o. A.; Compounds, Synthesis and characterization of novel yellow-green Al-doped $Y_3Fe_5O_{12}$ nano-pigments with high NIR reflectance. **2022,** *896*, 162883.

25. Shannon, R. D. J. A. c. s. A. c. p., diffraction, theoretical; crystallography, g., Revised effective ionic radii and systematic studies of interatomic distances in halides and chalcogenides. **1976,** *32* (5), 751-767.

26. Idrees, M.; Nadeem, M.; Siddique, M. J. C. a. p., Role of holes states on metal to insulator transition and collapse of magnetic ordering in $LaFe_{1-x}Ni_xO_3$ (x= 0.0–0.5). **2013**.

27. Ahmed, M.; Okasha, N.; Hussein, B. J. J. o. a.; compounds, Synthesis, characterization and studies on magnetic and electrical properties of $LaAl_yFe_{1-y}O_3$ nanomultiferroic. **2013,** *553*, 308-315.

28. Pal, M.; Pal, U.; Jiménez, J. M. G. Y.; Pérez-Rodríguez, F. J. N. r. l., Effects of crystallization and dopant concentration on the emission behavior of TiO_2: Eu nanophosphors. **2012,** *7*, 1-12.

29. Prabakar, K.; Venkatachalam, S.; Jeyachandran, Y.; Narayandass, S. K.; Mangalaraj, D. J. S. e. m.; cells, s., Optical constants of vacuum evaporated $Cd_{0.2}Zn_{0.8}Te$ thin films. **2004,** *81* (1), 1-12.

30. Murali, K.; Kalaivanan, A.; Perumal, S.; Pillai, N. N. J. J. o. A.; Compounds, Sol–gel dip coated CdO: Al films. **2010,** *503* (2), 350-353.

31. Anantharamaiah, P.; Mondal, S.; Manasa, K.; Saha, S.; Pai, M. J. C. I., Enhancing the catalytic activity of recyclable nanocrystalline $NiFe_2O_4$ by replacing Ni by Cu. **2020,** *46* (1), 1220-1226.

32. Lv, H.; Ma, L.; Zeng, P.; Ke, D.; Peng, T. J. J. o. M. C., Synthesis of floriated $ZnFe_2O_4$ with porous nanorod structures and its photocatalytic hydrogen production under visible light. **2010,** *20* (18), 3665-3672.

33. Wang, L.; Zhou, Q.; Li, F. J. p. s. s., Ionic disorder and yaffet–kittel angle in nanoparticles of $ZnFe_2O_4$ prepared by sol-gel method. **2004,** *241* (2), 377-382.

34. Suwan, M.; Sangwong, N.; Supothina, S. In Effect of Co and Pr doping on the properties of solar-reflective $ZnFe_2O_4$ dark pigment, IOP Conference Series: Materials Science and Engineering, IOP Publishing: 2017; p 012003.

35. Sutka, A.; Borisova, A.; Kleperis, J.; Mezinskis, G.; Jakovlevs, D.; Juhnevica, I. J. J. o. t. A. C. S., Effect of nickel addition on colour of nanometre spinel zinc ferrite pigments. **2012,** *48* (2), 150-155.

36. Xavier, C.; Candeia, R.; Bernardi, M.; Lima, S.; Longo, E.; Paskocimas, C.; Soledade, L.; Souza, A.; Santos, I. J. J. o. T. A.; Calorimetry, Effect of the modifier ion on the properties of $MgFe_2O_4$ and $ZnFe_2O_4$ pigments. **2007,** *87* (3), 709-713.

37. Yuan, L.; Han, A.; Ye, M.; Chen, X.; Ding, C.; Yao, L. J. C. I., Synthesis and characterization of novel nontoxic $BiFe_{1-x}Al_xO_3$/mica-titania pigments with high NIR reflectance. **2017,** *43* (18), 16488-16494.

38. James, V.; Rao, P. P.; Sameera, S.; Divya, S. J. C. I., Multiferroic based reddish brown pigments: $Bi_{1-x}M_xFeO_3$ (M = Y and La) for coloring applications. **2014,** *40* (1), 2229-2235.

39. Xiao, Y.; Huang, B.; Chen, J.; Sun, X. J. J. o. A.; Compounds, Novel Bi^{3+} doped and Bi^{3+}/Tb^{3+} co-doped $LaYO_3$ pigments with high near-infrared reflectances. **2018,** *762*, 873-880.

40. Dohnalová, Ž.; Šulcová, P.; Bělina, P.; Vlček, M.; Gorodylova, N. J. J. o. T. A.; Calorimetry, Brown pigments based on perovskite structure of $BiFeO_{3-\delta}$. **2018,** *133*, 421-428.

41. Buvaneswari, G.; Aswathy, V.; Rajakumari, R. J. D.; Pigments, Comparison of color and optical absorbance properties of divalent ion substituted Cu and Zn aluminate spinel oxides synthesized by combustion method towards pigment application. **2015,** *123*, 413-419.

42. Huang, B.; Xiao, Y.; Huang, C.; Chen, J.; Sun, X. J. D.; Pigments, Environment-friendly pigments based on praseodymium and terbium doped $La_2Ce_2O_7$ with high near-infrared reflectance: synthesis and characterization. **2017,** *147*, 225-233.

43. Radhika, S.; Sreeram, K. J.; Nair, B. U. J. J. o. C. S., Effective synthesis route for red-brown pigments based on Ce–Pr–Fe–O and their potential application for near infrared reflective surface coating. **2014,** *126*, 65-73.

44. Oka, R.; Shobu, Y.; Aoyama, F.; Tsukimori, T.; Masui, T. J. R. A., Synthesis and characterization of $SrY_{2-x}Ce_xO_4$ as environmentally friendly reddish-brown pigments. **2017,** *7* (87), 55081-55087.

45. Asadinia, E.; Pakshir, M.; Hosseini, S. E. J. P. i. O. C., Synthesis of $(Ba_4Zn_{2-x}Mn_xFe_{36}O_{60})$ U-type hexaferrite pigments and studying their influence on the protective performance, mechanical behavior and microwave absorption properties of polyurethane paint coatings. **2020,** *139*, 105435.

46. Jose, S.; Jayaprakash, A.; Laha, S.; Natarajan, S.; Nishanth, K.; Reddy, M. J. D.; Pigments, $YIn_{0.9}Mn_{0.1}O_3$-ZnO nano-pigment exhibiting intense blue color with impressive solar reflectance. **2016,** *124*, 120-129.

47. Ghasemi, E.; Ramezanzadeh, B.; Saket, S.; Ashhari, S. J. J. o. C. T.; Research, Electrochemical investigation of the epoxy nanocomposites containing $MnAl_2O_4$ and $CoAl_2O_4$ nanopigments applied on the aluminum alloy 1050. **2016,** *13* (1), 97-114.

48. Ziganshina, M.; Stepin, S.; Karandashov, S.; Mendelson, V. J. A.-C. M.; Materials, Complex oxides–non-toxic pigments for anticorrosive coatings. **2020,** *67* (4), 395-405.

49. Moulder, J. F.; Chastain, J., *Handbook of X-ray Photoelectron Spectroscopy: A Reference Book of Standard Spectra for Identification and Interpretation of XPS Data*. Physical Electronics Division, Perkin-Elmer Corporation: 1992.

50. Deroubaix, G.; Marcus, P. J. S.; Analysis, I., X-ray photoelectron spectroscopy analysis of copper and zinc oxides and sulphides. **1992,** *18* (1), 39-46.

51. Ahmed, N. M.; Abd El-Gawad, W. M.; Youssef, E. A.; Souaya, E. M. J. P.; Technology, R., Employment of new modified ferrite pigments in anticorrosive alkyd-based paints. **2014,** *43* (4), 201-211.

52. Abd El-Ghaffar, M. A.; Ahmed, N. M.; Youssef, E. A. J. J. o. C. T.; Research, A method for preparation and application of micronized ferrite pigments in anticorrosive solvent-based paints. **2010,** *7*, 703-713.

Development of new intense orange inorganic pigment from $Bi_4V_2O_{11}$

5.1. Abstract

The present study illustrates the development of an environmentally benign, intense orange inorganic pigment by substituting Si^{4+} metal ion at the Bi^{3+} site of $Bi_4V_2O_{11}$ via the solid-state method. The partial replacement of Si^{4+} induced a strain in the crystal lattice of the compound, which resulted in a substantial improvement in the visible light reflectance. A reduction in oxygen deficiency in the lattice structure facilitated the colour tuning of the pigment series from brownish red to orange and then to yellowish orange. The composition $Bi_{3.8}Si_{0.2}V_2O_{11+\delta}$ exhibited a bright orange hue with colour coordinates $a^* = 39$, $b^* = 34$ and $L^* = 52$. Furthermore, the NIR solar reflectance of the pigment was 86%, which is superior to the reported and commercial orange pigments. Compared to commercial pigment coatings, $Bi_{3.8}Si_{0.2}V_2O_{11+\delta}$ achieved a temperature reduction of 2 °C inside a foam model house. An exceptional corrosion resistance of 1.6×10^{10} Ωcm^2 was registered by the pigment loaded epoxy coating with good stability. The corrosion inhibition mechanism of the pigment operates through the hand-in-hand working of passive Bi-O and Si-O, active FeOOH and vanadate moiety. On the whole, the new multifunctional orange pigment has the potential to be a viable replacement for the toxic commercial pigments in the market.

5.2. Introduction

Inorganic orange pigments have a long history of being one of the most attractive colourants. The pigments α-As_4S_4 and As_2S_3 are a couple of ancient orange colourants derived from natural minerals. Mostly, it has been utilized in paintings and cloth colouring[1, 2]. However, the introduction of stable synthetic pigments with good weatherability and tinting strength, such as CdS-CdSe (cadmium orange), Fe_2O_3-FeO(OH) (bayferrox orange 960) and Zn, Sn rutile, has streamlined their application in exterior coatings[3]. Unfortunately, the presence of toxic metals As, Cd and Se hindered its consumption to a great extent[4]. Subsequent research for an environmentally benign alternative with equivalent colour strength is still in pursuit. Reports from Bae et al., and Yuan et al., provided two impressive compositions, $Sr_4Mn_2(Cu_{0.5}Zn_{0.5})O_9$ and $Bi_{0.6}La_{0.4}FeO_3$, respectively[1, 5]. Nevertheless, it falls far short of commercial pigments in terms of colour strength, necessitating more investigations and fine adjustments in future.

Unlike the traditional pigments, the contemporary inorganic colourants focus not only on the colour but also features like NIR reflectance, corrosion resistance, luminescence, hydrophobicity, etc[6-9]. In the context of rising UHI and concomitant increase in energy

consumption in urban buildings, the current work focuses on the NIR reflectance property of the pigment, which is well-known to mitigate the problem to some extent[10-14]. Since the commercial pigments offer high NIR reflectance, developing a better candidate with good colour intensity is highly challenging. Recently, Wendusu et al., succeeded in improving the red colour of $Bi_4V_2O_{11}$ pigment by introducing suitable dopants at the Bi^{3+} site and subsequent heating at O_2 atmosphere. Reduction of the intrinsic oxygen deficiency in the crystal lattice brought the desirable colour change in the pigment[15].

Inspired by the work, a set of metal ions was substituted at the Bi^{3+} site of $Bi_4V_2O_{11}$ to shift its brownish-red colour to bright orange. Since $Bi_4V_2O_{11}$ is a highly reflective pigment, the selection of the dopants was made in such a way that it should enhance its reflectance profile. Meanwhile, the pigment was also analyzed for anticorrosive property, which is essential for the sustainability of the exterior roof coating under constant climate changes[16, 17]. Overall, the current study establishes a new environmentally friendly, intense orange 'cool' inorganic pigment for the development of a stable roof coating.

5.3. Experimental section

5.3.1. Materials and methods

The pigment series $Bi_{3.9}M_{0.1}V_2O_{11}$ (M = Si^{4+}, Al^{3+}, Ti^{4+}, Y^{3+} and La^{3+}) and $Bi_{3-x}Si_xV_2O_{11+\delta}$ ($0 \leq x \leq 0.6$) were synthesized by solid-state method. Extra pure Bi_2O_3 (99%), V_2O_5 (99.9%), SiO_2 (99.5%), Al_2O_3 (99%), TiO_2 (99%), Y_2O_3 (99.99%) and La_2O_3 (99.9%) were purchased from Merck and used without further purification. Stoichiometric amounts of precursors were ground in an ethanol wetting medium and calcined in air atmosphere at 800 °C for 4 h. An acrylic coating of $Bi_{3.8}Si_{0.2}V_2O_{11+\delta}$ pigment was prepared on concrete and Al sheet. Subsequently, evaluated the thermal shielding ability of the acrylic coatings and compared with commercial orange pigment coating, (described in Experimental section, Chapter 2B)[16, 17]. Anticorrosive property of the pigment was analyzed by developing pigment ($Bi_{3.8}Si_{0.2}V_2O_{11+\delta}$) incorporated epoxy coatings on steel in 3.5 wt% NaCl solution (described in Experimental section, Chapter 2B). The thickness of acrylic and epoxy coatings of the pigment were maintained throughout the experiments for better comparison.

5.3.2. Characterization techniques

Phase determination of the synthesized pigment series was done by PXRD analysis (details given in Chapter 2A). Morphology and particle size distribution were identified through SEM and HRTEM analysis. EDS was conducted for pigment composition and DLS

for particle size measurement. Optical studies were performed using UV-Vis-NIR Spectrophotometer (details given in Chapter 2A). The coating thickness was measured using Optical microscope (for acrylic coatings) and Profilometer (for epoxy coatings). A multichannel potentiostat (Autolab) was used to study the anticorrosive property and respective corrosion mechanism was identified from XPS analysis (details given in Chapter 2B).

5.4. Results and discussion

5.4.1. Synthesis of $Bi_{4-x}M_xV_2O_{11}$ pigment series

A new non-toxic orange inorganic pigment was developed by introducing different metal ions Si^{4+}, Al^{3+}, Ti^{4+}, La^{3+} and Y^{3+} at the Bi^{3+} site of $Bi_4V_2O_{11}$. **Fig. 5.1a** shows the PXRD patterns of the synthesized pigments. $Bi_4V_2O_{11}$ exists in three polymorphs, α-monoclinic, β-orthorhombic and γ-tetrahedral[18-20]. All the prepared compounds were crystallized in low symmetric monoclinic structure with a C2/m space group. It was validated by the two exclusive features in the PXRD pattern. The peak splitting at 46⁰ is the characteristic of a monoclinic $Bi_4V_2O_{11}$, as illustrated in the inset of **Fig. 5.1b**[21]. However, it was not clearly evident for Al^{3+}, La^{3+} and Y^{3+} doped systems, which could be due to the relatively low intensity of the diffraction peak. Furthermore, the absence of a peak at 19.64⁰ indicated that the structure is not orthorhombic but rather monoclinic. The major peaks were indexed using JCPDS 082-1481, confirming that the dopants had successfully incorporated in place of the host ion. Meanwhile, traces of monoclinic $BiVO_4$ phase were visible in the PXRD patterns at diffraction angles 18.89, 28.95 and 44.80⁰, as indicated by * in **Fig. 5.1a**. The occurrence of monoclinic $BiVO_4$ phase as an impurity during the synthesis of $Bi_4V_2O_{11}$ has also been described in previous literatures[22]. The ionic radius of the Bi^{3+} is 1.03 Å, whereas all of the dopants except La^{3+} have a smaller radius[23]. As a result, when compared to $Bi_4V_2O_{11}$, the new pigment compositions have displayed a shift in the PXRD patterns towards higher diffraction angle. Thus, the corresponding crystal lattices undergo a shrinkage. At the same time, no apparent change in the pattern was seen for $Bi_{3.9}La_{0.1}V_2O_{11}$, since the ionic radius of La^{3+} and Bi^{3+} are comparable, **Fig. 5.1b**[22].
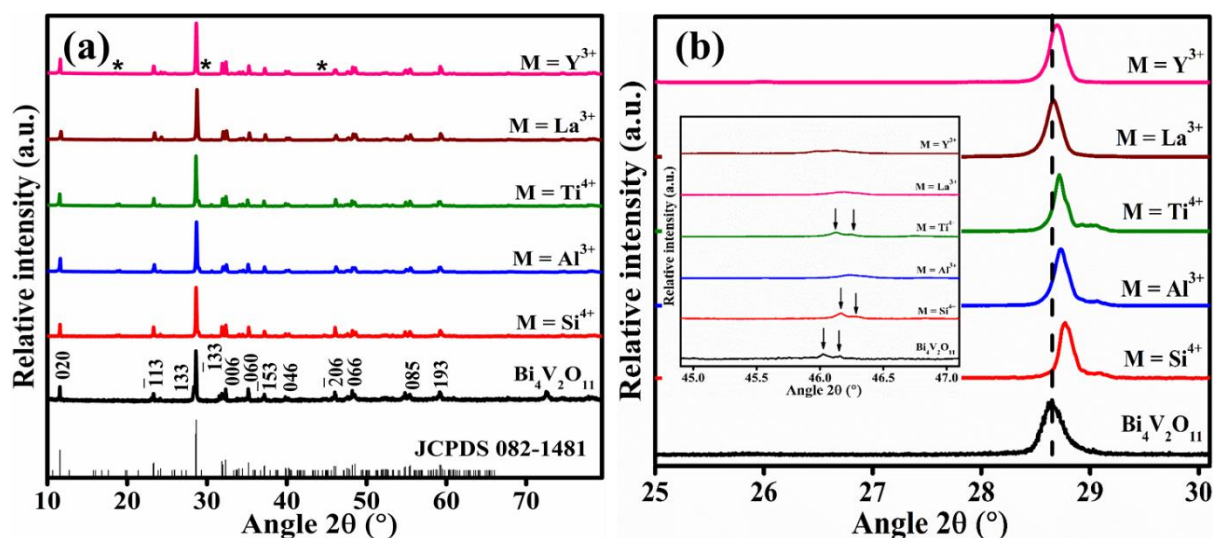
Fig. 5.1. (a) PXRD and (b) peak shift in PXRD patterns of $Bi_{3.9}M_{0.1}V_2O_{11}$ (M = Si^{4+}, Al^{3+}, Ti^{4+}, La^{3+} and Y^{3+}) (peak splitting at 46⁰ inset)

5.4.2. Optical and chromatic properties

Optical and chromatic properties of the pigments $Bi_{3.9}M_{0.1}V_2O_{11}$ (M = Si^{4+}, Al^{3+}, Ti^{4+}, La^{3+} and Y^{3+}) were determined by UV-Vis-NIR spectroscopic analysis. The obtained UV-visible DRS of the pigments were shown in **Fig. 5.2**. The pigments exhibited a strong absorption in the entire violet-green region and reflected the orange-red colours. Consequently, the pigments displayed different shades of orange-red colour. A charge transfer transition from the hybrid Bi_{6s}-O_{2p} to V_{3d} orbital is responsible for its visible light absorption[15]. **Fig. 5.3** depicted the photographs of the prepared compositions. The bandgap of each pigment was estimated from the respective DRS using the Kubelka–Munk function, $f(R) = (1-R)^2/2R$, where R is the reflectance and enumerated in **Table 5.1**[24, 25]. Despite the fact that there is no substantial change in the optical band gap, the percentage reflectance of the pigments was found to vary from each other. The orange-red colour was reflected more efficiently by Si^{4+} and Ti^{4+} doped pigments than by all other compositions, including $Bi_4V_2O_{11}$. As a result, the pigments $Bi_{3.9}Si_{0.1}V_2O_{11+\delta}$ and $Bi_{3.9}Ti_{0.1}V_2O_{11+\delta}$ appeared saffron and reddish-orange colours, respectively, **Fig. 5.3**.
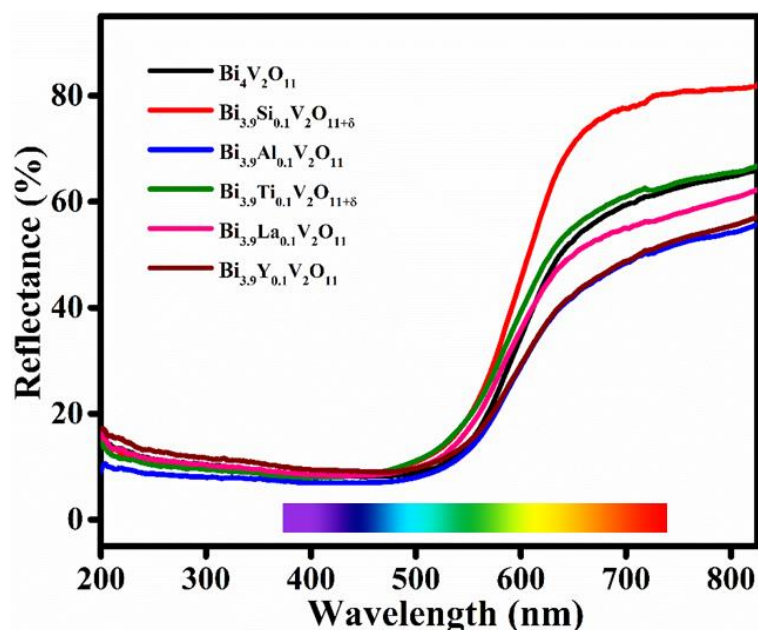
Fig. 5.2. UV-Visible reflectance spectra of $Bi_{3.9}M_{0.1}V_2O_{11}$ (M = Si^{4+}, Al^{3+}, Ti^{4+}, La^{3+}, Y^{3+})

CIE 1976 $L^*a^*b^*$ colour parameters of the pigments were summarized in **Table 5.1**. $Bi_4V_2O_{11}$ is a dark brownish-red pigment with a lightness of less than 45 and a^*, b^* values in the twenties. Hence, the dopants were chosen in such a way that it should be able to enhance the colour strength and lightness of the pigment. Among synthesized pigments, only Si^{4+} and Ti^{4+} doping resulted in a considerable colour change from brownish red. The colour parameters and lightness value of these pigments were greatly enhanced over the parent system. However, the Si^{4+} doped pigment outperformed the other candidate by increasing its redness from 25 to 36, and yellowness from 21 to 29. Furthermore, the particular composition has the highest colour saturation and its hue angle perfectly lies in the red region.
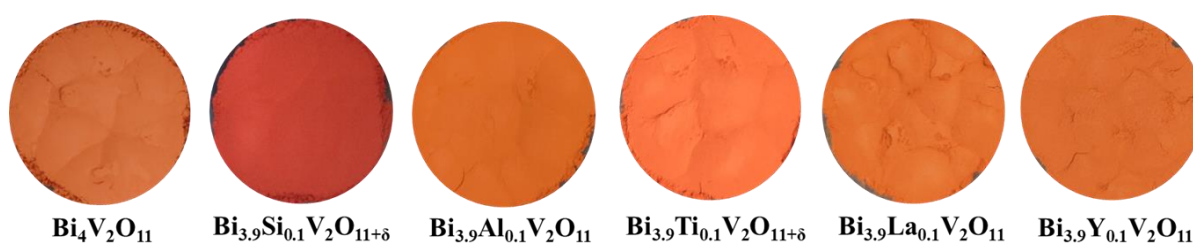
Fig. 5.3. Photographs of $Bi_{3.9}M_{0.1}V_2O_{11}$ (M = Si^{4+}, Al^{3+}, Ti^{4+}, La^{3+} and Y^{3+}) pigments

$Bi_4V_2O_{11}$ belongs to the Aurivillius structure, which is an intrinsic oxygen deficient species[26]. When higher valence cations (Si^{4+} and Ti^{4+}) are substituted at the Bi^{3+} site, in order to maintain neutrality and stability, the system lowers the oxygen deficiency. This will partially eliminate the impurity energy levels generated due to the oxygen deficit, increasing the reflectance in orange-red region. Furthermore, the lattice shrinkage induced in the

$Bi_{3.9}Si_{0.1}V_2O_{11+\delta}$ crystal structure as a result of an ionic size mismatch between the host and guest ions affected the pigment hue by modulating the width of the valence band[15]. Because the ionic radius of Si^{4+} is smaller than that of Ti^{4+}, the degree of lattice strain exerted by the former will be greater, resulting in a disparity in band width. Eventually, $Bi_{3.9}Si_{0.1}V_2O_{11+\delta}$ reflected the orange-red colour better and exhibited a vivid saffron colour. Moreover, a^* parameter of the pigment was superior to the commercial orange PY 216. As a result, even though Ti^{4+} doping produced a better outcome than the base compound, given the high a^* value and greater probability of resulting in an orange colour pigment, more emphasis was paid to the synthesis of $Bi_{4-x}Si_xV_2O_{11+\delta}$ pigment series.

Table 5.1. CIE colour coordinates of $Bi_{3.9}M_{0.1}V_2O_{11}$ (M = Si^{4+}, Al^{3+}, Ti^{4+}, La^{3+} and Y^{3+})

Sample	L^*	a^*	b^*	C^*	h^0	E_g (eV)
$Bi_4V_2O_{11}$	43.23	25.68	21.81	33.69	40.03	2.10
$Bi_{3.9}Si_{0.1}V_2O_{11+\delta}$	52.53	36.08	29.15	46.38	38.93	2.09
$Bi_{3.9}Al_{0.1}V_2O_{11}$	48.15	26.19	27.78	38.18	46.67	2.04
$Bi_{3.9}Ti_{0.1}V_2O_{11+\delta}$	51.29	30.69	28.88	42.14	43.26	2.16
$Bi_{3.9}La_{0.1}V_2O_{11}$	53.09	26.85	31.08	41.07	49.17	2.14
$Bi_{3.9}Y_{0.1}V_2O_{11}$	49.66	23.94	22.99	33.19	43.83	2.08
PY 216	62.55	34.88	59.09	68.62	59.44	-

5.4.3. XPS analysis

The XPS analysis of the pigment powder provided more details on the lattice changes in $Bi_{3.8}Si_{0.2}V_2O_{11+\delta}$. The presence of constituent elements Bi, Si, V, O and C can be seen in the survey spectrum, **Fig. 5.4a**. Peaks at 529.5 and 532.8 eV in the high-resolution deconvoluted O1s spectrum, **Fig. 5.4b**, were assigned to lattice oxygen and oxygen vacancy in the $Bi_{3.8}Si_{0.2}V_2O_{11+\delta}$ moiety. In addition, a shoulder peak appeared at 530.4 eV gives an indication of the decrease in oxygen vacancy. Similar results were also observed in the high-resolution V2p spectrum, **Fig. 5.4c**. In addition to the peaks at 516.5 and 523.9 eV, which correspond to $V2p_{3/2}$ and $V2p_{1/2}$, respectively, a shoulder peak at 517.8 eV indicated the presence of a slight excess oxygen in the lattice[15, 27]. It could be due to the incorporation of high valence cation at the Bi^{3+} site. Interestingly, the presence of a very low concentration of Bi^{5+} species was also detected in the high resolution Bi4f spectrum, **Fig. 5.4d**. The findings revealed that Si^{4+} substitution at Bi^{3+} site could able to reduce the oxygen deficiency in $Bi_4V_2O_{11}$ crystal lattice,

giving rise to a significant change in pigment hue from dark brownish red to bright reddish-orange.
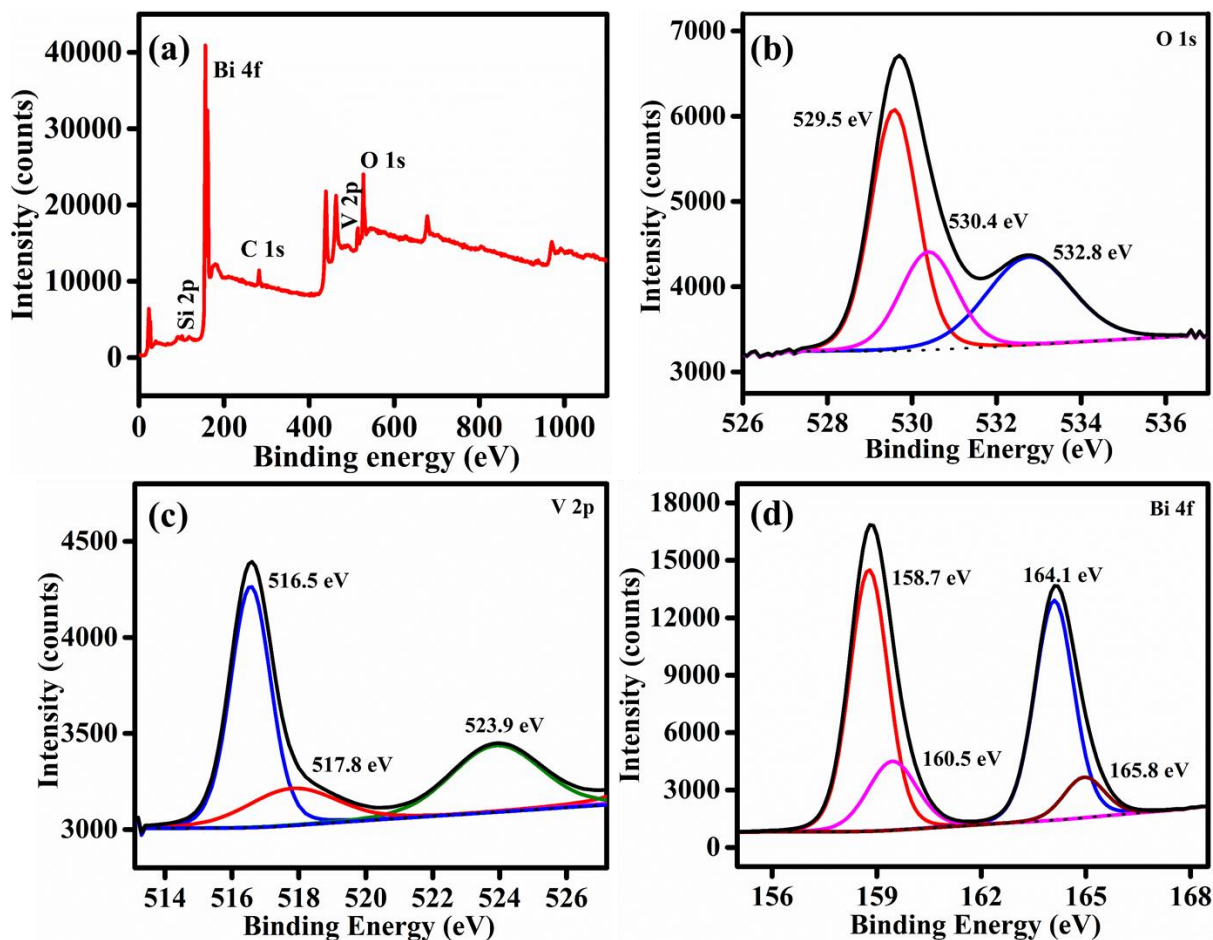
Fig. 5.4. XPS (a) survey spectrum, deconvoluted high-resolution spectra of (b) O1s, (c) V2p and (d) Bi4f of $Bi_{3.8}Si_{0.2}V_2O_{11+\delta}$

5.4.4. Synthesis of $Bi_{4-x}Si_xV_2O_{11+\delta}$ and optical studies

Fig. 5.5 demonstrates the PXRD patterns of the synthesized pigment series $Bi_{4-x}Si_xV_2O_{11+\delta}$ ($0 \leq x \leq 0.6$). Diffraction peaks of each composition were completely matched with its base compound and the major peaks were indexed using JCPDS 082-1481. Hence, it was confirmed that the compounds crystallized in monoclinic structure with a C2/m space group. The peak splitting at 46⁰ and absence of the peak at 19.64⁰ provided additional proof for the monoclinic phase formation (inset of **Fig. 5.5b**). Since, the ionic size of Si^{4+} is smaller than Bi^{3+}, a gradual peak shift towards higher diffraction angle was noticed as doping increased, **Fig. 5.5b**. Furthermore, a monoclinic $BiVO_4$ phase was observed in all the compositions, which found to increase while increasing the Si^{4+} doping, marked * in **Fig. 5.5a**.
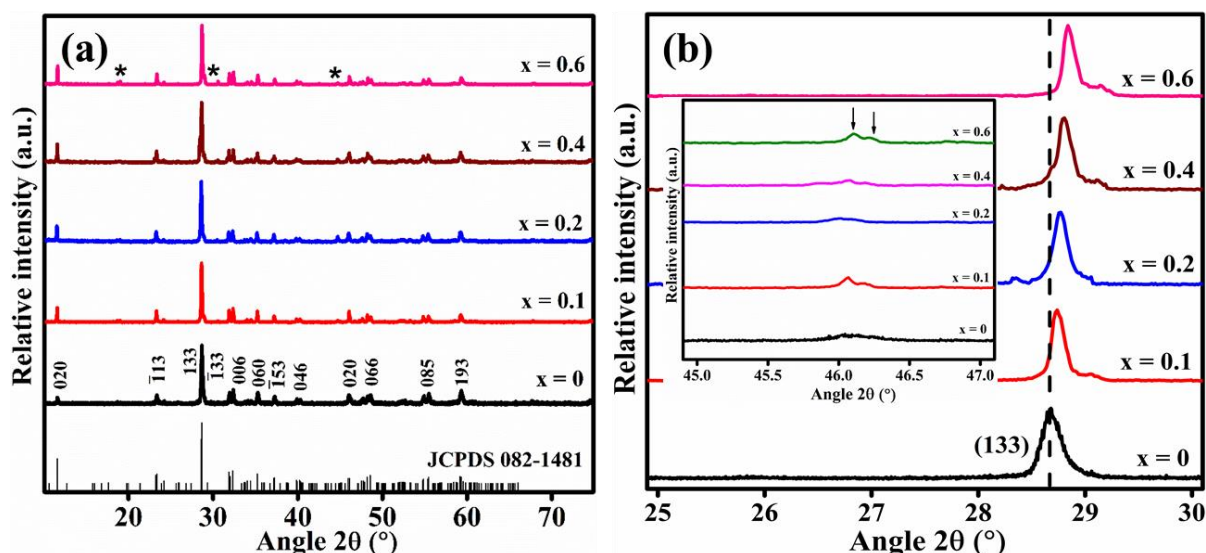
Fig. 5.5. (a) PXRD and (b) peak shift in PXRD patterns of $Bi_{3-x}Si_xV_2O_{11+\delta}$ ($0 \leq x \leq 0.6$)

According to the DRS showed in **Fig. 5.6**, the $Bi_{4-x}Si_xV_2O_{11+\delta}$ ($0.1 \leq x \leq 0.6$) pigment series reflected the orange-red colours in the visible spectrum more effectively than $Bi_4V_2O_{11}$. It is because of the fact that the introduction of Si^{4+} decreased the oxygen deficiency in $Bi_4V_2O_{11}$ and lattice size of the crystal structure. As a result, the pigment series exhibited an excellent colour modulation from brownish red to saffron, then to bright orange and ultimately to yellowish orange. **Fig. 5.7** shows photographs of the $Bi_{4-x}Si_xV_2O_{11+\delta}$ ($0.1 \leq x \leq 0.6$) pigment series. The CIE colour coordinates of the pigment series was summarized in **Table 5.2**. The colour properties of the new pigments were significantly improved when compared to $Bi_4V_2O_{11}$. The redness a^* was increased from 25 to 39 while the yellow shade b^* was increased from 22 to 40. Although there is a significant increase in a^* value at 2.5 mol% doping, the further addition of Si^{4+} did not yield the expected increase. This is due to the fact that Si^{4+} is not a chromophore and hence has no direct influence on the pigment colour. Hence, beyond improving the colour strength (a* value) through disturbances in crystal lattice, further addition of Si^{4+} contributed in diluting the colour intensity to orange and orange-yellow. Additionally, the presence of yellow $BiVO_4$ phase may also have an effect on this colour change.
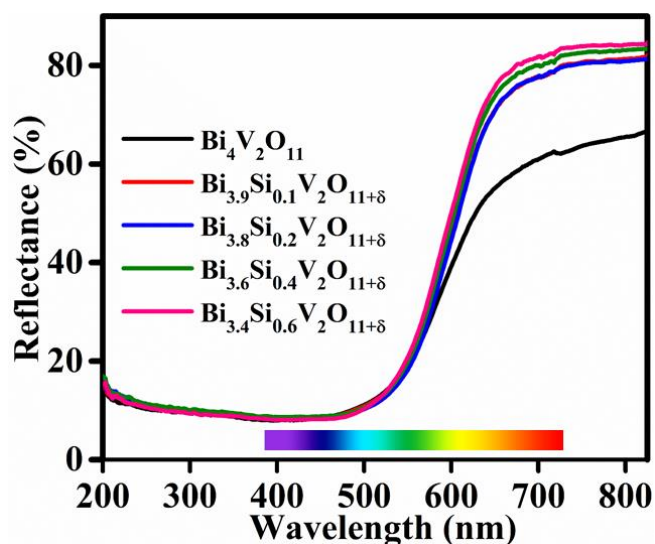
Fig. 5.6. UV-Visible reflectance spectra of $Bi_{4-x}Si_xV_2O_{11+\delta}$ ($0 \leq x \leq 0.6$) pigment series

The 5 mol% Si^{4+} doped sample found to be the ideal orange pigment in the synthesized pigment series. The estimated colour coordinates of the composition $a^* = 39$, $b^* = 34$ and $L^* = 52$, held its colour at orange with good brightness. Furthermore, it was superior to the commercial orange in terms of colour. Therefore, the composition $Bi_{3.8}Si_{0.2}V_2O_{11+\delta}$ was selected as the best candidate in the pigment series and taken for further studies.
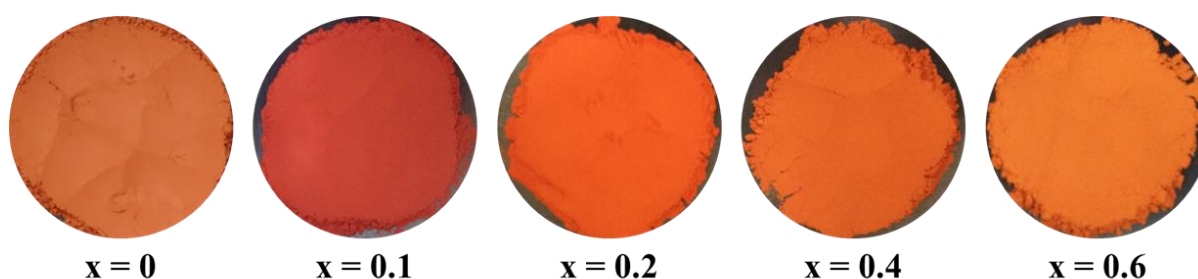
Fig. 5.7. Photographs of $Bi_{4-x}Si_xV_2O_{11+\delta}$ ($0 \leq x \leq 0.6$) pigment series

Table 5.2. CIE colour coordinates of $Bi_{4-x}Si_xV_2O_{11+\delta}$ ($0 \leq x \leq 0.6$) pigment series

Sample	L^*	a^*	b^*	C^*	h^o	E_g (eV)
$Bi_4V_2O_{11}$	43.23	25.68	21.81	33.69	40.03	2.10
$Bi_{3.9}Si_{0.1}V_2O_{11+\delta}$	52.53	36.08	29.15	46.38	38.93	2.09
$Bi_{3.8}Si_{0.2}V_2O_{11+\delta}$	52.01	38.89	34.12	51.74	41.26	2.16
$Bi_{3.6}Si_{0.4}V_2O_{11+\delta}$	52.77	39.04	35.06	52.47	41.92	2.20
$Bi_{3.4}Si_{0.6}V_2O_{11+\delta}$	52.80	39.59	39.88	56.20	45.20	2.18
PY 216	62.55	34.88	59.09	68.62	59.44	-

5.4.5. Morphology and particle size analysis

The SEM images of $Bi_4V_2O_{11}$ and $Bi_{3.8}Si_{0.2}V_2O_{11+\delta}$ pigment samples were demonstrated in **Fig. 5.8a, d**. $Bi_4V_2O_{11}$ did not have a well-defined morphology, whereas Si^{4+} doped $Bi_4V_2O_{11}$ exhibited a crumpled paper-like shape. Meanwhile, neither of the pigment particles has agglomerated. Particle size is very crucial in maintaining the dispersibility, adhesiveness and filling property of the pigment to establish a consistent paint formulation [22]. The particle size distribution obtained from the DLS analysis was consistent with the observed micrographs. $Bi_4V_2O_{11}$ had a fairly broad size distribution with an average particle size of 5 μm, **Fig. 5.8b**. At the same time, after Si doping the size distribution turned relatively narrower and average size was reduced to 3.2 μm, **Fig. 5.8e**. The presence of constituent elements Bi, V, O and Si was identified in the EDS spectrum of the respective samples. Further, the calculated and observed elemental composition of $Bi_4V_2O_{11}$ and $Bi_{3.8}Si_{0.2}V_2O_{11+\delta}$ pigments are found to be in close agreement, **Fig. 5.8c, f**.
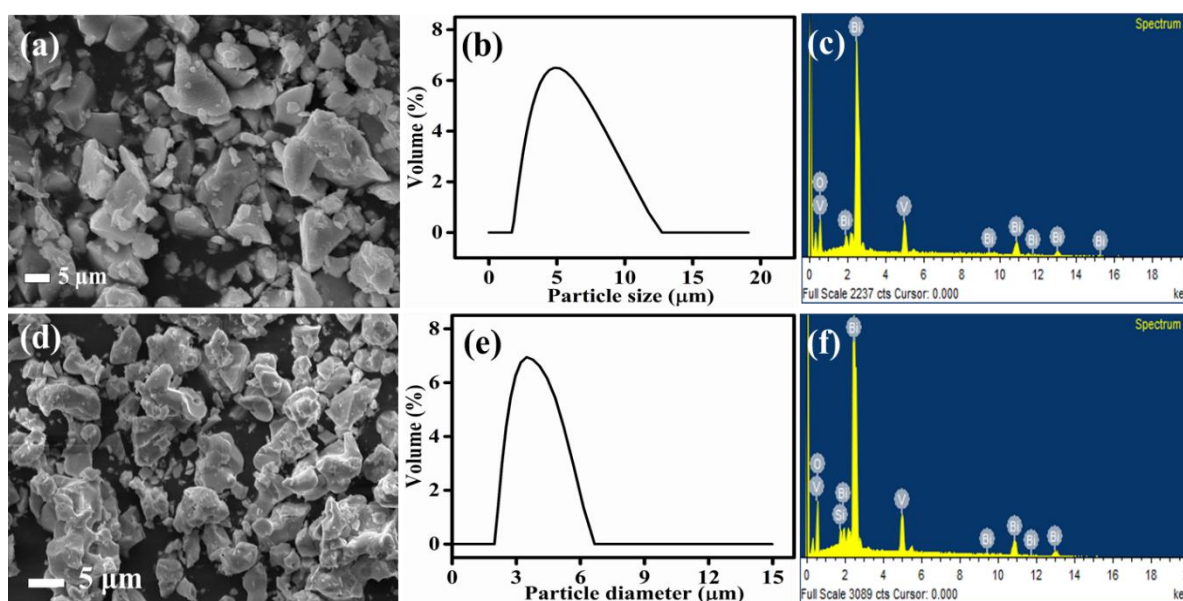
Fig. 5.8. SEM images of (a) $Bi_4V_2O_{11}$, (d) $Bi_{3.8}Si_{0.2}V_2O_{11+\delta}$, DLS curves of (b) $Bi_4V_2O_{11}$, (e) $Bi_{3.8}Si_{0.2}V_2O_{11+\delta}$ and SEM-EDS spectrum of (c) $Bi_4V_2O_{11}$, (f) $Bi_{3.8}Si_{0.2}V_2O_{11+\delta}$ pigments

5.4.6. Reflectance properties

PY 216 is a highly reflective material with an NIR solar reflectance of 80%. Therefore, it is very essential that the replacement pigment must have a nearly identical or better reflectance profile. **Fig. 5.9a, b** illustrates the UV-Vis-NIR and NIR solar reflectance spectra of $Bi_{4-x}Si_xV_2O_{11+\delta}$ ($0 \leq x \leq 0.6$) pigment series. Bismuth compounds are often highly reflective compounds[28, 29]. Hence, though $Bi_4V_2O_{11}$ pigment seemed dark reddish brown in colour, it showed a reflectance above 70%. Unlike colour, the incorporation of Si^{4+} had a positive impact

on reflectance property of the pigment. As the Si^{4+} concentration increased, the solar reflectance went up from 72 to a maximum of 88%, **Table 5.3**. Among which, the composition $Bi_{3.8}Si_{0.2}V_2O_{11+\delta}$ demonstrated 86% NIR solar reflectance. Hence, the pigment can be used as an efficient 'cool' pigment in exterior wall and roof coatings.

Table 5.3. Reflectance value of $Bi_{4-x}Si_xV_2O_{11+\delta}$ ($0 \leq x \leq 0.6$) pigment series

Sample	NIR (%) at 1100 nm	R^* (%)
$Bi_4V_2O_{11}$	76	72
$Bi_{3.9}Si_{0.1}V_2O_{11+\delta}$	89	87
$Bi_{3.8}Si_{0.2}V_2O_{11+\delta}$	88	86
$Bi_{3.6}Si_{0.4}V_2O_{11+\delta}$	90	88
$Bi_{3.4}Si_{0.6}V_2O_{11+\delta}$	90	88
Zn, Sn rutile	79	80
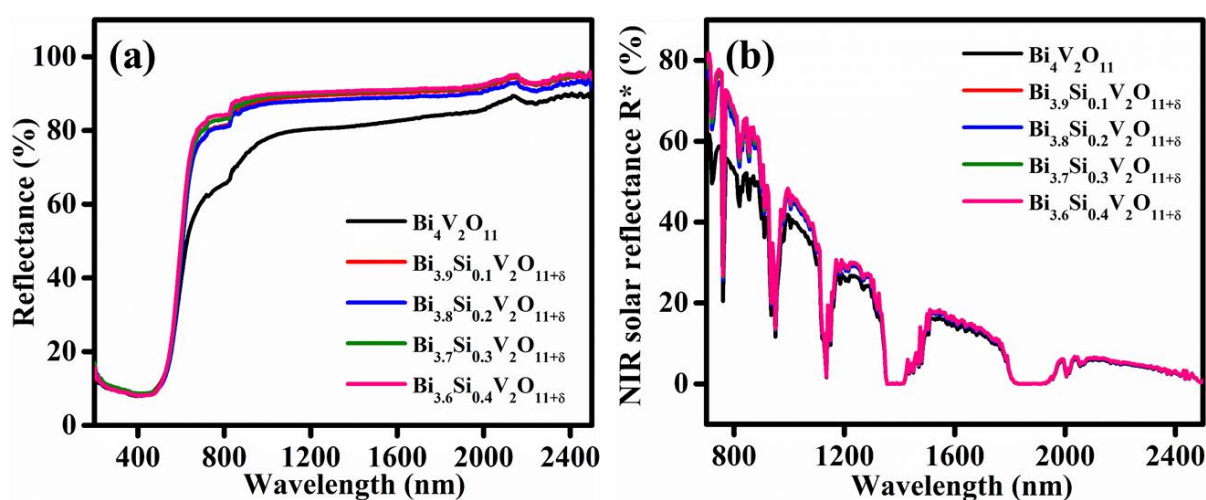
Fig. 5.9. (a) UV-Vis-NIR reflectance and (b) NIR solar reflectance spectra of $Bi_{4-x}Si_xV_2O_{11+\delta}$ ($0 \leq x \leq 0.6$) pigment series

The Si^{4+} substitution boosted the reflectivity of $Bi_4V_2O_{11}$ significantly without affecting its colour. Colour parameters and reflectance values of the reported pigments and commercial orange were compared with those of $Bi_{3.8}Si_{0.2}V_2O_{11+\delta}$, **Table 5.4**. The new pigment ranks top among these pigments. Interestingly, the dark shade of $Bi_4V_2O_{11}$ became an advantage in achieving good colour strength due to probable colour dilution imposed by Si^{4+} substitution at the Bi^{3+} site. Therefore, in the current scenario of UHI, $Bi_{3.8}Si_{0.2}V_2O_{11+\delta}$ orange is an extremely essential pigment as an environmentally friendly option with high reflectivity and outstanding colour intensity.

Table 5.4. Colour and reflectance comparison of $Bi_{3.8}Si_{0.2}V_2O_{11+\delta}$ with literature reports

Sample	L^*	a^*	b^*	R^*	Ref.
PY 216	62.55	34.88	59.09	80	Present study
Bayferrox orange	53.9	23.4	42.3	57	[1]
$Sr_4Mn_2(Cu_{0.5}Zn_{0.5})O_9$	64	19.8	52.3	83	[1]
$Bi_{1.5}Zr_{0.5}O_{3+\delta}$	68	34	69	-	[30]
$BiFe_{0.8}Al_{0.2}O_3$/mica-titania	62.27	15.16	37.88	53	[31]
$Bi_{2.6}Fe_{0.4}YO_6$	54	20	32	65	[32]
$Al_{0.92}Fe_{0.08}PO_4$	56.54	16.89	29.79	73	[33]
$Bi_{0.6}La_{0.4}FeO_3$	61.92	23.52	21.04	72	[5]
N-doped $Mg_{0.7}Fe_{0.3}TiO_{3+\delta}$	55.02	20.89	23.51	54	[34]
$Bi_2Ce_{1.5}Ti_{0.5}O_7$	72.36	13.38	34.49	65	[35]
$Bi_{3.8}Si_{0.2}V_2O_{11+\delta}$	**52.01**	**38.89**	**34.12**	**86**	**Present study**

5.4.7. Applications

The pigment stability was investigated in acid, basic, and aqueous media prior to coating tests. Each medium was applied to a pre-weighed amount of pigment powder for 1 h. It was then filtered, dried and the colour coordinates were measured, **Table 5.5**. The colour parameters revealed no significant colour variation between the pre-treated and treated samples. The estimated ΔE^*_{ab} found to be well below unity, hence, confirmed the stability[36, 37].

Table 5.5. Colour coordinates of $Bi_{3.8}Si_{0.2}V_2O_{11+\delta}$ after acid/alkali treatment

Sample	pH	L^*	a^*	b^*	c^*	h^o	ΔE^*_{ab}
$Bi_{3.8}Si_{0.2}V_2O_{11+\delta}$	-	52.01	38.89	34.12	51.74	41.26	-
Water	6.6	51.87	38.75	33.93	51.51	41.21	0.26
HNO_3	3.0	51.66	38.51	33.65	51.14	41.14	0.53
NaOH	10.5	51.71	38.63	33.81	51.33	41.19	0.51

Acrylic coatings of $Bi_{3.8}Si_{0.2}V_2O_{11+\delta}$ pigment were developed on concrete and Al sheet, and investigated its colour and reflectance properties. The results were summarized in **Table 5.6**, and the corresponding solar reflectance spectra were presented in **Fig. 5.10**. The coatings (inset of **Fig. 5.10**) exhibited better brightness and colour parameters than the pigment powder, demonstrating that the pigment could successfully maintain its colour strength in the coatings

as well. Meanwhile, a substantial enhancement was noticed in the NIR solar reflectance of the coatings around 95%. Therefore, the new orange pigment $Bi_{3.8}Si_{0.2}V_2O_{11+\delta}$ can be an outstanding 'cool' pigment to replace the toxic commercial orange.
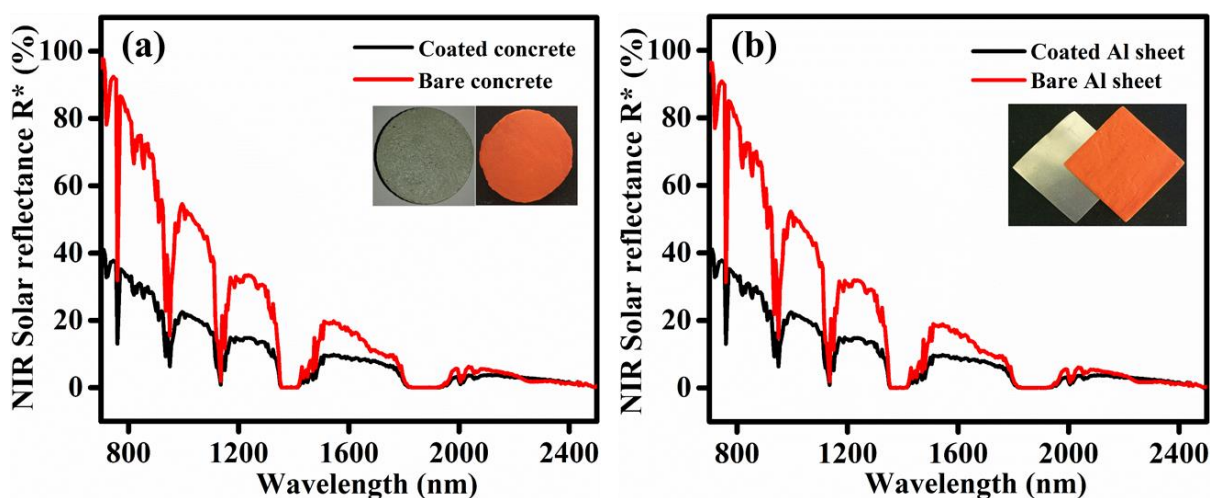
Fig. 5.10. Comparison in NIR solar reflectance spectra of $Bi_{3.8}Si_{0.2}V_2O_{11+\delta}$ coatings on (a) concrete block and (b) Al sheet with their bare surfaces

Table 5.6. Colour coordinates and reflectance of pigment coatings

Sample	L^*	a^*	b^*	C^*	$h^°$	NIR (%) at 1100 nm	R^* (%)
$Bi_{3.8}Si_{0.2}V_2O_{11+\delta}$	47.94	38.89	34.12	51.74	41.26	88	86
Concrete	57.79	41.36	42.12	59.03	45.51	99	96
Al sheet	58.91	41.09	43.96	60.18	46.93	97	93

5.4.8. Temperature shielding performance

The temperature shielding experiment was carried out in foam boxes with roofing made of PY 216 and $Bi_{3.8}Si_{0.2}V_2O_{11+\delta}$ acrylic coated Al sheet. (**Fig. 2B.1**). The coating thickness was maintained between 200-250 μm for better comparison. Further, temperature against time graphs for interior and coating surface temperature were plotted based on 1 h duration measurements, **Fig. 5.11a, b**. The temperature buildup pattern under commercial and $Bi_{3.8}Si_{0.2}V_2O_{11+\delta}$ coated roofs was very similar throughout the course of experiment. However, repeated measurements confirmed that $Bi_{3.8}Si_{0.2}V_2O_{11+\delta}$ coating was able to reduce approximately 2 ℃ interior temperature when compared to PY 216 coating.
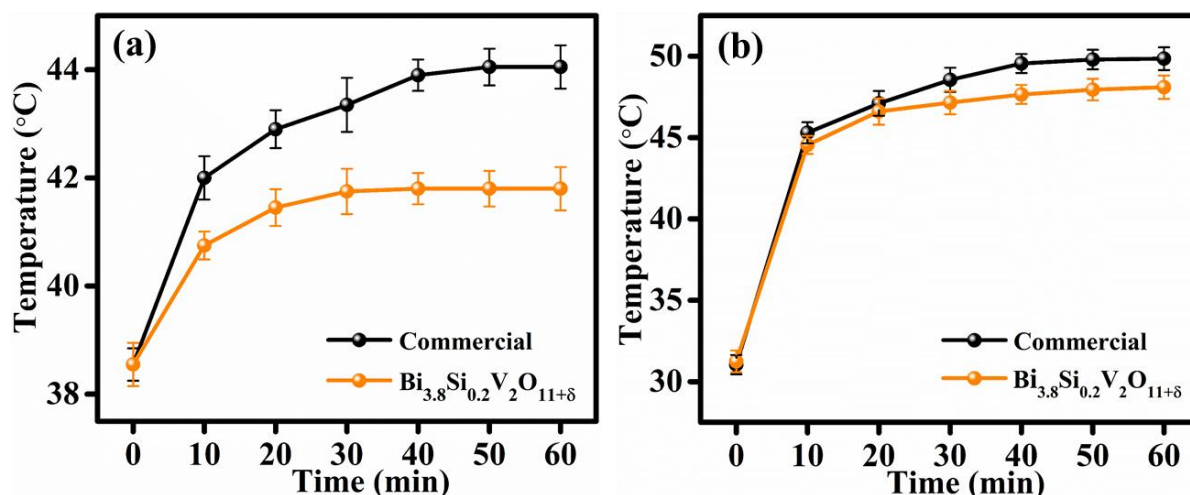
Fig. 5.11. Comparison in (a) interior temperature and (b) surface temperature build up between commercial orange and $Bi_{3.8}Si_{0.2}V_2O_{11+\delta}$ coatings roofed foam box

A comparable result was obtained in the case of coating surface temperature measurements. Thermal images of both coatings at 10 minute intervals were provided in the **Fig. 5.12**. The corresponding graph revealed that the heat build up on $Bi_{3.8}Si_{0.2}V_2O_{11+\delta}$ coating surface was approximately 2 ℃ lower than that of commercial orange due to its superior reflectance property. Both the results demonstrated that the use of $Bi_{3.8}Si_{0.2}V_2O_{11+\delta}$ orange pigment in exterior paints can significantly reduce the cooling energy consumption in buildings. Therefore, considering the increasing demand for orange hue, it is highly recommended to replace the toxic commercial pigment with the new $Bi_{3.8}Si_{0.2}V_2O_{11+\delta}$ orange.
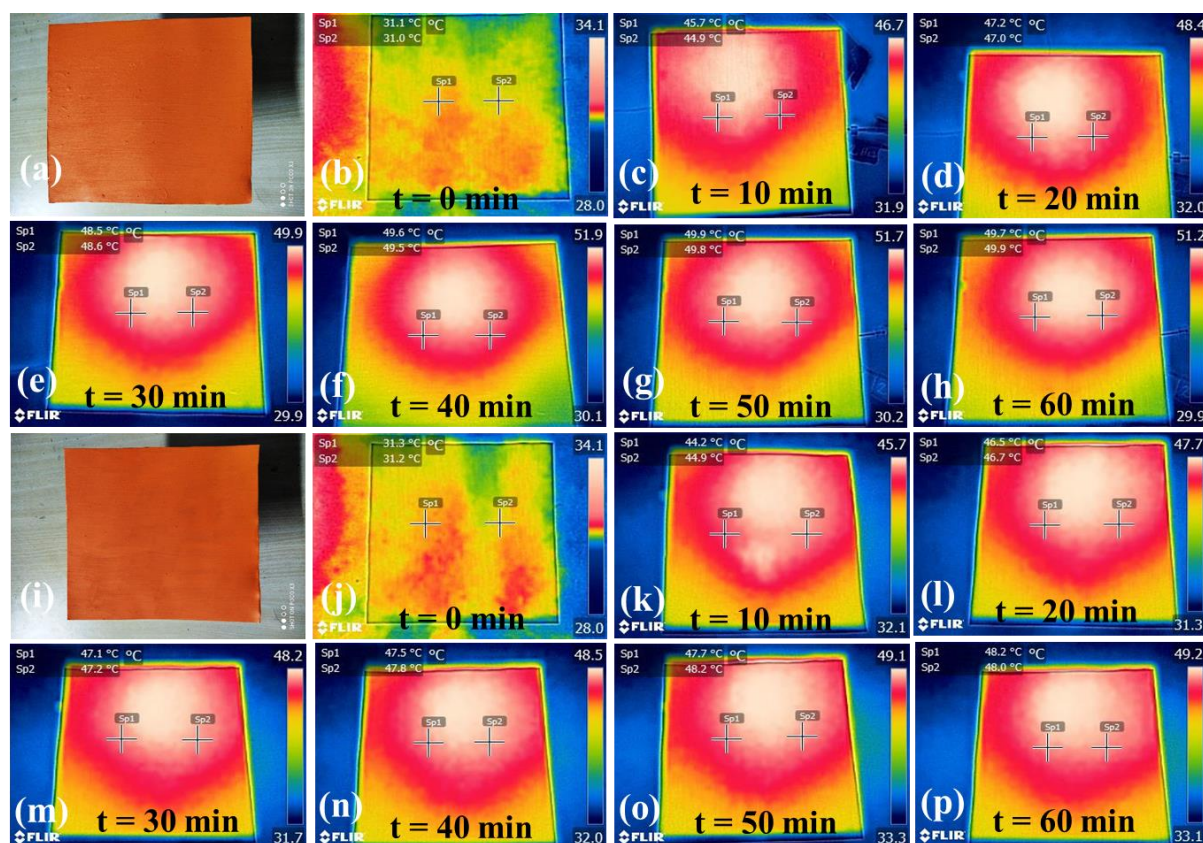
Fig. 5.12. Photographs of (a) commercial orange and (i) $Bi_{3.8}Si_{0.2}V_2O_{11+\delta}$ coatings on Al sheet, thermal images of (b-h) commercial orange and (j-p) $Bi_{3.8}Si_{0.2}V_2O_{11+\delta}$ coatings

5.4.9. Anticorrosive studies

Environmentally friendly vanadates are currently being looked at as a potential replacement for harmful chromates and phosphates in anticorrosive coatings[38, 39]. (Y.E. Bhoge et al.,). Therefore, a comprehensive investigation was conducted to evaluate the anticorrosive property of the new $Bi_{3.8}Si_{0.2}V_2O_{11+\delta}$ orange inorganic pigment. The experiment was performed on a pigment incorporated epoxy coating on steel in 3.5 wt% NaCl solution through EIS. A series of epoxy coatings were prepared by varying the $Bi_{3.8}Si_{0.2}V_2O_{11+\delta}$ concentration (5, 10, 15, 20 and 25) and the results were compared with that of the PY 216 coatings. In **Fig. 5.13**, Nyquist plots of commercial pigment and $Bi_{3.8}Si_{0.2}V_2O_{11+\delta}$ integrated epoxy coatings were displayed, with the corresponding EEC in the inset. The electrochemical parameters from impedance fitting were summarized in **Table 5.7**.
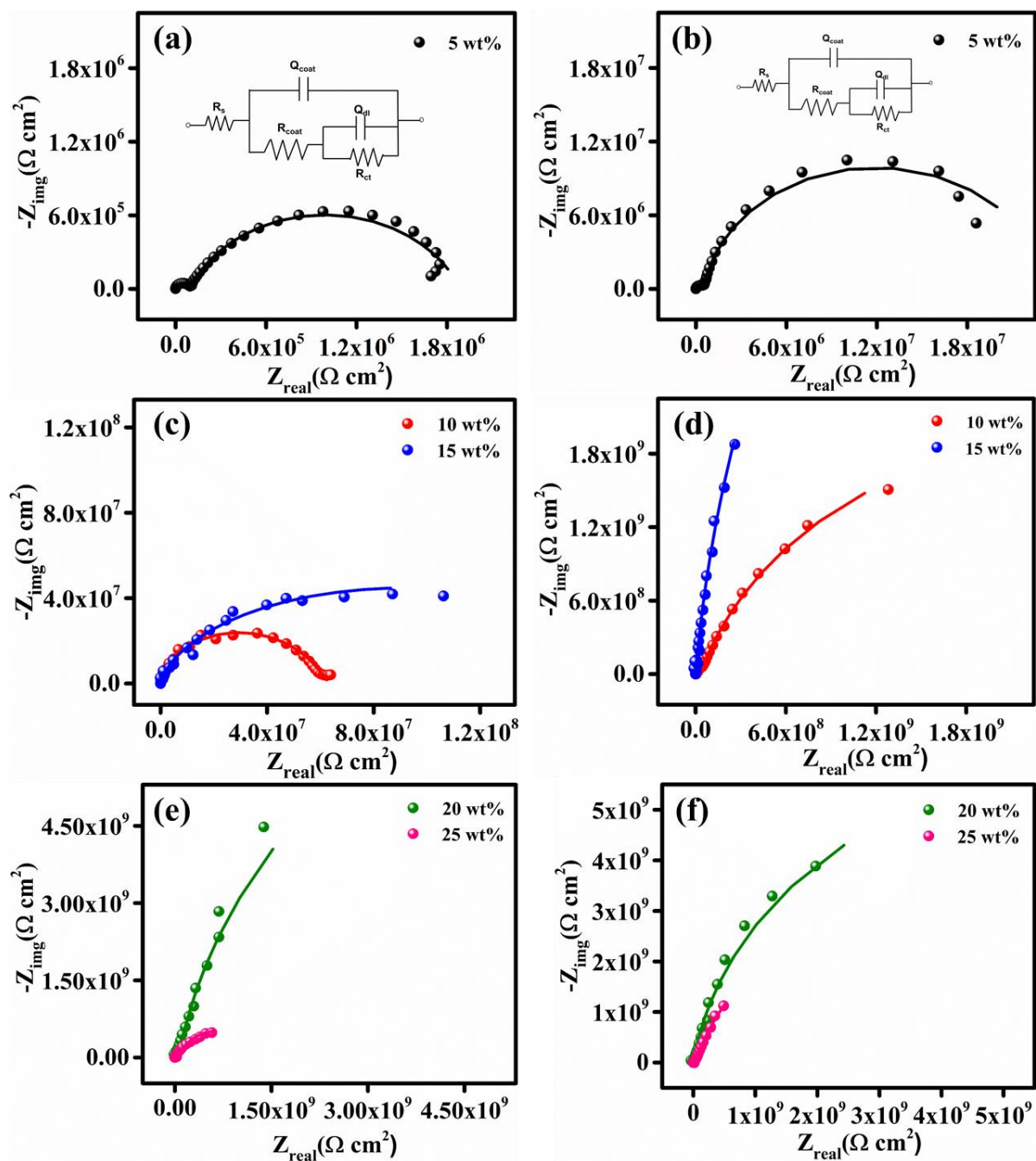
Fig. 5.13. Nyquist plots of (a, b) 5 wt% (EEC in inset), (c, d) 10 and 15 wt%, (e, f) 20 and 25 wt% commercial orange and $Bi_{3.8}Si_{0.2}V_2O_{11+\delta}$ loaded epoxy coatings, respectively

In presence of 5 wt% pigment loading itself the epoxy coating displayed a significant response in the EIS analysis for both commercial and $Bi_{3.8}Si_{0.2}V_2O_{11+\delta}$ orange. The R_{ct} recorded was one order higher than that of bare epoxy coating. On every successive 5 wt% addition, a consistent increase in resistance by one order was noticed for commercial pigment coating. The maximum $R_{ct} = 1.4\times10^9$ Ωcm^2, was obtained at 20 wt% pigment loading. In the meantime, $Bi_{3.8}Si_{0.2}V_2O_{11+\delta}$ incorporated epoxy coating exhibited superior performance over commercial

pigment. The R_{ct} enhanced from the order of 10^6 to a maximum of 10^{10} Ωcm^2. Regardless the fact that the highest corrosion inhibition was obtained at same PVC (20 wt%), the corresponding resistance was one order higher ($R_{ct} = 1.6 \times 10^{10}$ Ω cm^2) than that of commercial sample. The findings suggest that the synthesized pigment can be utilized as an efficient anticorrosive pigment for steel protection in marine medium. The pigment loading above 20 wt% caused a decrease in corrosion resistance to $R_{ct} = 9.1 \times 10^9$ Ω cm^2, which must be attributed to the inhomogeneous distribution of pigment particles in epoxy matrix and consequent agglomeration. The key inference from the EIS data is that both pigments are active in inhibiting corrosion on steel in marine medium, but the new vanadate pigment outperformed the commercial orange since it is a non-toxic candidate with high corrosion resistance.

Table 5.7. EIS parameters from Nyquist plots

Sample	Pigment loading (wt%)	EIS parameters			
		R_{coat} (Ωcm^2)	Q_{coat} (μFcm^{-2})	R_{ct} (Ωcm^2)	Q_{dl} (μFcm^{-2})
PY 216	5	5.7×10^3	3.0781	1.2×10^6	2.3162
	10	2.4×10^2	0.0018	6.3×10^7	0.0016
	15	3.2×10^3	0.0621	1.5×10^8	0.0013
	20	2.7×10^2	0.0081	1.4×10^9	0.0008
	25	1.4×10^3	0.0032	1.9×10^8	0.0013
$Bi_{3.8}Si_{0.2}V_2O_{11+\delta}$	5	9.4×10^4	0.4712	1.8×10^6	0.0295
	10	6.0×10^5	0.0227	2.3×10^7	0.0041
	15	7.1×10^6	0.0033	5.1×10^9	0.0109
	20	7.1×10^7	0.0018	1.6×10^{10}	0.0022
	25	6.6×10^7	0.0051	9.1×10^9	0.0341
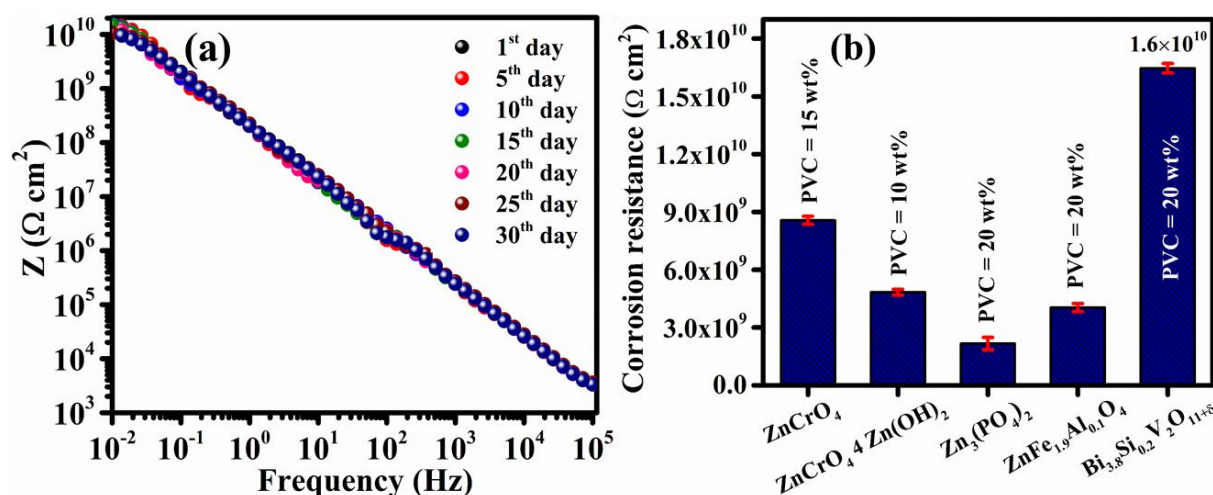
Fig. 5.14. (a) Bode plot of continuous one-month electrochemical study of 20 wt% $Bi_{3.8}Si_{0.2}V_2O_{11+\delta}$ loaded epoxy coating, (b) comparison in corrosion resistance of $Bi_{3.8}Si_{0.2}V_2O_{11+\delta}$ with commercial anticorrosive pigments

Table 5.8. EIS parameters from continuous electrochemical analysis

Sample	Corrosion resistance (Ωcm^2)						
	1st day	5th day	10th day	15th day	20th day	25th day	30th day
$Bi_{3.8}Si_{0.2}V_2O_{11+\delta}$	1.64×10^{10}	1.57×10^{10}	1.55×10^{10}	1.50×10^{10}	1.16×10^{10}	1.06×10^{10}	9.4×10^9

The Bode graphs in **Fig. 5.14a** provided quantitative information on the changes that occurred at the metal-electrolyte interfaces during a one-month continuous electrochemical study on steel in marine environment. **Table 5.8** summarizes the findings, which confirmed the stability of 20 wt% $Bi_{3.8}Si_{0.2}V_2O_{11+\delta}$ pigment loaded epoxy coating. The corrosion resistance remained nearly constant ($R_{ct} \sim 10^{10}$ Ω cm^2) until 25 days, ensuring that the coat was highly intact and free of corrodent attack. Later, only a marginal decrease to 9.4×10^9 Ωcm^2 was seen on the day the experiment was completed. Overall results guaranteed the stability of $Bi_{3.8}Si_{0.2}V_2O_{11+\delta}$ incorporated anticorrosive coating in NaCl medium, confirming that the new orange pigment is an exceptional anticorrosive pigment. Moreover, in terms of corrosion resistance, the existing anticorrosive inorganic pigments in the market lag far behind the new $Bi_{3.8}Si_{0.2}V_2O_{11+\delta}$ orange, **Fig. 5.14b** (values are given in **Table 4.9**). Therefore, it would be an ideal substitute for those toxic pigments. Furthermore, XPS surface analysis was performed on the metal strip acquired after the continuous electrochemical examination to establish the nature of inhibitive mechanism in the new pigment.

5.4.10. Anticorrosive mechanism

The XPS surface analysis of coat-removed steel strip, obtained after continuous electrolyte exposure, provided a preliminary idea of the compounds developed beneath the pigment-loaded epoxy coating. Presence of O, Bi, Si and Fe elements were detected in the survey spectrum, **Fig. 5.15a**. The high-resolution deconvoluted XPS spectra of O1s, Bi4f, Si2p and Fe2p were given in **Fig. 5.15b-e**. Element V was not detected by XPS, most likely due to its extremely low concentration on the metal surface. The low intensity BE peak at 529.8 eV in the O1s spectrum is attributed to the corrosion products Fe_2O_3, whereas the high intensity peak at 531.8 eV is ascribed to iron oxyhydroxide (FeOOH) species. Peaks at 159 and 164.3 eV in the deconvoluted Bi4f spectra correspond to Bi-O bonds (Bi_2O_3/BiO_2)[40]. Similarly, presence of Si-O interaction (SiO_2/SiO) was revealed by the high intensity peak at 102.14 eV in Si2p spectrum[41]. The corrosion intermediates (710.6 eV) and FeOOH (724.9 eV) were further corroborated by the Fe2p spectra, which aligned with the O1s spectrum[40].

Based on XPS results, the corrosion inhibition mechanism of $Bi_{3.8}Si_{0.2}V_2O_{11+\delta}$ pigment loaded epoxy coating was proposed. The passive nature of the pigment buried in epoxy matrix initially serves to prevent the elecrolyte from reaching the metal surface. However, long-term contact with NaCl solution activates a resistive mechanism in the pigment by establishing an alkaline environment at the metal-electrolyte interface. That is, the hydroxyl ions generated at the cathode reacts with the metal ions to form metal hydroxides, further resulting in an oxyhydroxide passive amorphous layer (eq. 5.1-5.3).

$$\text{Anodic oxidation}: \textbf{Fe} \rightarrow \textbf{Fe}^{2+} + \textbf{2e}^- \tag{5.1}$$

$$\text{Cathodic reduction}: \textbf{O}_2 + \textbf{2H}_2\textbf{O} + \textbf{4e}^- \rightarrow \textbf{4OH}^- \tag{5.2}$$

$$\textbf{Fe}^{3+} + \textbf{3OH}^- \rightarrow \textbf{Fe(OH)}_3 \rightarrow \textbf{FeOOH} \text{ (passive)} \tag{5.3}$$
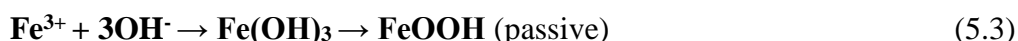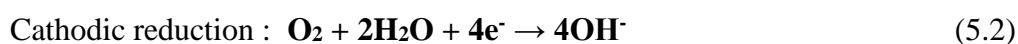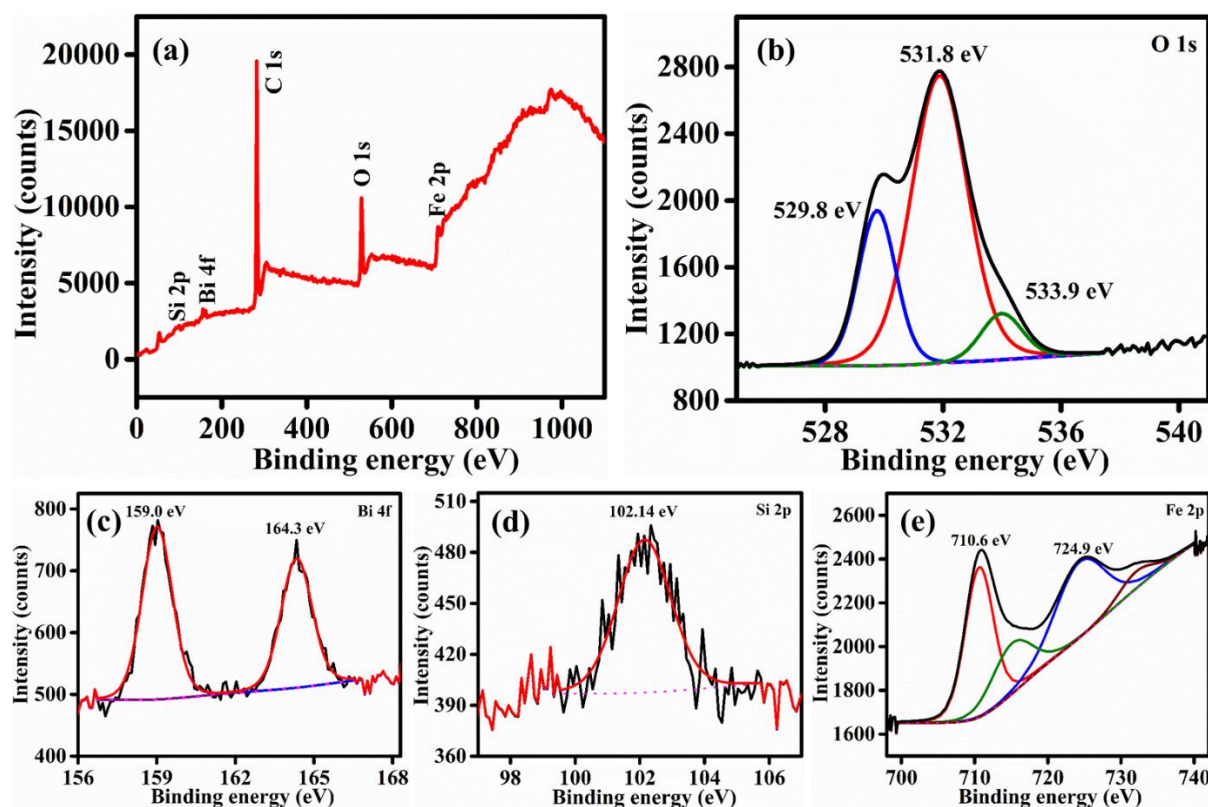
Fig. 5.15. (a) XPS survey spectrum, high resolution deconvoluted XPS spectrum of (b) O1s, (c) Bi4f, (d) Si2p and (e) Fe2p of inhibitive film beneath the 20 wt% $Bi_{3.8}Si_{0.2}V_2O_{11+\delta}$ loaded epoxy coat after continuous electrochemical analysis

More evidence was obtained from a one week immersion test (ASTM G-31 standard) employing 20wt% $Bi_{3.8}Si_{0.2}V_2O_{11+\delta}$ loaded epoxy coating[42]. A cross mark was made on the coating to induce the corrosion process. The SEM-EDS and elemental mapping results of the metal strip after the immersion test was given in the **Fig. 5.16**. The epoxy coating appeared as a smooth surface and the cross mark observed as a channel in the SEM image, **Fig. 5.16a**. The EDS and elemental mapping (**Fig. 5.16b-f**) performed on the cross mark detected the presence of V alongside Fe, O and Si. Under chloride environment, the passive amorphous oxyhydroxide layer developed on the metal substrate facilitated the inhibition process. In addition, the barrier property of Si-O and Bi-O species at the metal-electrolyte interface serve to prevent further corrodent penetration[43, 44]. Most importantly, the role of active vanadate species is undeniable in achieving a very high R_{ct}.
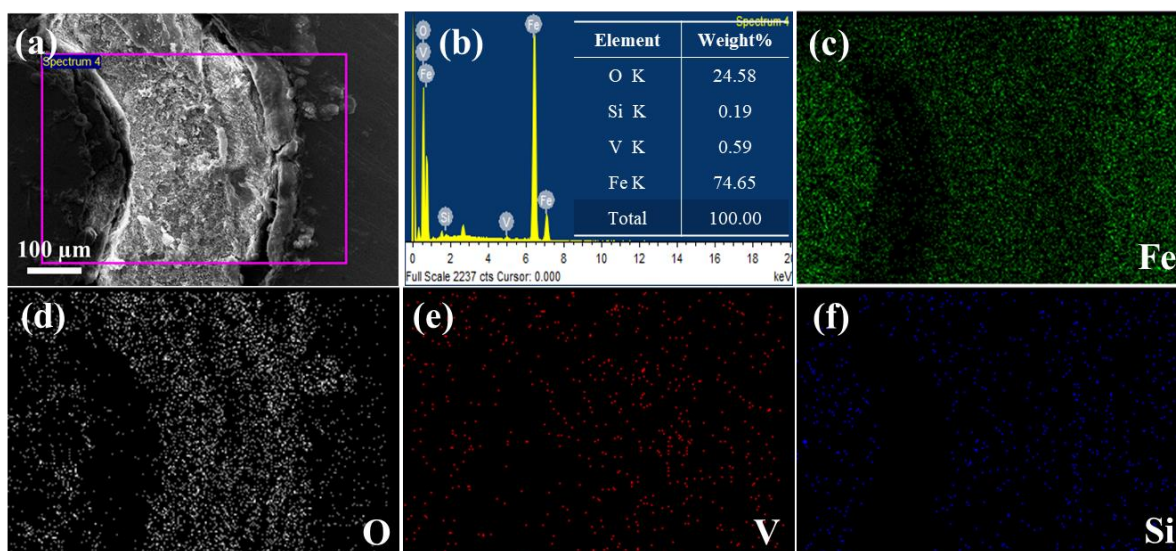
Fig. 5.16. (a) SEM image, (b) SEM-EDS and EDS mapping profile of $Bi_{3.8}Si_{0.2}V_2O_{11+\delta}$ incorporated epoxy coating after immersion test, (c) Fe (green), (d) O (white), (e) V (red) and (f) Si (blue)

A schematic representation of the anticorrosive mechanism involved in $Bi_{3.8}Si_{0.2}V_2O_{11+\delta}$ pigment coating was shown in **Fig. 5.17**. The collective action of passive barriers Bi-O and Si-O initially prevents electrolyte penetration and delays the corrosion process. However, the continuous electrolyte exposure destroys this passive barrier, allowing corrosion to initiate, which is where the active FeOOH and vanadate inhibitors come into action. The vanadate moiety plays a pivotal role in maintaining an extraordinary anticorrosive property and stability of $Bi_{3.8}Si_{0.2}V_2O_{11+\delta}$ orange pigment over an extended period of time[45, 46]. Eventually, the association of passive and active participants in the pigment loaded epoxy coat makes it suitable for long term application. Therefore, the developed pigment can be strongly recommended for replacing commercially available harmful anticorrosive chromates and phosphates.
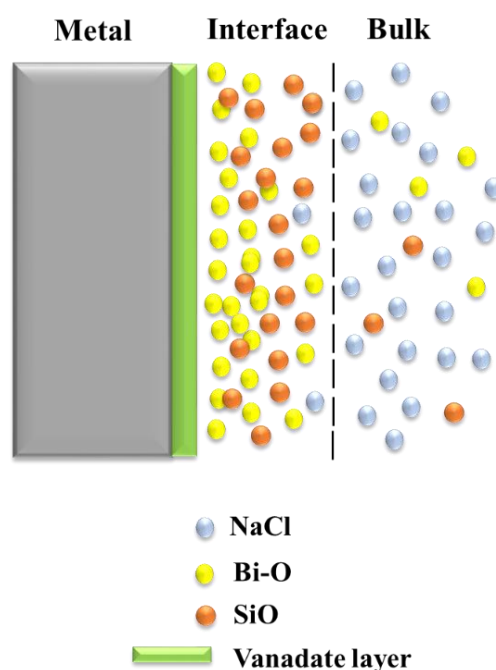
Fig. 5.17. Anticorrosive mechanism of $Bi_{3.8}Si_{0.2}V_2O_{11+\delta}$ incorporated epoxy coating

5.5. Conclusions

An environmentally friendly, intense orange inorganic pigment series was synthesized by incorporating Si^{4+} at the Bi^{3+} site of $Bi_4V_2O_{11}$ crystal lattice. The pigment series exhibited different shades of reddish-orange colours. Among these the composition $Bi_{3.8}Si_{0.2}V_2O_{11+\delta}$ displayed an intense orange hue, with colour coordinates $a^* = 39$, $b^* = 34$ and $L^* = 52$. The colour parameters revealed that the new pigment is better than the reported and commercial orange pigment. A lattice distortion and charge mismatch generated by the incorporation of Si^{4+} helped to reduce the inherent oxygen deficiency in $Bi_4V_2O_{11}$, consequently improving the reflection of orange-red region in the visible spectrum. XPS results further verified the minimization of oxygen deficiency in the compound. The pigment demonstrated a phenomenal NIR solar reflectance of 86%, which was greatly improved in its acrylic coatings. $Bi_{3.8}Si_{0.2}V_2O_{11+\delta}$ coating achieved a temperature reduction of 2 ºC compared to commercial orange in a specially designed experimental setup, substantiating that the new pigment can be employed as an excellent 'cool' roof pigment. The pigment incorporated epoxy coating exhibited an outstanding corrosion resistance with $R_{ct} = 1.6\times10^{10}$ Ωcm^2 on steel in marine conditions. Its superior stability was contributed by the combination of passive and active mechanisms from Bi-O, Si-O and FeOOH, vanadate moieties in the pigment composition, respectively. Therefore, the new multifunctional high-performance $Bi_{3.8}Si_{0.2}V_2O_{11+\delta}$ pigment is recommended as a potential replacement for the present toxic candidates in the market.

5.6. References

1. Bae, B.; Takeuchi, N.; Tamura, S.; Imanaka, N. J. D.; Pigments, Environmentally friendly orange pigments based on hexagonal perovskite-type compounds and their high NIR reflectivity. **2017,** *147*, 523-528.

2. FitzHugh, E. W., *Artists' pigments: a handbook of their history and characteristics.* National Gallery of Art: 1997.

3. De Keijzer, M., The history of modern synthetic inorganic and organic artists' pigments. In *Contributions to conservation: research in conservation at the Netherlands Institute for Cultural Heritage (ICN Instituut Collectie Nederland)*, 2002; pp 42-54.

4. Directive, E. J. O. J. E. C., Restriction of the use of certain hazardous substances in electrical and electronic equipment (RoHS). **2013,** *46*, 19-23.

5. Yuan, L.; Han, A.; Ye, M.; Chen, X.; Yao, L.; Ding, C. J. D.; Pigments, Synthesis and characterization of environmentally benign inorganic pigments with high NIR reflectance: lanthanum-doped $BiFeO_3$. **2018,** *148*, 137-146.

6. de Lima-Neto, P.; de Araujo, A. P.; Araujo, W. S.; Correia, A. N. J. P. i. O. C., Study of the anticorrosive behaviour of epoxy binders containing non-toxic inorganic corrosion inhibitor pigments. **2008,** *62* (3), 344-350.

7. Yan, Y.; Zhu, Y.; Guo, X.; Ge, M. J. T. R. J., The effects of inorganic pigments on the luminescent properties of colored luminous fiber. **2014,** *84* (8), 785-792.

8. Guo, Y.; Mishra, M. K.; Wang, F.; Jankolovits, J.; Kusoglu, A.; Weber, A. Z.; Van Dyk, A.; Beshah, K.; Bohling, J. C.; Roper Iii, J. A. J. L., Hydrophobic inorganic oxide pigments via polymethylhydrosiloxane grafting: Dispersion in aqueous solution at extraordinarily high solids concentrations. **2018,** *34* (39), 11738-11748.

9. Pfaff, G., *Inorganic pigments.* Walter de Gruyter GmbH & Co KG: 2023.

10. Malshe, V. C.; Bendiganavale, A. K. J. R. P. o. C. E., Infrared reflective inorganic pigments. **2008,** *1* (1), 67-79.

11. Jeevanandam, P.; Mulukutla, R.; Phillips, M.; Chaudhuri, S.; Erickson, L.; Klabunde, K. J. T. J. o. P. C. C., Near infrared reflectance properties of metal oxide nanoparticles. **2007,** *111* (5), 1912-1918.

12. Miller, W. B.; Akbari, H.; Levinson, R.; Loye, K.; Kriner, S.; Scichili, R.; Desjarlais, A.; Weil, S.; Berdahl, P. J. i. T. P. o. t. E. E. o. B., IX, proceedings of ASHRAE THERM VIII, Clearwater, FL., Dec, Special infrared reflective pigments make a dark roof reflect almost like a white roof. **2004**.

13. Akbari, H.; Kurn, D. M.; Bretz, S. E.; Hanford, J. W. J. E.; buildings, Peak power and cooling energy savings of shade trees. **1997,** *25* (2), 139-148.

14. Hyde, D. M.; Brannon, S. M. J. C., Investigation of infrared reflective pigmentation technologies for coatings and composite applications. **2006,** *1*.

15. Shiraishi, A.; Takeuchi, N.; Masui, T.; Imanaka, N. J. R. A., Novel environment friendly inorganic red pigments based on $Bi_4V_2O_{11}$. **2015,** *5* (56), 44886-44894.

16. Thejus, P.; Krishnapriya, K.; Nishanth, K. J. S. E. M.; Cells, S., A cost-effective intense blue colour inorganic pigment for multifunctional cool roof and anticorrosive coatings. **2021,** *219*, 110778.

17. Thejus, P.; Krishnapriya, K.; Nishanth, K. J. S. E., NIR reflective, anticorrosive magenta pigment for energy saving sustainable building coatings. **2021,** *222*, 103-114.

18. Zhang, Y.; Ueda, Y. J. I. C., Interlayer Switching of Reduction in Layered Oxide, $Bi_4V_2O_{11-\delta}$ ($0 \leq \delta \leq 1$). **2013,** *52* (9), 5206-5213.

19. Mairesse, G.; Roussel, P.; Vannier, R.; Anne, M.; Pirovano, C.; Nowogrocki, G. J. S. S. S., Crystal structure determination of α, β and γ-$Bi_4V_2O_{11}$ polymorphs. Part I: γ and β-$Bi_4V_2O_{11}$. **2003,** *5* (6), 851-859.

20. Mairesse, G.; Roussel, P.; Vannier, R.; Anne, M.; Nowogrocki, G. J. S. S. S., Crystal structure determination of α, β and γ- $Bi_4V_2O_{11}$ polymorphs. Part II: crystal structure of α-$Bi_4V_2O_{11}$. **2003,** *5* (6), 861-869.

21. Kaur, R.; Thakur, S.; Singh, K. J. P. B. C. M., Effect of two different sites substitution on structural and optical properties of $Bi_4V_2O_{11-\delta}$. **2014,** *440*, 78-82.

22. Nakajima, T.; Abe, H.; Suzuki, Y. J. J. o. t. C. S. o. J., Effect of transition metal oxides addition on the color tone of $Bi_4V_2O_{11}$-based red pigments. **2022,** *130* (2), 236-242.

23. Shannon, R. D. J. A. c. s. A. c. p., diffraction, theoretical; crystallography, g., Revised effective ionic radii and systematic studies of interatomic distances in halides and chalcogenides. **1976,** *32* (5), 751-767.

24. Eppler, D. R.; Eppler, R. A. In *Analyzing the color of reddish glazes*, A Collection of Papers Presented at the 97th Annual Meeting and the 1995 Fall Meetings of the Materials & Equipment/Whitewares: Ceramic Engineering and Science Proceedings, Wiley Online Library: 1996; pp 77-87.

25. Kato, M.; Takahashi, M. J. J. o. m. s. l., Synthesis of Cr-doped $NdAlO_3$-Al_2O_3 reddish pink pigment. **2001,** *20*, 413-414.

26. Kendall, K. R.; Navas, C.; Thomas, J. K.; zur Loye, H.-C. J. C. o. m., Recent developments in oxide ion conductors: Aurivillius phases. **1996,** *8* (3), 642-649.

27. Jiang, Z.; Liu, Y.; Li, M.; Jing, T.; Huang, B.; Zhang, X.; Qin, X.; Dai, Y. J. S. R., One-pot solvothermal synthesis of $Bi_4V_2O_{11}$ as a new solar water oxidation photocatalyst. **2016,** *6* (1), 22727.

28. Meenakshi, P.; Selvaraj, M. J. S. E. M.; Cells, S., Bismuth titanate as an infrared reflective pigment for cool roof coating. **2018,** *174*, 530-537.

29. Dolic, S. D.; Jovanovic, D. J.; Strbac, D.; Far, L. Dacanin, M. D. J. C. I., Improved coloristic properties and high NIR reflectance of environment-friendly yellow pigments based on bismuth vanadate. **2018,** *44* (18), 22731-22737.

30. Kusumoto, K. J. J. o. t. C. S. o. J., Synthesis of Bi_2O_3-ZrO_2 solid solutions for environment-friendly orange pigments. **2017,** *125* (5), 396-398.

31. Yuan, L.; Han, A.; Ye, M.; Chen, X.; Ding, C.; Yao, L. J. C. I., Synthesis and characterization of novel nontoxic $BiFe_{1-x}Al_xO_3$/mica-titania pigments with high NIR reflectance. **2017,** *43* (18), 16488-16494.

32. Chen, J.; Xie, W.; Guo, X.; Huang, B.; Xiao, Y.; Sun, X. J. C. I., Near infrared reflective pigments based on Bi_3YO_6 for heat insulation. **2020,** *46* (15), 24575-24584.

33. Shi, Y.; Zhong, M.; Zhang, Z.; Wang, D. J. C. I., Crystal structure and near-infrared reflective properties of Fe^{3+} doped $AlPO_4$ pigments. **2017,** *43* (8), 5979-5983.

34. Yang, R.; Han, A.; Ye, M.; Chen, X.; Yuan, L. J. S. E. M.; Cells, S., Synthesis, characterization and thermal performance of Fe/N co-doped $MgTiO_3$ as a novel high near-infrared reflective pigment. **2017,** *160*, 307-318.

35. Kavitha, K.; Sivakumar, A. J. I. C. C., Impact of titanium concentration in structural and optical behaviour of nano $Bi_2Ce_{2-x}Ti_xO_7$ (x = 0-1) high NIR reflective and UV shielding yellow and orange pigments. **2020,** *120*, 108163.

36. Jose, S.; Jayaprakash, A.; Laha, S.; Natarajan, S.; Nishanth, K.; Reddy, M. J. D.; Pigments, $YIn_{0.9}Mn_{0.1}O_3$-ZnO nano-pigment exhibiting intense blue color with impressive solar reflectance. **2016,** *124*, 120-129.

37. Ghasemi, E.; Ramezanzadeh, B.; Saket, S.; Ashhari, S. J. J. o. C. T.; Research, Electrochemical investigation of the epoxy nanocomposites containing $MnAl_2O_4$ and $CoAl_2O_4$ nanopigments applied on the aluminum alloy 1050. **2016,** *13* (1), 97-114.

38. Bhoge, Y.; Patil, V.; Deshpande, T.; Kulkarni, R. J. V., Synthesis and anticorrosive performance evaluation of zinc vanadate pigment. **2017,** *145*, 290-294.

39. Chen, Y.-X.; Zhou, D.; Yang, X.; Guo, X.-J.; Zhang, J.-Y.; Liu, J.-K. J. I.; Research, E. C., Enhancing Anticorrosion Properties of Micro-Nano Zinc Vanadate from Atomic Modulation Supplemented by Light Modification. **2021,** *60* (28), 10064-10075.

40. Moulder, J. F.; Chastain, J., *Handbook of X-ray Photoelectron Spectroscopy: A Reference Book of Standard Spectra for Identification and Interpretation of XPS Data*. Physical Electronics Division, Perkin-Elmer Corporation: 1992.

41. Mesarwi, A.; Fan, W.; Ignatiev, A. J. J. o. a. p., Oxidation of the Si (100) surface promoted by Sr overlayer: An xray photoemission study. **1990,** *68* (7), 3609-3613.

42. G31-12a, N. S. T., Standard Guide for Laboratory Immersion Corrosion Testing of Metals. **2012**.

43. Fedel, M.; Deflorian, F.; Rossi, S.; Kamarchik, P. J. P. i. O. C., Study of the effect of mechanically treated CeO_2 and SiO_2 pigments on the corrosion protection of painted galvanized steel. **2012,** *74* (1), 36-42.

44. Boudalia, M.; Laourayed, M.; El Moudane, M.; Sekkat, Z.; Campos, O. S.; Bellaouchou, A.; Guenbour, A.; Garcia, A. J.; Amin, H. M. J. J. o. A.; Compounds, Phosphate glass doped with niobium and bismuth oxides as an eco-friendly corrosion protection matrix of iron steel in HCl medium: Experimental and theoretical insights. **2023,** *938*, 168570.

45. Vega, J.; Granizo, N.; De La Fuente, D.; Simancas, J.; Morcillo, M. J. P. i. O. C., Corrosion inhibition of aluminum by coatings formulated with Al-Zn vanadate hydrotalcite. **2011,** *70* (4), 213-219.

46. Arunima, S.; Deepa, M.; Elias, L.; Thara, T. A.; Geethanjali, C.; Shibli, S. J. A. S. S., Tuning of surface characteristics of composite ($WO_3/BiVO_4$) zinc phosphate coatings for industrial applications. **2021,** *543*, 148822.

Summary and future scope of the thesis

Multifunctional inorganic pigments for cool coating application
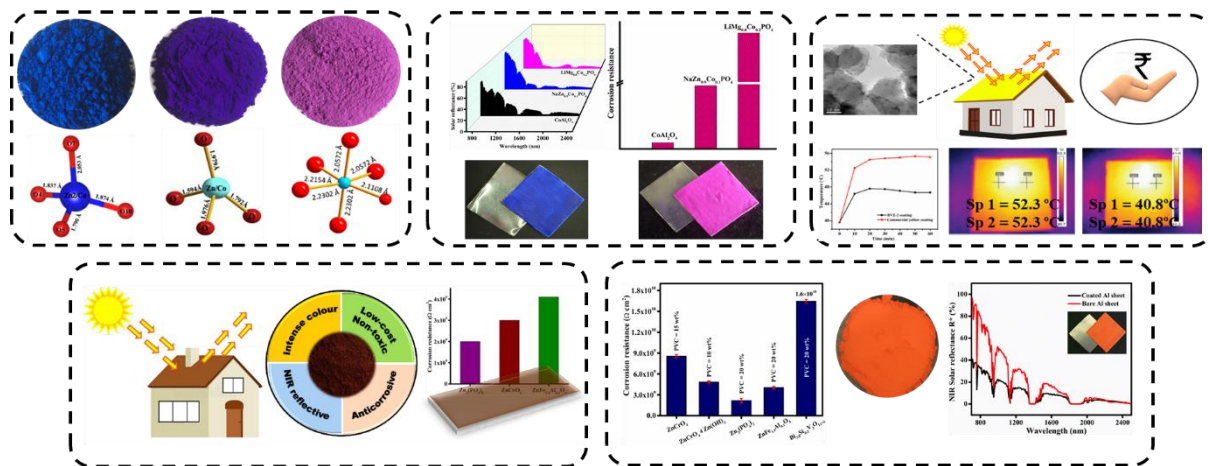
Global temperature rising has been bothering the scientific community for the past several decades. The recent acceleration in its trajectory is rather frightening, with UHI playing a significant role because of increasing urbanization. IR reflective inorganic pigment coatings, widely known as 'cool' coatings, have shown tremendous success in mitigating UHI and hence summer cooling energy demand. Understanding the drawbacks of the existing commercial and reported IR reflective inorganic pigments, the current thesis focused on developing low-cost, non-toxic, intense colour and IR reflective inorganic pigments for cool coating applications. The composition of the pigment was also designed to give the anticorrosive property since the stability of the cool coat is essential in defining its sustainable output.

Inorganic phosphate pigment with the general formula $ABPO_4$ was synthesized via the solid-state method, where A and B are monovalent and divalent cations, respectively. The A and B sites were varied to prepare three base compounds: $NaZnPO_4$, $LiZnPO_4$ and $LiMgPO_4$. Introduction of Co^{2+} chromophore at the B site of each pigment resulted in three different colour pigments, $NaZn_{1-x}Co_xPO_4$ blue, $LiZn_{1-x}Co_xPO_4$ purple and $LiMg_{1-x}Co_xPO_4$ magenta. Spectroscopic investigations of the pigments confirmed the tetrahedral geometry of the chromophore is responsible for the blue and purple colour, whereas octahedral geometry is the reason for the magenta hue. Despite having the same chromophore geometry, the Rietveld refinement structural analysis revealed that considerable distortion of the Co^{2+} geometry in $LiZn_{1-x}Co_xPO_4$ is responsible for the colour divergence from $NaZn_{1-x}Co_xPO_4$. Further, the pigment series of blue and magenta was collected for IR reflectance investigation.

The acrylic coatings of the best composition from each pigment series, $NaZn_{0.9}Co_{0.1}PO_4$ and $LiMg_{0.8}Co_{0.2}PO_4$, exhibited good reflectance property with substantial temperature reduction compared to commercial pigment. The corrosion resistance properties of these pigments were also tested by preparing pigment loaded epoxy coatings on steel in the marine medium. An active mechanism involving $FePO_4$ film formation at the metal electrolyte interface is responsible for the anticorrosive property of the pigment.

$BiVO_4$ is a non-toxic yellow pigment, but its use has been severely constrained because of its high price. $BiVO_4$ and the less expensive white pigment ZnO were combined to develop a complex pigment to reduce the pigment cost. The specific morphology of the complex pigment, $BiVO_4$ nanocrystals decorated spherical ZnO nanoparticles, helped to maintain nearly the same colour strength as pure $BiVO_4$ with improved IR reflectivity. The new complex pigment reduces the expensive $BiVO_4$ component by 75 wt%. Furthermore, compared to commercial yellow, acrylic coatings of the complex pigment exhibited a 7 ℃ temperature drop in the thermal shielding experiment.

Transformation of $ZnFe_2O_4$ from a dark brown colourant to a highly reflective multifunctional pigment was achieved by the substitution of Al^{3+} at the Fe^{3+} site. The cation doping has brought a slight distortion in the octahedral geometry of Fe^{3+} chromophore, resulting in a reduction in forbidden transition intensity, and consequently, enhancement of the pigment reflectance profile. The pigment composition $ZnFe_{1.9}Al_{0.1}O_4$ showed excellent corrosion resistance with good stability that works through a hydroxide film deposition at the metal electrolyte interface. Excitingly, the corrosion analysis results were comparable to the toxic commercial anticorrosive pigments.

An intense orange pigment was developed from a brownish-red $Bi_4V_2O_{11}$, where Si^{4+} was doped at the Bi^{3+} site by the solid-state method. The introduction of Si^{4+} could slightly reduce inherent oxygen deficiency in $Bi_4V_2O_{11}$ crystal lattice, thereby improved the reflectance in orange-red region. The composition $Bi_{3.8}Si_{0.2}V_2O_{11+\delta}$ displayed a better colour and reflectance properties than commercial orange pigment. Most importantly, the corrosion resistance of the same pigment was outstanding, with exceptional stability, which is superior to the commercial pigments. An active and passive mechanism together supported the stability of the pigment coating in the marine medium. Overall, the thesis highlights the development of outstanding multifunctional inorganic pigments that can be implemented as a potential alternative for commercial pigments in cool coating applications.

Future scope

- Cost reduction by fine tuning the synthetic strategies

- Exploration of nano architecture for enhancement in reflectance and corrosion resistance

- Accelerated weatherability studies of the prepared pigments

- Commercial validation of colour, reflectance and corrosion resistance

ABSTRACT

Name of the student: Thejus P K	**Registration No:10CC18A39003**
Faculty of study: Chemical sciences	**Year of submission: 2023**
CSIR Lab: National Institute for Interdisciplinary Science & Technology (CSIR-NIIST), TVM, Kerala	**Name of the Supervisor: Dr K G Nishanth**

Title of the thesis: *Design and development of multifunctional inorganic pigments for cool coating applications*

The thesis focuses on developing non-toxic, cost-effective, intense colour, IR reflective and corrosion resistant multifunctional inorganic pigments for cool coating applications. Thesis comprises five chapters. Chapter 1 gives a brief idea of the current status of global temperature rise, the UHI phenomenon, factors affecting and consequences of UHI. Later, it discusses the importance of cool coatings and IR reflective inorganic pigments in mitigating the issue finally, the need for a multifunctional inorganic pigment. Chapter 2 is divided into two sections, where Chapter 2A deals with the synthesis and colour analysis of three inorganic phosphate pigment series having blue, purple and magenta colours. Further, structural studies have performed to develop a correlation between the colour and tetrahedral geometry of the chromophore through Rietveld refinement analysis. Chapter 2B involves the IR reflectivity investigation of the blue and magenta pigment series. Subsequently, the best composition from the series was selected for thermal shielding and anticorrosive analysis. In Chapter 3, a complex yellow pigment was developed by combining $BiVO_4$ and ZnO via the citrate-gel method. The peculiar morphology of the complex pigment, $BiVO_4$ nanocrystals decorated on ZnO spherical particles, was able to reduce the weight percentage of costly $BiVO_4$ by 75% without compromising its colour strength. Synthesis of a high IR reflective $ZnFe_2O_4$ brown pigment series was discussed in Chapter 4. The incorporation of Al^{3+} at the Fe^{3+} site has brought a substantial enhancement in the reflectance profile of $ZnFe_2O_4$ without any colour deterioration. The pigment also had excellent corrosion resistance with good stability. Chapter 5 describes the development of an intense orange pigment from a dark brownish-red $Bi_4V_2O_{11}$. In addition to colour, Si^{4+} substitution at the Bi^{3+} site has brought significant enhancement in IR reflectance and high corrosion resistance with exceptional stability. The developed multifunctional inorganic pigments can be used as an alternative to the current pigments in the market.

Thesis outcomes

List of publications emanating from the thesis work

1. **P. K. Thejus**, K. G. Nishanth, Rational approach to synthesis low-cost $BiVO_4$-ZnO complex inorganic pigment for energy efficient buildings. *Sol. Energy Mater. Sol. Cells.* **2019**, 200, 109999.

2. **P. K. Thejus**, K. V. Krishnapriya, K. G. Nishanth, A cost-effective intense blue colour inorganic pigment for multifunctional cool roof and anticorrosive coatings. *Sol. Energy Mater. Sol. Cells*. 2021, 219, 10778.

3. **P. K. Thejus**, K. V. Krishnapriya, K. G. Nishanth, IR reflective, anticorrosive magenta pigment for energy saving sustainable building coatings. *Sol. Energy*. 2021, 222, 103-114.

4. **P. K. Thejus**, K. V. Krishnapriya, K. G. Nishanth, Inorganic ferrite brown; transformation towards a versatile pigment for energy efficient constructions. *J Ind. Eng. Chem*. 2023, 122, 349-358.

5. **P. K. Thejus**, K. V. Krishnapriya, K. G. Nishanth, Development of new intense orange multifunctional inorganic pigment from $Bi_4V_2O_{11}$ (Manuscript to be communicated)

List of publications not related to the thesis work

1. Krishnapriya K. V., **Thejus P. K.**, Nithyaa J., Nishanth K. G. Anticorrosive Performance of Mangifera indica L. Leaf Extract-Based Hybrid Coating on Steel. *ACS Omega*. 2019, 4, 10176−10184.

2. Krishnapriya K. V, Mohan B, **Thejus P. K.**, Sasidhar B. S, Nishanth K. G. Green approach in anticorrosive coating for steel protection by Gliricidia sepium leaf extract and silica hybrid. *J. Mol. Liq.* 2023, 369, 120967.

List of conference presentations

1. **Thejus P. K**., Nishanth K. G. poster presented entitled "Cool Roof Materials for Energy Efficient Buildings" in 8th East Asia Symposium on Functional Dyes and Advanced Materials EAS8 2017, CSIR-NIIST, Thiruvananthapuram.

2. **Thejus P. K.**, Nishanth K. G. poster presented entitled "IR reflective Intense Purple colour Inorganic Pigment" in National Conference on Emerging Trends in Science, Technology & Application of Electron Microscopy STAEM-2018. CSIR-NIIST, Thiruvananthapuram.

3. **Thejus P. K.**, Nishanth K. G. poster presented entitled "Multifunctional Inorganic blue pigment" in NMD-ATM 2019 International Symposium on "Advanced Materials for Industrial and Societal Applications" Kovalam, Thiruvananthapuram.
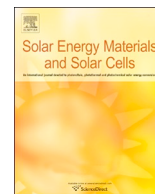
Rational approach to synthesis low-cost BiVO₄–ZnO complex inorganic pigment for energy efficient buildings

P.K. Thejus[a,b], K.G. Nishanth[a,b,*]

[a] Materials Science and Technology Division, CSIR-National Institute for Interdisciplinary Science and Technology (NIIST), Thiruvananthapuram, 695019, India
[b] Academy of Scientific and Innovative Research (AcSIR), Ghaziabad, 201002, India

ARTICLE INFO

ABSTRACT

Bismuth vanadate (BiVO₄) gathered great attraction as a yellow inorganic pigment which could replace the conventional chrome and cadmium yellow. However, its high cost over other yellow pigment restricted its usage. Therefore, there is a huge demand is existing to develop cost-effective BiVO₄ inorganic pigment without compromising its optical properties. In this work, we demonstrate an effective strategy to develop low-cost BiVO₄ complex pigments. Nano particles of BiVO₄ decoration on white pigment are achieved by the citrate-gel method. An appreciable decrease in BiVO₄ content (75%) has been observed. The reduction in the BiVO₄ have shown a remarkable impact on the economic viability of the new complex pigment. The developed complex inorganic pigment exhibited excellent greenish-yellow colour (a* = −6.28, b* = 76.45), which is similar to pure BiVO₄. An exceptional near infrared reflectance has been recorded, which is estimated as high as 90%. High reflective coatings of developed complex pigment displayed significant response for temperature shielding experiment, could achieve reduction of 8.4 °C in the interior temperature, compared to the commercially available yellow coating. Moreover, the present work demonstrates that developed complex pigment could be a potential replacement for BiVO₄ yellow pigment.

1. Introduction

Solar radiation fall on earth surface consists of 45% infrared (IR), 50% visible and 5% ultraviolet (UV) rays. Absorption of IR rays radiate heat energy and leads to heat island effect in heavily constructed urban sectors. Urban heat island effect (UHI) is the phenomenon of temperature accumulation in an urban area compared to the surrounded rural region due to human activities [1]. Beside UHI, global warming and atmospheric pollution also play a significant role in atmospheric temperature rise. Uncomfortable interior building temperature, electricity over consumption via space cooling appliances and shorter roof life are the primary concerns of this issue [2]. Reports suggest that increase of peak electricity load varies between 0.45 and 4.6% for rise in each degree of atmospheric temperature. Some of these problems have successfully addressed by employing exclusive 'cool pigment' coatings on exterior walls. Inorganic pigments which can reflect a high percentage of NIR rays from sunlight classified as 'cool pigments' [3–7]. Conventional yellow inorganic pigments like PbCrO₄, CdS, Pb₂Sb₂O₇,

As₂S₃ are excellent, intense colour inorganic pigments, though the inclusion of toxic metal chromophores is alarming [8]. Among which, BiVO₄ yellow stands out because of its non-toxicity and high NIR reflectance property [9–12]. It has been started to use over the last two decades in coatings, ceramics, plastics and inks. However, its consumption rate has been limited because of the very high cost. The main bottleneck for the widespread usage of this nontoxic yellow pigment is its cost because of the presence of expensive Bi content. Therefore, it is very much interested to develop a cost-effective BiVO₄ pigment without compromising its excellent properties.

Conventional cost-effective approach for pigment synthesis involves reduction of the expensive component in the material composition. It is achieved either by developing complex pigments or substitution pigments. Pigment particle supported over a relatively cheaper and readily available material describe complex pigments, whereas substitution of transition or lanthanide metal chromophore in the host lattice, involved in substitution pigments. It believed that complex pigment is a very effective strategy to reduce the cost of the expensive pigments without

---

compromising its properties. Complex materials generally have an advantage that it can acquire the properties of its constituents, offering a broad range of application. Recently, a couple of hybrid $BiVO_4$ pigments brought attention that, core-shell architecture $BaSO_4@BiVO_4$ by Lin Guan et al. and nano-decorated $BiVO_4$ on attapulgite rods [13,14]. A significant reduction in $BiVO_4$ content with good colour strength achieved by core-shell morphology. However, a detailed study on its NIR reflectance and thermal shielding performance of coatings are yet to explore. Even though superior colour strength with NIR reflectance above 80% achieved for nano $BiVO_4$-attapulgite, its processing temperature and cost are still on the higher side. $BiVO_4$ coated mica-TiO_2 sheets developed by Lin Yuan et al., exhibited good thermal insulation performance, attained a 4.5 °C decrease in inner surface temperature [15]. On the other hand, there are many substituted compounds also reported, Wendusu et al. (Bi, Ca, Zn, La)VO_4, Toshiyuki Masui et al. (Bi, Ca, Zn)VO_4, M C. Nevesa et al. Ce doped $BiVO_4$ are some of them having great yellow hue [16–18]. However, the majority of these works are not focused on the cost reduction point of view.

In this scenario, there is an excellent incentive for developing a profitable material combo for cost-effective $BiVO_4$ yellow pigment. Current work illustrates a synthetic strategy to develop a complex pigment, employing cheaper and readily available white pigments (WP) ZnO, TiO_2, SiO_2 and Al_2O_3 as supporting material. $BiVO_4$ particles are allowed to grow on white pigment surface through a citrate-gel method followed by a single stage firing. $BiVO_4$ incorporated hollow ZnO particle is previously reported, but detailed studies were lacking on its chromatic and reflectance properties [19]. The present study deals a detailed investigation on morphology, chromatic and reflectance properties of various $BiVO_4$ based complex pigments. Solar thermal shielding performance of the developed pigment was evaluated and compared with commercial yellow paint, to demonstrate cool coating nature.

2. Experimental

2.1. Materials and methods

$BiVO_4$ complex pigment synthesised by the citrate-gel method. Analytical grade chemicals purchased from Sigma-Aldrich, were used as received without further purification. Three mmol $BiVO_4$ precursor solution was prepared for the synthesize of $BiVO_4$–ZnO complex pigment, in which, 50 ml solution of $Bi(NO_3)_3.5H_2O$ (3 mmol) and citric acid monohydrate (6 mmol) were prepared in distilled water and mixed under continuous stirring. Subsequently, 50 ml NH_4VO_3 solution was added dropwise under vigorous stirring. The resultant yellow solution heated at 150 °C for 1 h after the slow addition of WP. It was dried to get solid xerogel form and ground well, afterwards calcined at 500 °C for 3 h under air atmosphere. $BiVO_4$–ZnO complex pigment loaded with different wt% $BiVO_4$ have synthesized by changing the weight of WP. Weight of WP has shown in parenthesis, 50% $BiVO_4$–ZnO (1 g), 25% $BiVO_4$–ZnO (3 g), 15% $BiVO_4$–ZnO (5.6 g), 10% $BiVO_4$–ZnO (9 g) and denoted as BVZ-1, BVZ-2, BVZ-3 and BVZ-4, respectively. Among which BVZ-2 exhibited best colour strength, hence rest of the complex pigment combinations with Al_2O_3, SiO_2 and TiO_2 have also prepared at 25 wt% $BiVO_4$, represented as BVA-2, BVS-2, BVT-2 respectively and pure $BiVO_4$ as BVO. Further, BVZ-2 mixed pigment prepared by the physical mixing of BVO and ZnO in 1:3 ratio followed by calcination at 500 °C and compared with BVZ-2 complex pigment.

BVZ-2 has used for coating applications on concrete block and Al sheet. Pigment (3 g) and acrylic binder (3 g) 1:1 ratio dispersion (50% pigment volume concentration) has prepared by ultrasonication, which was painted over the TiO_2 base coated concrete block and Al sheet [20–22]. Thermal shielding performance of BVZ-2 and commercial yellow coatings were compared by constructing an experimental setup, schematic diagram shown in Fig. A1 [23]. Initially, BVZ-2 and commercial yellow coatings were prepared on 19 × 19 cm Al sheets by the

same procedure described above. Coated Al sheets were roofed on two different foam boxes (size = 15 × 15 × 15 cm) without any air gap and then exposed under IR lamp (Philips,250 W) for 1 h. Rooftop and IR lamp kept at a distance (h) of 40 cm. A thermocouple fixed 2 cm below the coated roof, and temperature variation was recorded at 10 min intervals using a temperature sensor. Same experiment was followed using commercial yellow coated Al sheet.

2.2. Characterization

Synthesised complex pigments characterized by Powder X-ray Diffraction analysis using Philips X'pert Pro diffractometer, Ni-filtered Cu-Kα (λ = 0.154060 nm) radiation. Data were collected by step scanning over a 2θ range from 10 to 75° with a step size of 0.03° and 20 s counting time at each step. Morphology studies were done using a Scanning Electron Microscope (SEM) JEOL JSM-5600 model. Pigment coating thickness was measured using optical microscope. Energy Dispersive X-ray Spectroscopy (EDS) was conducted using a silicon drift detector X-MaxN attached with a Carl Zeiss EVO SEM apparatus. High-Resolution Transmission Electron Micrographs (HRTEM) were recorded on a FEI (Tecnai 30 G2 S-TWIN, The Netherlands) operating at an accelerating voltage of 300 kV. Particle size measured by Dynamic Light Scattering experiment using Malvern Instruments Zeta sizer nano Zis Model No: ZEN 3600. UV–vis–NIR Spectrophotometer (Shimadzu UV-3600 with an integrating sphere attachment, ISR-2200) used for the optical studies of pigment samples and coatings with Barium sulfate as a reference for UV–Vis range (300–700 nm) and polytetra-fluoroethylene (PTFE) for NIR range (700–2500 nm). The parameter C^* (chroma) represents saturation of the colour and defined as $C^* = \sqrt{(a^*)^2 + (b^*)^2}$ the hue angle, h^o is expressed in degrees and ranges from 0 to 360° and is calculated by using the formula $h^o = \tan^{-1}(b^*/a^*)$. The NIR solar reflectance (R^*) in the wavelength range from 700 to 2500 nm was calculated according to ASTM standard number E891-87 as reported elsewhere [24–26]. Further measurement details are described in our previous report [27].

$$R^* = \frac{\int_{700}^{2500} r(\lambda)i(\lambda)d(\lambda)}{\int_{700}^{2500} i(\lambda)d(\lambda)}$$

where $r(\lambda)$ is the experimentally obtained spectral reflectance (Wm^{-2}), and $i(\lambda)$ is the solar spectral irradiance ($Wm^{-2} nm^{-1}$) obtained from ASTM standard E891-87.

3. Results and discussion

3.1. PXRD analysis

Cost-effective BVO complex yellow pigments have developed by incorporating commercially available inexpensive WP via citrate gel method. Calcination temperature for the synthesis was optimised to obtain monoclinic scheelite crystal structure (m-s) BVO, which is the well-known vivid yellow pigment [14]. Temperature optimization has carried out for the composition BVZ-2 from 300 to 500 °C at a dwell time of 3 h, and the corresponding PXRD pattern was analysed, exhibited in Fig. 1a. Well-defined crystal plane reflections of ZnO and m-s BVO obtained at each temperature. However, an impurity peak at 2θ = 24.40° identified at 300 and 400 °C (marked as *), which correspond to the Bi_2O_3 phase [28]. Further, elevation to 500 °C it is found that the impure phase is disappeared, hence fixed it as the optimum synthetic temperature. It is worth noting that the particular synthetic route could reduce the BVO processing temperature to 500 °C for 3 h, which was rather prepared via solid state route at high temperature 800 °C and long dwell time 6 h including intermediate grinding [29,30].

Fig. 1b shows the PXRD of synthesised complex pigments with different compositions of BVO and ZnO. The m-s BVO (marked *) phase is indexed using JCPDS file no.14–0688. Hence, confirmed the
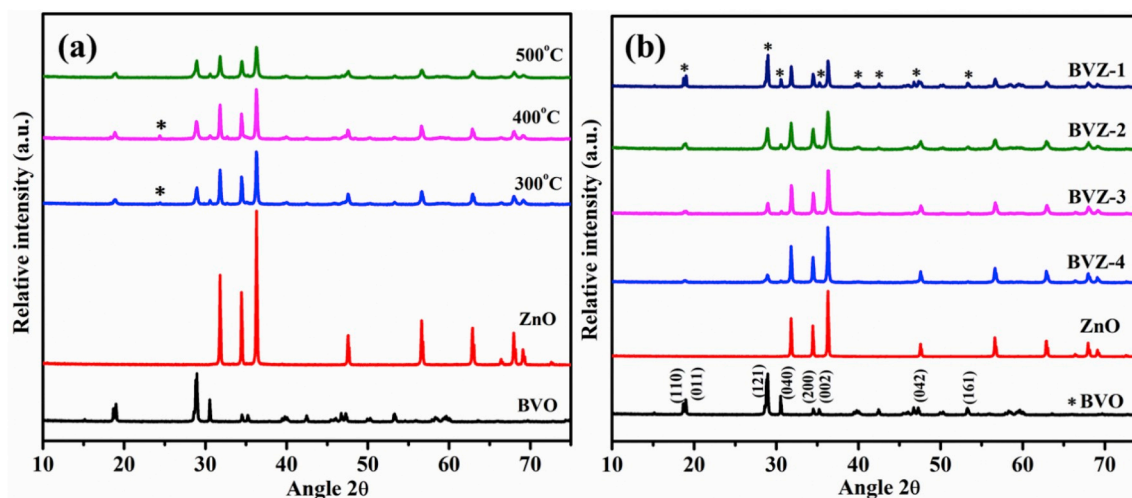
Fig. 1. PXRD pattern of (a) temperature optimization of BVZ complex pigment (b) BVZ with different compositions.
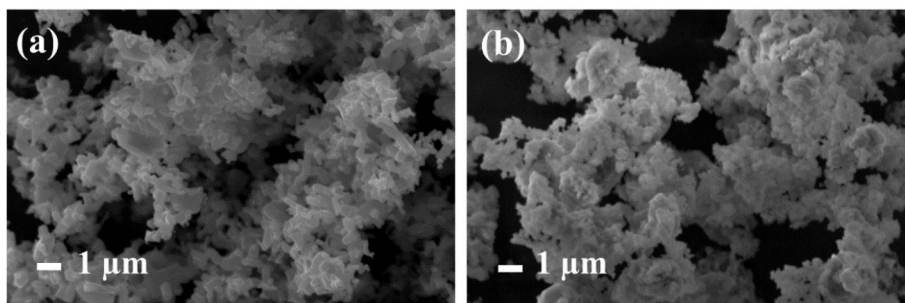
Fig. 2. SEM image of pristine (a) ZnO and (b) BVZ-2 complex pigment.

formation of BVZ complex pigment. Phase formation of rest of the pigment combinations BVS-2, BVA-2 and BVT-2 have also ensured from the respective PXRD graph, shown in Fig. A2. The XRD peak intensity of BVO and ZnO in BVZ has strictly followed the expected trend, viz from BVZ-1 to BVZ-4 with a decrease in BVO content it has shown a proportional decrease in BVO peak intensity and vice versa for ZnO. Interesting observation is that (121) diffraction peak intensity of BVO in complex pigments have slightly decreased particularly for BVZ-2, BVS-2 and BVT-2. Typically, precursors Bi^{3+} and $(VO_4)^{3-}$ expected to deposit

over pristine WP allowing free growth of yellow BVO at 500 °C. Consequently, the extent of BVO coverage proportionally intensifies the XRD peaks. Hence, the decreasing peak intensity in XRD attributed to limited surface coverage on WP could be due to lower BVO to WP wt% ratio and aggregating nature of BVO particles.

3.2. Morphology and particle size

In order to have a detailed understanding of the morphology of
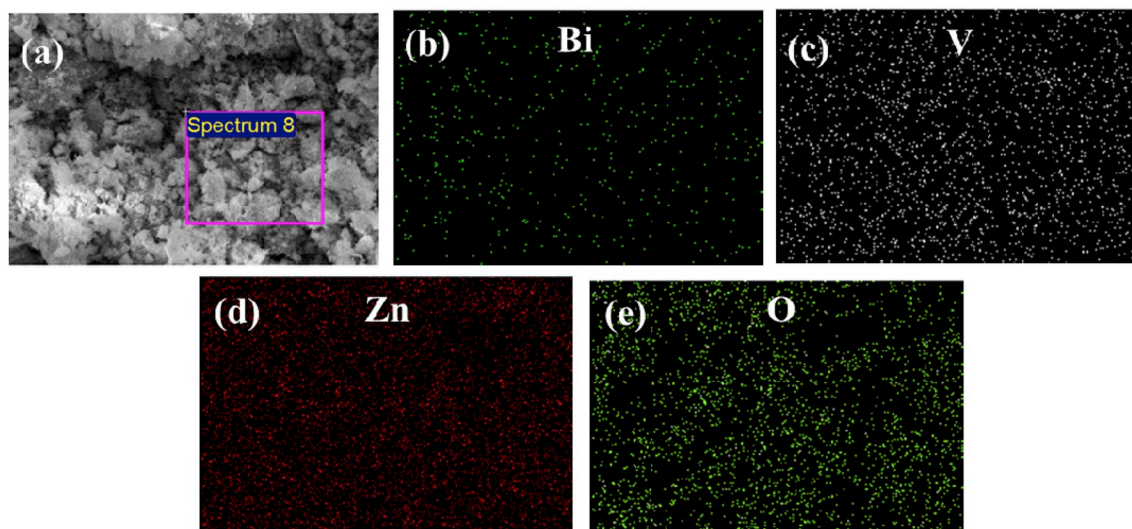
Fig. 3. EDS mapping profile of BVZ-2 complex pigment, (a) SEM image, (b) Bi (green), c) V (white) (d) Zn (red) and (e) O (greenish yellow). (For interpretation of the references to colour in this figure legend, the reader is referred to the Web version of this article.)

Table 1

DLS particle size of precursor WP and complex pigments.

Precursor WP	Particle size (nm)	Complex pigment	Particle size (nm)
ZnO	184	BVZ-1	197
		BVZ-2	204
SiO$_2$	227	BVZ-3	212
		BVZ-4	224
TiO$_2$	177	BVS-2	345
		BVT-2	228
Al$_2$O$_3$	229	BVA-2	581

complex pigments SEM analysis was conducted. The aggregation due to the free growth of BVO over WP formed a coral-like morphology, particularly for BVZ-2, shown in Fig. 2 and A3. However, unlike a perfect surface coverage, it was decorated discontinuously throughout the WP surface. Calculation of average particle size from the SEM image appeared difficult due to agglomeration. Subsequently, DLS particle size of all the precursor WP and respective complex pigments have shown in Table 1. Average particle size of the complex pigments ranges from 150 to 600 nm, 204 nm particularly for BVZ-2 (Fig. A4), which is excellent in terms of coating application. Elemental mapping of BVZ-2 pigment has displayed in Fig. 3, where the distribution of Bi, V, O and Zn elements illustrates the successful formation of the complex pigment. Further, compositional confirmation has obtained from EDS plot (Fig. A5) in which weight percentage of BVO in the synthesised complex pigment estimated to be 25%, Table 2.

TEM image Fig. 4a shows the presence of well dispersed homogeneous BVZ-2 nanoparticles having granular shape with an average particle size between 15 and 25 nm. The particle size from DLS attributed to the bulk particle, whereas HRTEM reveals the size of monodispersed primary particles. SAED pattern displayed in Fig. 4b indicated the high degree of crystallinity of the pigment material. Excitingly, BVO particles formed over ZnO composed of randomly distributed
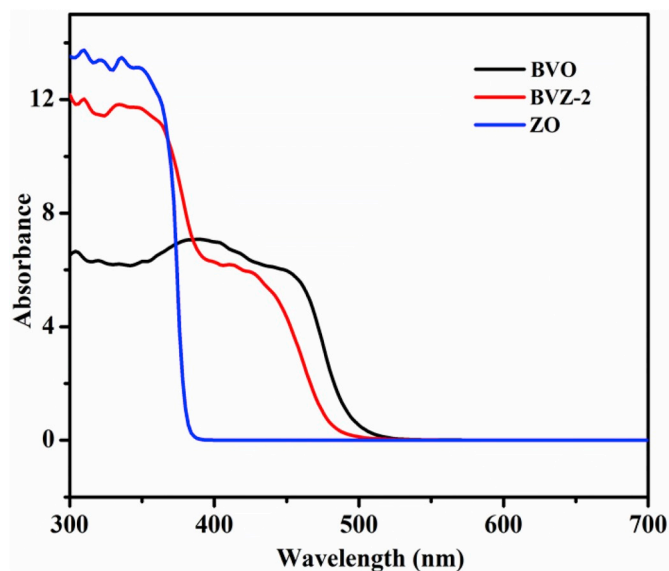
Fig. 5. UV–Vis absorption spectrum of BVZ-2 compared with its constituents.

nanocrystallites with diameter 2–5 nm, Fig. 4c. Ordered fringes corresponding to the crystalline planes of ZnO observed from the HRTEM image shown in Fig. 4d. The lattice spacing measured to be 0.24 nm corresponding to (101) plane of ZnO match with PXRD. EDS in Fig. A6 confirmed high purity and stoichiometry of BVZ-2 as well.

3.3. UV–Vis–NIR absorption properties

UV–Vis absorption spectrum of BVZ-2 has depicted in Fig. 5, shows two broad, intense absorption bands, which composed of BVO and ZnO
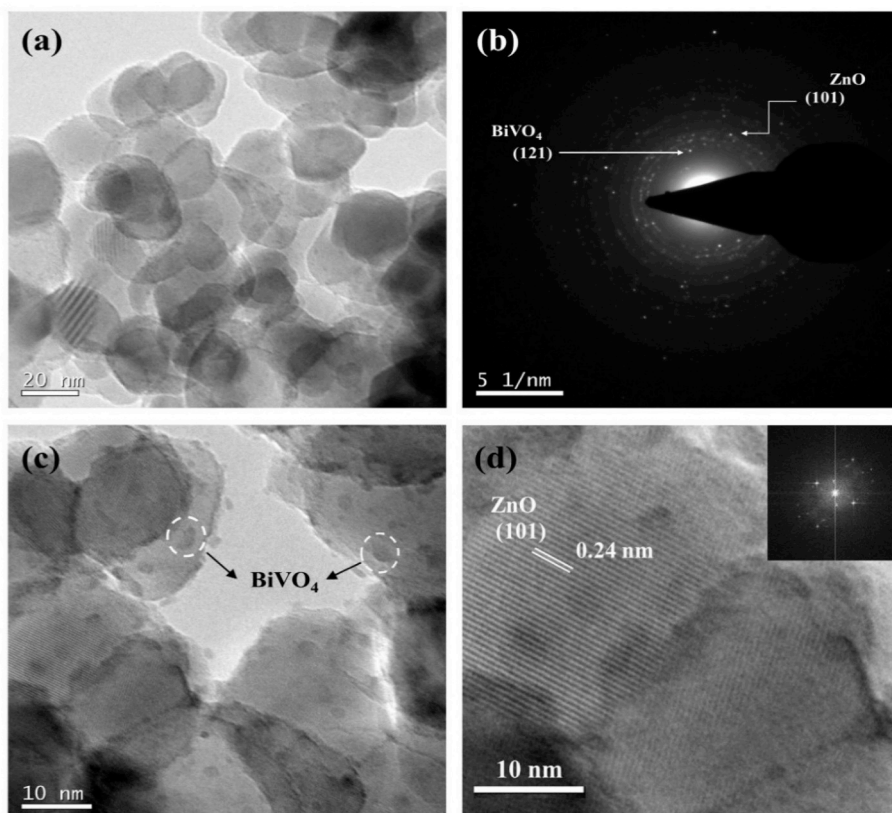
Fig. 4. (a), (c) TEM image, (b) SAED pattern and (d) crystal lattice of BVZ-2 sample, diffraction pattern shown in the inset.

Table 2
EDS analysis of complex pigments.

Element	Weight %	Element	Weight %	Element	Weight %
BVZ-2		BVS-2		BVA-2	
O K	20.01	O K	53.12	O K	46.72
V K	4.39	V K	3.15	V K	4.27
Zn K	55.53	Si K	29.82	Al K	28.94
Bi M	20.07	Bi M	13.91	Bi M	20.08
Total	100.00	Total	100.00	Total	100.00

absorption profile, validates that both the constituents were present without any chemical modifications in the synthesized complex pigment. Absorption at 395–500 nm is the characteristic absorption of BVO attributed to the charge transfer from valence band formed by complex orbitals Bi6s and O2p to the conduction band V3d orbital [31]. BVO absorption extended slightly towards the blue region of the visible spectrum, which is the reason for the +ve a* value of the material.

BVZ-2 shown slightly blue-shifted absorption band to that of BVO, where the bandgap calculated for BVZ-2 and BVO was 2.49 and 2.40 eV, respectively. It could be due to the ZnO secondary phase and surface defects in the material [32,33]. It strictly confined the absorption spectrum in violet-indigo region, allow to have a brighter and pure yellow colour for the pigment. Absorption at 350 nm can be assigned to the $\pi \rightarrow \pi^*$ electronic transitions of ZnO from the valence band to the conduction band (O2p $\rightarrow$ Zn3d) [19,34–36].

3.4. Chromatic and reflectance properties

Colour co-ordinates of all the prepared pigments have measured using CIE 1976 L*a*b* system and summarised in Table 3. Compounds BVZ-1 and BVZ-2 were observed to be the best compositions since it precisely matching with BVO in their colour quality. Colour co-ordinates b* > 76 with a slight negative a* provided exceptional yellow hue for both BVZ-1 and BVZ-2. Moreover, 85-95° hue angle and C* > 75 colour purity were also supportive of its vibrant yellow colour, photograph displayed in Fig. 6. Visible light absorption of the devel-

Fig. 6. Photographs of (a) BVZ-2, (b) BVS-2, (c) BVA-2, (d) BVT-2 complex pigments and (e) BVZ-2 mixed pigment.

Table 3
Colour co-ordinates of synthesized complex pigments.

Sample	L*	a*	b*	C*	h°	NIR reflectance* (%) at 1100 nm	NIR Solar reflectance R* (%)
BVO	82.43	4.25	76.26	76.38	86.80	75.94	73.51
BVZ-1	89.06	−1.34	76.64	76.65	91.01	95.37	89.40
BVZ-2	91.53	−6.28	76.45	76.78	94.78	98.33	90.18
BVZ-3	86.79	4.92	53.50	53.73	84.74	99.64	92.43
BVZ-4	90.87	2.88	41.81	41.91	86.05	98.13	90.71
BVS-2	89.84	−2.67	72.41	72.46	92.12	92.43	85.86
BVA-2	89.15	−3.83	72.90	73.00	93.02	87.75	85.45
BVT-2	87.42	−3.88	62.42	62.54	93.56	90.98	85.79
BVZ-2 mixed pigment	92.73	−3.45	47.88	48.00	94.13	94.99	93.67
Core shell BaSO$_4$@BiVO$_4$[12]	74.92	−8.32	76.26	76.71	96.23	–	–
BiVO$_4$ coated mica – TiO$_2$[13]	83.09	4.07	53.07	53.16	–	–	–

Fig. 7. (a) NIR reflectance, (b) NIR solar reflectance spectra of BVZ-2 compared with BVO.

Fig. 8. TGA graph of BVO and BVZ-2.

Table 4

CIE L*a*b* colour co-ordinates of BVZ-2 complex pigment after chemical treatment.

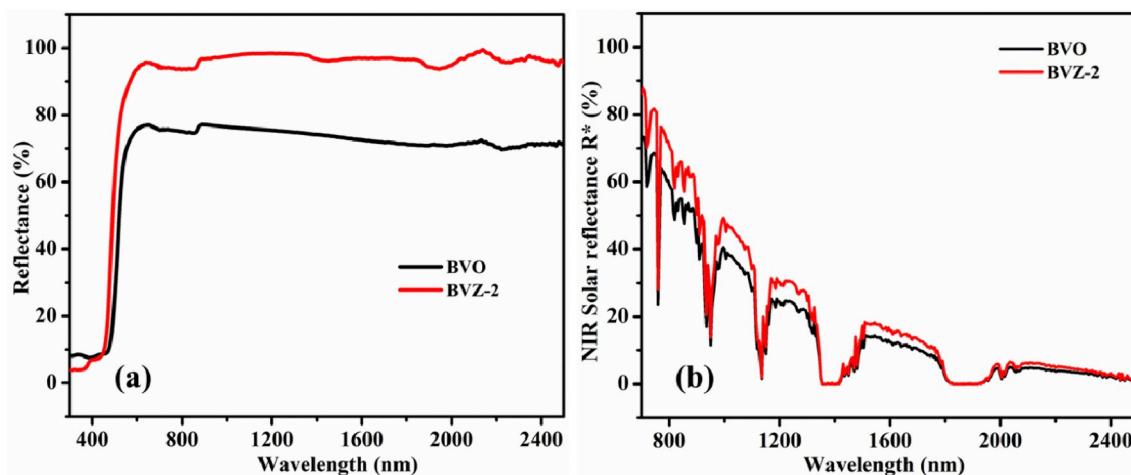| Sample	pH	L*	a*	b*	c*	# ΔE^*_{ab}
BVZ-2	–	91.53	−6.28	76.45	76.78	–
Water	7.00	91.45	−5.99	76.22	76.45	0.38
HCl	3.05	90.88	−5.86	76.30	76.52	0.78
HNO_3	3.17	91.10	−6.08	75.85	76.09	0.76
H_2SO_4	3.18	90.92	−5.62	75.69	75.89	1.17
NaOH	10.52	90.96	−5.95	76.01	76.24	0.79

of synthetic strategy of present complex pigment.

3.5. Thermal and chemical stability

Thermal behaviour of complex pigment has analysed by TGA measurement carried out between 30 and 900 °C temperature range, as shown in Fig. 8. Negligible weight loss observed up to 150 °C for BVZ-2 and BVO pigments, attributed to the removal of adsorbed water molecules [39]. Subsequently, two step weight loss has observed for the parent BVO pigment, from 150 to 620 °C and 620–900 °C. Further, it is interesting to notice that, 2% overall weight loss was calculated for BVZ-2 whereas 3.6% for BVO, which indicate the thermal stability is slightly improved for the complex pigment. Presence of thermally stable ZnO supportive matrix could influence the temperature stability of the BVZ-2 complex pigment. Moreover, further growth in $BiVO_4$ nano crystals can occur at temperature higher than the formation temperature. Both contribute to the decrease in weight loss for BVZ-2. The chemical stability of BVZ-2 ensured in aqueous, acid and base media [23]. Colour co-ordinate measurements after the chemical treatment enumerated in Table 4. The colour difference with the untreated sample stayed well within the industrial limit $\Delta E^*_{ab} \leq 1$ unit [24–26]. Hence confirmed the chemical stability of the synthesised complex pigment BVZ-2.

3.6. Coating studies

Coating applications have performed to establish the quality of the BVZ-2 complex pigment. A conventional concrete block and Aluminum sheet were chosen as coating substrates. NIR solar reflectance spectra of the bare and pigment coated surface have displayed in Fig. 9. As seen, both the coatings have exhibited excellent colour saturation with significant improvement in NIR solar reflectance to that of its bare surface, 25% and 31% for Al sheet and concrete block respectively, Table 5. It
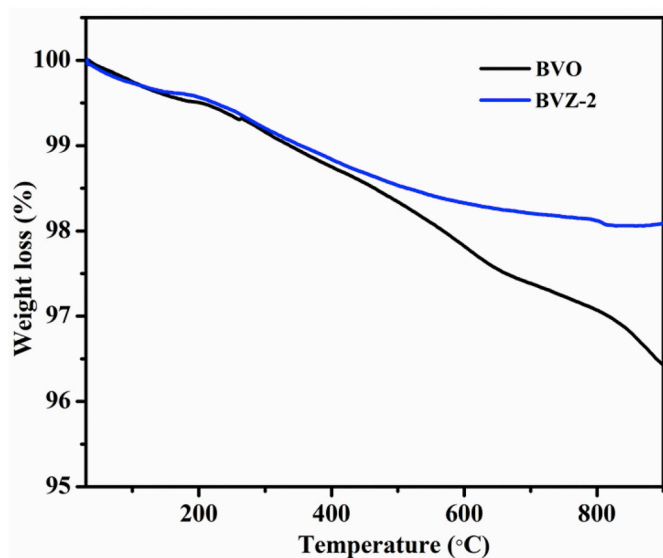
oped BVO outer layer holds the key for such an exquisite observation. Comparing with literature reports BVZ-2 exhibit excellent colour intensity and superior brightness with L* = 91.53, Table 3. Further, reduction in BVO content reflected on cost of the material, which favoured the selection of BVZ-2 than BVZ-1. While decreasing BVO wt% again colour of the pigment found to decrease sharply in the case of BVZ-3 and BVZ-4. It estimates the minimum BVO content required to develop quality BVZ complex pigment. Hence, it was not preferred to opt BVZ-3 and BVZ-4 over BVZ-2 even though a decrease in BVO component lead to a reduction in cost. BVS-2 and BVA-2 also displayed good colour strength (b* > 72), suggest them as good contenders for BVO. The closeness in the magnitude of b* value with BVO let BVZ-2 be the standout candidate among all other compositions.

Compared to BVO, exposed ZnO surface in BVZ-2 enhanced the NIR reflectance and NIR solar reflectance to 98% and 90% respectively, Fig. 7, which transformed it into exciting 'cool' roof pigment. Therefore, the synergistic effect of BVO and ZnO was incredible to develop low-cost, high-performance BVZ complex pigment. Complex BVZ-2 and mixed pigment with same compositions have compared for colour and reflectance. By dilution effect, where ZnO occasionally shield the BVO particles, mixed pigment shown a dull yellow colour (Fig. 6e), b* = 47.88 (Table 3) [7,37,38]. Moreover, it justifies the significance
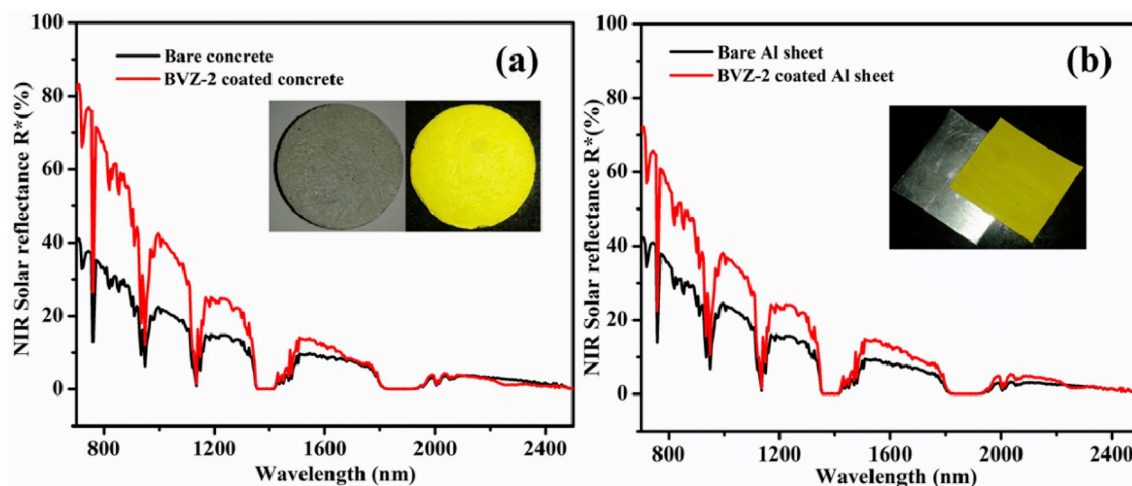

Fig. 9. Comparison of NIR solar reflectance (R*) of (a) bare and pigment coated concrete block, (b) bare and pigment coated Al sheet (inset shows photographs of coatings).

Table 5
CIE L*a*b* colour co-ordinates and NIR solar reflectance of BVZ-2 pigment coatings.

Sample	L*	a*	b*	NIR reflectance (%) at 1100 nm	Solar reflectance R* (%)
BVZ-2	91.53	−6.28	76.45	98.33	90.18
Al sheet coating	81.93	−7.64	70.09	73.43	70.00 (44.87)
Concrete coating	85.74	−3.97	76.97	77.21	75.31 (43.72)

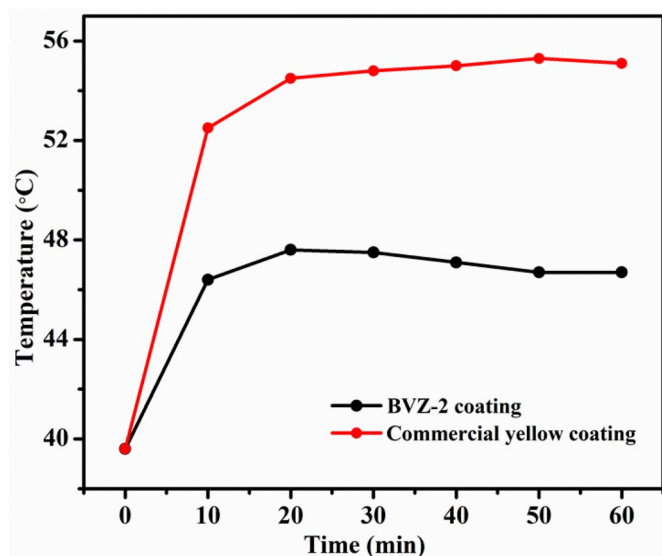NB: R* of the respective bare surface given in bracket.

Fig. 10. Temperature shielding comparison of BVZ-2 and commercial yellow pigment coatings. (For interpretation of the references to colour in this figure legend, the reader is referred to the Web version of this article.)
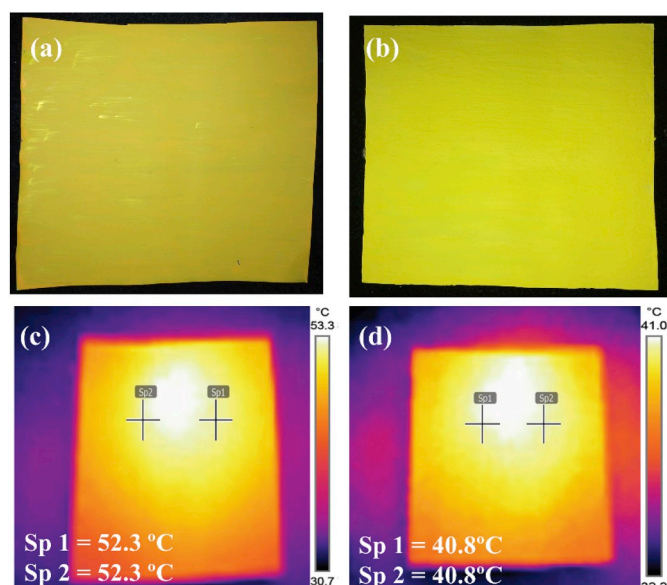
Fig. 11. Digital image of (a) Commercial yellow and (b) BVZ-2 coatings on Al sheet, thermal image of (c) commercial yellow and (d) BVZ-2 coatings. (For interpretation of the references to colour in this figure legend, the reader is referred to the Web version of this article.)

demonstrates the quality of the synthesised complex pigment BVZ-2.

Appendix B. Supplementary data

Supplementary data to this article can be found online at https://doi.org/10.1016/j.solmat.2019.109999.

3.7. Thermal shielding performance

Thermal shielding performance of the complex pigment BVZ-2 was studied using experimental setup shown in schematic diagram Fig. A1. BVZ-2 and commercially available yellow coatings have prepared for comparison. Average coating thickness of BVZ-2 and commercial yellow measured from the respective optical image as 272 and 220 μm, together with TiO_2 it was 316 and 416 μm, respectively, Fig A7. A thermocouple placed 2 cm below that of roof surface allowed accurate measurement of temperature rise inside the foam box due to IR absorption. Time-dependent temperature measurement up to 1 h shows that there is a steep increase in the temperature rise within the initial 10 min, followed by a gradual increase and then stabilised within 30 min (Fig. 10). Estimated temperature rise below BVZ-2 pigment coated Al roof found to be 8.4 °C lower than that of commercial yellow paint coated roof, which proves the efficiency of the developed complex pigment. Moreover, a thermal image of commercial yellow and BVZ-2 Al roof coatings have captured using FLIR C2 Thermal Imaging camera, after 1 h continuous exposure of IR rays shown in Fig. 11. The surface temperature readings at the selected points display 11.5 °C lower temperature for BVZ-2 coating, which establishes the better reflectivity and 'cool' nature of the developed complex pigment. Overall results suggest that complex pigment BVZ-2 can be an excellent alternative to BVO yellow pigment since it retained the general properties of core pigment with a substantial reduction in material cost and improvement in thermal stability.

4. Conclusions

BVO based complex pigment has successfully synthesized employing commercially available inexpensive WP as a supportive partner. PXRD ensured the complex pigment formation, and SEM analysis revealed the peculiar coral-like morphology. HRTEM studies show that 2–5 nm particle size BVO decorated over ZnO support. The nanoparticle decoration rendered excellent colour property with reduced BVO loading than that of pure BVO. Therefore, it is noteworthy that, the present study is able to bring down 75% of the costly BVO component without compromising its colour and NIR reflectivity. Thermal shielding experiment shows around 8.4 °C reduction in the interior temperature in relation to the commercial paint coated roof. Results illustrate the successful synthesis of a promising new cost-effective BVO complex pigment.

Acknowledgements

Appendix A
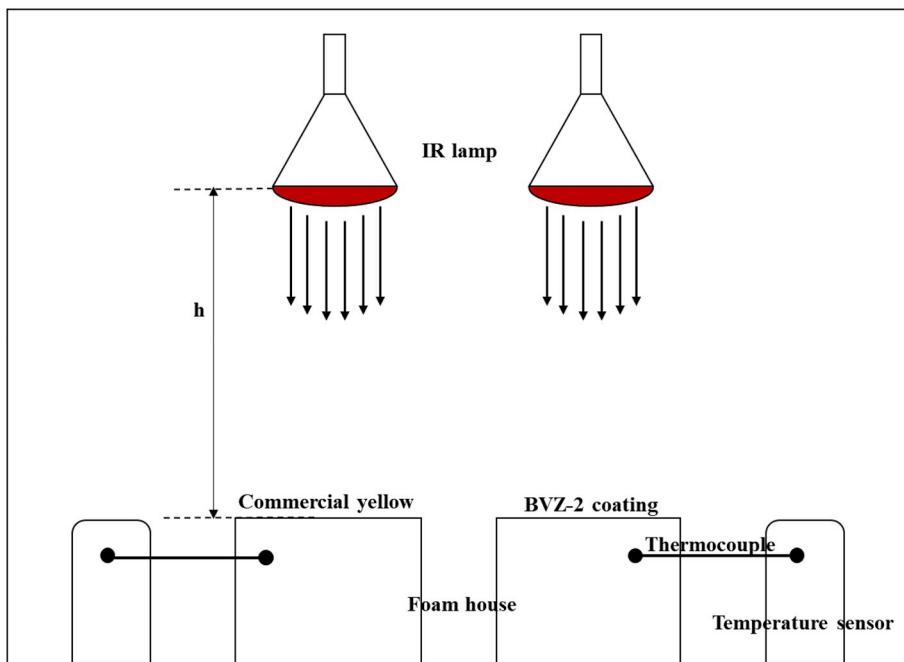
Fig. A.1. Schematic representation of experimental setup for thermal shielding performance of pigment coatings.
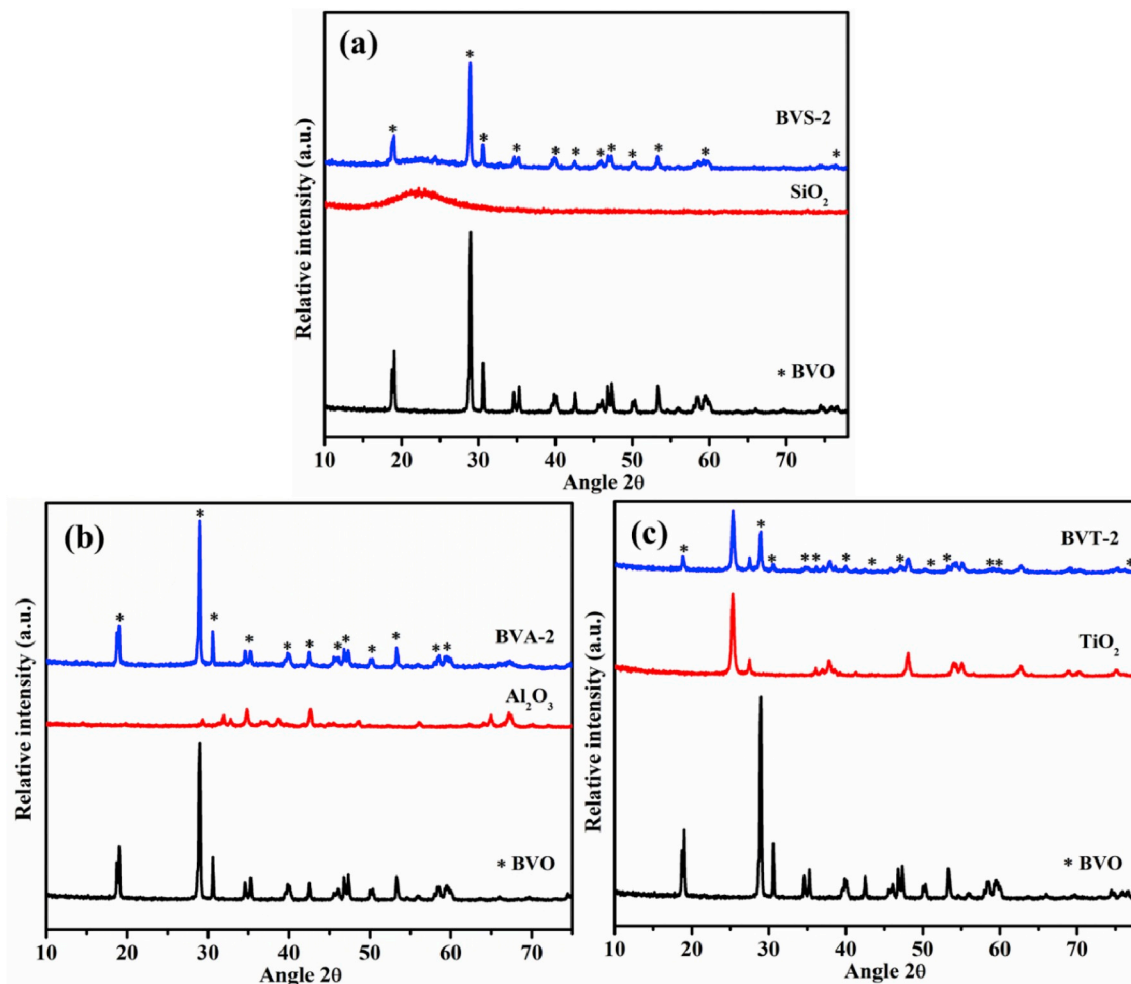
Fig. A.2. PXRD pattern of (a) BVS-2, (b) BVA-2 and (c) BVT-2 complex pigments.
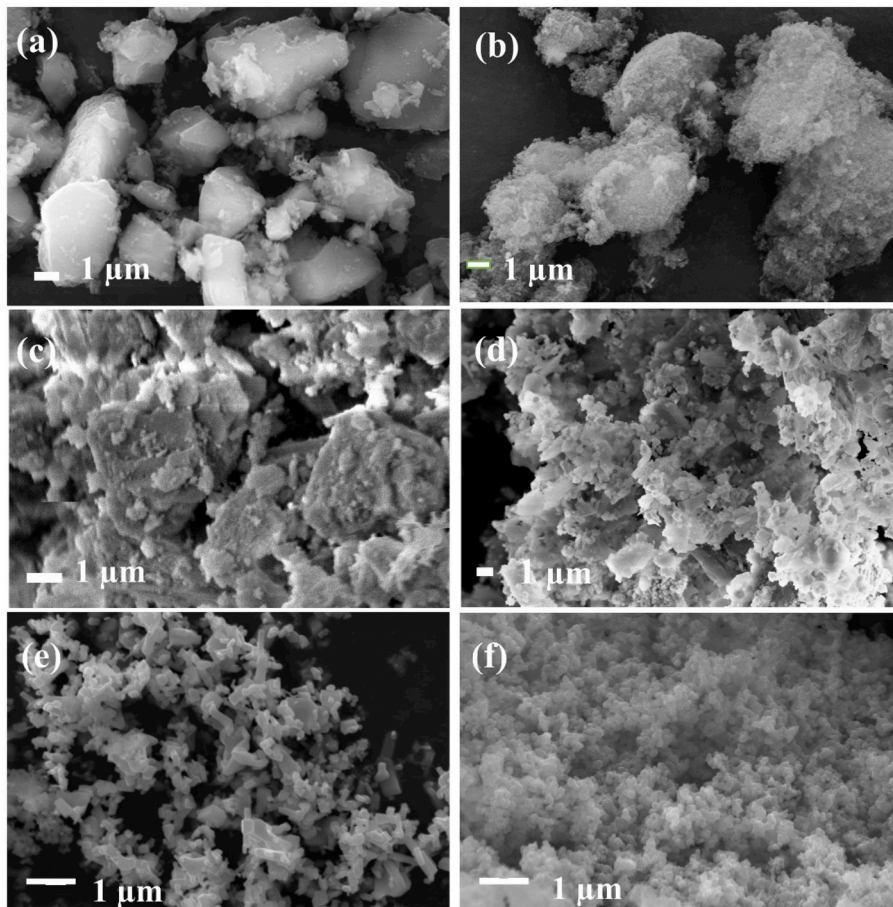
Fig. A.3. SEM image of pristine (a) SiO_2, (c) Al_2O_3, (e) TiO_2 and (b) BVS-2, (d) BVA-2, (f) BVT-2 complex pigments.
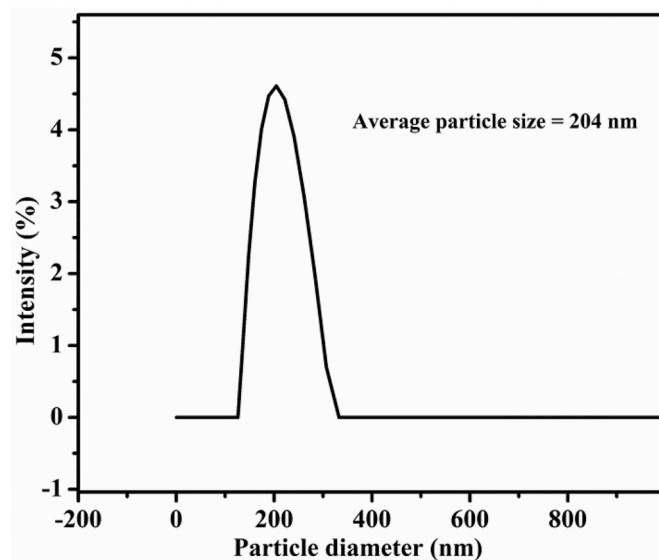
Fig. A.4. DLS particle size distribution of BVZ-2 complex pigment.
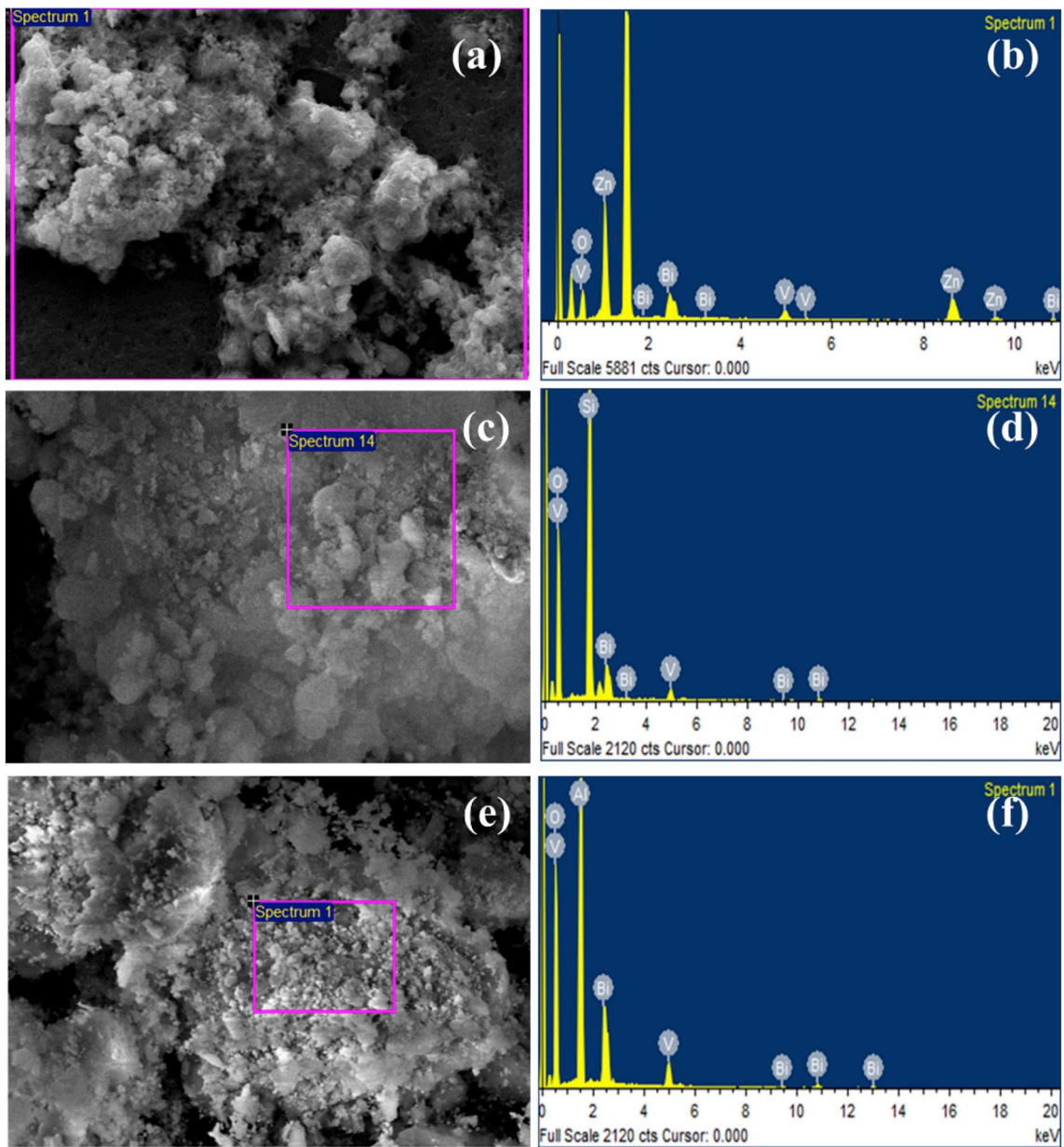
Fig. A.5. SEM-EDS of (a-b) BVZ-2, (c-d) BVS-2 and (e-f) BVA-2 complex pigments.
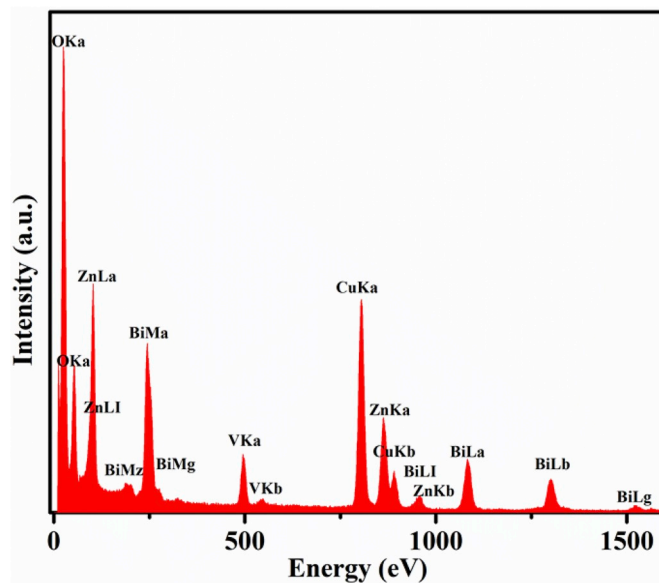
Fig. A.6. HRTEM-EDS of BVZ-2 complex pigment.
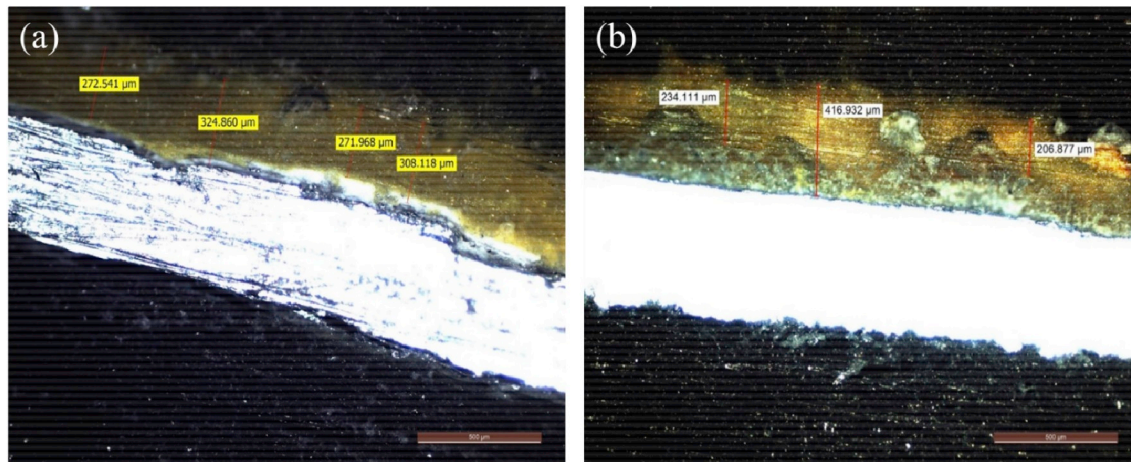
Fig. A.7. Optical image (a) BVZ-2 and (b) commercial yellow coat on Al sheet.

References

[1] K. Ashwini, C. Vinod malshe Bendiganavale, Infrared reflective inorganic pigments, Recent Pat. Chem. Eng. 1 (2008) 67–79.

[2] L. Yanga, F. Feng Qiana, D. Songa, K. Zheng, Research on urban heat-island effect, Procedia Eng 169 (2016) 11–18.

[3] M. Santamouris, C. Cartalis, A. Synnefa, D. Kolokotsa, On the impact of urban heat island and global warming on the power demand and electricity consumption of buildings–A review, Energy Build. 98 (2015) 119–124.

[4] L.M. Schabbach, D.L. Marinoski, S. Güths, A.M. Bernardin, M.C. Fredel, Pigmented glazed ceramic roof tiles in Brazil: thermal and optical properties related to solar reflectance index, Sol. Energy 159 (2018) 113–124.

[5] M. Santamouris, A. Synnefa, T. Karlessi, Using advanced cool materials in the urban built environment to mitigate heat islands and improve thermal comfort conditions, Sol. Energy 85 (2011) 3085–3102.

[6] M. Santamouris, Cooling the cities – a review of reflective and green roof mitigation technologies to fight heat island and improve comfort in urban environments, Sol. Energy 103 (2014) 682–703.

[7] A. Synnefa, T. Karlessi, N. Gaitani, M. Santamouris, D.N. Assimakopoulos, C. Papakatsikas, Experimental testing of cool colored thin layer asphalt and estimation ofits potential to improve the urban microclimate, Build. Environ. 46 (2011) 38–44.

[8] P. Jeevanandam, R.S. Mulukutla, M. Phillips, S. Chaudhuri, L.E. Erickson, K.J. Klabunde, Near infrared reflectance properties of metal oxide nanoparticles, J. Phys. Chem. C 111 (2007) 1912–1918.

[9] D.T. Harshada, V.P. Dilip, Stability testing of non-toxic bismuth vanadate according to pharmaceutical criteria, Int. J. Innov. Res. Sci. Eng. Technol. 4 (2015) 5350–5354.

[10] M.A. Barata, M.C. Neves, C.P. Neto, T. Trindade, Growth of BiVO4 particles in cellulosic fibres by in situ reaction, Dyes Pigments 65 (2005) 125–127.

[11] T. Masui, T. Honda, N. Wendusu Imanaka, Novel and environmentally friendly (Bi, Ca, Zn)VO4 yellow pigments, Dyes Pigments 99 (2013) 636–641.

[12] S.F. Sameera, P.P. Rao, L.S. Kumari, V. James, S. Divya, Potential NIR reflecting yellow pigments in (BiV)1-x(YNb)xO4 solid solutions, Chem. Lett. 42 (2013) 521–523.

[13] L. Guan, J. Fan, Y. Zhang, Y. Guo, H. Duan, Y. Chen, H. Li, H. Liu, Facile preparation of highly cost-effective BaSO4@BiVO4 core-shell structured brilliant yellow pigment, Dyes Pigments 128 (2016) 49–53.

[14] X. Wang, B. Mu, A. Hui, Q. Wang, A. Wang, Low-cost bismuth yellow hybrid pigments derived from attapulgite, Dyes Pigments 149 (2018) 521–530.

[15] L. Yuan, A. Han, M. Ye, X. Chen, C. Ding, L. Yao, Preparation, characterization and thermal performance evaluation of coating colored with NIR reflective pigments: BiVO4 coated mica-titanium oxide, Sol. Energy 163 (2018) 453–460.

[16] H. Taihei Wendusu, M. Toshiyuki, I. Nobuhito, Novel environmentally friendly (Bi, Ca, Zn, La)VO4 inorganic yellow pigments, RSC Adv. 3 (2013) 24941–24945.

[17] M. Toshiyuki, H. Taihei, Wendusu, I. Nobuhito, Novel and environmentally friendly (Bi,Ca,Zn)VO4 yellow pigments, Dyes Pigments 99 (2013) 636–641.

[18] C.N. Márcia, L. Marian, S. Rosário, L.c. Lubomir. Jr., T. Tito, Chemical bath deposition of cerium doped BiVO4, Dyes Pigments 59 (2003) 181–184.

[19] C.N. Márcia, T. Tito, Preparation of hollow shells of zinc oxide/bismuth(III) vanadate, Mater. Res. Bull. 38 (2003) 1013–1020.

[20] S. Jose, A. Jayaprakash, S. Laha, S. Natarajan, K.G. Nishanth, M.L.P. Reddy, YIn0.9Mn0.1O3-ZnO nano-pigment exhibiting intense blue color with impressive solar reflectance, Dyes Pigments 124 (2016) 120–129.

[21] S. Jose, A. Prakash, S. Laha, S. Natarajan, M.L.S.C. Reddy, Green colored nano-pigments derived from Y2BaCuO5: NIR reflective coatings, Dyes Pigments 107 (2014) 118–126.

[22] S. Jose, M.L.P. Reddy, Lanthanum-strontium copper silicates as intense blue inorganic pigments with high near-infrared reflectance, Dyes Pigments 98 (2013) 540–546.

[23] R. Yang, A. Han, M. Ye, X. Chen, L. Yuan, Synthesis, characterization and thermal performance of Fe/N co-doped $MgTiO_3$ as a novel high near-infrared reflective pigment, Sol. Energy Mater. Sol. Cells 160 (2017) 307–318.

[24] R. Levinson, H. Akbari, P. Berdahl, Measuring solar reflectance - Part I : defining a metric that accurately predicts solar heat gain, Sol. Energy 84 (2010) 1717–1744.

[25] R. Levinson, H. Akbari, P. Berdahl, Measuring solar reflectance - Part 2 + : review of practical methods, Sol. Energy 84 (2010) 1745–1759.

[26] T. Thongkanluang, T. Kittiauchawal, P. Limsuwan, Preparation and characterization of Cr_2O_3-TiO_2-Al_2O_3-V_2O_5 green pigment, Ceram. Int. 37 (2011) 543–548.

[27] P.K. Thejus, K. Biplab, K.G. Nishanth, An intense purple chromophore based on Co^{2+} in distorted tetrahedral coordiation, Dyes Pigments 158 (2018) 267–276.

[28] H. Oudghiri-Hassani, S. Rakass, F.T. Al Wadaan, K.J. Al-ghamdi, A. Omer, M. Messali, Abboudi, Synthesis, characterization and photocatalytic activity of α-Bi_2O_3 nanoparticles, J. Taibah Univ. Sci. 9 (2015) 508–512.

[29] S. Sameera, P. Prabhakar Rao, S. Divya, K.V.R. Athira, T.R. Aju Thara, High IR reflecting $BiVO_4$-$CaMoO_4$ based yellow pigments for cool roof applications, Energy Build. 154 (2017) 491–498.

[30] S. Sameera, P. Prabhakar Rao, V. James, S. Divya, K.V.R. Athira, Influence of (LiLa) $1/2MoO_4$ substitution on the pigmentary properties of $BiVO_4$, Dyes Pigments 104 (2014) 41–47.

[31] G.Q. Tan, L.L. Zhang, H.J. Ren, S.S. Wei, J. Huang, A. Xia, Effects of pH on the hierarchical structures and photocatalytic performance of $BiVO_4$ powders prepared via the microwave hydrothermal method, ACS Appl. Mater. Interfaces 5 (2013) 5186–5193.

[32] L. Xu, Y. Wei, W. Guo, Y. Guo, Y. Guo, One-pot solvothermal preparation and enhanced photocatalytic activity of metallic silver and graphene co-doped $BiVO_4$ ternary systems, Appl. Surf. Sci. 332 (2015) 682–693.

[33] J. Zhang, H. Cui, B. Wang, C. Li, J. Zhai, Q. Li, Fly ash cenospheres supported visible light-driven $BiVO_4$ photocatalyst: synthesis, characterization and photocatalytic application, Chem. Eng. Sci. 223 (2013) 737–746.

[34] A.K. Zak, M.E. Abrishami, W.H.A. Majid, R. Yousefi, S.M. Hosseini, Effects of annealing temperature on some structural and optical properties of ZnO nanoparticles prepared by a modified sol–gel combustion method, Ceram. Int. 37 (2011) 393–398.

[35] H. Liu, Z. Zhigang, T. Xiaosheng, Synthesis mechanism and optical properties of well nanoflower-shaped ZnO fabricated by a facile method, Opt. Mater. Express 4 (2014) 1762–1769.

[36] M. Achehboune, M. Khenfouch, I. Boukhoubza, B. Mothudi, I. Zorkani, A. Jorio, Structural and optical characterization of Holmium coated ZnO nanorods, J. Phys. Conf. Ser. 984 (2018) 012007.

[37] W. Zheng, J. Zou, Synthesis and characterization of blue TiO_2/$CoAl_2O_4$ complex pigments with good colour and enhanced near-infrared reflectance properties, RSC Adv. 5 (2015) 87932.

[38] L. Jiang, X. Xue, J. Qu, J. Qin, J. Song, Y. Shi, W. Zhang, Z. Song, J. Li, H. Guo, T. Zhang, The methods for creating energy efficient cool gray building coatings—Part II: preparation from pigments of complementary colors and titanium dioxide rutile, Sol. Energy Mater. Sol. Cells 130 (2014) 410–419.

[39] X. Xue, J. Qin, J. Song, J. Qu, Y. Shi, W. Zhang, Z. Song, L. Jiang, J. Li, H. Guo, T. Zhang, The methods for creating energy efficient cool gray building coatings — Part I: preparation from white and black pigments, Sol. Energy Mater. Sol. Cells 130 (2014) 587–598.
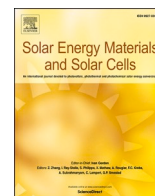
A cost-effective intense blue colour inorganic pigment for multifunctional cool roof and anticorrosive coatings

P.K. Thejus [a,b], K.V. Krishnapriya [a,b], K.G. Nishanth [a,b,*]

[a] Materials Science and Technology Division, CSIR-National Institute for Interdisciplinary Science and Technology (NIIST), Thiruvananthapuram, 695019, India
[b] Academy of Scientific and Innovative Research (AcSIR), Ghaziabad, 201002, India

ARTICLE INFO

ABSTRACT

An enormous attention has been paid to cobalt aluminate ($CoAl_2O_4$) blue pigments owing to their significant hue of blue colour. Nevertheless, several serious disadvantages, such as high cost due to the high cobalt consumption and poor solar reflectance, are associated with this pigment. Therefore, the development of cost effective and sustainable blue pigments with reduced Co content and improved solar reflectivity is a major focused area in pigment research. Herein, a new series of multifunctional blue coloured inorganic pigments with low cobalt content were prepared via the solid-state method. The structural and spectroscopic evaluations were indicated that the strong blue colour could be generated because of the distorted tetrahedrally organized cobalt chromophore. This structural distortion of the chromophore geometry was linked to the covalency and electron affinity factors. Colour ($b^* = -59.21$) and solar reflectance ($R^* = 64\%$) measurements of the optimized composition ($NaZn_{0.9}Co_{0.1}PO_4$) was observed to be superior than the commercially available $CoAl_2O_4$ blue pigment. Meanwhile, the optimized pigment loaded epoxy coated steel substrate in marine medium exhibited impressive corrosion resistance properties. The anticorrosive mechanism, further established through the XPS results, validated that the phosphatized inhibitive film served as the barrier for corrosion. The estimated Co content in $NaZn_{0.9}Co_{0.1}PO_4$ was found to be around 10 times lower than the $CoAl_2O_4$ blue pigment indicating the cost-effective nature. The optimized pigment was able to retain its optical properties in the prepared acrylic coatings on Al sheet and concrete block. Further, the temperature shielding studies ensured a reduction of ~4 °C in comparison with $CoAl_2O_4$ coatings. Therefore, the developed multifunctional blue pigment could be employed for the economic production of blue exterior paint for anticorrosive cool roof coatings.

1. Introduction

Inorganic pigments are greatly admired throughout the history of mankind owing to their potential usage in paints, inks, glazes etc as colourants [1–3]. Meanwhile, the research advancement has brought new dimensions for pigments apart from its aesthetics. In this connection, the near-infrared reflective (NIR) inorganic pigments, known as cool pigments, evolved as the latest development in the area of pigment technology. The NIR reflective paints coated on the exterior walls as well as on the roofing sheets can effectively mitigate the interior heat build-up thereby reduce peak electricity demand in summer. It is worth to mention that the rise in atmospheric temperature due to Urban Heat Island effect and global warming were major concern behind the thought of NIR reflective pigments [4–7]. Some well known cooling

pigments such as TiO_2, ZnO, $BiVO_4$ etc. have the NIR reflectance over 80% [8–11]. It is important to note that metallic roofing sheets particularly iron rich alloys exhibit severe corrosion problem on long-term exposure to the environmental conditions. In this connection corrosion resistant inorganic pigments are very useful for the making of anticorrosive paints and primers. In this class, $PbCrO_4$, Cr_2O_3, $Zn_3(PO)_4$ etc. are the prominent candidates with the corrosion resistance property because of their combined active and passive inhibition mechanisms [12–14]. For constructing a durable cool roof coating, anticorrosive paints are extremely important. Presently, the multilayer coating protocol in which the cool paint over the anticorrosive primer is followed to get the desired properties. However, this technology is associated with severe drawbacks including large material consumption, enormous workload, long working durations, and exceptionally high expense. In

* Corresponding author. Materials Science and Technology Division, CSIR-National Institute for Interdisciplinary Science and Technology (NIIST), Thiruvananthapuram, 695019, India.
  E-mail address: nishanthkg@niist.res.in (K.G. Nishanth).

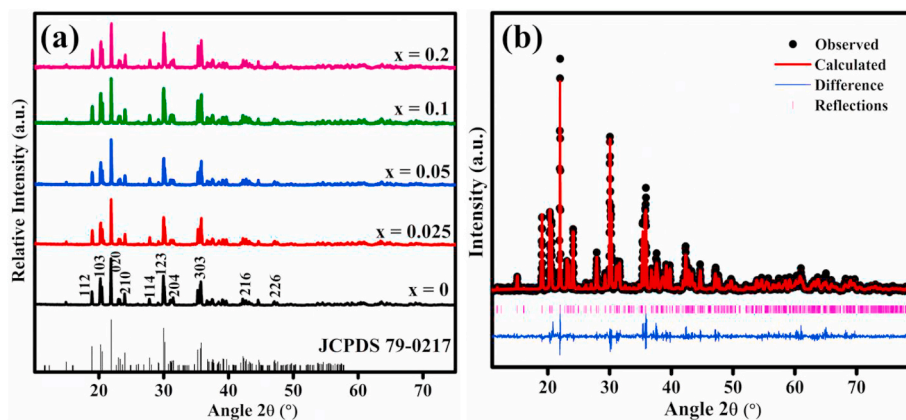**Fig. 1.** (a) PXRD pattern of NaZn$_{1-x}$Co$_x$PO$_4$ ($0 \leq x \leq 0.2$), (b) Rietveld refined PXRD pattern of NaZn$_{0.9}$Co$_{0.1}$PO$_4$.

this scenario, the rise of demands for the multifunctional inorganic pigments having NIR reflectivity and anticorrosivity is natural.

The blue colour has a long history of eternal fascination due to its unique dimension that carried in the arts, science and culture. There were massive efforts in various directions to explore a stable blue colour in history. Azurite (Cu$_3$(CO$_3$)$_2$(OH)$_2$), Egyptian blue (CaCuSi$_4$O$_{10}$), Chinese blue (BaCuSi$_4$O$_{10}$), lapis lazuli (Na,Ca)$_8$[SiAlO$_4$]$_6$(S,SO$_4$), prussian blue (Fe$_4$[Fe(CN)$_6$]$_3$), ultramarine (Na$_7$Al$_6$Si$_6$O$_{24}$S$_3$) are among the major landmarks in the quest, in which most of the pigments are not employed for long owing to the serious durability issue [15–17]. Currently, CoAl$_2$O$_4$ blue (Pigment Blue 28) spinel-type material has considered as the most accepted pigment in the market, due to its excellent chemical and thermal stability, many applications in ceramic, glass, plastics and paint industries. However, the pigment is not the ideal choice for a good solar reflective and anticorrosive coating [18]. In addition, the preparation of CoAl$_2$O$_4$ pigment suffers various disadvantages such as large consumption (~33 wt%) of scarce and expensive Co and high processing temperature (~1200 °C), that leads to high production cost [19–21]. Recent report by Smith et al., revealed a new pigment, Mn doped YInO$_3$, which exhibited an intense blue hue but the cost is still debatable [22]. In this context, it is important to develop a low-cost blue pigment with reduced cobalt content without compromising its colour properties.

Herein a new inorganic pigment series of Co doped NaZnPO$_4$ has been introduced. The optimized phase pure composition exhibited deep blue colour, excellent solar reflectance (R*) and corrosion resistance property. For checking the market potential, the comparative studies were performed between the optimized composition and the commercially available Co blue (CoAl$_2$O$_4$). The optimized composition revealed superior colour tone, reflectance property, corrosion resistance and temperature shielding ability than those of Co blue. Further, the estimated Co content in the pigment composition and synthesis temperature was significantly lower than that used in CoAl$_2$O$_4$, which could eventually reflect in the material cost. Thus, the synthesized blue inorganic pigment could be an excellent candidate to modulate a multifunctional exterior and interior coatings.

2. Experimental section

2.1. Materials and methods

For the synthesis, extra pure Na$_2$CO$_3$ (99%), ZnO (99.9%), NH$_4$H$_2$PO$_4$ (≥98%) and CoCO$_3$ (99.99%) were purchased from Merck. Stoichiometric amounts of precursors homogeneously mixed in ethanol wetting medium and calcined at 500 °C for 3 h followed by 800 °C for 5 h [23].

Anticorrosive performance of the pigment was analyzed by using pigment loaded epoxy coatings on steel, having composition C = 0.24,

Mn = 0.90, Al = 0.03, Si = 0.20, Cr = 0.04, V = 0.10, P = 0.08, Cu = 0.06 and remaining Fe. Steel coupons were cut into 4 × 3 × 0.2 cm dimension then mechanically abraded with SiC paper grade 220 to 1000 subsequently acetone degreased and dried. Different wt% (15, 20 and 25) of pigment sample was dispersed in n-butanol-epoxy-polyamide (2:2:1) system by ultrasonication. The dispersion was dip coated on polished specimens at a dipping rate of 80 mm/min and allowed to cure for 24 h.

Acrylic emulsion of pigment was prepared by dispersing pigment and acrylic binder in the ratio of 1:4, by ultrasonication. The emulsion was coated on TiO$_2$ base coated concrete and Al sheet. IR reflectance studies were carried out on both concrete and Al sheet coatings, temperature shielding performance was investigated by means of an experimental setup shown in Fig. A1 and compared with CoAl$_2$O$_4$ pigment (commercial blue). Two identical model houses have constructed out of foam, having dimensions (size = 15 × 15 × 15 cm), roofed with 19 × 19 cm Al sheet pigment coatings. Model houses were exposed to IR lamp (Philips, 250 W) for 1 h and temperature measurements were done using two thermocouples T1 (top) and T2 (bottom) in each. The distance between rooftop and the IR lamp was maintained at 40 cm with fixed T1 and T2 of 2 cm below the roof and 3 cm above the base, respectively. Surface temperature was analyzed in the same experiment using FLIR C2 thermal imaging camera. Thickness of all the prepared coatings were measured using profilometer.

2.2. Characterization techniques

Synthesized pigments were characterized by Powder X-ray Diffraction (PXRD) analysis using Philips X'pert Pro diffractometer, Ni-filtered Cu-Kα (λ = 0.154060 nm) radiation. The XRD data were collected by step scanning over a 2θ range from 10 to 70° with a step size of 0.03° and 20 s counting time at each step. The Rietveld refinement analysis was carried out employing the software GSAS-II. Morphology studies were done using a Scanning Electron Microscope (SEM) JEOL JSM-5600 model. The distributions of particle sizes were measured by Dynamic Light Scattering experiment using Malvern Instruments Zeta sizer nano Zis Model No: ZEN 3600. UV–Vis–NIR Spectrophotometer (Shimadzu UV-3600 with an integrating sphere attachment, ISR-2200) used for the optical studies of pigment samples and coatings with barium sulfate as a reference for UV–Vis range (300–700 nm) and polytetrafluoroethylene (PTFE) for NIR range (700–2500 nm). The parameter C* (chroma) represents saturation of the colour and defined as C* = $\sqrt{(a*)^2 + (b*)^2}$ the hue angle, h^o is ranges from 0 to 360° and calculated using the formula h^o = tan^{-1}(b*/a*). The NIR solar reflectance (R*) between wavelength 700–2500 nm was calculated according to ASTM standard number E891-87 as reported elsewhere [24–26]. Further measurement details are described in our previous report [23].

Table 1
Rietveld data and experimental conditions for data collection.

Formula	NaZnPO$_4$ [28]	NaZn$_{0.9}$Co$_{0.1}$PO$_4$
Symmetry	Monoclinic	Monoclinic
Space group	P2$_1$/n	P2$_1$/n
Unit cell parameters	a = 8.65600 Å, b = 8.10600 Å, c = 15.26000 Å, β = 89.8000°	a = 8.66944 Å, b = 8.13078 Å, c = 15.27168 Å, β = 89.7897°
Volume	1070.719582 Å^3	1076.483132 Å^3
Z	12	12
Dc	3.38 gcm^{-3}	3.39 gcm^{-3}
Radiation	Cu Kα1 = 1.54059 Å	Cu Kα1 = 1.54060 Å
Measuring range	10° ≤ 2θ ≤ 80°	10° ≤ 2θ ≤ 80°
R$_p$ factor	1.9%	12.37%

$$R* = \frac{\int_{700}^{2500} r(\lambda)i(\lambda)d(\lambda)}{\int_{700}^{2500} i(\lambda)d(\lambda)}$$

Where r(λ) is the experimentally obtained spectral reflectance (Wm^{-2}), and i(λ) is the solar spectral irradiance (Wm^{-2} nm^{-1}) obtained from ASTM standard E891-87.

The comparative corrosion resistance studies of CoAl$_2$O$_4$ and NaZn$_{0.9}$Co$_{0.1}$PO$_4$ were performed using a multichannel potentiostat/galvanostat (Autolab) having a three-electrode cell in which saturated calomel (SCE) and graphite act as the reference and counter electrodes respectively. Steel with surface area 1.2 cm^2 was acted as the working electrode in 3.5 wt% NaCl solution. Open circuit potential was stabilized for 30 min. Electrochemical impedance spectroscopy (EIS) was conducted in the frequency range of 10^5–10^{-2} Hz and AC signal of 5 mV amplitude. EIS Nyquist plots were analyzed by Nova 2.1 software. Experiments were reiterated thrice for each coated specimen.

3. Results and discussions

3.1. PXRD analysis

The PXRD of the series of inorganic pigments, NaZn$_{1-x}$Co$_x$PO$_4$ (0 ≤ x ≤ 0.2), are illustrated in Fig. 1a to identify the phase and study the effect of Co doping on the NaZnPO$_4$ crystal lattice. All the prepared samples are found to be crystalline in nature, as indicated by the sharp diffraction peaks, and crystallized in monoclinic crystal structure with P2$_1$/n space group. The perfect match in XRD patterns between the parent and Co doped compounds ensured the phase purity. Further, the major peaks are indexed in accordance to JCPDS 79–0217 of NaZnPO$_4$ phase, which confirms that the Co^{2+} ions are successfully incorporated in to the Zn^{2+} sites within the host lattice [27].

Rietveld refinement analysis for the composition NaZn$_{0.9}$Co$_{0.1}$PO$_4$ has been carried out to study the crystal structure, employing the data of NaZnPO$_4$ reported by L. Elammari et al. [28]. The refined XRD pattern is shown in Fig. 1b, and the calculated structure refinement parameters are tabulated in Table 1. In the complex structure of NaZn$_{0.9}$Co$_{0.1}$PO$_4$, Na$^+$, Zn^{2+} and P^{5+} ions are occupied in three different sites, as displayed in Fig. 2. These sites are as follows; Na$^+$ in NaO$_8$ polyhedra (Na1) and NaO$_6$ distorted octahedra (Na2 and Na3), Zn^{2+} in ZnO$_4$ distorted tetrahedra (Zn1, Zn2 and Zn3), and P^{5+} in PO$_4$ tetrahedra (P1, P2 and P3). The
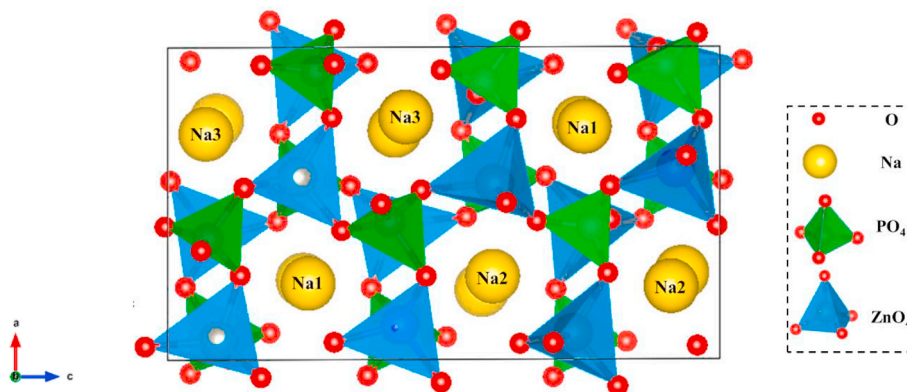
Fig. 2. Crystal structure of NaZn$_{0.9}$Co$_{0.1}$PO$_4$.
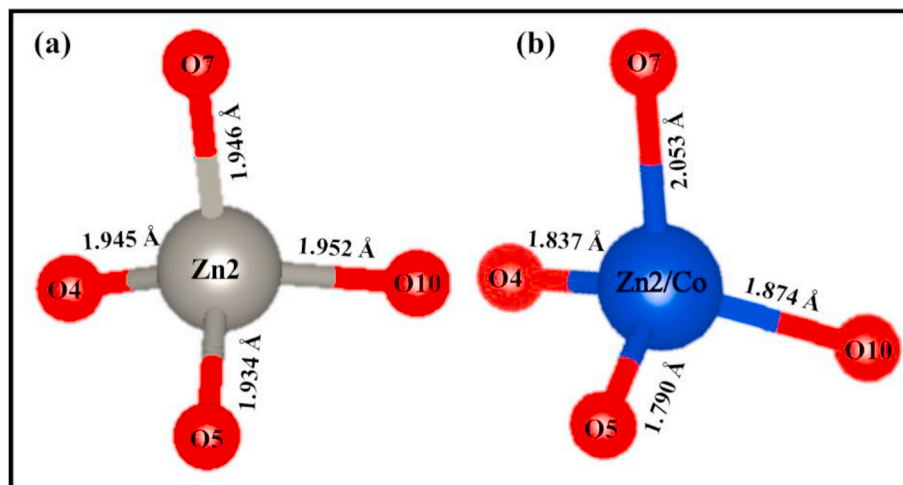
Fig. 3. Coordination environment of (a) Zn(2)O$_4$ in NaZnPO$_4$ and (b) Zn(2)/CoO$_4$ in NaZn$_{0.9}$Co$_{0.1}$PO$_4$.
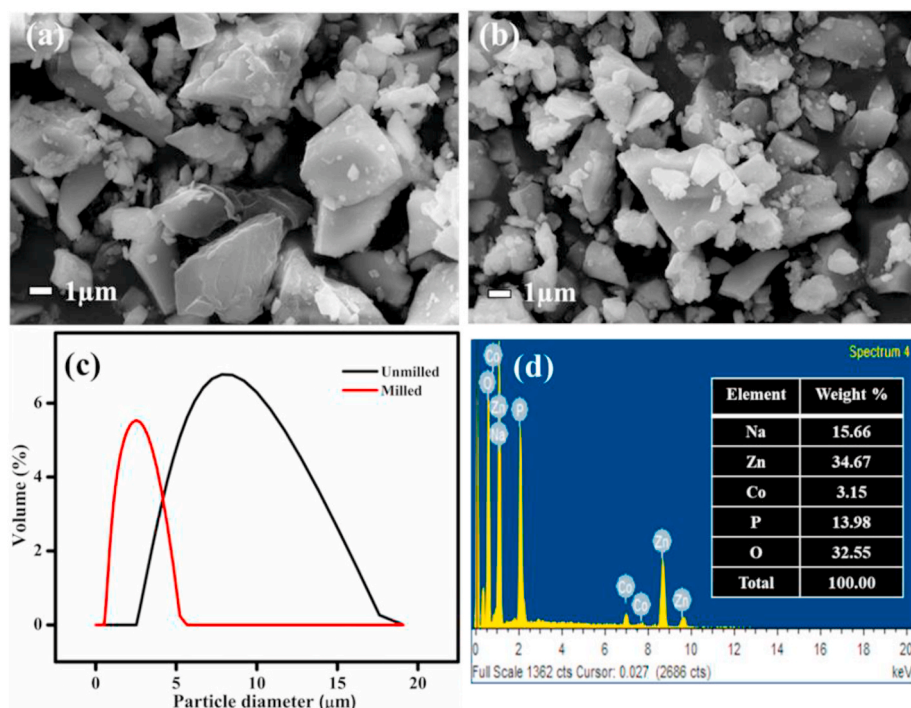
Fig. 4. (a), (b) SEM images of unmilled and milled $NaZn_{0.9}Co_{0.1}PO_4$, (c) particle size comparison of unmilled and milled $NaZn_{0.9}Co_{0.1}PO_4$, (d) EDS of $NaZn_{0.9}Co_{0.1}PO_4$.

results derived from the refinement calculations speculated that in $NaZn_{0.9}Co_{0.1}PO_4$ monoclinic structure, Co^{2+} ions are associated with the Zn(2) tetrahedral site. Detailed crystallographic data, respective bond length and bond angle of $Zn(2)O_4$ and $Zn(2)/CoO_4$ tetrahedra are tabulated in Table A1 and A2, respectively. The Co doped tetrahedron carry three shorter and one longer Co–O bonds than that of $Zn(2)O_4$ structure. In addition, significant deviations are noted down in the bond angles.

The observations evaluate that the substitution effect brought significant distortions in the $Zn(2)O_4$ geometry by the reduction in Co–O bond length, Fig. 3. The major factors that influence the bond length could be variation in ionic size and electron affinity of the host and dopant ions. Even the slight difference in ionic size between Zn^{2+} (0.60 Å) and Co^{2+} (0.58 Å) can bring the covalency factor into picture. Smaller the ionic size higher will be the covalency, in turn shorter will be the metal oxygen bond length [23]. Moreover, the electron affinity (Zn = 0 kJ/mol; Co = 63.7 kJ/mol) and bond length are inversely related. Overall, shortening of Co–O bond length led to a shrinkage of Zn (2)/CoO_4 tetrahedron. However, this shrinkage of $Zn(2)/CoO_4$ tetrahedra did not allow the subsequent contraction of associated corner

shared PO_4 and NaO_8 polyhedra, rather elongated the bonds (P1–O4, P3–O10, Na2–O5 and Na2–O7) and persuaded the expansion of unit cell. Therefore, the doping resulted an isotropic increase in lattice parameters and cell volume (Table 1).

3.2. Morphology studies

According to the micrographs, the particles of the as obtained pigment composition $NaZn_{0.9}Co_{0.1}PO_4$ are grannular in nature having the sizes ranging 1–10 μm, as shown in Fig. 4a. Eventually, such broad particle size distribution is also confirmed via the DLS measurements, which shows the average particles size of 8 μm. The particle size and size homogeneity have crucial role in determining the dispersibility of pigments in paint formulation, since it essentially affect the hiding strength [29]. It has been achieved later by the high energy planetary ball mill performed for 30 min (135 rpm). Subsequent SEM images displayed nonaggregate narrow particle size distribution of 1–3 μm with much better uniformity, as described in Fig. 4b. This data is also supported by the more sharp DLS curve with the resulted average particle size of 2.5 μm (Fig. 4c). The EDS analysis identified the presence of Na, Zn, Co, P,
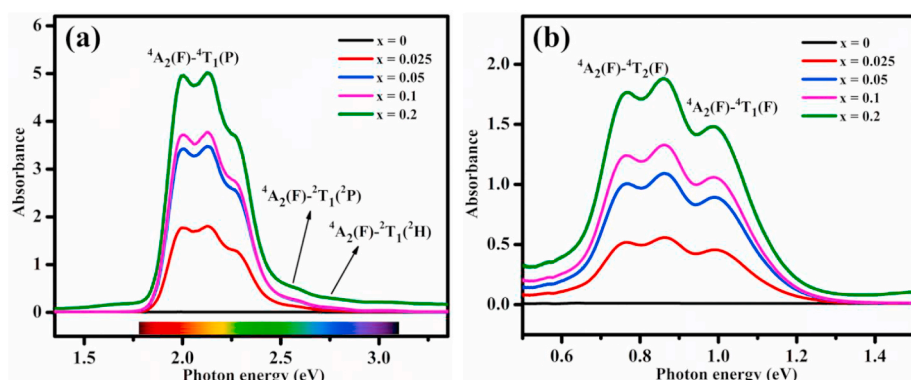
Fig. 5. (a) UV–Vis and (b) NIR absorption spectra of $NaZn_{1-x}Co_xPO_4$ ($0 \leq x \leq 0.2$).
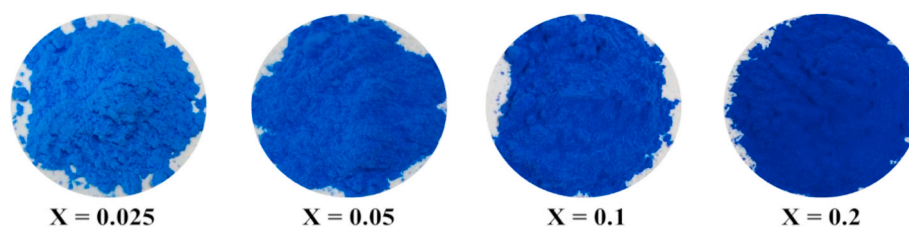
Fig. 6. Photographs of NaZn$_{1-x}$Co$_x$PO$_4$ (0.025 ≤ x ≤ 0.2) pigments.

Table 2
CIE L*a*b* colour co-ordinates of NaZn$_{1-x}$Co$_x$PO$_4$ (0 ≤ x ≤ 0.2).

Sample	L*	a*	b*	C*	h°	NIR reflectance at 1100 nm (%)	R* (%)
x = 0	92.13	0.15	−0.32	0.35	295	87	87
x = 0.025	60.43	3.68	−41.66	41.82	275	56	67
x = 0.05	52.05	8.99	−49.57	50.38	280	50	65
x = 0.1	51.78	10.70	−59.21	60.17	280	49	64
x = 0.2	44.31	17.31	−56.66	59.25	287	32	52
CoAl$_2$O$_4$	44.80	2.10	−32.70	–	–	–	29 [3]

and O elements (Fig. 4d). Moreover, the experimentally determined stoichiometric composition of pigment was in close agreement to the calculated value, displayed at the inset of Fig. 4d.

3.3. Optical and chromatic properties

Fig. 5a illustrates the UV–Vis absorption spectra of the synthesized pigments NaZn$_{1-x}$Co$_x$PO$_4$ (0 ≤ x ≤ 0.2). As seen from Fig. 5a, a broad absorption band in the range of 1.78–2.76 eV is observed for the Co substituted compounds in the visible region. This band is having 3 peaks at 1.99, 2.12 and 2.27 eV indicated the prominent absorption in the entire red, orange and yellow regions. In addition, the absorption valley extended over to the green region as well thereby displaying the complimentary blue colour. Tanabe-Sugano diagram established that the strong absorption is attributed to the spin allowed ligand field transition $^4A_2(F) \rightarrow {}^4T_1(P)$, from the tetrahedrally coordinated Co^{2+} [30–36]. Further, the spin forbidden transitions $^4A_2(F) \rightarrow {}^2T_1(^2P)$ and $^4A_2(F) \rightarrow {}^2T_1(^2H)$ identified at 2.57 and 2.75 eV as weak absorptions, respectively, substantiated the tetrahedral chromophore geometry. The absorption peak splitting is originated from the spin-orbit coupling effect and Jahn-Tellar distortion of the tetrahedral structure, where the increase in Co concentration further enhanced these effects owing to which an associated peak broadening has been observed [37,38]. Relatively broader and weaker absorption is registered in the NIR region of 0.6–1.25 eV (Fig. 5b). This triplet peak is accounted for the transitions

$^4A_2(F) \rightarrow {}^4T_2(F)$ at 0.60–0.93 eV and $^4A_2(F) \rightarrow {}^4T_1(F)$ at 0.93–1.25 eV [39].

Pigment colour is quantified using CIE 1976 L*a*b* colour system, through hue, chroma and brightness. The digital photographs of the pigment samples are exhibited in Fig. 6 and the respective chromatic coordinates for different pigment compositions have been summarized in Table 2. The Co substitution at Zn site developed a deep blue colour, indicated by the negative b* and 270–290° hue angle. The increase in Co concentration proportionally increased b* magnitude and colour richness value C*. The maximum blue colour has been registered for 0.1 mol % of Co doping (b* = −59.21), which is about 26 units higher than that of reported CoAl$_2$O$_4$ (b* = −32.70) [3,40]. Moreover, the synthesis of NaZn$_{0.9}$Co$_{0.1}$PO$_4$ was achieved at relatively lower temperature and the estimated Co concentration in NaZn$_{0.9}$Co$_{0.1}$PO$_4$ (3.22 wt%) is 10 times lower than that of CoAl$_2$O$_4$ (33.31 wt%). Since the processing temperature and chromophore concentration are some of the critical parameters in deciding the pigment cost, in the background of rising energy consumption and cobalt market price issues the present synthesis method and the new blue pigment, respectively, acquires great significance [19]. Further, higher doping concentration developed a slight colour deviation from blue to navy blue, resolved from the rise of red component a*. The brightness of the pigment explicitly related to cobalt content that followed the usual inverse trend in the present work as well [41]. Hence the result provided a remarkable prospective for NaZn$_{0.9}$Co$_{0.1}$PO$_4$ pigment.

3.4. Reflectance properties

The demand for heat shielding NIR reflective pigments have increased in recent past due to urban heat island effect. In order to investigate the reflectance behavior of the new pigment, the NIR (Fig. 7a) and solar reflectance spectral analysis (Fig. 7b) have been performed. Cobalt pigments generally fall in the low reflective category due to the characteristic absorbance at NIR region of 700–2500 nm. The NIR solar reflectance of CoAl$_2$O$_4$ (R* = 29%) and CoCr$_2$O$_4$ (R* = 30%) are the well-known examples [3,42]. Unlike traditional colourants, the developed pigment series NaZn$_{1-x}$Co$_x$PO$_4$ (0 ≤ x ≤ 0.1) shown promising NIR reflectance at 1100 nm and R* (Table 2). Since the emphasis given
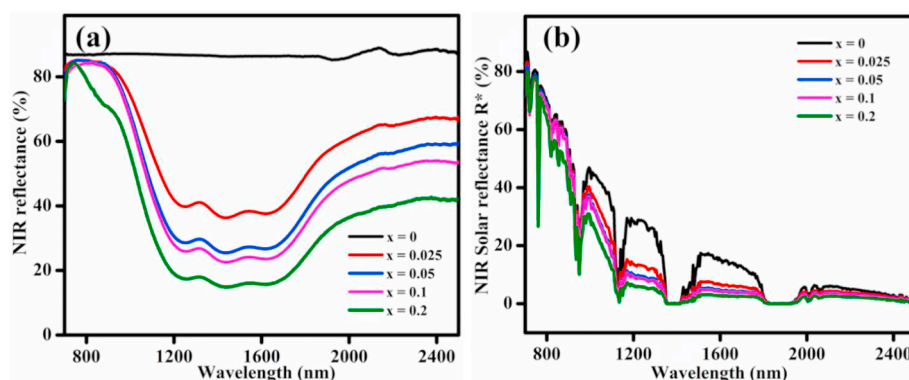

Fig. 7. (a) NIR and (b) NIR solar reflectance spectra of NaZn$_{1-x}$Co$_x$PO$_4$ (0 ≤ x ≤ 0.2).

Table 3
EIS parameters from Nyquist plot.

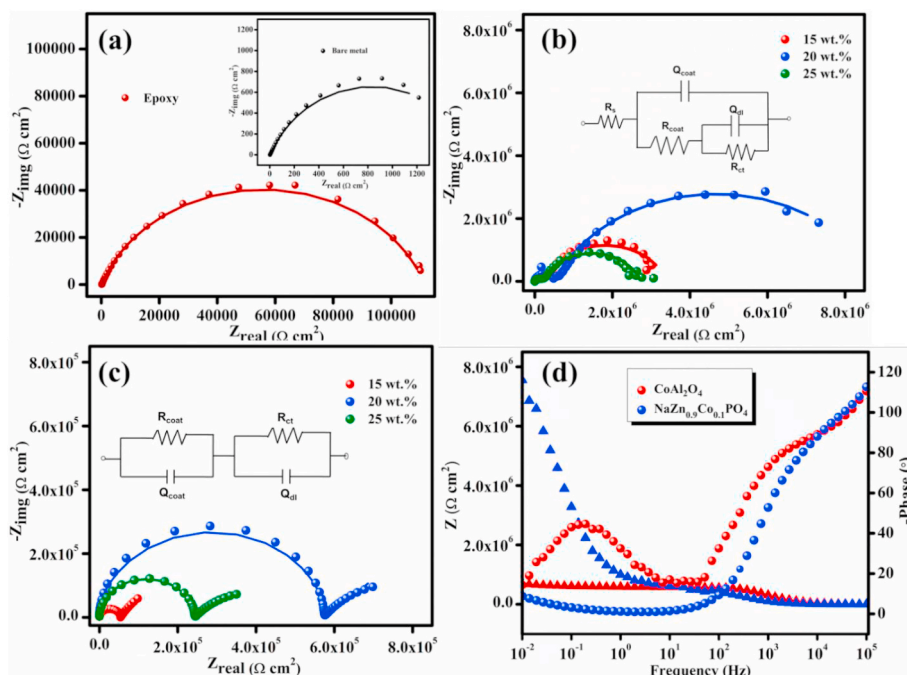| EIS parameters	Bare metal	Bare epoxy	NaZn$_{0.9}$Co$_{0.1}$PO$_4$ (wt.%)			CoAl$_2$O$_4$ (wt.%)		
			15	20	25	15	20	25
Rcoat (Ωcm^2)	–	159.8	2.3×10^5	5.7×10^5	1.9×10^5	5.3×10^4	5.4×10^5	2.4×10^5
Qcoat (μFcm^{-2})	–	4.2	1.6	0.15	0.35	2.8	0.53	2.1
Rct (Ωcm^2)	1.2×10^3	1.2×10^5	3.4×10^6	8.8×10^6	2.8×10^6	3.4×10^5	8.7×10^5	4.3×10^5
Qdl (μFcm^{-2})	744	0.028	0.017	0.016	0.021	0.061	0.026	0.034

Fig. 8. Nyquist plots of (a) bare epoxy and bare metal (inset), different wt% (b) NaZn$_{0.9}$Co$_{0.1}$PO$_4$ and (c) CoAl$_2$O$_4$, (d) Bode plot of 20 wt% NaZn$_{0.9}$Co$_{0.1}$PO$_4$ and CoAl$_2$O$_4$.

to coloured NIR reflective pigments, NaZn$_{0.9}$Co$_{0.1}$PO$_4$ chosen as the best composition because of its equal excellence in both perspective. The calculated values of b* and R* for this composition are −59.21 and 64%, respectively, which could essentially help to mitigate the interior heat buildup as a potential cool pigment.

A comparison with literature reports is summarized in Table A3, which indicate the uniqueness of the new pigment. Even though, some of the reported pigments shown better colour or R*, NaZn$_{0.9}$Co$_{0.1}$PO$_4$ ascertained as the best in terms of colour and R* together. Without confining on a single problem, the developed blue inorganic pigment can be able to resolve multiple facet issues, there by perfectly fit in the group of modern era materials. Thus, the new low-cost blue pigment permit to establish an extremely beneficial interior and exterior coat.

3.5. Anticorrosive property of NaZn$_{0.9}$Co$_{0.1}$PO$_4$

The corrosion resistant inorganic pigments have significant role in developing the protective coatings for metal substrates. Herein, NaZn$_{0.9}$Co$_{0.1}$PO$_4$ examined in this direction to explore the anticorrosive property. Epoxy coatings of thickness ~11 μm have prepared with different pigment loadings (15, 20 and 25 wt%). Further, the EIS experiments have been performed on the bare and pigment incorporated coatings, on steel in 3.5 wt% NaCl. The respective Nyquist plots are displayed in Fig. 8a-c.

Impedance spectra of NaZn$_{0.9}$Co$_{0.1}$PO$_4$ coatings (Fig. 8b) have been modeled with the electrochemical equivalent circuit (EEC) [Q$_{coat}$/(R$_{coat}$ + Q$_{dl}$/R$_{ct}$)]. The solution resistance R$_s$ is negligible thus excluded from

the circuit. R$_{coat}$ and R$_{ct}$ correspond to the coating resistance and charge transfer resistance, respectively, where R$_{coat}$ defines the coat intactness, and R$_{ct}$ is the associated charge transfer reactions at the metal electrolyte interface. The constant phase element Q$_{coat}$ (coating capacitance) and Q$_{dl}$ (double layer capacitance), account for the non-ideal behavior of polymer coat and double layer, respectively [43,44]. The impedance fitting data are tabulated in Table 3, where the maximum corrosion resistance obtained for 20 wt% pigment loading, R$_{ct}$ 8.8 × 10^6 Ωcm^2 with minimum Q$_{dl}$ 0.016 μFcm^{-2}. The findings substantiate the formation of a passive film at the interface that prevent rapid corrodent penetration [45]. However, the resistance followed a descending trend at higher pigment concentration indicating the coat saturation. Above saturation point pigment particles deceives the coat by developing porosity which facilitate the corrodent attack.

Subsequently, a comparative study has been performed with the commercial CoAl$_2$O$_4$ blue coatings having same pigment loading as that of NaZn$_{0.9}$Co$_{0.1}$PO$_4$, Fig. 8c. The equivalent circuit [Q$_{coat}$/R$_{coat}$ + Q$_{dl}$/R$_{ct}$] is used to fit the impedance spectra of CoAl$_2$O$_4$. The collected R$_{ct}$ data is observed to increase in the order 15 < 25 < 20 wt%. Even though, the pigment is not able to provide a promising corrosion resistance over the bare epoxy coat. On evaluating the R$_{ct}$ data, the developed pigment found to offer a one order increment in corrosion resistance than CoAl$_2$O$_4$ blue, which concurrently supported by the double layer capacitance.

The Bode plots of NaZn$_{0.9}$Co$_{0.1}$PO$_4$ and CoAl$_2$O$_4$ coatings with maximum R$_{ct}$ exhibited in Fig. 8d. The f-shaped phase angle curve of CoAl$_2$O$_4$ coat present two time constant at the initial stage of immersion,
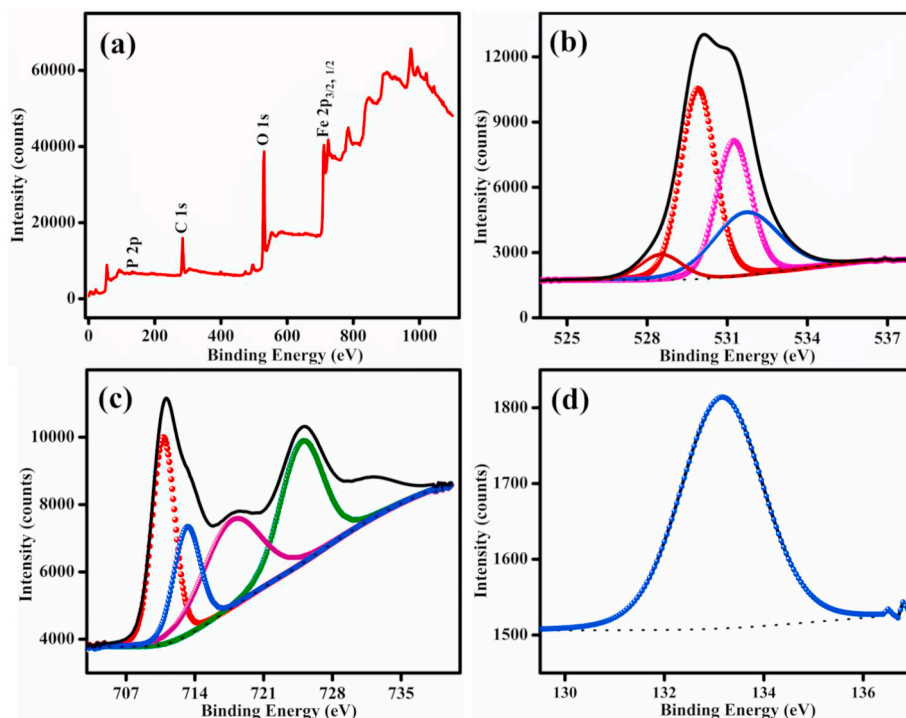
Fig. 9. XPS curve fitting of (a) survey spectrum, (b) O1s, (c) Fe 2p and (d) P 2p of inhibitive film beneath the NaZn$_{0.9}$Co$_{0.1}$PO$_4$ loaded epoxy coat on steel in 3.5 wt% NaCl after 30 days of immersion.

imply the electrolyte penetration through the coat. But NaZn$_{0.9}$Co$_{0.1}$PO$_4$ coat shows only one time constant characteristic that guarantee the protective nature of coating [21,45]. The phase angle above −100° at higher frequency range further justified the coat integrity in corrosive environment [46]. Findings confirmed the corrosion resistance property of synthesized blue pigment over commercial blue that extend the application in to the design of a blue anticorrosive paint or primer. By the virtue of which the need of duplex coats that render colour and corrosion resistance in separate can be avoided.

3.6. XPS surface analysis and corrosion inhibition mechanism

More insights on chemical changes beneath the pigment loaded epoxy coat are figured out from the XPS surface characterization. The corrosion resistant coat has been immersed in 3.5 wt% NaCl for one month, subsequently removed the coat and XPS analyzed. The survey spectrum of the metallic specimen confirmed the presence of Fe, P, and O, as displayed in Fig. 9a. By referencing the C 1s level, the high resolution spectra of O 1s, Fe 2p, and P 2p were deconvoluted and shown in Fig. 9b-d.

The O1s spectrum exhibited binding energy peaks at 529.8 (red) and 531.2 eV (magenta), corresponds to Fe$_2$O$_3$/Fe$_3$O$_4$/FeO and Fe(OH)$_2$/Fe(OH)$_3$, respectively. Further, the presence of FePO$_4$ species is confirmed on the metal surface associated with 532 eV (blue) peak. The two binding energy peaks at 710.7 (red) and 713.2 eV (blue) in Fe 2p spectrum validated the formation of iron oxides and iron phosphates, respectively. In the P 2p spectrum, BE = 133.3 eV attributed to FePO$_4$ formation [47,48].

Table 4
Colour coordinates and R* of pigment coatings.

Sample	L*	a*	b*	C*	h°	R* (%)
x = 0.1	51.78	10.70	−59.21	60.17	280.25	64.17
Concrete	49.90	1.61	−49.98	50.01	271.85	61.33 (43.72) [#]
Al sheet	47.46	6.01	−55.24	55.56	276.21	62.05 (44.87) [#]

With the assistance of XPS results, an expected corrosion inhibition mechanism is proposed. The iron oxides (Fe$_2$O$_3$/Fe$_3$O$_4$/FeO) and hydroxides (Fe(OH)$_2$/Fe(OH)$_3$) are the typical corrosion products formed at initial immersion period. However, prolonged immersion induced NaZn$_{0.9}$Co$_{0.1}$PO$_4$ to release (PO$_4$)$^{3-}$ anion and reacted with steel surface. In aqueous medium (PO$_4$)$^{3-}$ reacts on steel surface to produce iron phosphate film composed of FePO$_4$, Fe$_2$O$_3$ and FeO (Eqs. (1) and (2)) [43,44]. Presence of iron oxides in FePO$_4$ inhibitive film contributed to the higher peak area at 529.8 eV.

$$Fe \rightarrow Fe^{2+} + 2e^- \tag{1}$$

$$3Fe^{2+} + 2PO_4^{3-} + 8H_2O \rightarrow Fe_3(PO_4)_3.8H_2O + Fe_2O_3 + FeO \downarrow \tag{2}$$
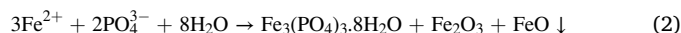
The iron phosphate film acts as corrosion barrier at metal surface and prevent corrodent attack during continuous immersion. Similar to traditional phosphate pigments, with active phosphatization, NaZn$_{0.9}$Co$_{0.1}$PO$_4$ can also have passive inhibitive nature for the initial few days of immersion [43,44]. Therefore, we concluded that the chemistry behind the excellent anticorrosive property of NaZn$_{0.9}$Co$_{0.1}$PO$_4$ would be contributed by active phosphatization and passive inhibitive film formation together.

$$Co^{2+} + 2OH^- \rightarrow Co(OH)_2 \downarrow \tag{3}$$

In the case of CoAl$_2$O$_4$, the pigment releases Co^{2+} and precipitated as hydroxide film on metal surface (Eq. (3)). However, its low solubility in NaCl decreases the rate of hydroxide precipitation. As a result CoAl$_2$O$_4$ could not form a better inhibitive film on the steel surface, and eventually accelerate corrosion [49].

3.7. Application studies

The bright colour, high solar reflectance and good corrosion resistivity endowed a high-quality pigment that needs to be studied in real coatings. However, before taking to the application studies acid-base stability of the pigment has been ensured. The pigment samples treated with acid, base and aqueous media for 30 min. Subsequently

Fig. 10. Comparison in NIR solar reflectance spectra of $NaZn_{0.9}Co_{0.1}PO_4$ coatings on (a) concrete and (b) Al sheet with their bare surfaces.

Fig. 11. Temperature shielding comparison between $NaZn_{0.9}Co_{0.1}PO_4$ and $CoAl_2O_4$ coatings (a) interior temperature of model houses (b) surface temperature on model house roofs.
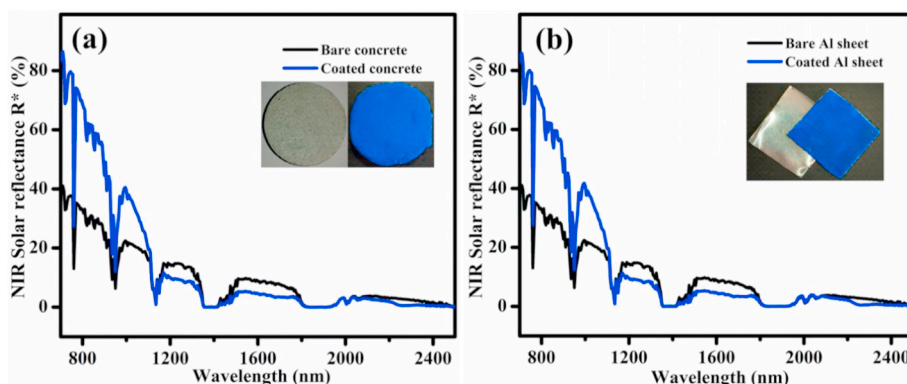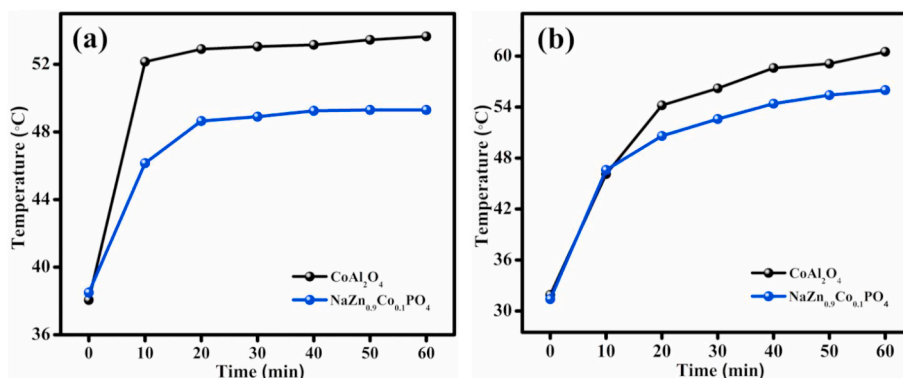
washed and dried before the chromatic measurements (Table A4). The colour difference with untreated sample stayed well within the industrial limit $\Delta E^*_{ab} \leq 1$ unit, hence confirmed the stability [40,49].

NB #: Bare surface R* is given in parenthesis.

Though the new pigment possesses intense colour and reflectance, its coatings has to be tested and confirmed for the same properties. Thus, about 20 wt% pigment loaded acrylic coatings on concrete and Al roofing sheet with 200–250 μm coating thickness evaluated for cool roof applications. The NIR solar reflectance spectra of concrete and Al sheet coatings along with its bare surface is exhibited in Fig. 10, photographs of the respective coatings are provided in the inset. The value of R* above 61% and that of the colour parameter b* above −50 suggests that the prepared coatings are highly solar reflective without much depletion in the colour strength from that of pigment powder, Table 4.

3.8. Temperature shielding performance

Temperature build up inside $CoAl_2O_4$ and $NaZn_{0.9}Co_{0.1}PO_4$ coatings (thickness 200–250 μm) roofed model houses is analyzed using the experimental set up shown in Fig. A1. The constructed model houses are exposed to IR rays continuously for 1 h. Temperature readings on T1 and T2 are monitored from t = 0–60 min at each 10 min interval. The average of T1 and T2 represented as the interior temperature, which is plotted against time and displayed in Fig. 11a. After 30 min IR exposure, interior temperature found to be stabilized, then the temperature difference calculated between both the model houses after 1 h was ~4 °C.

Further, surface temperature measurements of the coatings have studied by capturing thermal images at each 10 min interval during the IR ray exposure, as shown in Fig. A2 and A3. Fig. 11b represents the observed trend in surface temperature with time of IR exposure, where the temperature development on $NaZn_{0.9}Co_{0.1}PO_4$ is significantly lower

than (~4 °C) that of $CoAl_2O_4$ coating. Thus, the overall results suggest that $NaZn_{0.9}Co_{0.1}PO_4$ coatings can perform well as a cool roof pigment, facing the issue of rising temperature in summer. Moreover, the new blue pigment is a better pigment than the currently available $CoAl_2O_4$ for the application of IR reflective paint.

4. Conclusions

A novel deep blue inorganic pigment was developed by incorporating Co chromophore in to the Zn sites of the $NaZnPO_4$ host by solid-state reaction. Rietveld studies established the geometry of Co substituted ZnO_4 tetrahedra, where the higher covalency and electron affinity factors in response to the doping effect triggered the distortion of geometry. Spectroscopic investigations further substantiated the tetrahedral (CoO_4) geometry of chromophore and unleashed the chemistry behind blue colour. Colour strength of the pigment composition $NaZn_{0.9}Co_{0.1}PO_4$ (b* = −59.21) remained superior to that of commercial $CoAl_2O_4$, even with 10 times lesser Co content, which will have an impact on the material market value. Further, the excellent solar reflectance (R* = 64%) and remarkable corrosion resistance features furnished a multifunctional perspective for the colourant. Twenty wt% pigment loaded epoxy coatings exhibited the best corrosion resistance performance on steel in marine environment with $R_{ct} = 8.8 \times 10^6$ Ωcm^2 and $Q_{dl} = 0.016$ μFcm^{-2}, established by the electrochemical impedance spectroscopy. Later, XPS surface analysis of the coatings provided the adequate evidence for phosphatization process involved in corrosion prevention. A primary study on $NaZn_{0.9}Co_{0.1}PO_4$ acrylic coatings developed over concrete blocks and Al sheet demonstrated good colour retention and reflectance property. In addition, ~4 °C reduction in temperature at the surface and interior of the $NaZn_{0.9}Co_{0.1}PO_4$ coating compared to $CoAl_2O_4$ evaluate the new pigment as an excellent cool roof

pigment. Thus, the synthesized blue pigment can be a promising candidate for developing a multifunctional low-cost paint that could offer a primer less anticorrosive cool exterior coat.

CRediT authorship contribution statement

P.K. Thejus: Formal analysis, Writing - original draft. **K.V. Krishnapriya:** Formal analysis, Writing - original draft. **K.G. Nishanth:** Writing - original draft.

Declaration of competing interest

The authors declare that they have no known competing financial

interests or personal relationships that could have appeared to influence the work reported in this paper.

Acknowledgements
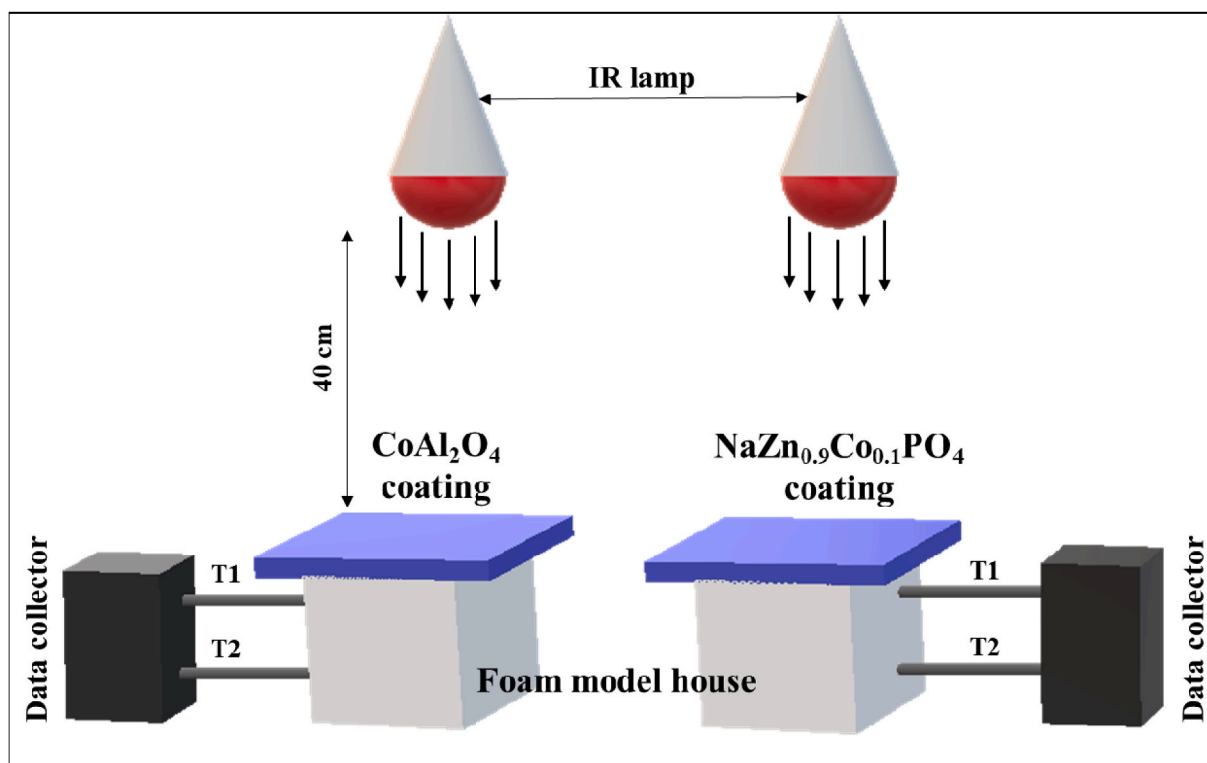
Appendix A

Fig. A.1. Schematic representation of experimental setup for thermal shielding performance of pigment coatings.
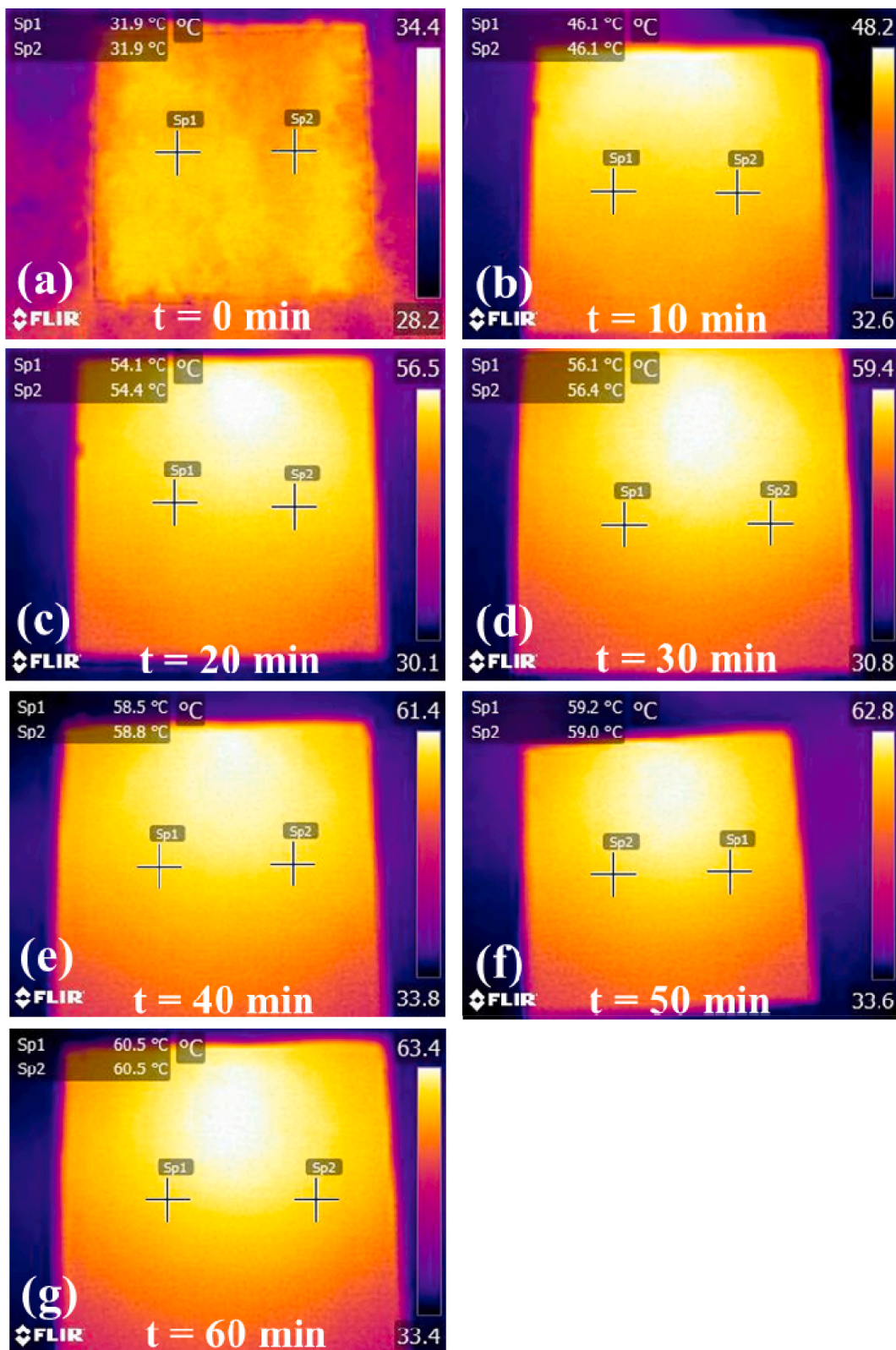
Fig. A.2. (a-g) Thermal images of CoAl$_2$O$_4$ coating during 10 min interval of IR rays exposure.

Fig. A.3. (a-g) Thermal images of NaZn$_{0.9}$Co$_{0.1}$PO$_4$ coating during 10 min interval of IR rays exposure.

Table A.1
Crystallographic data for $NaZn_{0.9}Co_{0.1}PO_4$.

Atoms	x	y	z	Occupancy	U_{iso}
Zn1	0.43650	0.22120	0.40790	1.000	0.007
Zn2/Co1	0.11010	0.71300	0.42010	0.900	0.010
Zn3	0.91519	0.21582	0.26519	1.000	0.016
Na1	0.24460	0.54700	0.25450	1.000	0.065
Na2	0.73351	0.53815	0.41150	1.000	0.002
Na3	0.72330	0.47100	0.06900	1.000	0.027
P1	0.44161	0.81623	0.40235	1.000	0.004
P2	0.11057	0.33077	0.42704	1.000	−0.007
P3	0.92387	0.82590	0.26770	1.000	0.013
O1	−0.00200	0.47900	0.88670	1.000	0.051
O2	0.95700	0.24300	0.04090	1.000	0.007
O3	0.08600	0.23000	0.18480	1.000	0.029
O4	0.23331	0.33510	0.03191	1.000	0.106
O5	0.15040	0.50000	0.43980	1.000	0.035
O6	0.94915	0.33602	0.36189	1.000	0.049
O7	0.07300	0.20900	0.50500	1.000	0.022
O8	0.23000	0.22600	0.36870	1.000	0.063
O9	0.55300	0.50400	0.19840	1.000	0.051
O10	0.44400	0.20900	0.19850	1.000	0.024
O11	0.72400	0.23700	0.20310	1.000	1.000
O12	0.55656	0.34216	0.33097	1.000	0.115

Table A.2
Bond length and bond angle involved in $Zn(2)O_4$ and $Zn(2)/CoO_4$ tetrahedra.

Bond length	$NaZnPO_4$ (Å)	$NaZn_{0.9}Co_{0.1}PO_4$ (Å)
Zn2–O4	1.94471(0)	1.83656(0)
Zn2–O5	1.93433(0)	1.79(4)
Zn2–O7	1.94630(0)	2.05(3)
Zn2–O10	1.95222(0)	1.87(4)
P1–O4	1.53472(0)	1.82207(0)
P2–O5	1.52413(0)	1.43(4)
Na2–O5	2.35600(0)	2.51(4)
Na2–O7	2.91002(0)	2.95(4)
Na3–O7	2.31721(0)	2.19(4)
Na1–O10	2.41236(0)	2.22(5)
P3–O10	1.53821(0)	1.58(4)
Bond angle	**$NaZnPO_4$ (°)**	**$NaZn_{0.9}Co_{0.1}PO_4$ (°)**
O10–Zn2–O4	113.4543	125.7(11)
O10–Zn2–O5	107.6766	101.3(15)
O10–Zn2–O7	113.0930	110.4(14)
O4–Zn2–O7	108.1093	100.5(9)
O7–Zn2–O5	109.6051	110.8(13)
O5–Zn2–O4	104.5194	108.1(10)

Table A.3
Comparison of colour and solar reflectance with reported pigments.

Sample	a*	b*	R*
$YIn_{0.9}Mn_{0.1}O_3$–ZnO	−0.88	−40.55	70 [40]
$Sr_{0.8}Eu_{0.2}CuSi_4O_{10+\delta}$	−4.9	−27.5	72 [50]
$K_{0.3}WO_3$	−1.82	−10.23	66 [51]
$Sr_{0.7}La_{0.3}Cu_{0.7}Li_{0.3}Si_4O_{10}$	10.4	−51.7	66 [52]
$LaGa_{0.8}Mn_{0.2}Ge_2O_7$	14.92	−35.12	29 [41]
$CoCr_{1.5}Al_{0.5}O_4$	−20.3	−11.4	43 [42]
$YIn_{0.8}Mn_{0.2}O_3$	9.6	−38.9	41 [53]
Al:Cu:Co:Ce:Nd 2:0.2:0.2:0.15:0.05	−8.49	−21.29	39 [54]
$Zn_{0.9}Co_{0.1}Al_2O_4$	−3.7	−39.0	63 [55]
Kaolin-$CoAl_2O_4$ hybrid	−8.98	−39.06	60 [56]
$NaZn_{0.9}Co_{0.1}PO_4$	10.70	−59.21	64 [Current study]

Table A.4
Colour coordinates of $NaZn_{0.9}Co_{0.1}PO_4$ pigment after chemical treatment.

Sample	pH	L*	a*	b*	C*	ΔE^*_{ab}
$NaZn_{0.9}Co_{0.1}PO_4$	–	51.78	10.70	−59.21	60.17	–
Water	6.59	51.65	10.04	−59.11	59.95	0.68
HNO_3	3.17	51.31	9.87	−58.66	59.48	1.10
NaOH	10.52	51.53	10.28	−58.91	59.80	0.57

References

[1] M. Pastoureau, Blue, the History of a Color, Princeton University Press, Princeton, USA, 2001.

[2] L. Samain, F. Grandjean, G.J. Long, Relationship between the synthesis of prussian blue pigments, their color, physical properties, and their behavior in paint layers, J. Phys. Chem. C 117 (2013) 9693, https://doi.org/10.1021/jp3111327, 9172.

[3] M. Ocana, J.P. Espinos, J.B. Carda, Synthesis, through pyrolysis of aerosols, of $YIn_{1-x}Mn_xO_3$ blue pigments and their efficiency for colouring glazes, Dyes Pigments 91 (2011) 501–507, https://doi.org/10.1016/j.dyepig.2011.03.009.

[4] P. Jeevanandam, R.S. Mulukutla, M. Philips, S. Chaudhuri, L.E. Erickson, K. J. Klabunde, Near infrared reflectance properties of metal oxide nanoparticles, J. Phys. Chem. C 111 (2007) 1912–1918, https://doi.org/10.1021/jp066363o.

[5] A.K. Bendiganavale, V.C. Malshe, Infrared reflective inorganic pigments, Recent Pat. Chem. Eng. 1 (2008) 67–79.

[6] P.J. Berdahl, Pigments to reflect the infrared radiation from fire, Heat Transfer 117 (1995) 355–358, https://doi.org/10.1115/1.2822529.

[7] J.A. Haines. U.S. Patent 2,005,215,685, 2005.

[8] S. Kumar, N.K. Verma, M.L. Singla, Size dependent reflective properties of TiO_2 nanoparticles and reflectors made thereof, Dig. J. Nanomater. Biostruct. 7 (2012) 607.

[9] N. Kiomarsipour, R.S. Razavi, Hydrothermal synthesis of ZnO nanopigments with high UV absorption and VIS/NIR reflectance, Ceram. Int. 40 (2014) 11261–11268, https://doi.org/10.1016/j.ceramint.2014.03.178.

[10] L. Guan, J. Fan, Y. Zhang, Y. Guo, H. Duan, Y. Chen, H. Li, H. Liu, Facile preparation of highly cost-effective $BaSO_4@BiVO_4$ core-shell structured brilliant yellow pigment, Dyes Pigments 128 (2016) 49–53, https://doi.org/10.1016/j.dyepig.2016.01.013.

[11] P.K. Thejus, K.G. Nishanth, Rational approach to synthesis low-cost $BiVO_4$–ZnO complex inorganic pigment for energy efficient buildings, Sol. Energy Mater. Sol. Cell. 200 (2019), 109999, https://doi.org/10.1016/j.solmat.2019.109999.

[12] R. Naderi, Y.S. Arman, S.H. Fouladvand, Investigation on the inhibition synergism of new generations of phosphate-based anticorrosion pigments, Dyes Pigments 105 (2014) 23–33, https://doi.org/10.1016/j.dyepig.2014.01.015.

[13] M.J. Palimi, M. Rostami, M. Mahdavian, B. Ramezanzadeh, Application of EIS and salt spray tests for investigation of the anticorrosion properties of polyurethane-based nanocomposites containing Cr_2O_3 nanoparticles modified with 3-amino propyl trimethoxy silane, Prog. Org. Coating 77 (2014) 1935–1945, https://doi.org/10.1016/j.porgcoat.2014.06.025.

[14] K. White, D. Teresa, M. Verellen, J. Tully, M.P.S. Krekeler, An investigation of lead chromate (crocoite-$PbCrO_4$) and other inorganic pigments in aged traffic paint samples from Hamilton, Ohio: implications for lead in the environment, Environ. Earth Sci. 71 (2014) 3517–3528, https://doi.org/10.1007/s12665-013-2741-0.

[15] H. Berke, The invention of blue and purple pigments in ancient times, Chem. Soc. Rev. 36 (2007) 15–30, https://doi.org/10.1039/B606268G.

[16] H. Berke, Chemistry in ancient times: the development of blue and purple pigments, Angew. Chem. Int. Ed. 14 (2002) 41.

[17] E.D. Federico, W. Shofberger, J. Schelvis, S. Kapetanaki, L. Tyne, A. Jerschow, Insight into framework destruction in ultramarine pigments, Inorg. Chem. 45 (2006) 1270, https://doi.org/10.1021/ic050903z.

[18] W. Zheng, J. Zou, Synthesis and characterization of blue $TiO_2/CoAl_2O_4$ complex pigments with good colour and enhanced near-infrared reflectance properties, RSC Adv. 5 (2015) 87932–87939, https://doi.org/10.1039/C5RA17418J.

[19] M. Yoneda, K. Gotoh, M. Nakanishi, T. Fujii, Y. Konishi, T. Nomura, Solid-state synthesis and characterization of cobalt blue core-shell pigment particles, J. Am. Ceram. Soc. 102 (2019) 3468–3476, https://doi.org/10.1111/jace.16191.

[20] L.K.C. de Souza, J.R. Zamian, G.N. da Rocha Filho, L.E.B. Soledade, I.M.G. dos Santos, A.G. Souza, T. Scheller, R.S. Angelica, C.E.F. da Costa, Blue pigments based on $Co_xZn_{1-x}Al_2O_4$ spinels synthesized by the polymeric precursor method, Dyes Pigments 81 (2009) 187–192, https://doi.org/10.1016/j.dyepig.2008.09.017.

[21] M. Llusar, A. Fores, J.A. Badenes, J. Calbo, M.A. Tena, G. Monros, Colour analysis of some cobalt-based blue pigments, J. Eur. Ceram. Soc. 21 (2001) 1121–1130, https://doi.org/10.1016/S0955-2219(00)00295-8.

[22] A.E. Smith, H. Mizoguchi, K. Delaney, N.A. Spaldin, A.W. Sleight, M. A. Subramanian, Mn^{3+} in trigonal bipyramidal coordination: a new blue chromophore, J. Am. Chem. Soc. 131 (2009) 17084–17086, https://doi.org/10.1021/ja9080666.

[23] P.K. Thejus, K. Biplab, K.G. Nishanth, An intense purple chromophore based on Co^{2+} in distorted tetrahedral coordination, Dyes Pigments 158 (2018) 267–276, https://doi.org/10.1016/j.dyepig.2018.05.054.

[24] R. Levinson, H. Akbari, P. Berdahl, Measuring solar reflectance - Part I: defining a metric that accurately predicts solar heat gain, Sol. Energy 84 (2010) 1717–1744, https://doi.org/10.1016/j.solener.2010.04.018.

[25] R. Levinson, H. Akbari, P. Berdahl, Measuring solar reflectance - Part II: review of practical methods, Sol. Energy 84 (2010) 1745–1759, https://doi.org/10.1016/j.solener.2010.04.017.

[26] T. Thongkanluang, T. Kittiauchawal, P. Limsuwan, Preparation and characterization of Cr_2O_3-TiO_2-Al_2O_3-V_2O_5 green pigment, Ceram. Int. 37 (2011) 543–548, https://doi.org/10.1016/j.ceramint.2010.09.044.

[27] L. Liu, A. Han, M. Ye, W. Feng, The evaluation of thermal performance of cool coatings colored with high near-infrared reflective nano-brown inorganic pigments: Mg doped $ZnFe_2O_4$ compounds, Sol. Energy 113 (2015) 48–56, https://doi.org/10.1016/j.solener.2014.12.034.

[28] L. Elammari, J. Durand, L. Cot, B. Elouadi, The structure of $NaZnPO_4$, Zeitschrift fur Kristallographie 180 (1987) 137–140.

[29] S.K. Janardhanan, S. Kumeresan, S. Radhika, S.V. John, C. Muralidharan, N. B. Unni, T. Ramasami, Use of mixed rare earth oxides as environmentally benign pigments, Dyes Pigments 76 (2008) 243–248, https://doi.org/10.1016/j.dyepig.2006.08.036.

[30] T. Mimani, S. Ghosh, Combustion synthesis of cobalt pigments: blue and pink, Curr. Sci. 78 (2000) 7.

[31] R. Pozas, V.M. Orera, M. Ocaña, Hydrothermal synthesis of Co-doped willemite powders with controlled particle size and shape, J. Eur. Ceram. Soc. 25 (2005) 3165–3172, https://doi.org/10.1016/j.jeurceramsoc.2004.07.006.

[32] C.M. Álvarez-Docio, J.J. Reinosa, A. Campo, J.F. Fernández, 2D particles forming a nanostructured shell: a step forward cool NIR reflectivity for $CoAl_2O_4$ pigments, Dyes Pigments 137 (2017) 1–11, https://doi.org/10.1016/j.dyepig.2016.09.061.

[33] M. Llusar, A. Forés, J.A. Badenes, J. Calbo, M.A. Tena, G. Monrós, Colour analysis of some cobalt-based blue pigments, J. Eur. Ceram. Soc. 21 (2001) 1121–1130, https://doi.org/10.1016/S0955-2219(00)00295-8.

[34] H.A. Weakliem, Optical spectra of Ni^{2+}, Co^{2+}, and Cu^{2+} in tetrahedral sites in crystals, J. Chem. Phys. (1962), https://doi.org/10.1063/1.1732840.

[35] C. Angeletti, F. Pepe, P. Porta, Structure and catalytic activity of $Co_xMg_{1-x}Al_2O_4$ spinel solid solutions. Part 1.-Cation distribution of Co^{2+} ions, J. Chem. Soc. Faraday. Trans. 1 (73) (1977) 1972–1982, https://doi.org/10.1039/F19777301972.

[36] M. Ardit, G. Cruciani, M. Dondi, Structural relaxation in tetrahedrally coordinated Co^{2+} along the gahnite-Co-aluminate spinel solid solution, Am. Mineral. 97 (2012) 1394–1401, https://doi.org/10.2138/am.2012.4093.

[37] C.R. Bambord, The application of the ligand field theory to coloured glasses, Phys. Chem. Glasses 3 (1962) 189–202.

[38] T. Bates, Ligand field theory and absorption spectra of transition metal ions in glasses, Vol. 2, in: J.D. Mackenzie (Ed.), Modern Aspects of the Vitreous State, Butterworths, London, 1961, pp. 195–254.

[39] M. Gaudon, P. Deniard, L. Voisin, G. Lacombe, F. Darnat, A. Demourgues, How to mimic the thermo-induced red to green transition of ruby with control of the temperature via the use of an inorganic materials blend? Dyes Pigments 95 (2012) 344–350, https://doi.org/10.1016/j.dyepig.2012.04.017.

[40] S. Jose, J. Anaswara, S. Laha, S. Natarajan, K.G. Nishanth, M.L.P. Reddy, $YIn_{0.9}Mn_{0.1}O_3$-ZnO nano-pigment exhibiting intense blue color with impressive solar reflectance, Dyes Pigments 124 (2016) 120–129, https://doi.org/10.1016/j.dyepig.2015.09.014.

[41] S. Divya, P.P. Rao, S. Sameera, V. James, A.K.V. Raj, Monoclinic $LaGa_{1-x}Mn_xGe_2O_7$: a new blue chromophore based on Mn^{3+} in trigonal bipyramidal coordination with longer apical bonds, RSC Adv. 5 (2015) 27278–27281, https://doi.org/10.1039/C5RA01714A.

[42] H.R. Hedayati, A.A. Sabbagh Alvani, H. Sameie, R. Salimi, S. Moosakhani, F. Tabatabaee, A. Amiri Zarandi, Synthesis and characterization of $Co_{1-x}Zn_xCr_{2-y}Al_yO_4$ as a near infrared reflective color tunable nano-pigment, Dyes Pigments 113 (2015) 588–595.

[43] Y. Hao, F. Liu, E. En-Hou Han, S. Anjum, G. Xu, The mechanism of inhibition by zinc phosphate in an epoxy coating, Corrosion Sci. 69 (2013) 77–86, https://doi.org/10.1016/j.corsci.2012.11.025.

[44] Y. Shao, C. Jio, G. Meng, T. Zhang, F. Wang, The role of a zinc phosphate pigment in the corrosion of scratched epoxy-coated steel, Corrosion Sci. 51 (2009) 371–379, https://doi.org/10.1016/j.corsci.2008.11.015.

[45] X.X. Zhao, Y. Qi, Z. Zhang, K. Li, Z. Li, Electrochemical impedance spectroscopy investigation on the corrosive behaviour of waterborne silicate micaceous iron oxide coatings in seawater, Coatings 9 (2019) 415, https://doi.org/10.3390/coatings9070415.

[46] Y. Xie, M. Chen, D. Xie, L. Zhong, X. Zhang, A fast, low temperature zinc phosphate coating on steel accelerated by graphene oxide, Corrosion Sci. 128 (2017) 1–8, https://doi.org/10.1016/j.corsci.2017.08.033.

[47] Y. Barbaux, M. Dekiouk, D. Le Maguer, L. Gengembre, D. Huchette, J. Grimblot, Bulk and surface analysis of a Fe-P-O oxydehydrogenation catalyst, Appl. Catal., A 90 (1992) 51–60, https://doi.org/10.1016/0926-860X(92)80247-A.

[48] J.F. Moulder, W.F. Stickle, P.E. S'obol, K.D. Bomben, Handbook of Xray Photoelectron Spectroscopy, Perkin-Elemer Corporation, USA, 1993.

[49] E. Ghasemi, B. Ramezanzadeh, S. Saket, S. Ashhari, Electrochemical investigation of the epoxy nanocomposites containing $MnAl_2O_4$ and $CoAl_2O_4$ nanopigments applied on the aluminum alloy 1050, J. Coating Technol. Res. 13 (2016) 97–114, https://doi.org/10.1007/s11998-015-9728-6.

[50] Y. Zhang, Y. Zhang, X. Zhao, Y. Zhang, Sol-gel synthesis and properties of europium-strontium copper silicates blue pigments with high near-infrared reflectance, Dyes Pigments 131 (2016) 154–159, https://doi.org/10.1016/j.dyepig.2016.04.011.

[51] L. Cai, X. Wu, Q. Gao, Y. Fan, Effect of morphology on the near infrared shielding property and thermal performance of $K_{0.3}WO_3$ blue pigments for smart window applications, Dyes Pigments 156 (2018) 33–38, https://doi.org/10.1016/j.dyepig.2018.03.074.

[52] S. Jose, M.L. Reddy, Lanthanum-strontium copper silicates as intense blue inorganic pigments with high near-infrared reflectance, Dyes Pigments 98 (2013) 540–546, https://doi.org/10.1016/j.dyepig.2013.04.013.

[53] A.E. Smith, M.C. Comstock, M.A. Subramanian, Spectral properties of the UV absorbing and near-IR reflecting blue pigment, $YIn_{1-x}Mn_xO_3$, Dyes Pigments 133 (2016) 214–221, https://doi.org/10.1016/j.dyepig.2016.05.029.

[54] S.P. Radhika, K.J. Sreeram, B.U. Nair, Rare earth doped cobalt aluminate blue as an environmentally benign colorant, J. Adv. Ceram. 1 (2012) 301–309, https://doi.org/10.1007/s40145-012-0029-6.

[55] R. Ianos, E. Muntean, C. Pacurariu, R. Lazau, C. Bandas, G. Delinescu, Combustion synthesis of a blue Co-doped zinc aluminate near-infrared reflective pigment, Dyes Pigments 142 (2017) 24–31, https://doi.org/10.1016/j.dyepig.2017.03.016.

[56] W. Liu, T. Du, Q. Ru, S. Zuo, X. Yang, C. Yao, Y. Kong, Facile synthesis and characterization of 2D kaolin/CoAl$_2$O$_4$: a novel inorganic pigment with high near-infrared reflectance for thermal insulation, Appl. Clay Sci. 153 (2018) 239–245, https://doi.org/10.1016/j.clay.2017.12.030.
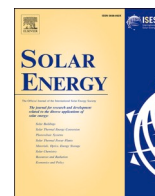
Check for updates

NIR reflective, anticorrosive magenta pigment for energy saving sustainable building coatings

P.K. Thejus, K.V. Krishnapriya, K.G. Nishanth[*]

Materials Science and Technology Division, CSIR-National Institute for Interdisciplinary Science and Technology (NIIST), Thiruvananthapuram 695019, India
Academy of Scientific and Innovative Research (AcSIR), Ghaziabad 201002, India

A B S T R A C T

A series of inorganic pigments $LiMg_{1-x}Co_xPO_4$ have synthesized by conventional solid-state method. Optical features of the phase pure compounds have investigated, the characteristic absorption spectra confirmed the octahedral geometry of Co^{2+} chromophore. The spin allowed d-d transition in the visible region attributed to the excellent magenta hue of the pigment series. The best composition $LiMg_{0.8}Co_{0.2}PO_4$ exhibited colour a* = 26.45, b* = −26.83 and NIR reflectance 67% and total solar reflectance (TSR) 55%. Acrylic coatings of $LiMg_{0.8}Co_{0.2}PO_4$ on concrete and Al roofing sheet have successfully retained the pigment properties. Subsequent temperature shielding experiment and thermal images of coatings revealed 7 °C reduction in interior temperature for the magenta coatings compared to commercial $CoAl_2O_4$. The pigment $LiMg_{0.8}Co_{0.2}PO_4$ shown excellent corrosion resistance on steel epoxy coatigs, because of the active phosphatization mechanism. The charge transfer resistance $R_{ct} = 9.3 \times 10^9$ Ωcm^2, of the coatings are 4 order higher than that of bare and $CoAl_2O_4$ loaded epoxy coatings. In addition, 10 wt% of the pigment shown an intense colour in transparent PMMA matrix, substantiated the colour deliverability of the material. Eventually, the studies concluded that $LiMg_{0.8}Co_{0.2}PO_4$ could be a potential inorganic pigment for developing an anticorrosive 'cool' paint for energy efficient buildings.

1. Introduction

The rising atmospheric temperature has become alarming in recent time due to the increasing greenhouse gas emissions. Inflating urbanization and depleting forestation further worsen the scenario by introducing heat island effect. Escalating energy demand for air conditioning, heat related health issues and mortality are some of the consequences of this longlasting issue (Rossi et al., 2020, Santamouris et al., 2015, Bendiganavale and Malshe 2008). Hence, there is an aggregating demand for the development of cooling materials for the prevention of climate disruption and mitigation of the environmental impacts. Different from the conventional techniques, materials that can regulate the heat generating near infrared rays (NIR) in the solar spectrum, attracted a huge interest in the current decade. This passive radiative cooling materials, having high NIR reflectance, are efficient in reducing the interior heat build-up of constructions (Yin et al., 2020). Inorganic pigments TiO_2, ZnO etc are already been established in this category by virtue of its inherent white colour and reflectivity (Kumar et al., 2012, Kiomarsipour and Razavi, 2014). Meanwhile, the aesthetics driven

efforts also have unveiled a few coloured cool pigments in market, like $BiVO_4$ yellow, YInMn blue etc (Thejus and Nishanth, 2019, Smith et al., 2009). An appreciable amount of high reflective inorganic cool pigments such as $Zn_{0.9}Co_{0.1}Al_2O_4$, $Al_{1.95}Cr_{0.05}O_3$, $LaAl_{1-x}Fe_xO_3$, $Sr_{1-x}La_xCu_{1-y}Li_{y-}Si_4O_{10}$, Fe doped $La_2Mo_{2-x}Fe_xO_9$, $Bi_{3-x}Fe_xYO_6$, $Y_{2-x}Tb_xZr_{2-y}Fe_yO_{7-y/2}$ etc have reported by this time yet the necessity is still growing for better alternatives (Ianos et al., 2017a, 2017b, 2018, Jose and Reddy, 2013, Han et al., 2014, Chen et al., 2020, Jovaní et al., 2016).

Roof coatings, whether it is on concrete or metallic sheet, aquired primary importance while constructing a potential cool building. At the same time, durability of the roof is much more significant to get a sustainable output from their top cool coatings. Unfortunately, it is inferior for metallic roofs, which are subjected to corrosion under long-term exposure of aggressive environmental conditions. Although, tradtional anticorrosive pigments $PbCrO_4$, Cr_2O_3, $Zn_3(PO)_4$ can sort out the issue to an extent, toxicity of the material, high expense, huge material consumption and enormous labour work makes it vulnerable (White et al., 2014, Palimi et al., 2014, Naderi et al., 2014). Hence, integrating the features colour, reflectance and corrosion resistance on a single

material can resolve all these allegations, which will have a massive impact in the industrial sector and will be highly beneficial for society and environment.

Very recently our research group have reported two new pigments, $LiZn_{0.9}Co_{0.1}PO_4$ purple and $NaZn_{0.9}Co_{0.1}PO_4$ blue, which exhibited excellent NIR reflectance property greater than 65%. Among which the blue pigment was also efficient in preventing the metallic corrosion (Thejus et al., 2018, 2021). Similar to these phosphate systems a novel magenta colour pigment, Co doped $LiMgPO_4$, was introduced by B. Serment et al., 2019. Resembling the phosphate compounds, couple of borate magenta pigments, Ni doped $LiZnBO_3$ and Co doped $Mg_2B_2O_5$ have also published previously (Tamilarasan et al., 2016, Mimani and Ghosh, 2000). Though the articles illustrated the structural as well as colour features of the pigment series in detail, no real efforts have done in their application perspective. Magenta pigments are commonly used in printing or displays as e-book readers, but their attractive colour tone brought its demand in exterior coatings as well (B. Serment et al., 2019). Therefore, continuing the effort to develop new multifunctional Co pigments for durable metallic roof coatings, we have made an attempt to explore the reflectance and anticorrosive properties of the pigment series Co doped $LiMgPO_4$. The $CoAl_2O_4$ blue and $CoCr_2O_4$ green, the highly prevalent Co pigments in the consumer market, are poor in reflectance and anticorrosion behaviour. Thus, initiatives for the development of a new multifunctional Co based inorganic pigment would be extremely relevant (Radhika et al., 2013, Hedayati et al., 2015).

2. Experimental section

2.1. Materials and methods

Extra pure Li_2CO_3 (99.9%), MgO (99.9%), $NH_4H_2PO_4$ (98%) and $CoCO_3$ (99.99%) chemicals were procured from Merck. The pigment series $LiMg_{1-x}Co_xPO_4$ ($0 \leq x \leq 1$) synthesized by solid state method. Stoichiometric quantity of precursors ground well in ethanol medium and calcined. The calcination process involves a preliminary heating at 500 °C for 3 h, during which decomposition of volatile NH_3, CO_2 and H_2O molecules occurs and subsequent grinding helps to keep the homogeneity of the precursor mixture so that the following secondary heating at 800 °C for 5 h produces the phase pure pigment powder. The experiment was repeated and analyzed the phase purity to ensure the reproducibility.

Acrylic coating of the optimized pigment composition was prepared and evaluated for its colour and IR reflectance. The coating suspension formulated by dispersing pigment and acrylic binder in 1:1 mass ratio through ultrasonication. It is brushed over TiO_2 base coated concrete block and Al roofing sheet, dried for 24 h. The acrylic coating of commercial $CoAl_2O_4$ and optimised magenta pigment composition on Al sheet (dimension $= 19 \times 19$ cm) was compared for its temperature shielding performance. The experimental setup (Fig. A1) consist of two foam model houses (dimension $= 15 \times 15 \times 15$ cm) with pigments coated Al sheet roofs. Two thermocouples T1 (top) and T2 (bottom) were placed on each foam house, 2 cm below the roof and 3 cm above the base, respectively, which helped to measure the internal temperature buildup precisely. The house roof exposed for 1 h continuous IR rays from the IR lamp (Philips, 250 W) kept at 40 cm above the roof top, during which the internal temperature was measured. Same setup was used for surface temperature measurements by capturing thermal images at regular time intervals using FLIR C2 thermal imaging camera.

The synthesized pigment samples were analyzed for corrosion inhibition property. The exiperiment was performed on pigment loaded epoxy coatings on steel substrate of $4 \times 3 \times 0.2$ cm dimension. Chemical composition of the purchased steel specimen is given as follows; C = 0.24, Mn = 0.90, Al = 0.03, Si = 0.20, Cr = 0.04, V = 0.10, P = 0.08, Cu = 0.06 and remaining Fe. Steel coupons mechanically abraded with SiC paper (grade 220 to 1000), acetone degreased and dried. Pigment

loading was varied in different wt% in a dispersion of n-butanol-epoxy-polyamide (2:2:1) system, by ultrasonication. The polished steel specimens dip coated in this dispersion at 80 mm/min dipping rate and cured for 24 h.

Synthesized pigment was incorporated in transparent PMMA polymer matrix to identify the extent of colour delivering capacity. PMMA dissolved in acetone and 10 wt% pigment powder was dispersed in it for optimization. (Vishnu et al., 2011). Obtained viscous liquid moulded into cylindrical shape after 24 h curing, resulted in magenta PMMA cylinders. It was continued for all the compositions and colour coordinates measurements were carried out.

2.2. Characterization techniques

Thermogravimetry analysis (TGA) was carried out in the temperature range of 30–1000 °C using an SII Nanotechnology Inc., TG/DTA 6200 in an air atmosphere at a heating rate of 10 °C/min. The pigments are characterised by Powder X-ray Diffraction (PXRD) Philips X'pert Pro diffractometer Ni–filtered Cu-Kα ($\lambda = 0.154060$ nm) radiation. The data collection was done by step scanning over a 2θ range $10 - 75°$ with a step size of 0.03° and 20 s counting time at each step. Scanning Electron Microscope (SEM) JEOL JSM-5600 and Dynamic Light Scattering instrument Malvern Instruments Zeta sizer nano Zis Model No: ZEN 3600 were utilized for morphology and particle size analysis, respectively. UV–Vis-NIR Spectrophotometer (Shimadzu UV-3600 with an integrating sphere attachment, ISR-2200) used for the optical feature analysis with references barium sulfate for UV–Vis range (300–700 nm) and polytetrafluoroethylene (PTFE) for NIR range (700–2500 nm). The measurement conditions are illuminant D65, 10° complementary observer and measuring geometry d/8°. The colour coordinates measurements were done with analytical software (UVPC Colour Analysis Personal Spectroscopy Software V3, Shimadzu) coupled with the UV-3600 spectrophotometer. The CIE 1976 L*a*b* colourimetric method was used, as recommended by the Commission Internationale del'Eclairage (CIE). In this method, L* is the colour lightness (L* = 0 for black and L* = 100 for white), a* is the green (-)/red (+) axis, and b*is the blue (-)/yellow (+) axis. The parameter C* (chroma) represents saturation of the colour and is defined as $C^* = \sqrt{(a^*)^2 + (b^*)^2}$ the hue angle, h° is expressed in degrees and ranges from 0 to 360° and is calculated by using the formula $h° = tan^{-1}(b^*/a^*)$. For each colourimetric parameter of a sample, measurements were made in triplicate, and an average value was taken as the result. Typically, for a given sample, the standard deviation of the measured CIE-L*a*b* value is less than 0.10, and the relative standard deviation less than 1%, indicating that the measurement error can be ignored. Optical measurements were carried out in the 700–2500 nm range. The NIR solar reflectance (R*) in the wavelength range from 700 to 2500 nm was calculated according to the ASTM standard number E891-87 as reported elsewhere (Levinson et al., 2010a, 2010b, Thongkanluang et al., 2011). The NIR solar reflectance or the fraction of solar radiation incident at wavelengths between 700 and 2500 nm that is reflected by a surface is the irradiance-weighted average of its spectral reflectance, r(λ), and can be determined using the relation,

$R^* = \frac{\int_{700}^{2500} r(\lambda)i(\lambda)d(\lambda)}{\int_{700}^{2500} i(\lambda)d(\lambda)}$ Where r(λ) is the experimentally obtained spectral reflectance (Wm^{-2}) and i(λ) is the solar spectral irradiance (Wm^{-2} nm^{-1}) obtained from ASTM standard E891-87. ASTM standard E903 was used for calculating the TSR. Electrochemical analysis of the pigment sample was performed in a multichannel potentiostat/ galvanostat (Autolab), consisting of three-electrode corrosion cell. The electrode system include saturated calomel (SCE) as reference, graphite as counter and pigment coated steel as working electrode, respectively. Open circuit potential was stabilized for 30 min. prior to the EIS experiments. The same was done in the frequency range of 10^5-10^{-2} Hz with 5 mV AC signal and the experiments were reiterated thrice for each coated specimen. Nova 2.1 software was utilized for EIS Nyquist plot
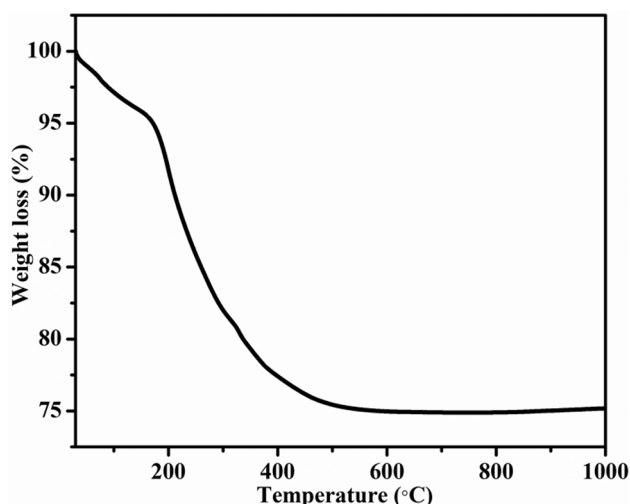
Fig. 1. TGA curve of LiMg$_{0.8}$Co$_{0.2}$PO$_4$ precursor mixture.

analysis. Surface analysis of the corrosion tested steel specimens were carried out using X-ray Photoelectron Spectrometer (XPS) (PHI 5000 Versa Probe II). Further data analysis and curve fitting was accomplished with CasaXPS software.

3. Results and discussion

3.1. Thermogravimetric analysis

Thermogravimetric analysis of LiMg$_{0.8}$Co$_{0.2}$PO$_4$ precursor mixture exhibited two-step weight loss at 30–115 °C and 115–610 °C, (Fig. 1). Initial 3.5% weight loss attributed to desorption of water molecules condensed on the sample surface (Umbreit and Paukszta, 2009). The solid-state reaction of the precursor mixture was given in Eq. (1), accordingly decomposition of NH$_3$ and CO$_2$ was observed in TGA at 160–310 °C and 320–600 °C, respectively. Further, no significant weight loss was observed, indicates the beginning of phase formation (Pardo et al., 2017). Hence, in order to get phase purity and better crystallinity, calcination temperature was fixed at 800 °C.

$$0.5Li_2CO_3 + 0.9MgO + 0.1CoCO_3 + NH_4H_2PO_4 \rightarrow LiMg_{0.9}Co_{0.1}PO_4 + 0.6CO_2 + NH_3 + 1.5H_2O \quad (1)$$
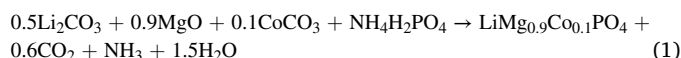
3.2. Powder X-ray diffraction analysis

The PXRD patterns of synthesised pigment series LiMg$_{1-x}$Co$_x$PO$_4$ (0 ≤ x ≤ 1) are depicted in Fig. 2. Calcination at 800 °C resulted in highly crystalline pigment powder evident from the sharp diffraction peaks. The Co doped composition upto 0.4 mol% are well matched with the parent system LiMgPO$_4$ and standard JCPDS 032–0574, Fig. 2a. It ensured the phase purity of compounds, which was crystallized in orthorhombic structure and Pmnb space group (No.62). Further increment in dopant concentration made significant changes in PXRD

Fig. 2. PXRD pattern of LiMg$_{1-x}$Co$_x$PO$_4$ (a) (0 ≤ x ≤ 0.4) (b) (0.6 ≤ x ≤ 1).

Fig. 3. (a) SEM image and (b) DLS particle size distribution of LiMg$_{0.8}$Co$_{0.2}$PO$_4$ pigment.

Fig. 4. Absorption spectra of LiMg$_{1-x}$Co$_x$PO$_4$; ($0 \leq x \leq 1$) (a) UV–Vis region (b) NIR region.

pattern. The secondary phase reflections observed at 17.5°, 23.0° and 25.8° (marked * in Fig. 2b), associated to LiCoPO$_4$ (JCPDS 032–0552).

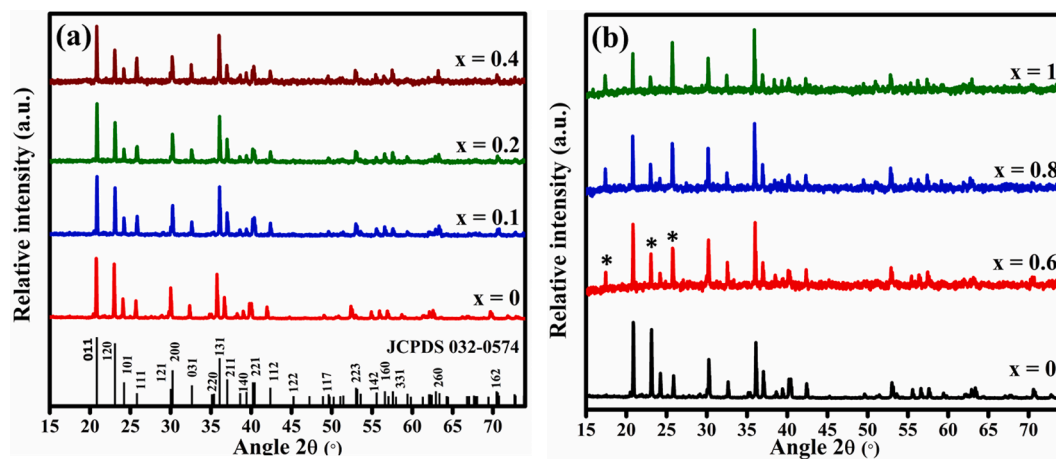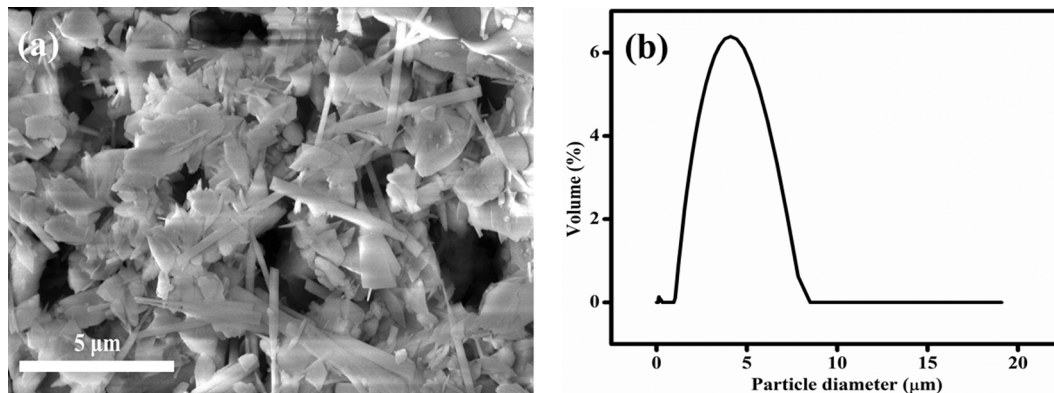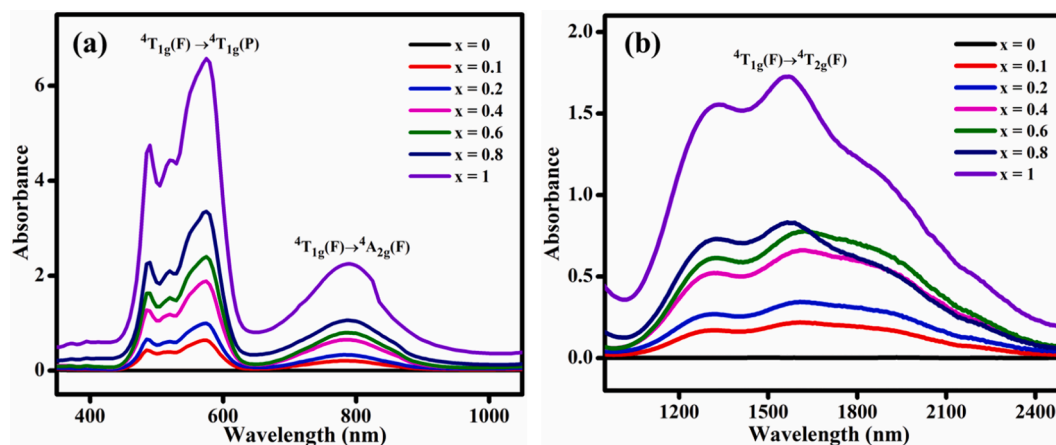No peak shift was observed in the PXRD pattern of magenta pigment series as a result of Co^{2+} doping at Mg^{2+} site. It is due to the closeness of Mg^{2+} and Co^{2+} ionic radii in the 6-coordinated site, 0.72 and 0.745 Å, respectively. The calculated cell volume and crystallite size using Scherrer formula for each composition are shown in the supporting information Table A1. Since, there was no significant peak shift in PXRD pattern, the calculated lattice parameter and cell volume of the unit cell remained unchanged as expected, on varying the Co^{2+} concentration. However, crystallite size of the phase pure Co doped compounds calculated to be ~ 71 nm, which is substantially lower than its parent compound (105 nm). It suggests that the incorporation of the dopant metal ion increased the rate of nucleation, thereby generated smaller crystallites. Further, it was expected to show a decrease in crystallite size at x = 0.6 composition due to the influence of secondary phase LiCoPO$_4$. But the change was identified at x = 0.8 composition, where there is concentration of LiCoPO$_4$ secondary phase is enough to stimulate more nucleation in turn smaller crystallites.

3.3. Morphology and particle size analysis

The submicron particle size distribution is highly essential in developing a good pigment dispersion (Sreeram et al., 2008). Therefore, as prepared LiMg$_{0.8}$Co$_{0.2}$PO$_4$ magenta pigment was subjected to high energy planetary ball milling at 135 rpm for 1 h. The SEM images of the

ball milled pigment sample was shown Fig. 3a. A mixed morphology of rods and flakes are observed for the pigment in the micrograph. The rod shaped particles are approximately 5 μm in length and 0.3 μm in width, whereas, flakes have the size distribution from 1 to 8 μm. Further, particle size distribution was obtained from the DLS analysis, Fig. 3b. A broad size distribution curve ranging from 1 to 8 μm, with an average particle size 4.5 μm, exactly corroborates the observations from electron micrographs.

3.4. Optical and chromatic properties

Absorption spectra of all the synthesized pigment compositions LiMg$_{1-x}$Co$_x$PO$_4$; ($0 \leq x \leq 1$) in the spectral range 200–2500 nm are depicted in Fig. 4. The spectra consists of three major absorption bands distributed in the visible and NIR region. An intense broad absorption at 434–643 nm (visible region) having 3 peaks at 488, 521, 577 nm and another two broad bands at 653–984 nm (visible-NIR region), 1034–2480 nm (NIR region). For a d^7 system the electronic transitions correspond to these absorptions can be assigned on the basis of Tananbe-Sugano diagram. It is the spin allowed d-d transitions $^4T_{1g}(F) \rightarrow ^4T_{1g}(P)$, $^4T_{1g}(F) \rightarrow ^4A_{2g}(F)$ and $^4T_{1g}(F) \rightarrow ^4T_{2g}(F)$ are responsible for the absorptions at 434–643, 652–984 and 1034–2480 nm, respectively (Gaudon et al., 2012, Robertson et al., 2011). The observed transitions shed light on the typical octahedral geometry of the chromophore. More informations on the geometry was aquired from the analysis of peak splittings and peak broadening. Triplet splitting of the high energy
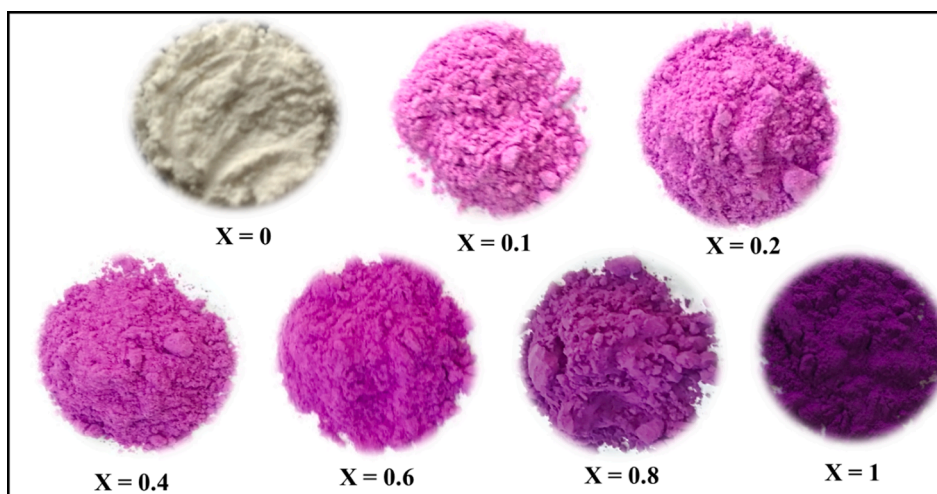

Fig. 5. Digital photographs of LiMg$_{1-x}$Co$_x$PO$_4$; ($0 \leq x \leq 1$) pigments.

Table 1

Colour co-ordinates and reflectance value of $LiMg_{1-x}Co_xPO_4$; ($0 \le x \le 1$).

Sample	L*	a*	b*	c*	h°	NIR (%) at 1100 nm	R* (%)	TSR (%)
x = 0	94.80	0.26	−0.03	0.26	353.63	96	95	94
x = 0.1	70.17	23.08	−22.53	32.25	315.70	74	64	62
x = 0.2	65.19	26.45	−26.83	37.68	314.60	67	57	55
x = 0.4	56.99	32.63	−31.66	45.47	315.87	58	47	45
x = 0.6	53.88	36.20	−34.95	50.32	316.01	57	45	42
x = 0.8	48.30	31.85	−30.69	44.23	316.07	52	40	37
x = 1	39.71	33.56	−32.91	47.00	315.57	36	27	24
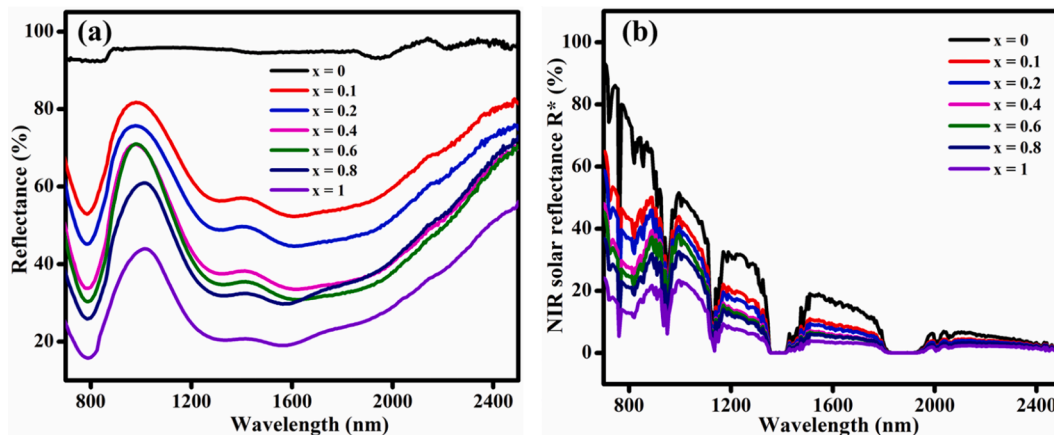
Fig. 6. (a) NIR reflectance and (b) NIR solar reflectance spectra of $LiMg_{1-x}Co_xPO_4$;($0 \le x \le 1$).

absorption was attributed to spin–orbit (L-S Russell-Saunders) coupling effect and Jahn-Tellar distortion, which in turn give rise to a peak broadening on increasing the Co concentration (Ardit et al., 2012).

The synthesized pigments have shown prominent absorbtion of green and yellow colours in the visible spectra. Thus, the pigment appeared to be the combination of their complementary colours (red and violet), magenta, Fig. 5. CIE 1976 colour co-ordinates of each composition was summarized in Table 1. The colour parameters a* (red) and -b* (blue) in equal proprtion go in line with observations in absorption spectra, similarly the hue angle 300-320°. While moving the dopant concentration ahead, no remarkable colour change is noted for phase pure compositions, instead of rise in intensity. However, the presence of $LiCoPO_4$ secondary phase brought an obvious colour variation towards violet, at 0.8 mol% doping.

3.5. Reflectance property

Beyond aesthetics inorganic pigments are now investigated for their ability to mitigate heat island effect, which was categorized as 'cool' pigments. In this focus, reflectance property of the prepared pigment series was studied in detail. Observed NIR solar reflectance spectra was displayed in Fig. 6. Since the characteristic d-d transition spread over the NIR region, Co pigments are generally poor NIR reflective materials hence not picked in the class of cool pigments (Divya et al., 2018). However, the as prepared magenta pigments have shown excellent NIR and solar reflectance, with a maximum of 74 and 64%, respectively. Since, an inverse relation holds between reflectance and Co ion concentration in turn colour, an optimized composition was necessary for further investigations. Therefore, providing equal importance for colour as well as reflectance properties, $LiMg_{0.8}Co_{0.2}PO_4$ was selected as the best compound, since it exhibited good NIR reflectance (>66%), NIR
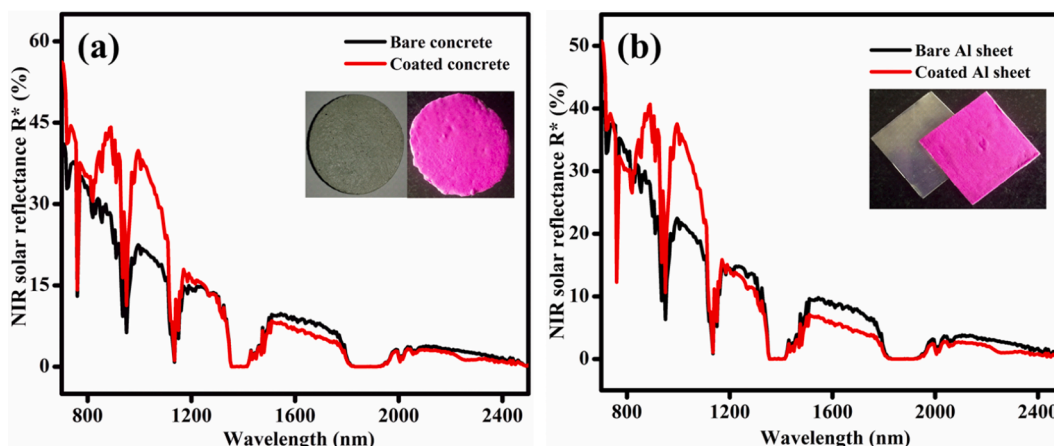
Fig. 7. Comparison of NIR solar reflectance spectrum of $LiMg_{0.8}Co_{0.2}PO_4$ coated (a) concrete block (b) Al sheet with their bare surfaces (Photographs of coatings shown inset).
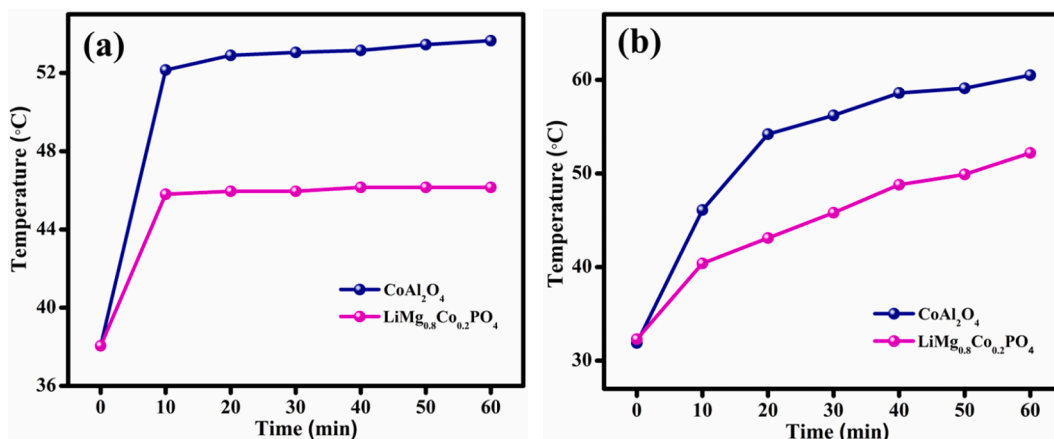
Fig. 8. Temperature shielding comparison between $LiMg_{0.8}Co_{0.2}PO_4$ and $CoAl_2O_4$ coatings (a) interior temperature of model houses (b) surface temperature on model house roofs.

solar reflectance (>57%) and colour tone (a* = 26.45, b* = −26.83).

3.6. Acrylic coatings

In the present work, a preliminary acrylic coating was developed using $LiMg_{0.8}Co_{0.2}PO_4$ on conventional building materials like concrete and Al sheet. Photographs of the coatings are displayed along with its bare substrate, inset of Fig. 7. CIE colour co-ordinates (Table A2) suggest that the coatings have retained the pigment colour sucessfully. Importantly, the calculated solar reflectance (R*), 53 and 47 on concrete and Al sheet, respectively, was higher than that of the bare surfaces (Fig. 7). Therefore the synthesized pigment can be established as a potential coloured cool pigment.

3.7. Temperature shielding performance

High solar reflective acrylic coatings encouraged the investigation to determine the temperature shielding ability. Pigment coated Al sheet (dimension = 19 × 19 cm) was roofed on a model foam house equiped with two thermocouples T1 and T2. The commercial Co pigment, $CoAl_2O_4$ coating was used for comparison following the same experimental set up. Thickness of the coatings was measured to be 200–250 μm. House roofs exposed to IR rays for 1 h, during which the interior temperature variation was monitored at each 10 min interval. Average of T1 and T2 quantified the interior temperature build-up and it was plotted with time of IR exposure, Fig. 8a. At the initial 10 min the temperature shooted up to a maximum, then maintained for rest of the experiment. But, importantly temperature inside magenta roofed house

Fig. 9. Nyquist plots of (a) bare epoxy and bare metal (inset), different wt% (b) $LiMg_{0.8}Co_{0.2}PO_4$ and (c) $CoAl_2O_4$, (d) Bode plot of 15 wt% $LiMg_{0.8}Co_{0.2}PO_4$ and 20 wt% $CoAl_2O_4$.

Table 2
EIS parameters from Nyquist plot.

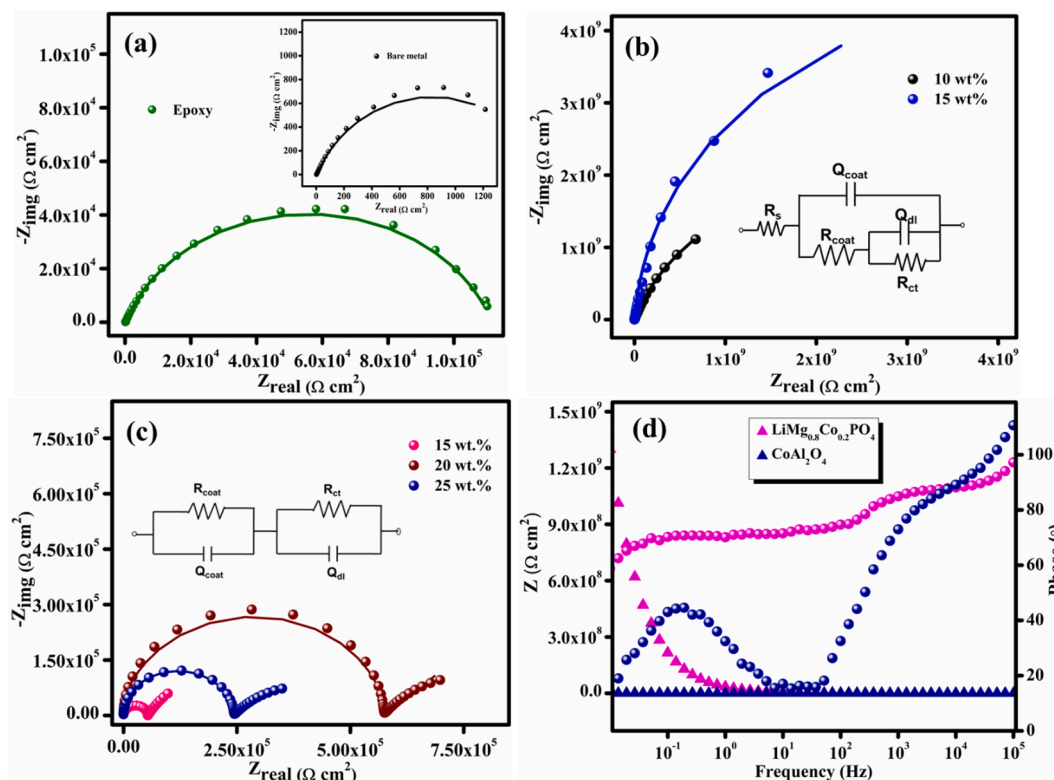| EIS parameters	Bare metal	Bare epoxy	LiMg$_{0.8}$Co$_{0.2}$PO$_4$ (wt.%)				CoAl$_2$O$_4$ (wt.%)		
			5	10	15	20	15	20	25
R$_{coat}$ (Ωcm^2)	–	159.8	9.3×10^5	4.0×10^6	3.1×10^7	9.2×10^4	5.3×10^4	5.4×10^5	2.4×10^5
Q$_{coat}$ (μFcm^{-2})	–	4.2	6.05	5.82	1.24	4.81	2.8	0.53	2.1
R$_{ct}$ (Ωcm^2)	1.2×10^3	1.2×10^5	2.6×10^6	5.3×10^9	9.3×10^9	4.5×10^7	3.4×10^5	8.7×10^5	4.3×10^5
Q$_{dl}$ (μFcm^{-2})	744	0.028	1.75	0.93	0.84	2.47	0.061	0.026	0.034

was approximately 7 °C lower than that of CoAl$_2$O$_4$ roof. The initial temperature rise was attribted to the instantaneous IR absorption of the coatings and subsequent heat transfer to the interior. Infact it strictly rely on the IR reflectivity of pigment component in the coating. Since R* of LiMg$_{0.8}$Co$_{0.2}$PO$_4$ is superior to CoAl$_2$O$_4$ (R* = 29), the magenta coating could able to prevent the absorption of IR rays to a large extent, in turn reduce heat transfer and interior heat build up. After 10 min the temperature attained an equilibrium so that no further fluctuation was observed in the trend. Importantly, the substatntial temperature difference of 7 °C can be highly beneficial to bring down the consumption of air coolers in summer season.

Further study on temperature shielding capability of magenta and CoAl$_2$O$_4$ coatings was performed by thermal imaging technique, Fig. A2 and Fig. A3. Surface temperature obtained from the images was plotted aginst IR exposure time and shown in Fig. 8b. Similar to the interior temperature plot, roof surface temperature also followed almost the similar trend. But unlike the earlier case an immediate temperature equilibration was not observed instead a decrease in rate of temperature buildup. Essentially, a significant temperature reduction (~8 °C) was

observed on magenta coatings than that of CoAl$_2$O$_4$, after 1 h. It corroborate that LiMg$_{0.8}$Co$_{0.2}$PO$_4$ magenta coating can be used to develop an efficient IR reflective cool coating on building substrates.

3.8. Anticorrosive epoxy coatings

Ability of the metallic roof coatings to withstand corrosion process is a great challenge. Anticorrosive paints played the major role in this concern in combination with coloured paints. The well known anticorrosive pigment Zn$_3$(PO$_4$)$_2$ is sucessful in this problem by virtue of the phosphatization mechanism (Hao et al., 2013, Shao et al., 2009, Xie et al., 2017). Focused on (PO)$_4^{3-}$ group in the pigmet composition, corrosion inhibition property of the new magenta pigment was analyzed via EIS. The pigment loaded (5, 10, 15 and 20 wt%) epoxy coatings were prepared on steel substrate, electrochemically tested and optimized. The coating thickness measured to be ~ 11 μm. Nyquist plots of bare and pigment incorporated epoxy coatings in 3.5 wt% saline media were exhibited in Fig. 9 and Fig. A4.

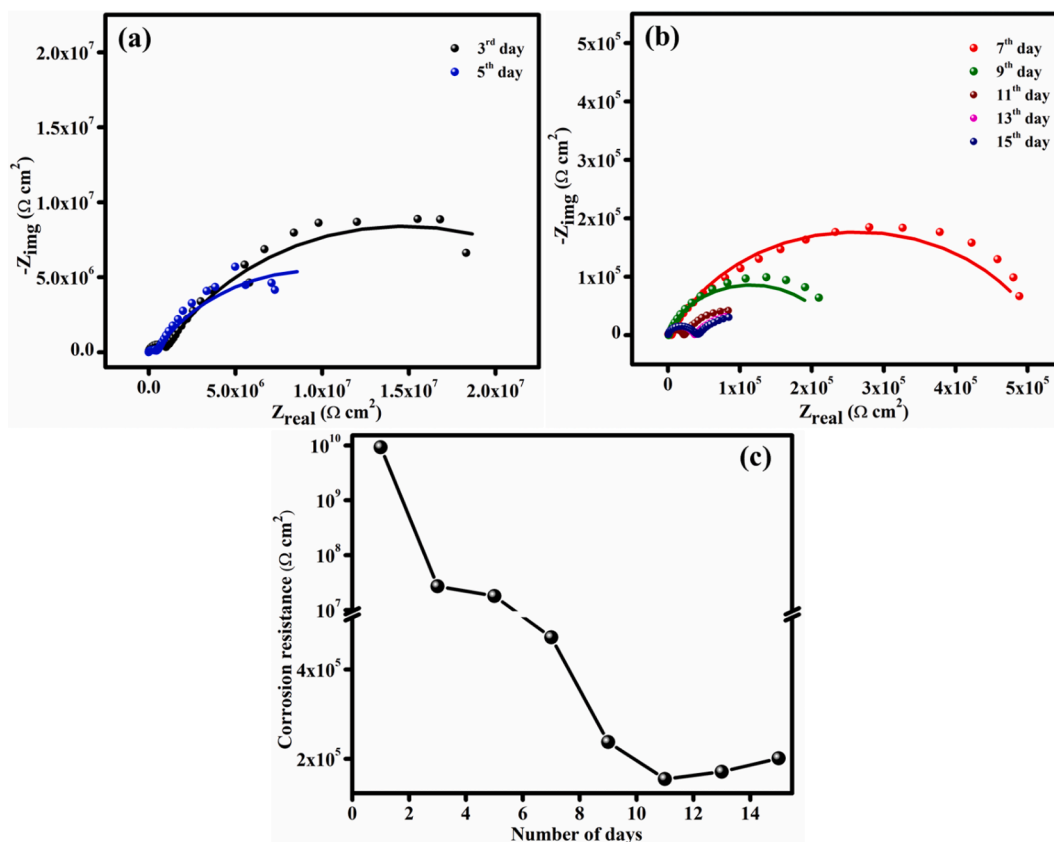Fig. 9b displayed the Nyquist diagram of LiMg$_{0.8}$Co$_{0.2}$PO$_4$

Fig. 10. (a-b) Nyquist plots of 15 days continuous electrochemical analysis of 15 wt% LiMg$_{0.8}$Co$_{0.2}$PO$_4$ loaded epoxy coating (c) trend in corrosion resistance with days of EIS experiment.
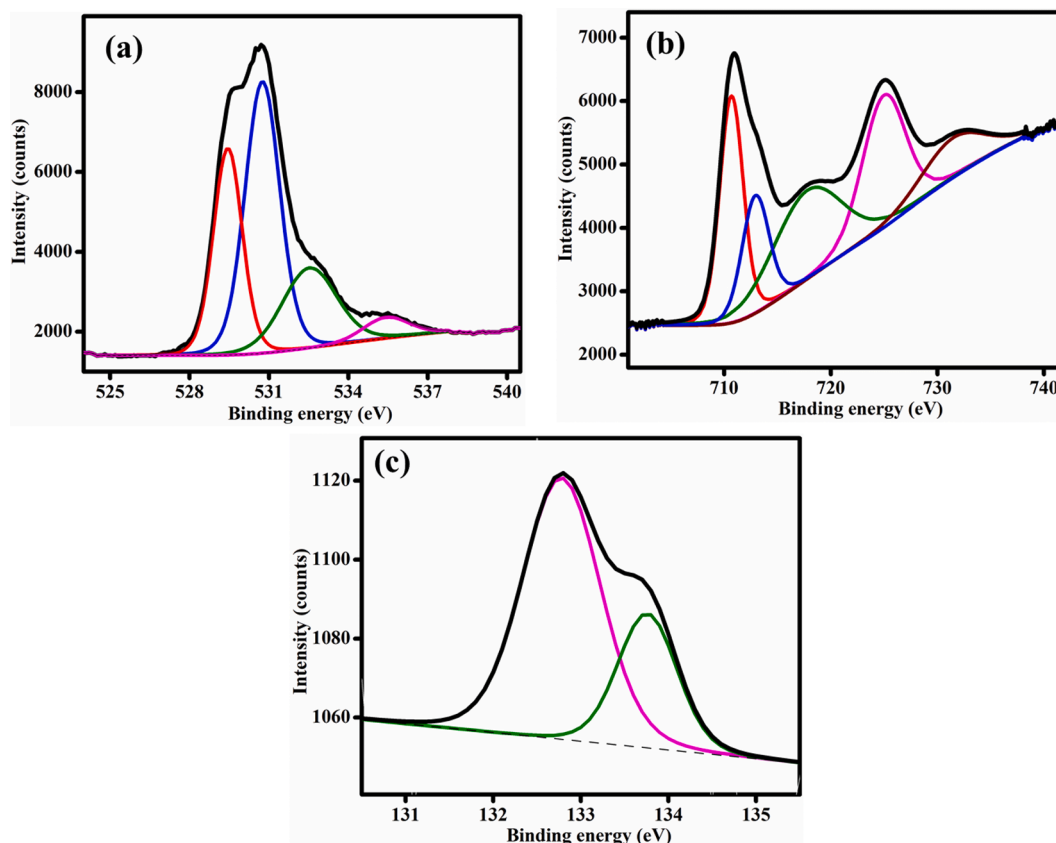
Fig. 11. XPS deconvoluted spectra of (a) O1s, (b) Fe2p and (c) P2p of inhibitive film beneath the 15 wt% $LiMg_{0.8}Co_{0.2}PO_4$ loaded epoxy coat on steel in 3.5 wt% NaCl after 15 days of EIS analysis.

incorpoarted epoxy coating. The electrochemical behaviour of the coatings were modeled with electrochemical equivalent circuit (EEC) $[Q_{coat}/(R_{coat} + Q_{dl}/R_{ct})]$. The solution resistance R_s found to be negligible, hence, removed from the circuit. R_{coat} defines the resistance offered by polymer coat, and R_{ct} is the resistance due to charge transfer mechanism at steel electrolyte interface. Q_{coat} and Q_{dl} are the constant phase elements, which express the polymer coat capacitance and double layer capacitance in the non-ideal condition, respectively (Hao et al., 2013). The EIS parameters obtained from the Nyquist plots were summarized in Table 2. Irrespective of the pigment concentration, magenta coatings have exhibited a positive response towards corrosion resistance property than bare epoxy. The R_{coat} and R_{ct} found to increase from 5 to 15 wt% and declined at 20 wt% pigment loading. The maximum R_{coat} and R_{ct} obtained at 15 wt%, was 3.1×10^7 and 9.3×10^9 Ωcm^2, respectively. The inverse trend in capacitance Q_{coat} and Q_{dl} obtained for the coatings, also substantiated these findings. The four order hike in R_{ct} compared to bare epoxy coat suggests that $LiMg_{0.8}Co_{0.2}PO_4$ is a potential anticorrosive pigment and 15 wt% is the optimum pigment volume concentration for fabricating the best anticorrosive coating out of it. Subsequent increment in pigment concentration from 15 wt% developed aggregation of particles and initiated pore formation in coatings, that resulted in deterioration of R_{ct} value.

A comparitive study was performed with commercially available $CoAl_2O_4$ pigment loaded epoxy coatings (15, 20 and 25 wt% loading) and corresponding Nyquist plots were displayed in Fig. 9c. The impedance data were fitted using EEC $[Q_{coat}/R_{coat} + Q_{dl}/R_{ct}]$. Contrastingly, at 15 wt% pigment concentration, $CoAl_2O_4$ showed $R_{ct} = 3.4 \times 10^5$ Ωcm^2, and only a slight increment ($R_{ct} = 8.7 \times 10^5$ Ωcm^2) was observed in the resistance at higher (20 wt%) loading. Therefore, the four order enhancement in resistance for magenta at lesser concentration proved that the material is an excellent anticorrosive pigment.

Bode plots of 15 wt% $LiMg_{0.8}Co_{0.2}PO_4$ and 20 wt% $CoAl_2O_4$ coatings

(Fig. 9d) have displayed the resistance in accordace with Nyquist plots. Phase angle (-θ) above 90° at higher frequency range indicated the consistency of both the coatings. However, their phase angle curve behaviour was fairly different while moving in to the low frequency end. $CoAl_2O_4$ posessed two time constants whereas one time constant for $LiMg_{0.8}Co_{0.2}PO_4$. The two time constant indicates electrolyte penetration in to the epoxy coat and one time constant represented the coat intactness (Hao et al., 2013). It reveals that the incorporated pigment components operate entirely in different manner while in contact with corrosive medium.

In the case of $CoAl_2O_4$ coatings, interaction of the pigment with electrolyte results in the formation of cobalt hydroxide films on the metallic surface.

$$Co^{2+} + 2OH^- \rightarrow Co(OH)_2 \downarrow \tag{2}$$

However, low solubility of $CoAl_2O_4$ in NaCl medium decreases the rate of $Co(OH)_2$ precipitation and weakens the active mechanism (Eq (2)). Hence, it leads to coat delamination, eventually corrosion on the metal surface. Further, detailed investigations have made using 15 wt% $LiMg_{0.8}Co_{0.2}PO_4$ loaded epoxy coatings, to figure out the protective mechanism, through 15 days of continuous electrochemical study and successive surface analysis. The Nyquist plots of the coating was shown no apparent difference in curve shape up to the 9th day of analysis. But the resistance found to decrease gradually from 9.3×10^9 to 1.8×10^7 Ω cm^2 (5th day), then to 5.1×10^5 Ω cm^2 (7th day) and 2.3×10^5 Ω cm^2 (9th day). It illustrates that the continous electrolyte exposure has developed permeation of electrolyte into the coating in turn allowed the penetration of corrodent. Later, the impedance spectrum has changed its profile on 11th day from arc shape to a combination of semicircular loop and arc (Fig. 10a-b). The presence of semicircular loop indicates the facts such as destruction of passivity of the epoxy coating followed by
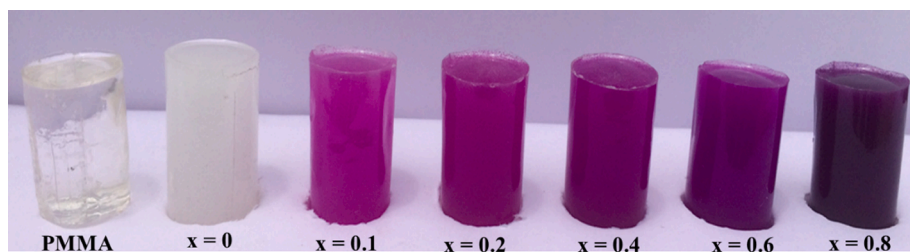
Fig. 12. Photgraph of pure PMMA and different compositions of 10 wt% pigment loaded PMMA cylinder.

the contact of electrolyte with metal surface and most importantly corrosion initiation. Interestingly, after 11 days, R_{ct} value slightly enhanced from 1.7×10^5 to 1.8×10^5 Ω cm^2, and which carried on till 15th day (2.0×10^5 Ω cm^2) of experiment, Fig. 10c. It ensured the existence of an active inhibition mechanism works between the metal electrolyte interface and stability of the anticorrosive coating.

3.9. XPS surface analysis and corrosion resistance mechanism

The speculated corrosion inhibition mechanism of the pigment loaded epoxy coating was identified by the XPS surface analysis of specimen utilized in continuous EIS analysis. The deconvoluted spectra of O 1s, Fe 2p and P 2p were displayed in Fig. 11(a-c). Three major peaks have identified from the O 1s spectrum, at 529.4, 530.7 and 532.5 eV, attributed to the corrosion products Fe_3O_4/ Fe_2O_3, corrosion intermediates $Fe(OH)_2$/$Fe(OH)_3$/FeOOH and importantly $FePO_4$, respectively. High resolution Fe2p spectrum consists of binding energy peaks corresponding to the corrosion products at 710.7 eV as well as corrosion inhibitive $FePO_4$ at 712.9 eV. Similarly P 2p spectrum also authenticated the presence of $FePO_4$ on steel surface via the binding energy peak at 133.3 ± 0.3 eV (Moulder et al., 1993, Barbaux et al., 1992). The insight of XPS results supported the assistance of corrosion inhibition mechanism via phosphatization. Under long-term exposure to corrosive medium, the corrodent breaks through the passivation offered by the polymer coat and initiate corrosion. At the same time precipitation of phosphate protective layer occurs at the metal electrolyte interphase, by the reaction of phosphate ion with steel which prevent further corrodant penetration. The possible mechanism can be written as follows (Eq (3) and (4)).

$$Fe \rightarrow Fe^{3+} + 3e^- \quad (3)$$

$$3Fe^{3+} + 3PO_4^{3-} + 8H_2O \rightarrow Fe_3(PO_4)_3 \cdot 8H_2O \quad (4)$$
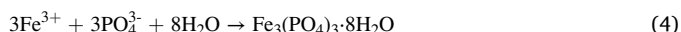
The passive nature of $LiMg_{0.8}Co_{0.2}PO_4$ incorporated epoxy coating prevent NaCl penetration at the initial days of continuous electrochemical experiment. But, when the corrodent attack destroy this mechanism the active phosphatization inhibition process comes into picture. The phosphatization barrier developed at the metal electrolyte interface provide stability and durability to the coating under continous exposure to aggressive media. Altogether, the passive and active inhibitive mechanism worked hand in hand to establish an efficient, durable anticorrosive magenta pigment applicable for metallic roofs.

3.10. Polymer colouration

Inspired from the pleasing colour tone of the pigments, the material has been employed to impart colour in polymer system. The analysis was conducted by incorporating 10 wt% pigment sample in transparent PMMA matrix. Photographs of the prepared magenta-violet PMMA cylinders using each pigment composition including base compound was shown in Fig. 12. The PMMA cylinders were highly attractive and exhibited exceptional colour intensity. Moreover, the colour coordinates (Table A1) obtained for the polymer cylinders are superior to that of respective pigment composition, where transparency of polymer matrix helps to showcase the superlative colour intensity of the pigment (Zhou et al., 2018). Hence, the developed pigment formulation can be recommended to improve the quality and aesthetics of various polymer utensils. Further, the ability of the pigment to protect from IR rays guarantee much longer material life.

4. Conclusions

The inorganic pigment series Co substituted $LiMgPO_4$ was synthesised by solid-state ceramic route. Phase pure composition obtained up to 0.4 mol% Co doping, crystallized in orthorhombic structure. The ball milled pigment possessed a broad size distribution curve with an average particle size of 4.5 μm. Octahedral Co geometry established the pleasant magenta colour because of the spin allowed d-d transitions from $^4T_{1g}$(F) ground state. $LiMg_{0.8}Co_{0.2}PO_4$ composition presented excellent reflectance property NIR = 67% and R* = 57%. Temperature shielding experiments using the pigment coated roofs have unveiled 7 °C reduction in interior temperature for magenta roofed foam house compared to $CoAl_2O_4$. Surface temperature measurements from thermal images were also substantiated the results. $LiMg_{0.8}Co_{0.2}PO_4$ epoxy coating have shown impressive corrosion inhibition performance on steel in marine media. The highest R_{ct} 9.3×10^9 Ωcm^2 was obtained at 15 wt% loading, which is 4 order higher than that of pure and $CoAl_2O_4$ loaded epoxy coating. The continuous electrochemical experiments on the coatings and subsequent surface analysis illustrated the formation of iron phosphate layer at the metal electrolyte interphase responsible for the corrosion protection mechanism. In addition, colouring ability of the pigment in transparent PMMA polymer matrix was tested, which extended its application in plastic industry. Therefore, $LiMg_{0.8}Co_{0.2}PO_4$ magenta pigment can be regarded as a promising inorganic multifunctional pigment for developing an anticorrosive 'cool' paint for energy saving buildings.

Declaration of Competing Interest

The authors declare that they have no known competing financial interests or personal relationships that could have appeared to influence the work reported in this paper.

Appendix A

See Figs. A1-A4
See Tables A1-A2
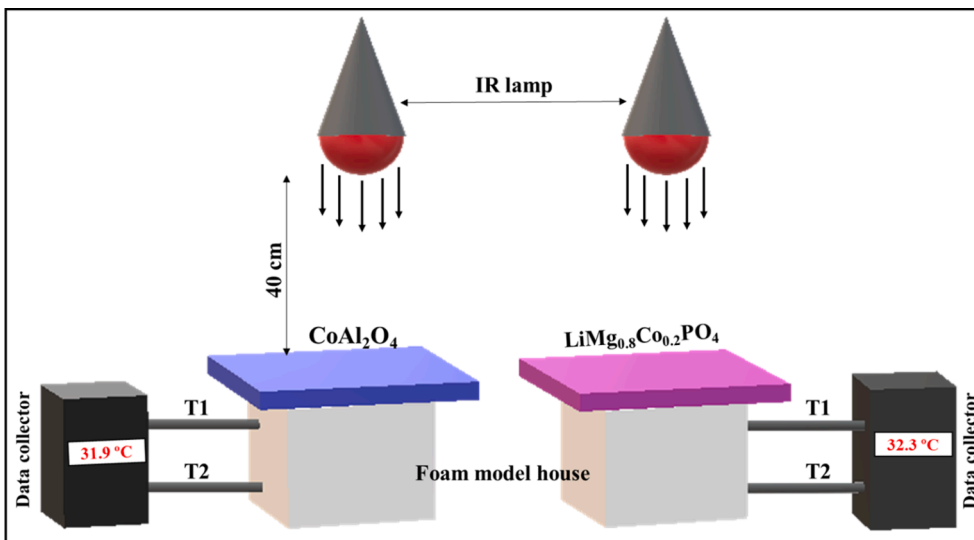
Fig. A1. Schematic representation of experimental setup for thermal shielding performance of pigment coatings.
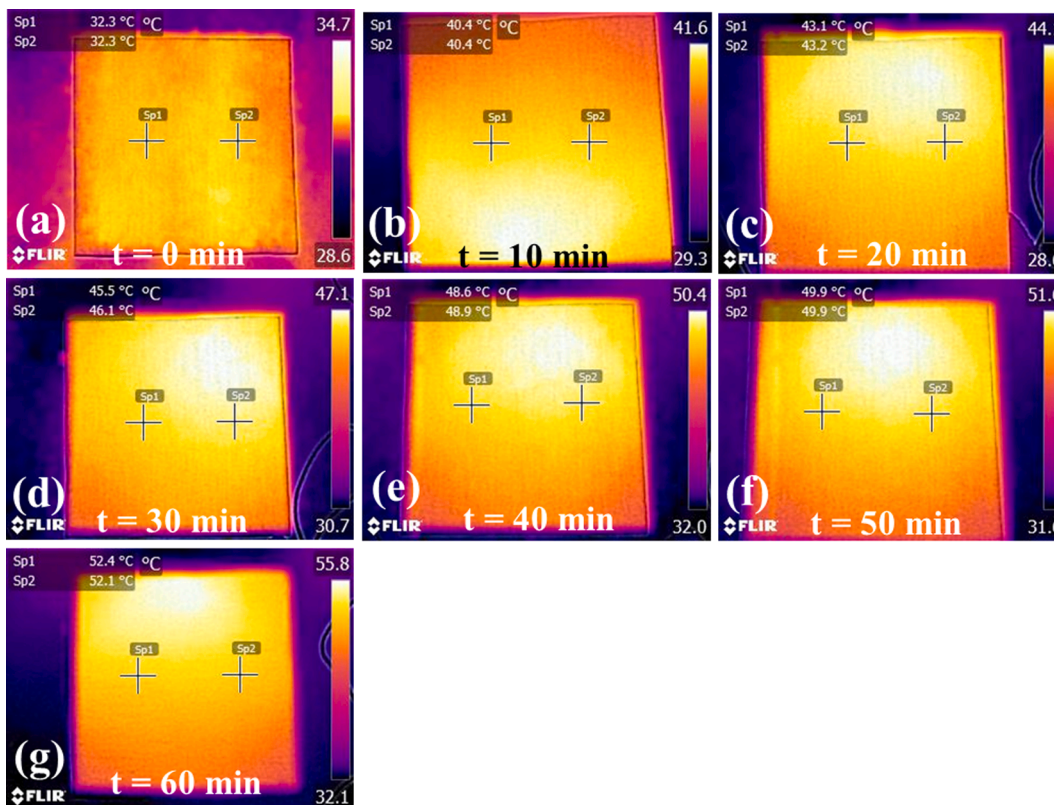
Fig. A2. (a-g) Thermal images of $LiMg_{0.8}Co_{0.2}PO_4$ coating during 10 min interval of IR rays exposure.
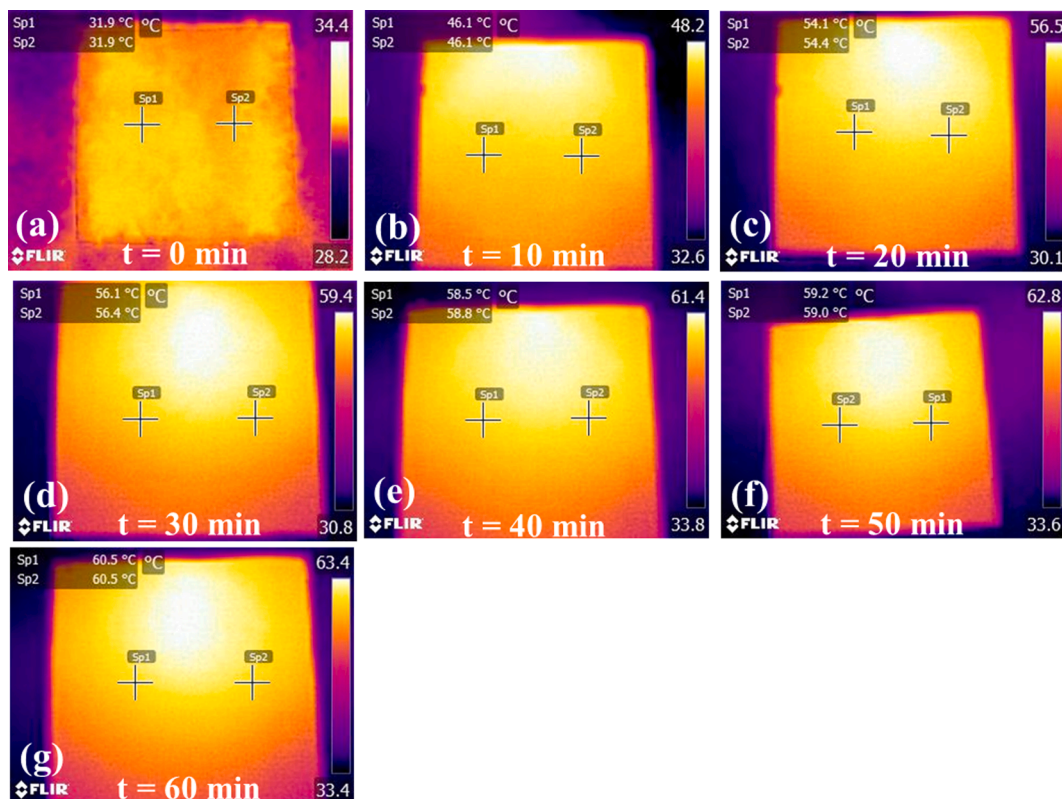
Fig. A3. (a-g) Thermal images of $CoAl_2O_4$ coating during 10 min interval of IR rays exposure.
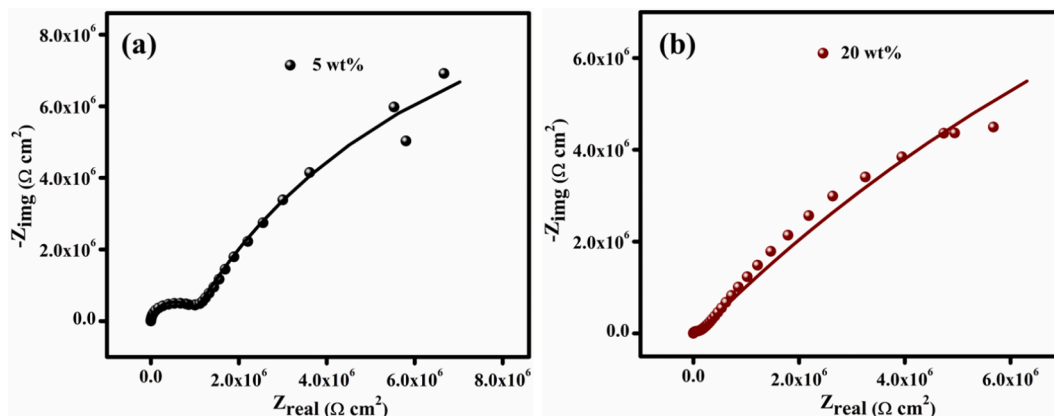
Fig. A4. Nyquist plots of (a) 5 wt%, (b) 20 wt% $LiMg_{0.8}Co_{0.2}PO_4$ loaded epoxy coating.

Table A1
Cell volume and calculated crystallite size of $LiMg_{1-x}Co_xPO_4$; $(0 \leq x \leq 1)$.

Sample	Cell volume (Å³)	Crystallite size (nm)
$LiMgPO_4$	281.325	105.188
$LiMg_{0.9}Co_{0.1}PO_4$	281.351	71.29
$LiMg_{0.8}Co_{0.2}PO_4$	281.548	71.15
$LiMg_{0.6}Co_{0.4}PO_4$	281.553	71.02
$LiMg_{0.4}Co_{0.6}PO_4$	281.641	71.01
$LiMg_{0.2}Co_{0.8}PO_4$	281.972	62.72
$LiCoPO_4$	284.498	55.07

Table A2
Colour co-ordinates and R* of $LiMg_{0.8}Co_{0.2}PO_4$ coatings and PMMA cylinders.

Sample		L*	a*	b*	R* (%)
Concrete block		66.48	24.82	−21.65	53 (45)
Al sheet		62.49	27.00	−23.36	47 (43)
$LiMg_{1-x}Co_xPO_4$ – PMMA cylinder	x = 0	59.90	−0.53	−0.81	–
	x = 0.1	36.22	29.25	−25.34	–
	x = 0.2	33.32	31.06	−25.87	–
	x = 0.4	31.44	39.05	−33.36	–
	x = 0.6	26.26	47.49	−39.47	–
	x = 0.8	19.17	27.33	−24.59	–

NB: R* of respective bare surface is given in bracket.

References

Ardit, M., Cruciani, G., Dondi, M., 2012. Structural Relaxation in Tetrahedrally Coordinated Co^{2+} along the gahnite-Co-aluminate Spinel Solid Solution. Am. Mineral. 97, 1394–1401.

Barbaux, Y., Dekiouk, M., Le Maguer, D., Gengembre, L., Huchette, D., Grimblot, J., 1992. Bulk and surface analysis of a Fe-P-O oxydehydrogenation catalyst. Appl. Catal. A 90, 51–60.

Bendiganavale, A.K., Malshe, V.C., 2008. Infrared Reflective Inorganic Pigments. Recent Patents Chem. Eng. 1, 67–79.

Chen, J., Xie, W., Guo, X., Huang, B., Xiao, Y., Sun, X., 2020. Near infrared reflective pigments based on Bi_3YO_6 for heat insulation. Ceram. Int. 46, 24575–24584. https://doi.org/10.1016/j.ceramint.2020.06.245.

Divya, S.P., Rao, P., Athira, K.V.R., Aju Thara, T.R., 2018. Intense Blue Colors in Wolframite-Type Co^{2+}: $MgWO_4$ Oxides Through Distortion in Co^{2+} Octahedra. ChemistrySelect. 3, 410–417.

Gaudon, M., Deniard, P., Voisin, L., Lacombe, G., Darnat, F., Demourgues, A., 2012. How to mimic the thermo-induced red to green transition of ruby with control of the temperature via the use of an inorganic materials blend? Dyes Pigm. 95, 344–350.

Han, A., Ye, M., Liu, L., Feng, W., Zhao, M., 2014. Estimating thermal performance of cool coatings colored with high near-infrared reflective inorganic pigments: Iron doped $La_2Mo_2O_7$ compounds. Energ. Build. 84, 698–703. https://doi.org/10.1016/j.enbuild.2014.08.024.

Hao, Y., Liu, F., Han, E., Anjum, S., Xu, G., 2013. The mechanism of inhibition by zinc phosphate in an epoxy coating. Corros. Sci. 69, 77–86.

Hedayati, H.R., Sabbagh Alvani, A.A., Sameie, H., Salimi, R., Moosakhani, S., Tabatabaee, F., Amiri Zarandi, A., 2015. Synthesis and characterization of $Co_{1-x}Zn_xCr_{2-y}Al_yO_4$ as a near infrared reflective color tunable nano-pigment. Dyes Pigm. 113, 588–595.

Ianos, R., Muntean, E., Pacurariu, C., Lazau, R., Bandas, C., Delinescu, G., 2017. Combustion synthesis of a blue Co-doped zinc aluminate near-infrared reflective pigment. Dyes Pigm. 142, 24–31.

Ianoş, R., Muntean, E., Băbuţă, R., Lazău, R., Păcurariu, C., Bandas, C., 2017. Combustion synthesis of pink chromium-doped alumina with excellent near-infrared reflective properties. Ceram. Int. 43, 2568–2572.

Ianoş, R., Muntean, E., Lazău, R., Băbuă, R., Moacă, E., Păcurariu, C., Dabici, A., Hulk, I., 2018. One-step synthesis of near-infrared reflective brown pigments based on iron-doped lanthanum aluminate, $LaAl_{1-x}Fe_xO_3$. Dyes Pigm. 152, 105–111.

Jose, S., Reddy, M.L., 2013. Lanthanum strontium copper silicates as intense blue inorganic pigments with high near-infrared reflectance. Dyes Pigm. 98, 540–546. https://doi.org/10.1016/j.dyepig.2013.04.013.

Jovaní, M., Sanz, A., Beltran-Mir, H., Cordoncillo, E., 2016. New red-shade environmental-friendly multifunctional pigment based on Tb and Fe doped $Y_2Zr_2O_7$ for ceramic applications and cool roof coatings. Dyes Pigm. 133, 33–40.

Kiomarsipour, N., Razavi, R.S., 2014. Hydrothermal synthesis of ZnO nanopigments with high UV absorption and VIS/NIR reflectance. Ceram. Int. 40, 11261–11268. https://doi.org/10.1016/j.ceramint.2014.03.178.

Kumar, S., Verma, N.K., Singla, M.L., 2012. Size dependent reflective properties of TiO_2 nanoparticles and reflectors made thereof. Dig. J. Nanomater. Biostruct. 7, 607.

Levinson, R., Akbari, H., Berdahl, P., 2010a. Measuring Solar Reflectance - Part I: Defining a Metric that Accurately Predicts Solar Heat gain. Sol. Energy. 84, 1717–1744.

Levinson, R., Akbari, H., Berdahl, P., 2010b. Measuring Solar Reflectance - Part II: Review of Practical Methods. Sol. Energy. 84, 1745–1759.

Mimani, T., Ghosh, S., 2000. Combustion synthesis of cobalt pigments: blue and pink. Curr. Sci. 78, 7.

Moulder, J.F., Stickle, W.F., S'obol, P.E., Bomben, K.D., 1993. Handbook of Xray Photoelectron Spectroscopy, Perkin-Elemer Corporation, USA.

Naderi, R., Arman, Y.S., Fouladvand, S.H., 2014. Investigation on the inhibition synergism of new generations of phosphate-based anticorrosion pigments. Dyes Pigm. 105, 23–33. https://doi.org/10.1016/j.dyepig.2014.01.015.

Palimi, M.J., Rostami, M., Mahdavian, M., Ramezanzadeh, B., 2014. Application of EIS and salt spray tests for investigation of the anticorrosion properties of polyurethanebased nanocomposites containing Cr_2O_3 nanoparticles modified with 3-amino propyl trimethoxy silane. Prog. Org. Coating 77, 1935–1945. https://doi.org/10.1016/j.porgcoat.2014.06.025.

Pardo, A., Romero, J., Ortiz, E., 2017. High-temperature behaviour of ammonium dihydrogen phosphate. J. Phys. Conf. Ser. 935, 0120500.

Radhika, S.P., Sreeram, K.J., Nair, B.U., 2013. Rare earth doped cobalt aluminate blue as an environmentally benign colorant. J. Adv. Ceram. 1, 301–309.

Robertson, L., Duttine, M., Gaudon, M., Demourgues, A., 2011. Cobalt-zinc molybdates as New Blue Pigments Involving Co^{2+} in Distorted Trigonal Bipyramids and Octahedra. Chem. Mater. 23, 2419–2427.

Rossi, S., Calovi, M., Dalpiaz, D., Fedel, M., 2020. The Influence of NIR Pigments on Coil Coatings' Thermal Behaviors. Coatings 10, 514. https://doi.org/10.3390/coatings10060514.

Santamouris, M., Cartalis, C., Synnefa, A., Kolokotsa, D., 2015. On the impact of urban heat island and global warming on the power demand and electricity consumption of buildings - A Review, Energ. Buildings 98, 119–124. https://doi.org/10.1016/j.enbuild.2014.09.052.

Serment, B., Corucho, L., Demourgues, A., Hadziioannou, G., Brochon, C., Cloutet, E., Gaudon, M., 2019. Tailoring the chemical composition of LiMPO4 (M = Mg Co, Ni) orthophosphates to design new inorganic pigments from magenta to yellow hue. Inorg. Chem. 58, 7499–7510.

Shao, Y., Jia, C., Meng, G., Zhang, T., Wang, F., 2009. The role of a zinc phosphate pigment in the corrosion of scratched epoxy-coated steel. Corros. Sci. 51, 371–379.

Smith, A.E., Mizoguchi, H., Delaney, K., Spaldin, N.A., Sleight, A.W., Subramanian, M.A., 2009. Mn^{3+} in trigonal bipyramidal coordination: a new blue chromophore. J. Am. Chem. Soc. 131, 17084–17086. https://doi.org/10.1021/ja9080666.

Sreeram, K.J., Kumeresan, S., Radhika, S., John Sundar, V., Muralidharan, C., Balachandran, U.N., Ramasami, T., 2008. Use of mixed rare earth oxides as environmentally benign pigments. Dyes Pigm. 76, 243–248.

Tamilarasan, S., Reddy, M.L.P., Natarajan, S., Gopalakrishnan, J., 2016. Developing intense blue and magenta colors in α-$LiZnBO_3$: The role of 3d-metal substitution and coordination. Chem. Asian J. 11, 3234–3240.

Thejus, P.K., Biplab, K., Nishanth, K.G., 2018. An intense purple chromophore based on Co^{2+} in distorted tetrahedral coordination. Dyes Pigm. 158, 267–276. https://doi.org/10.1016/j.dyepig.2018.05.054.

Thejus, P.K., Krishnapriya, K.V., Nishanth, K.G., 2021. A cost-effective intense blue colour inorganic pigment for multifunctional cool roof and anticorrosive coatings. Sol. Energy Mater. Sol. Cells 219, 110778.

Thejus, P.K., Nishanth, K.G., 2019. Rational approach to synthesis low-cost BiVO4–ZnO complex inorganic pigment for energy efficient buildings. Sol. Energy Mater. Sol. Cell 200, 109999. https://doi.org/10.1016/j.solmat.2019.109999.

Thongkanluang, T., Kittiauchawal, T., Limsuwan, P., 2011. Preparation and Characterization of Cr_2O_3-TiO_2-Al_2O_3-V_2O_5 Green Pigment. Ceram. Int. 37, 543–548.

Umbreit, M.H., Paukszta, D., 2009. The influence of temperature (20–1000 °C) on binary mixtures of solid solutions of $CH_3COOLi.2H_2O$–$MgHPO_4.3H_2O$. Phys. B 404, 3620–3636.

Vishnu, V.S., Jose, S., Reddy, M.L., 2011. Novel Environmentally Benign Yellow Inorganic Pigments Based on Solid Solutions of Samarium-Transition Metal Mixed Oxides. J. Am. Ceram. Soc. 94, 997–1001.

White, K., Teresa, D., Verellen, M., Tully, J., Krekeler, M.P.S., 2014. An investigation of lead chromate (crocoite-$PbCrO_4$) and other inorganic pigments in aged traffic paint samples from Hamilton, Ohio: implications for lead in the environment. Environ. Earth Sci. 71, 3517–3528. https://doi.org/10.1007/s12665-013-2741-0.

Xie, Y., Chen, M., Xie, D., Zhong, L., Zhang, X., 2017. A fast, low temperature zinc phosphate coating on steel accelerated by graphene oxide. Corros. Sci. 128, 1–8.

Yin, X., Yang, R., Tan, G., Fan, S., 2020. Terrestrial radiative cooling: Using the cold universe as a renewable and sustainable energy source. Science 370, 786–791. https://doi.org/10.1126/science.abb0971.

Zhou, Y., Jiang, P., Lei, H., Li, Y., Cao, W., Kuang, J., 2018. Synthesis and properties of novel turquoise-green pigments based on $BaAl_{2-x}Mn_xO_{4+y}$. Dyes Pigm. 155, 212–217.

Inorganic ferrite brown; transformation towards a versatile pigment for energy efficient constructions

Thejus Peringattu Kalarikkal [a,b], Krishnapriya Karattu Veedu [a,b], Nishanth Karimbintherikkal Gopalan [a,b,*]

[a] Materials Science and Technology Division, CSIR-National Institute for Interdisciplinary Science and Technology (NIIST), Thiruvananthapuram 695019, India
[b] Academy of Scientific and Innovative Research (AcSIR), Ghaziabad 201002, India

ARTICLE INFO

ABSTRACT

The present work demonstrates a multifunctional brown inorganic ferrite pigment series, which is free of highly toxic elements, via solid-state ceramic method. Partial replacement of chromophore Fe^{3+} by Al^{3+} in the pigment composition ($ZnFe_{1.9}Al_{0.1}O_4$) brought structural distortion in its octahedral geometry that further induced compressive stress inside the crystal unit cell. The introduction of even 5 mol% of Al^{3+} ions incorporated in place of Fe^{3+} could able to promote the pigment reflectance profile 25 units higher compared to parent system, particularly with significant colour improvement. Acrylic coating of the pigment on Al substrate was equally well in displaying good colour strength and temperature shielding ability ($\sim$2 °C) with respect to $ZnFe_2O_4$. The pigment stands out with its promising anticorrosive performance over the commercial toxic candidates, chromates and phosphates, exhibiting excellent R_{ct} = 4.1 $\times$ 10^9 Ωcm^2. The durability of 20 wt% pigment loaded epoxy coating on steel activates through combined action of $Zn(OH)_2$ and $FeOOH$ film mechanism. Since, the pigment exhibits intense colour, high NIR solar reflectance and robust corrosion resistance properties, their use as a high-performance multifunctional pigment is indispensable.

© 2023 The Korean Society of Industrial and Engineering Chemistry. Published by Elsevier B.V. All rights reserved.

Introduction

Inorganic dark pigments are favoured over light pigments owing to their aesthetics and ease of maintenance. In fact, it is more beneficial, since different colour shades can be achieved in convenience by dilution. Spinel ferrites are an exciting class of non-toxic dark inorganic colourant that exhibits high thermal and chemical stability [1]. Mostly, variations of black and brown colours are available in ferrite pigments [2,3]. Charge transfer transition from O^{2-} to Fe^{3+}, results in broad absorption in the visible spectrum, derived its attractive colour tones [4,5]. However, subsequent ligand field transitions at NIR region made it strong solar heat recipient, which brings urban heat island effect in action [5,6]. In a rapid population growth and urbanization, assistance of NIR reflective cool pigments that alleviate urban heat island effect is indispensable for human comfort [7–10]. Hence, in the last few decades, a fair amount of works has been undergone in concern of enhancing NIR reflectivity of ferrite pigments [11–14].

Brown is a customary colour choice for roofs and exterior wall coatings. In this aspect $ZnFe_2O_4$ turn into a highly recommended inexpensive ferrite pigment which is free of toxic elements. Various innovations have tried on this ceramic pigment to overcome NIR reflectivity issue, in which most of them were ended up in compromising its colour intensity while achieving their target. Liu et al., attempted to incorporate Mg^{2+} at Zn^{2+} site of $ZnFe_2O_4$, where they could reach 58% R* for compound $Zn_{0.6}Mg_{0.4}Fe_2O_4$ [15]. The report by Suwan et al., described on Ni doped $ZnFe_2O_4$, in which composition $Zn_{0.9}Ni_{0.1}Fe_2O_4$, exhibited much better R* $\sim$ 63% [16]. Unfortunately, colour parameters for all these compositions were gone worst compared to its parent ferrite. Similar effort from Elakkiya et al., where they have synthesized $ZnAl_{0.78}Fe_{0.2}$-$Ce_{0.02}O_4$, with very high R* 80%, but again colour found to be very feeble brown [17]. It was surprising to observe that, most of these works has been preferred to partially replace Zn^{2+} site of $ZnFe_2O_4$ with different metal ions. At the same time, from the spectral features it was already clear that transitions in Fe^{3+} is responsible for low reflectance of ferrites in NIR region [5]. Hence, it would be ideal to manipulate the Fe^{3+} site of $ZnFe_2O_4$, to accomplish improvement in NIR reflectance without colour deterioration.

NIR reflective coatings alone will not be sufficient to attain a durable temperature regulation under metallic roofing since metals are subjected to corrosion under oscillating aggressive climatic conditions. Therefore, an anticorrosive base coat is adequate to

---

* Corresponding author.
  E-mail address: nishanthkg@niist.res.in (N. Karimbintherikkal Gopalan).

prevent destruction of metal substrate thereby persist the cool coat for long [18,19]. Currently, lead chromate, zinc chromate and zinc phosphate are widely used anti-corrosive pigments. Since, chromates are categorized as hazardous material and zinc phosphate requires at high material concentration, implementing these pigment coatings under cool coat will be inappropriate [20–22]. Moreover, avoiding this conventional duplex coating mechanism is more profitable, energy and time conservative. Fortunately, $ZnFe_2O_4$ is known for its excellent anticorrosive property, but beyond preliminary investigations a comprehensive study of the pigment in coatings is limited [23–28]. Thus, it will be a massive transformation for $ZnFe_2O_4$, if we could enhance NIR reflectivity alongside exploiting its anticorrosive property to develop a sustainable cool coating.

Herein, a rational approach was followed to enhance the reflectance profile of $ZnFe_2O_4$ in NIR region without compromising colour strength, by substituting Fe^{3+} site of $ZnFe_2O_4$ with different metal ions. The best composition selected out of the synthesized compounds, investigated for structural and spectroscopic features. Further, its corrosion resistance behavior is evaluated. Colour, reflectance, stability and temperature shielding performance of the prepared acrylic coatings were commendable. Therefore, the present work could be a new insight to overcome the drawbacks of $ZnFe_2O_4$ and simultaneously exploit its multifunctional properties to escalate the market value.

Experimental section

Materials and methods

Solid-state method was used for $ZnFe_{1.9}M_{0.1}O_4$ (M = Al^{3+}, Si^{4+}, Ti^{4+}, La^{3+} and Y^{3+}) and $ZnFe_{2-x}Al_xO_4$ ($0 \leq x \leq 0.8$) pigment synthesis. Extra pure ZnO (99.9%), Fe_2O_3 (99%), Al_2O_3 (99%), SiO_2 (99.5%), TiO_2 (99%), La_2O_3 (99.9%) and Y_2O_3 (99.99%) were purchased from Merck. Stoichiometric amounts of precursors mixed homogeneously through 3 h grinding in ethanol medium and calcined at 1100 °C for 4 h in air atmosphere. All the prepared compositions and quantity of precursor utilized in each composition was tabulated in **Table S1**.

An acrylic emulsion of $ZnFe_{1.9}Al_{0.1}O_4$ pigment was prepared by dispersing pigment and acrylic binder in 1:4 ratio. Further, coatings were developed on TiO_2 base coated concrete and Al sheet and evaluated the NIR reflectance property. Similarly, temperature shielding performance was investigated, utilizing acrylic coatings on Al sheet, by means of an experimental setup shown in our previous reports and compared with commercial brown pigment coating [18,19]. Thickness of all the prepared coatings were measured using profilometer.

The pigment $ZnFe_{1.9}Al_{0.1}O_4$ was analyzed for anticorrosive property by developing epoxy coatings on steel, loaded with respective pigment powder. Steel specimen employed for the experiment have the composition C = 0.24, Mn = 0.90, Al = 0.03, Si = 0.20, Cr = 0.04, V = 0.10, P = 0.08, Cu = 0.06 and remaining Fe. Steel coupons of 4 × 3 × 0.2 cm dimension mechanically abraded with 220 to 1000 SiC paper grade subsequently acetone degreased and dried. The best anticorrosive coating was determined from different pigment loading (5, 10, 15, 20 and 25 wt%), where the pigment dispersion in n-butanol-epoxy-polyamide (2:2:1) was dip coated on polished specimens at a dipping rate of 80 mm/min and cured for 24 h.

Characterization techniques

Phase purity and crystal structure of the prepared pigment series $ZnFe_{2-x}Al_xO_4$ were analyzed by Powder X-ray Diffraction

(PXRD) analysis using Philips X'pert Pro diffractometer, Ni-filtered Cu-Kα (λ = 0.154060 nm) radiation. The Rietveld refinement was carried out using GSAS-II software. Morphology and particle size distribution were identified through JEOL JSM-5600 model Scanning Electron Microscope (SEM) and Transmission Electron Microscope (TEM) on a JEOL JEM F-200 microscope operated at 200 kV, respectively. UV–Vis-NIR Spectrophotometer (Shimadzu UV-3600 with an integrating sphere attachment, ISR-2200) used for colour and reflectance analysis of pigment samples and coatings. The NIR solar reflectance (R*) between wavelength 700–2500 nm was calculated according to ASTM standard number E891-87 as reported elsewhere [29–31]. The corrosion resistance analysis of $ZnFe_{1.9}Al_{0.1}O_4$ was performed using a multichannel potentiostat/galvanostat (Autolab) having a three-electrode cell in which saturated calomel (SCE) and graphite act as the reference and counter electrodes, respectively. Further measurement details of reflectance and corrosion analysis are described in our previous report [18]. The surface mechanism of pigment loaded epoxy coatings on steel surface was studied via PHI 5000 Versa Probe II X-ray Photoelectron Spectroscopy (XPS) using CasaXPS software.

Results and discussion

Synthesis of metal ion substituted $ZnFe_2O_4$

Different metal ions such as Al^{3+}, Si^{4+}, Ti^{4+}, La^{3+} and Y^{3+} have introduced at the Fe^{3+} site of $ZnFe_2O_4$, anticipating an improvement in NIR reflectance without colour deterioration. The criteria for selecting these metal ions as the dopant were such that all of them were exceptional candidates for providing high NIR reflectance property [32–35]. Powder XRD of all the doped samples including the base compound $ZnFe_2O_4$ are illustrated in Fig. 1**a**. Except La^{3+} and Y^{3+} doped ferrites, PXRD patterns shown the formation of a highly crystalline single-phase compound that exactly matching with the parent system $ZnFe_2O_4$. Major peaks were very well indexed to a cubic structure using JCPDS 022–1012. The ionic radii of Fe^{3+}, Si^{4+}, Al^{3+}, Ti^{4+}, Y^{3+} and La^{3+} are 0.645, 0.4, 0.535, 0.605, 0.9 and 1.032 Å, respectively. Since, Si^{4+}, Al^{3+}, Ti^{4+} are smaller than Fe^{3+}, they could able to successfully replace Fe^{3+} ion in the crystal lattice and develop phase pure compounds. In the case of La^{3+} and Y^{3+}, because of the much larger ionic size, the extent of doping was incomplete, resulting in the generation of impurity phases $LaFeO_3$ (JCPDS 075–0541) and $YFeO_3$ (JCPDS 073–1345), respectively, (marked *). When smaller ions replace the larger ions, the unit cell experience a reduction in volume and dimensions, in turn, a higher angle shift in X-ray diffraction patterns and vice versa. As expected, the reduction in cell parameter, volume (**Table S2)** and shift in XRD patterns (Fig. S1**a**) are noticed for Si^{4+}, Al^{3+}, Ti^{4+} doping, whereas, no significant variations are identified for La^{3+} and Y^{3+} doping. This can also substantiate the inconsistency of substitution due to ionic radii mismatch between host and guest ions.

NIR reflectance analyses of all the prepared samples were performed and the obtained spectra were displayed in Fig. 1**b**. The phase pure compounds have exhibited a good enhancement in the reflectance profile, by reason of potential metal ion substituents in the host lattice. At the same time, it is essential to investigate colour strength of the synthesized pigments. Because, introducing such metal ions can seriously dilute brown colour of $ZnFe_2O_4$ pigment, which will be detrimental to its quality. Among phase pure substituted pigments, Al^{3+} appeared as the best choice compared to rest of the compounds, both in terms of colour and reflectance (Table 1). The pigment $ZnFe_{1.9}Al_{0.1}O_4$ provided colour parameters a* = 25 and b* = 31, combination of strong red with feeble yellow, delivered intense brown colour amid the prepared compositions. Moreover, hue angle closer to 45^0 supported this
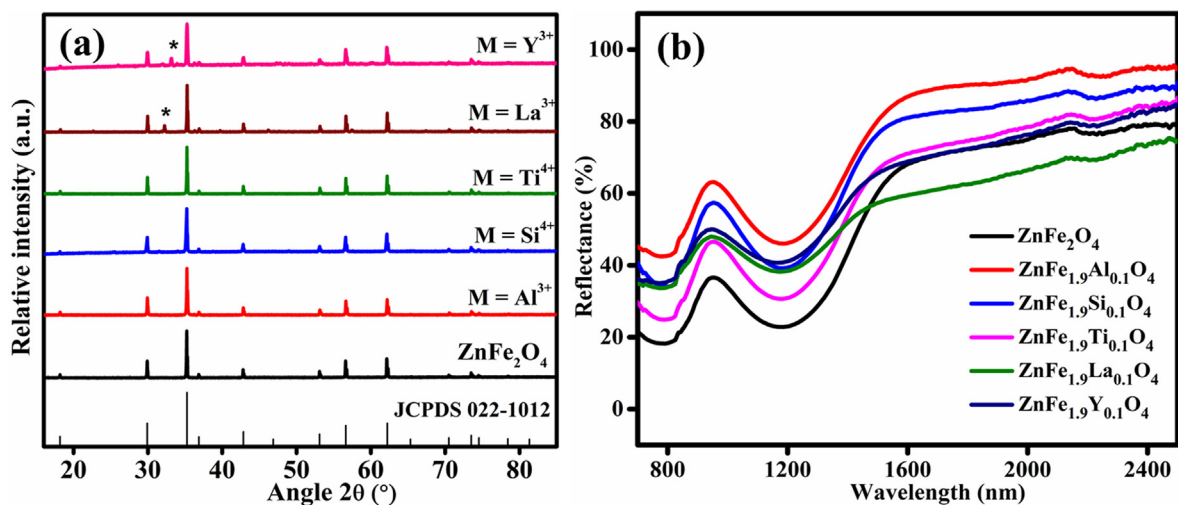
Fig. 1. (a) PXRD patterns and (b) NIR reflectance spectra of $ZnFe_{2-x}M_xO_4$ (M = Al^{3+}, Si^{4+}, Ti^{4+}, La^{3+} and Y^{3+}).

Table 1
Colour and reflectance values of $ZnFe_{2-x}M_xO_4$ (M = Al^{3+}, Si^{4+}, Ti^{4+}, La^{3+} and Y^{3+}).

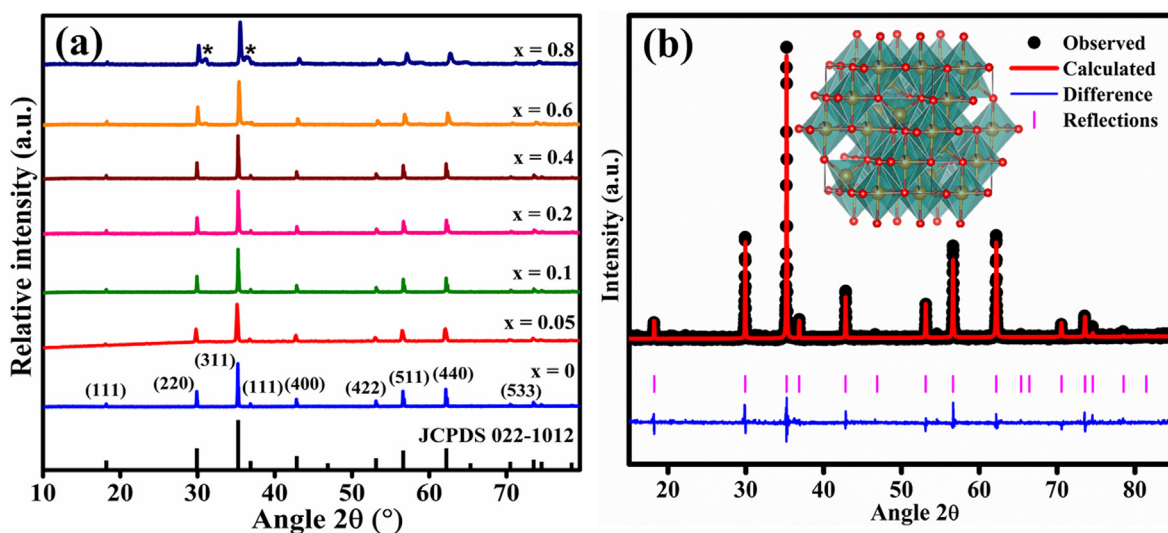| Sample	L*	a*	b*	C*	h°	NIR (%) at 1100 nm	R* (%)
$ZnFe_2O_4$	38.93	22.46	25.05	33.64	48.11	25	34
$ZnFe_{1.9}Al_{0.1}O_4$	46.54	25.05	31.01	39.86	51.06	50	58
$ZnFe_{1.9}Si_{0.1}O_4$	45.14	25.34	34.24	42.60	53.49	43	51
$ZnFe_{1.9}Ti_{0.1}O_4$	39.54	22.23	20.98	30.57	43.33	34	41
$ZnFe_{1.9}La_{0.1}O_4$	37.72	21.59	19.37	29.00	41.89	40	44
$ZnFe_{1.9}Y_{0.1}O_4$	42.86	23.01	23.62	32.98	45.74	42	48

Fig. 2. (a) PXRD patterns of $ZnFe_{2-x}Al_xO_4$ ($0 \leq x \leq 0.8$) and (b) Rietveld refined PXRD pattern of $ZnFe_{1.9}Al_{0.1}O_4$ (crystal structure inset).

colour determination and high colour richness $C^* \sim 40$, further validated its selection. Subsequently, $ZnFe_{2-x}Al_xO_4$ pigment series was developed, emphasizing colour as well as reflectance properties, and selected the best composition out of them.

Synthesis of $ZnFe_{2-x}Al_xO_4$ pigment series and Rietveld refinement

The powder XRD patterns of synthesized pigment series $ZnFe_{2-x}Al_xO_4$ ($0 \leq x \leq 0.8$) was shown in Fig. 2a. The diffraction peaks up to composition x = 0.6 are well matched to the parent cubic $ZnFe_2$-

O_4 with a spinel structure and indexed using JCPDS 022–1012. Beyond which, $AlFeO_3$ (JCPDS 08–2154) observed as an impurity phase (marked *).

In comparison with parent system, addition of Al^{3+} ions give rise to a shift in diffraction peaks to higher diffraction angle. As an example, Fig. S1b, specified the shift of PXRD peaks correspond to (220) and (311) Miller planes. It suggested that a larger fraction of Al^{3+} was able to successfully replace Fe^{3+} in $ZnFe_2O_4$. However, when smaller Al^{3+} (0.535 Å) incorporated at larger Fe^{3+} (0.645 Å) site of $ZnFe_2O_4$ crystal, a lattice strain was generated into the sys-

tem [36]. As dopant concentration increased, the induced lattice distortion also increased, resulted into the reduction in lattice periodicity and crystal symmetry. It was identified from the PXRD patterns, which exhibited a shift in Bragg reflections, depletion in peak intensity and peak broadening, from composition x = 0 to 0.8, Fig. S1**b**, [5]. The calculated lattice parameter and unit cell volume from the PXRD patterns also accounts for the developed compressive strain in the $ZnFe_2O_4$ unit cell. Both cell parameter and cell volume followed a steady decrease with increase in Al^{3+} concentration, **Table S3**. The average crystallite size, calculated by Scherrer equation, $D = K\lambda / \beta \cos \theta$, was declined from 139.5 to 62 nm, indicates the systematic drop in crystallinity during the incorporation of Al^{3+} [37]. Further, the lattice strain (ε) induced and dislocation density (δ) were calculated using the formula, $\varepsilon = \beta \cos \theta / 4$ and $\delta = 1/D^2$, respectively [38,39]. Both these factors illustrated the strain and defects exerted by the dopant ion on the parent crystal lattice that found to increase with increase in Al^{3+} content.

The crystal structure modification due to Al^{3+} doping was understood through Rietveld refinement analysis of the composition $ZnFe_{1.9}Al_{0.1}O_4$. The refined XRD pattern with Rp factor 3.6%, was shown in Fig. 2**b**, and crystallographic data was tabulated in **Table S4**. Calculated bond length and bond angle revealed that, in $ZnFe_2O_4$ structure Zn^{2+} and Fe^{3+} exists in a nearly perfect tetrahedral and octahedral geometry, respectively. But after the substitution of Al^{3+} ion, Fe-O bonds in FeO_6 geometry reduced significantly, **Table S5**. That developed a compression in the FeO_6 octahedron thereby a distortion in its structure, **Fig. S2**. The obtained crystal structure for $ZnFe_{1.9}Al_{0.1}O_4$ exhibited inset Fig. 2**b**. Eventually, this reduction in bond length became the root cause for generating the compressive strain throughout the $ZnFe_{1.9}Al_{0.1}O_4$ crystal system.

Morphology and particle size analysis

The SEM images of $ZnFe_2O_4$ and $ZnFe_{1.9}Al_{0.1}O_4$ pigment samples were illustrated in Fig. 3. The micrographs show smooth particles of irregular morphology and little agglomeration. The $ZnFe_2O_4$ micro particles were nearly uniform in size and shown a size distribution range from 1–1.3 µm, Fig. 3**a**. Whereas, comparably smaller $ZnFe_{1.9}Al_{0.1}O_4$ particles exhibited broad size distribution 0.2–1 µm, Fig. 3**b**. Further, EDS analysis confirmed the presence of constituent elements Zn, Fe, Al and O, **Fig S3**. The experimentally determined elemental composition of $ZnFe_2O_4$ and $ZnFe_{1.9}Al_{0.1}O_4$, from EDS, shown close agreement with calculated value, inset **Fig. S3**.

Morphology and size distribution from TEM images were shown in Fig. 4, which was consistent with SEM results. $ZnFe_2O_4$ displayed a narrow particle size distribution, meanwhile it was

broadened after Al^{3+} doping. In addition, average particle size was also reduced after the doping process, from ∼ 1 to ∼ 0.5 µm. Fig. 4**c and 4f** are the HRTEM images, displayed the highly ordered lattice fringes. The d-spacing measured for the lattice planes (220), (311) and (400) of $ZnFe_{1.9}Al_{0.1}O_4$, was smaller than that of $ZnFe_2O_4$. It further confirmed the unit cell shrinkage experienced by $ZnFe_{1.9}$-$Al_{0.1}O_4$ lattice, due to Al^{3+} substitution. Since, dopant inclusion disturbed host crystal lattice, the crystal growth in turn particle growth is affected and resulted in smaller particles.

Optical and chromatic properties

Optical properties of the pigment series $ZnFe_{2-x}Al_xO_4$ ($0 \leq x \leq 0.8$) were investigated by UV–Vis-NIR absorption spectroscopy, Fig. 5**a**. Three major absorptions are distributed at 200–655 nm, 685–935 and 988–1417 nm region. The intense broad peak at 200–655 nm is a combination of two absorption bands with λ_{max} 293 and 423 nm. The absorption lies in UV region correspond to the charge transfer transitions involving Zn^{2+} orbitals [5]. Further, strong absorption at high energy part of the visible spectrum was originated from $O_{2p} \rightarrow Fe_{3d}$ charge transfer transition [5,40–42]. Starting from UV region the absorption edge extended over to orange colour in visible spectrum, leaving behind the entire low energy red rays to get reflected. Remaining absorptions at 785 and 1182 nm were attributed to intra-atomic d-d transitions in Fe^{3+}. But, according to Tanabe-Sugano diagram, in an octahedral field all the d-d transitions from Fe^{3+} high-spin d^5 electronic configuration are both spin and Laporte forbidden. Hence, intensity of these absorptions is found to be very low with respect to the charge transfer transition. Respective forbidden transitions are identified as $^6A_{1g} \rightarrow ^4T_{1g}$ and $^6A_{1g} \rightarrow ^4T_{2g}$ for peaks at 785 and 1182 nm, [5,40–42].

When Al^{3+} replaced Fe^{3+}, intensity of the absorption profile decreased due to decrease in concentration of the chromophore and colour dilution effect brought by the dopant. Further, analysis revealed that it is predominantly the absorption associated with Fe^{3+} (423, 785 and 1182 nm) exhibited a significant intensity drop with regard to 293 nm peak. The charge transfer transition in chromophore has shown a slight blue shift with respect to increase in Al substitution. It must be associated with the structural strain implemented through the doping process.

Colour strength of the pigment series was determined by CIE 1976 L*a*b* colour system, shown in Table 2. The pigments samples are intense brown in colour, Fig. 5**a** (inset), obtained as the combination of colour parameters a* (red) and b* (yellow) positive axes. The hue angles closer to 45-50⁰ and rising colour saturation also supported this observation. As expected, the intensity of brown colour tend to decrease with increase in added amount of
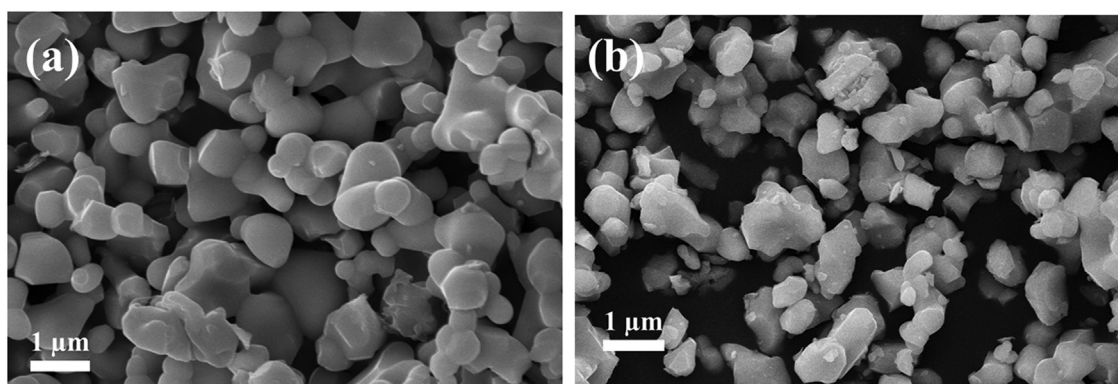

Fig. 3. SEM images of (a) $ZnFe_2O_4$ and (b) $ZnFe_{1.9}Al_{0.1}O_4$, respectively.
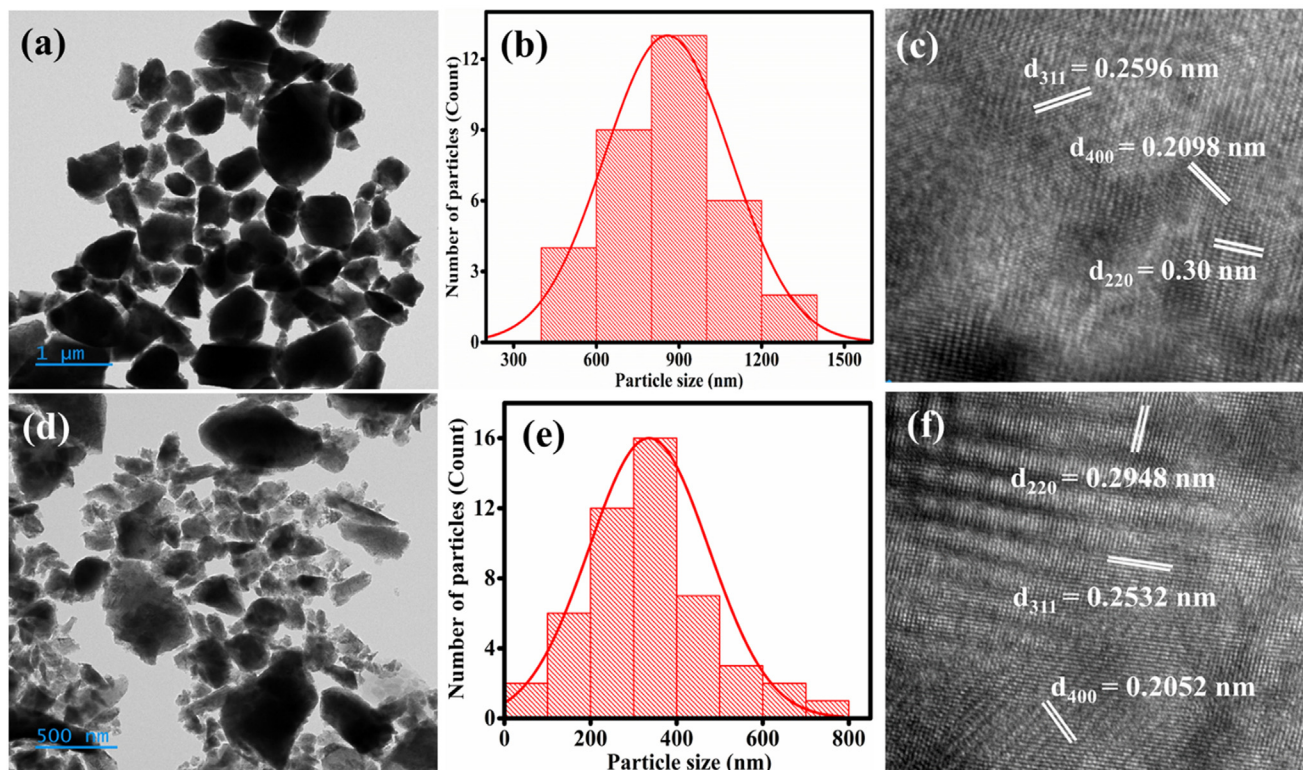
Fig. 4. (a, d) TEM images, (b, e) particle size distribution curves, and (c, f) HRTEM images of $ZnFe_2O_4$ and $ZnFe_{1.9}Al_{0.1}O_4$, respectively.
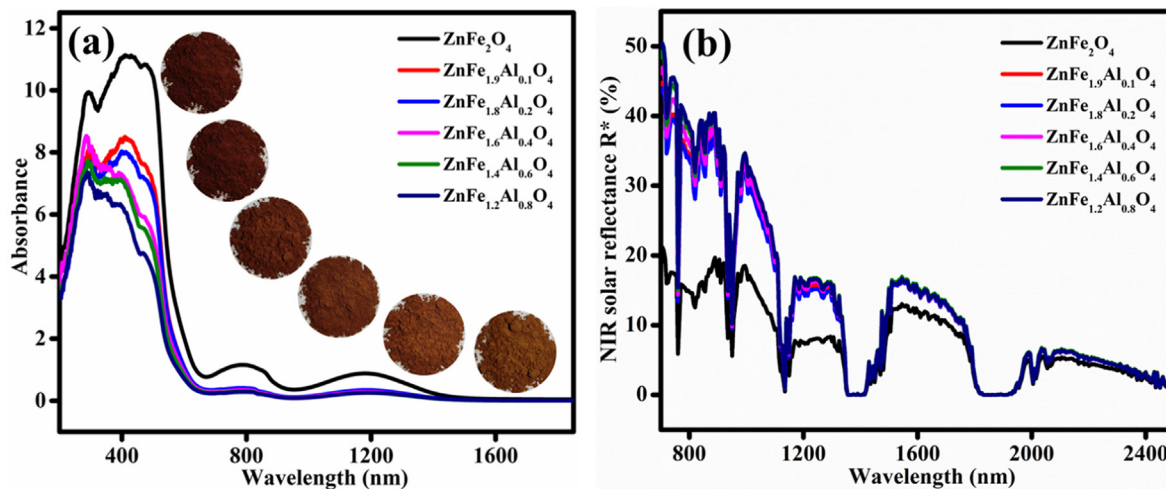
Fig. 5. (a) UV–Vis-NIR absorption spectra (photograph of pigments inset) and (b) NIR solar reflectance spectra of $ZnFe_{2-x}Al_xO_4$ ($0 \leq x \leq 0.8$).

Table 2
Colour co-ordinates and reflectance of $ZnFe_{2-x}Al_xO_4$ ($0 \leq x \leq 0.8$).

Sample	L^*	a^*	b^*	C^*	h°	NIR (%) at 1100 nm	R^* (%)
x = 0	38.93	22.46	25.05	33.64	48.11	25	34
x = 0.05	43.64	24.86	26.80	36.55	47.15	45	53
x = 0.1	46.54	25.05	31.01	39.86	51.06	50	58
x = 0.2	46.82	24.28	30.08	38.66	51.09	48	56
x = 0.4	47.08	22.79	30.22	35.83	52.98	51	59
x = 0.6	51.21	22.65	31.96	39.17	54.67	53	61
x = 0.8	53.27	21.38	31.66	38.20	55.96	53	61

Al^{3+}, indicated by the increase in L* from 38 to 53. Fortunately, it was not hugely influenced to bring a colour change in the pigment series. For $ZnFe_{1.9}Al_{0.1}O_4$, a* and b* proportionally increased from that of its base compound, which led into colour strength improvement. Later, a* and b* tend to decrease and increase, respectively, suggesting a drop in red tinge along with the rise in yellow. It was observed as gradually fading brown tone in appearance.

Reflectance properties

Inorganic brown is a customary choice for buildings and roofs. But, being very dark shade, to attain a high NIR reflectance for brown pigment is always challenging. Looking forward to break this drawback, the prepared inorganic brown pigment series $ZnFe_{2-x}Al_xO_4$ ($0 \leq x \leq 0.8$), were investigated for their reflectance property, where, respective NIR and NIR solar reflectance spectra were displayed in **Fig. S4** and Fig. 5**b**, respectively. The NIR and NIR solar reflectance of the base system noted as 25 and 34%, respectively. As soon as Fe^{3+} replaced by Al^{3+}, an appreciable enhancement was monitored in the reflectance profile of pigment series. It was able to stretch the reflectance value R* upto 61% by maximum doping with retention of phase purity. The two forbidden transitions of Fe^{3+} at NIR region is accountable for the low reflectance of $ZnFe_2O_4$. Meanwhile, substitution of Fe^{3+} by Al^{3+} diminishes these characteristic transitions in turn reduces the intensity of these absorptions. Both the factors contributed simultaneously, to enhance the spectral reflectance of developed pigments. Since colour strength cannot be compromised for spectral reflectance, $ZnFe_{1.9}Al_{0.1}O_4$ chosen as the best composition for further studies. Therefore, $ZnFe_{1.9}Al_{0.1}O_4$ can be considered as an efficient cool roof pigment for exterior coatings.

Generally, an intense brown colour was identified through CIE L*a*b* colour system as a* and b* almost in 1:1 ratio with L* < 50. But, too low or very high L* will influence reflectance or colour strength of the pigment, respectively. Hence, high magnitude a*, b* along with L* just below 50 will be an ideal requirement. Comparative colour analyses with some of the reported pigments were shown in **Table S6**, [14–16,42–53] Certainly $ZnFe_{1.9}Al_{0.1}O_4$ is the better candidate over the other compositions, because of high magnitude colour co-ordinates with appropriately maintained proportion. Most of the pigments listed in **Table S6**, achieved high reflectance by compromising the colour strength. Different from others, $ZnFe_{1.9}Al_{0.1}O_4$ could able to attain relatively high R* = 58%, without any colour fade.

Anticorrosive studies

Durability of metal coatings is hugely relied on the corrosion resistance property of coating material. Different from conventional duplex coating practice, reflective layer over anticorrosive base, a single layer anticorrosive cool coating can conserve energy, expense and time drastically. This motivated to explore the anticorrosive property of developed $ZnFe_{1.9}Al_{0.1}O_4$ brown inorganic pigment systematically. Herein, corrosion resistance of $ZnFe_{1.9}Al_{0.1}O_4$ was investigated on steel in marine medium. Epoxy coatings of thickness $\sim$ 11 μm have prepared with different pigment loadings (5, 10, 15, 20 and 25 wt%) for corrosion analysis. Further, EIS experiments have performed and respective Nyquist plots of bare epoxy (Fig. S5**a**) and pigment incorporated epoxy coatings on steel in 3.5 wt% NaCl, have shown in Fig. 6**a-b** and Fig. S5**b**.

The electrical equivalent circuit (EEC) used to fit all the impedance spectra of $ZnFe_{1.9}Al_{0.1}O_4$ epoxy coatings is [R_{coat}/ ($Q_{coat} + Q_{dl}$/ R_{ct})] shown in inset Fig. 6**b**. Solution resistance R_s is negligible thus omitted from the circuit. R_{coat} explains the stability of polymer coating and R_{ct} associated charge transfer resistance at the metal electrolyte interface. Corresponding constant phase elements Q_{coat}

(coating capacitance) and Q_{dl} (double layer capacitance), account for the non-ideal behavior of polymer coating on metallic surface [18]. The electrochemical parameters from impedance fitting tabulated in Table 3.

Incorporation of pigment powder brought incredible improvement in epoxy coat resistance on metal surface, of the order 10^5 to 10^7 Ωcm^2. This it indicates potential of the material as an anticorrosive pigment. More details were extracted out by evaluating obtained R_{ct} values. Initial 5 wt% pigment loading recorded one order hike in R_{ct} from 2×10^5 to 2.8×10^6 Ωcm^2. Further increment in loading up to 20 wt% illustrated a steady one order enhancement in corrosion resistance. The maximum $R_{ct} = 4.1 \times 10^9$ Ωcm^2 was recorded for 20 wt% loading with minimum Q_{dl} 0.002 μFcm^{-2}, which immediately dropped down to 7.4×10^6 at 25 wt%. Therefore, primary inference from the EIS results is that prepared ferrite pigment shows excellent resistance towards mild steel corrosion in marine medium, on top of which, the trend in resistance value implied a resistive mechanism that works at its best for 20 wt% loading. Further, a corrosion inhibition mechanism was suggested based on a passive hydroxide film formation at metal-electrolyte interface for optimum pigment volume concentration. Later it failed to work above saturation point where pigment particles develop pores in polymer coating which facilitated the corrodent penetration.

Durability of 20 wt% pigment loaded coating was ensured by one-month continuous electrochemical analysis on steel in marine environment. Results were tabulated in Table 4 and Bode plot of continuous study was shown in Fig. 6**c**. During the period of each 5 days from day 1 to 10, the resistance value depleted in the order of one, 10^9 to 10^8 Ωcm^2, then 10^8 to 10^7 Ωcm^2. Later, it was maintained throughout till completion of the experiment without much deterioration, which substantiated the pigment durability. Meanwhile, a comparitive anlysis of corrosion resistance with zinc based commercial anticorrosive pigments, appeared to be highly encouraging, Fig. 6**d**. Though, the critical pigment volume concentration is slightly on higher side, since we were able to replace the toxic chromium ions from the composition, R_{ct} of the same order is invaluable, (**Table S7**). Literature reports suggest that, stability of ferrite pigments are subjected to the formation of barely soluble hydroxides on metallic surface during immersion in saline medium, which can act as inhibitive barrier to prevent corrodent attack [54]. Hence, we have gone for XPS analysis on metal surface, obtained after continuous analysis, to determine the presence of hydroxide inhibitive layer.

XPS surface analysis

XPS surface analysis of coat removed steel strip provided clear idea on the compounds formed beneath pigment loaded epoxy coating after continuous electrochemical study. Survey spectrum (Fig. 7**a**) recognized the presence of O, Zn, Fe and Al. With respect to C1s level, high resolution spectrum of elements responsible for corrosion inhibition mechanism O1s, Zn2p and Fe2p were deconvoluted and shown in Fig. 7**b-d**.

In O1s spectrum, binding energy peak at 531.1 eV corresponds to iron oxyhydroxide (FeOOH) compound and 532.5 eV peak attributed to $Zn(OH)_2$ formation on steel surface. The findings were in good ageement with Zn2p and Fe2p spectra, Fig. 7**c and d**. Zn2p and Fe2p spectra validated the formation of $Zn(OH)_2$ and FeOOH with a binding energy peak at 1021.8 and 711.9 eV, respectively [55,56].

XPS results certainly helped to explain the corrosion inhibition mechanism involved in the prepared ferrite pigment loaded epoxy coating. Initially, interaction of NaCl solution with $ZnFe_{1.9}Al_{0.1}O_4$ pigment activated the resistive mechanism, by building an alkaline environment at metal-electrolyte interface via sparingly soluble
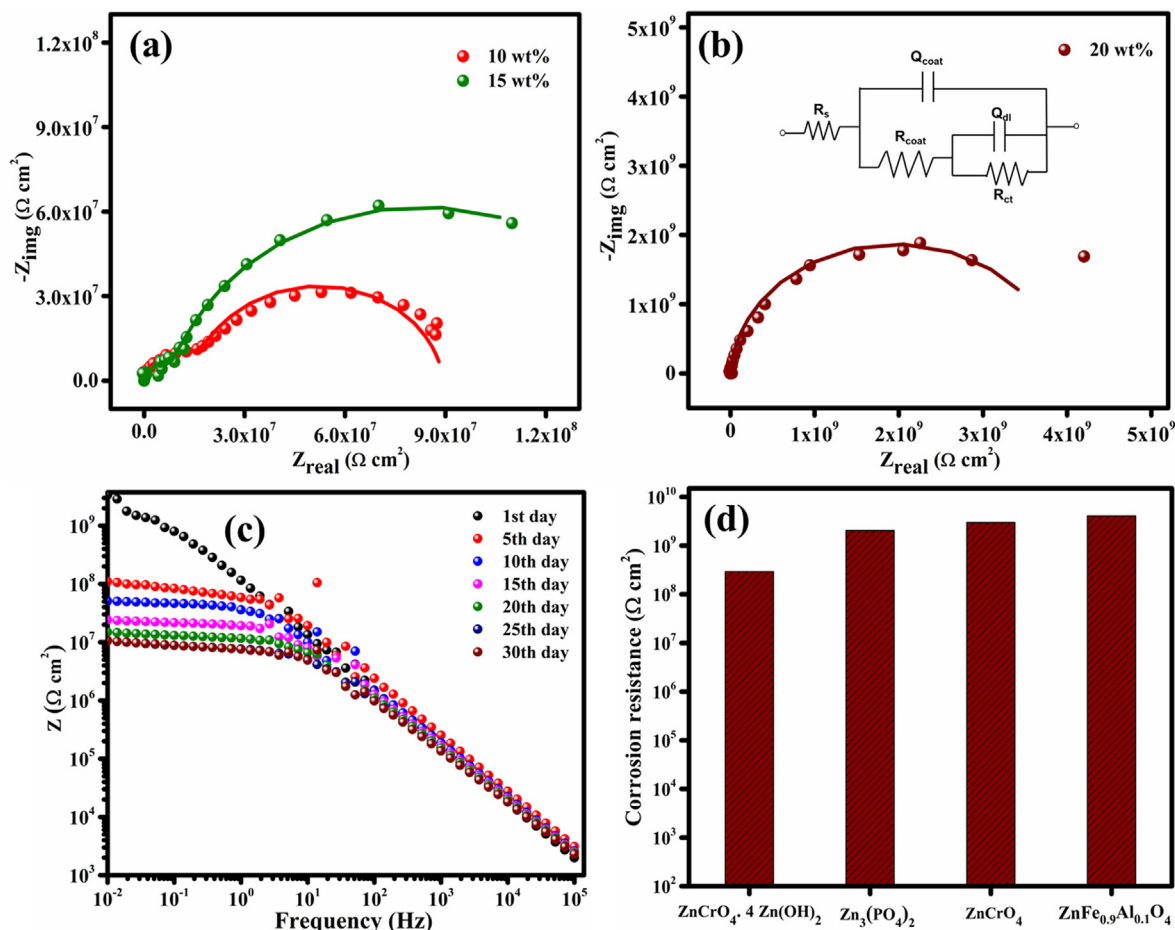
Fig. 6. Nyquist plots of (a) 10 and 15 wt% (b) 20 wt% (EEC in inset), (c) Bode plot of continuous one-month electrochemical study of 20 wt% $ZnFe_{1.9}Al_{0.1}O_4$ loaded epoxy coating, (d) comparison in corrosion resistance of $ZnFe_{1.9}Al_{0.1}O_4$ with commercial anticorrosive pigments.
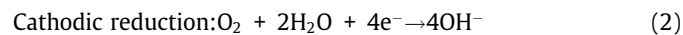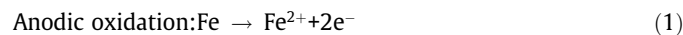
Table 3
EIS parameters from Nyquist plot.

EIS parameters	Bare metal	Bare epoxy	$ZnFe_{1.9}Al_{0.1}O_4$ (wt%)				
			5	10	15	20	25
R_{coat} (Ωcm^2)	-	159.8	2.8×10^5	2.1×10^7	1.3×10^7	9.8×10^7	2.2×10^5
Q_{coat} (μFcm^{-2})	-	4.2	0.14	0.016	0.06	0.005	0.23
R_{ct} (Ωcm^2)	1.5×10^3	1.2×10^5	2.8×10^6	6.8×10^7	1.4×10^8	4.1×10^9	7.4×10^6
Q_{dl} (μFcm^{-2})	744	0.028	0.03	0.004	0.011	0.002	0.03

Table 4
EIS parameters from continuous electrochemical analysis.

Sample	Corrosion resistance (Ωcm^2)						
	1st day	5th day	10th day	15th day	20th day	25th day	30th day
$ZnFe_{1.9}Al_{0.1}O_4$	4.1×10^9	1.1×10^8	5.1×10^7	2.4×10^7	1.4×10^7	1.1×10^7	1.1×10^7

metal hydroxides formation, which protected steel from further contact with saline environment, as follows, (Eqs. (1) and (2)).

$$\text{Anodic oxidation:} Fe \rightarrow Fe^{2+} + 2e^- \qquad (1)$$

$$\text{Cathodic reduction:} O_2 + 2H_2O + 4e^- \rightarrow 4OH^- \qquad (2)$$

The hydroxyl species formed at cathode, reacted with metal ions present in ferrite pigment (Zn^{2+} and Fe^{3+}) and formed corresponding hydroxides followed by passive oxyhydroxides (Eqs. (3) and (4)).

$$Zn^{2+} + 2OH^- \rightarrow Zn(OH)_2 (\text{slightly soluble}) \qquad (3)$$

$$Fe^{3+} + 3OH^- \rightarrow Fe(OH)_3 \rightarrow FeOOH(\text{passive}) \qquad (4)$$
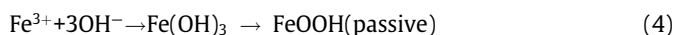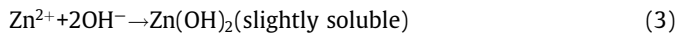
The less soluble zinc hydroxide complex formed between pigment coating and metal substrate inhibits corrosion reaction in chloride environment. This stable passivating barrier assisted to achieve high corrosion resistance for $ZnFe_{1.9}Al_{0.1}O_4$ pigment. Moreover, ferrite pigments passivated the steel surface also by forming amorphous passive FeOOH layer along with zinc hydroxide
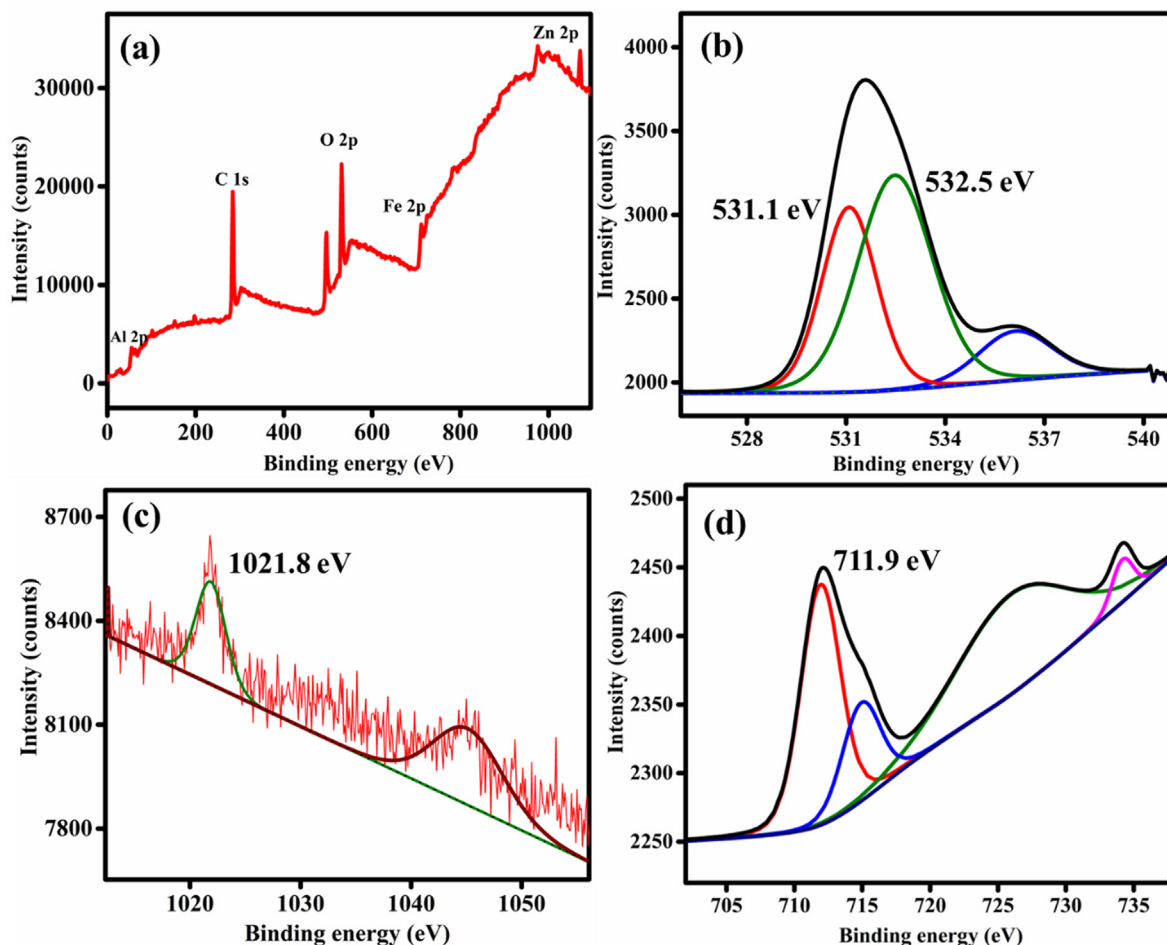
Fig. 7. XPS (a) survey spectrum, fitted high resolution spectrum of (b) O1s, (c) Zn 2p and (d) Fe 2p of inhibitive film beneath the 20 wt % $ZnFe_{1.9}Al_{0.1}O_4$ loaded epoxy coat after immersion test.

[54,57,58]. Both $Zn(OH)_2$ and FeOOH formation subsidize anticorrosive mechanism of $ZnFe_{1.9}Al_{0.1}O_4$, which makes it qualify as a potential candidate for protecting steel from marine environmental corrosion.

Applications

Stability of synthesized pigment was analyzed in different aggressive media, such as acid, base, and water. Pre-weighed pigment sample vigorously stirred for 1 h in different media, subsequently dried, weighed and measured the colour property, Table S8. No significant colour change was noticed between pretreated and treated sample, where estimated ΔE^*_{ab} not deviated away from unity. Hence, confirmed stability of the pigment [59,60].

Colour deliverability is another area of concern for most of the inorganic pigments, hence, it was established through developing coatings on conventional substrates. The pigment emulsion brush coated over concrete block and Al sheet substrates, which dried and analyzed for colour and reflectance. Obtained results are tabulated in Table 5 and solar reflectance graphs were illustrated in

Fig. 8. Generally, dark colours experience serious colour deterioration while coating. But, in the case of $ZnFe_{1.9}Al_{0.1}O_4$, the coatings were appeared to be brighter than the pigment powder, indicated by enhancement in L*. Moreover, estimated colour parameters and solar reflectance suggested no significant deterioration in its colour strength and reflectance as well. Thus, it is definitely an ideal candidate as an alternative for present brown pigment in the market.

Temperature shielding performance

Enhancement in reflectance property for $ZnFe_{1.9}Al_{0.1}O_4$ over $ZnFe_2O_4$, impelled to organize the temperature shielding experiment. The pigment coatings of thickness 200–250 μm was employed for roofing foam boxes. Temperature against time plot for the experiment indicated an abrupt rise in interior temperature during initial 20 minutes and saturation thereafter, Fig. 9a. Apparently due to immediate IR absorption and heat transfer to the interior at the beginning and equilibration of the process thereafter. It was delighted to mark nearly 2.5 °C drop in temperature beneath $ZnFe_{1.9}Al_{0.1}O_4$ coated roof, after 1 h scrutiny.

Table 5
Colour coordinates and R* of pigment coatings.

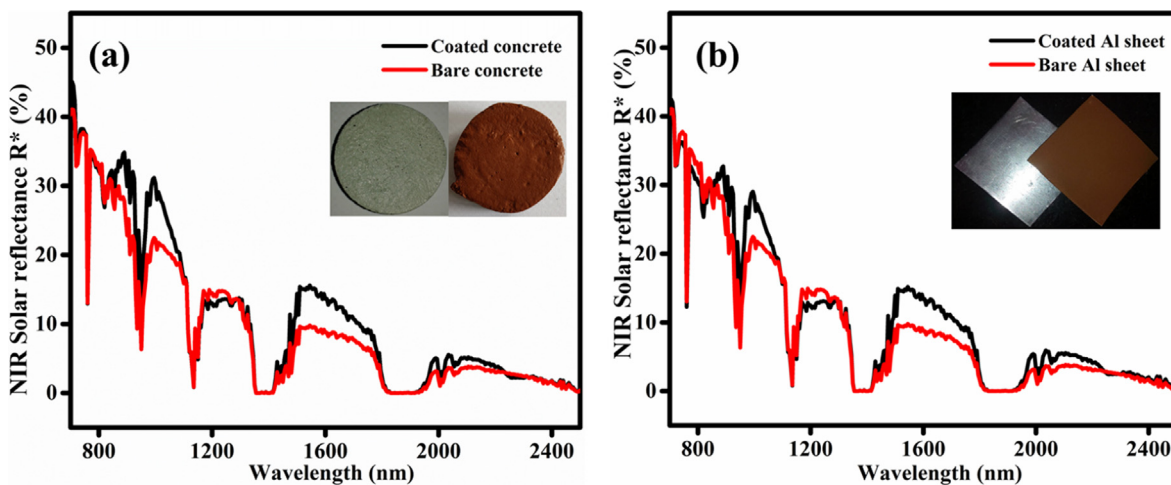| Sample	L*	a*	b*	C*	h°	R* (%)
$ZnFe_{1.9}Al_{0.1}O_4$	46.54	25.05	31.01	39.86	51.06	58
Concrete	57.75	20.50	32.67	38.56	57.89	50
Al sheet	49.71	21.41	31.79	38.33	56.04	52

Fig. 8. Comparison in NIR solar reflectance spectra of $ZnFe_{1.9}Al_{0.1}O_4$ coatings on (a) concrete block and (b) Al sheet with their bare surfaces.

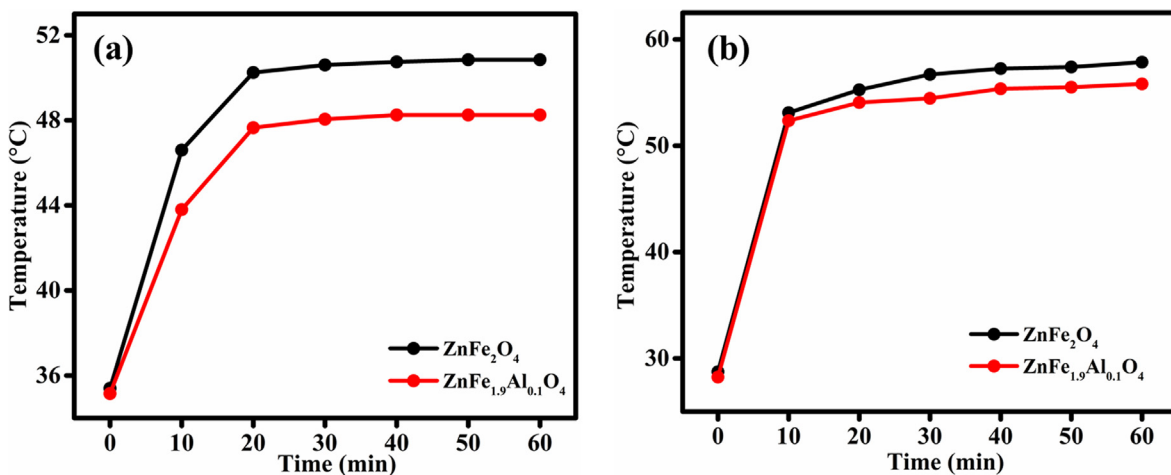**Fig. 9.** Comparison in (a) interior temperature and (b) surface temperature build up, between $ZnFe_2O_4$ and $ZnFe_{1.9}Al_{0.1}O_4$ coatings roofed foam box.

Almost similar progression was observed in the case of surface temperature build-up. Thermal images of the coating surfaces were illustrated in **Fig. S6 and S7**. Since, IR lamp focus was at the centre of coating, heatzone was concentrated in this region, observed as red contour in thermal image. Further, heat propagated over the surface towards edges, appeared as orange, yellow and green colours in decreasing order of temperature. Therefore, two temperature measurement points were fixed at the red contour and its average was plotted versus time, **Fig. 9b**. Importantly, temperature build up on $ZnFe_{1.9}Al_{0.1}O_4$ coating was ~ 3 $^{\circ}C$ lower than $ZnFe_2O_4$. Overall, Al^{3+} doping at $ZnFe_2O_4$ was highly beneficial to bring reduction in heat generation by NIR rays absorption. Therefore, switching from traditional brown to new cool brown coating can have a great impact on energy conservation in huge constructions.

Conclusions

- A low-cost multifunctional brown inorganic pigment was synthesized based on Al^{3+} substituted $ZnFe_2O_4$.
- The best composition $ZnFe_{1.9}Al_{0.1}O_4$, in the pigment series, $ZnFe_{2-x}Al_xO_4$ ($0 \leq x \leq 0.8$) exhibited $a^* = 25.05$, $b^* = 31.01$ and $R^* = 58\%$, is higher than the reported brown pigments.
- Al^{3+} substitution at Fe^{3+} site brought reduction in Fe-O bonds in FeO_6 octahedra, led into unit cell shrinkage, thereby lattice distortion, decrease in crystallinity and crystal symmetry.

- The charge transfer transition O2p → Fe3d and d-d forbidden transitions in Fe^{3+} chromophore was responsible for brown colour of the pigment.
- Approximately, 2.5 $^{\circ}C$ temperature reduction was achieved for $ZnFe_{1.9}Al_{0.1}O_4$ over $ZnFe_2O_4$ coating, which confirmed potential of the pigment as a cool colourant.
- Anticorrosive performance ($R_{ct} = 4.1 \times 10^9$ Ωcm^2) of the pigment was appreciably higher than toxic chrome pigments, under marine conditions with respectable durability.
- The passivating $Zn(OH)_2$ and FeOOH layers formed at metal electrolyte interface deploys the inhibitive mechanism involved in the pigment.

Declaration of Competing Interest

The authors declare that they have no known competing financial interests or personal relationships that could have appeared to influence the work reported in this paper.

Acknowledgements

Appendix A. Supplementary material

Supplementary data to this article can be found online at https://doi.org/10.1016/j.jiec.2023.02.035.

References

[1] P. Chand, S. Vaish, P. Kumar, Phys. B Condens Matter. 524 (2017) 53–63, https://doi.org/10.1016/j.physb.2017.08.060.
[2] Y. Li, Y. Ma, W. Liu, Z. Wang, H. Liu, X. Wang, H. Wei, S. Zeng, N. Yi, G.J. Cheng, Sol. Energy 226 (2021) 180–191, https://doi.org/10.1016/j.solener.2021.08.047.
[3] N. Sangwong, M. Suwan, S. Supothina, Mater. Today: Proc. 17 (2019) 1595–1601, https://doi.org/10.1016/j.matpr.2019.06.187.
[4] M. Elias, C. Chartier, G. Prévot, H. Garay, C. Vignaud, Mater. Sci. Eng. B 127 (2006) 70–80, https://doi.org/10.1016/j.mseb.2005.09.061.
[5] N. Pailhé, A. Wattiaux, M. Gaudon, A. Demourgues, J. Solid State Chem. 181 (2008) 1040–1047, https://doi.org/10.1016/j.jssc.2008.02.009.
[6] P. Jeevanandam, R.S. Mulukutla, M. Philips, S. Chaudhuri, L.E. Erickson, K.J. Klabunde, J. Phys. Chem. C 111 (2007) 1912–1918, https://doi.org/10.1021/jp066363o.
[7] K. Ashwini, C.V.M. Bendiganavale, Chem. Eng. 1 (2008) 67–79.
[8] L. Yanga, F. Feng Qiana, D. Songa, K. Zheng, Procedia Eng. 169 (2016) 11–18, https://doi.org/10.1016/j.proeng.2016.10.002.
[9] P.K. Thejus, K.G. Nishanth, Sol. Energy Mater. Sol. Cells 200 (2019), https://doi.org/10.1016/j.solmat.2019.109999.
[10] S. Jose, D. Joshy, S.B. Narendranath, P. Periyat, Sol. Energy Mater. Sol. Cells 194 (2019) 7–27, https://doi.org/10.1016/j.solmat.2019.01.037.
[11] S. Balamurugan, B.C. Brightlin, V.S.A. Kiruba, J. Nanosci. Nanotechnol. 15 (2015) 1–6, https://doi.org/10.1166/jnn.2015.10335.
[12] Y. Li, Y. Ma, W. Liu, Z. Wang, H. Liu, X. Wang, H. Wei, S. Zeng, N. Yi, G.J. Cheng, Sol. Energy 226 (2021) 180–191, https://doi.org/10.1016/j.solener.2021.08.047.
[13] N. Sangwong, M. Suwan, S. Supothina, Chiang Mai J. Sci. 47 (2020) 686–699.
[14] L. Liu, A. Han, M. Ye, M. Zhao, Sol. Energy Mater. Sol. Cells 132 (2015) 377–384, https://doi.org/10.1016/j.solmat.2014.08.048.
[15] L. Liu, A. Han, M. Ye, W. Feng, Sol. Energy 113 (2015) 48–56, https://doi.org/10.1016/j.solener.2014.12.034.
[16] M. Suwan, N. Sangwong, S. Supothina, Ceramics-Silikáty 64 (2020) 172–179, https://doi.org/10.13168/cs.2020.0006.
[17] V. Elakkiya, S. Sumathi, J. Alloys Compd 820 (2020), https://doi.org/10.1016/j.jallcom.2019.153174.
[18] P.K. Thejus, K.V. Krishnapriya, K.G. Nishanth, Sol. Energy Mater. Sol. Cells 219 (2021), https://doi.org/10.1016/j.solmat.2020.110778.
[19] P.K. Thejus, K.V. Krishnapriya, K.G. Nishanth, Sol. Energy 222 (2021) 103–114, https://doi.org/10.1016/j.solener.2021.05.017.
[20] T. Schauer, W.M. Liu, L. Dulog, Eur. Coat. J. 3 (1997) 233.
[21] Y. Hao, F. Liu, E. Han, S. Anjum, G. Xu, Corros. Sci. 69 (2013) 77–86, https://doi.org/10.1016/j.corsci.2012.11.025.
[22] M.C. Deya, R. Romagnoli, B. del Amo, Corros. Rev. 22 (2004) 1–17, https://doi.org/10.1515/CORRREV.2004.22.1.1.
[23] A. Kalendová, P. Rysánek, K. Nechvílová, Prog. Org. Coat. 86 (2015) 147–163, https://doi.org/10.1016/j.porgcoat.2015.05.009.
[24] H.S. Emira, Anti-Corros. Methods M. 53 (2006) 224–231, https://doi.org/10.1108/00035590610678929.
[25] A. Kalendová, D. Veselý, Anti-Corros. Methods M 54 (2007) 3–15, https://doi.org/10.1108/00035590710717339.
[26] S. Mahvidi, M. Gharagozlou, M. Mahadavian, S. Naghibi, The pigment extract study 20 (2017) 1492–1502, https://doi.org/10.1590/1980-5373-MR-2016-0772.
[27] S. Mahvidi, M. Gharagozlou, M. Mahdavian, S. Naghibi, Prog. Color Colorants Coat. 12 (2019) 57–70. http://pccc.icrc.ac.ir/files/cu113se1up3540.pdf.
[28] N.M. Ahmed, A.M. Fathi, M.G. Mohamed, W.M. Abd El-Gawad, Prog. Org. Coat. 140 (2020).
[29] R. Levinson, H. Akbari, P. Berdahl, Sol. Energy 84 (2010) 1717–1744, https://doi.org/10.1016/j.solener.2010.04.018.
[30] R. Levinson, H. Akbari, P. Berdahl, Sol. Energy 84 (2010) 1745–1759, https://doi.org/10.1016/j.solener.2010.04.017.
[31] T. Thongkanluang, T. Kittiauchawal, P. Limsuwan, Ceram. Int. 37 (2011) 543–548, https://doi.org/10.1016/j.ceramint.2010.09.044.
[32] X. Zhao, Y. Zhang, Y. Huang, H. Gong, J. Zhao, Dyes Pigm. 116 (2015) 119–123, https://doi.org/10.1016/j.dyepig.2015.01.018.
[33] L. Yuan, A. Han, M. Ye, X. Chen, L. Yao, C. Ding, Dyes Pigm. 148 (2018) 137–146, https://doi.org/10.1016/j.dyepig.2017.09.008.
[34] K. Kavitha, A. Sivakumar, Inorg. Chem. Comm. 120 (2020), https://doi.org/10.1016/j.inoche.2020.108163.
[35] W. Zhou, J. Yea, S. Zhuo, D. Yu, P. Fang, R. Peng, Y. Liu, W. Chen, J. Alloys Compd. 896 (2022), https://doi.org/10.1016/j.jallcom.2021.162883.
[36] M. Pal, U. Pal, J.M.G.Y. Jiménez, F. Pérez-Rodríguez, Nanoscale Res. Lett. 7 (2012) 1, https://doi.org/10.1186/1556-276X-7-1.
[37] K. Prabakar, S. Venkatachalam, Y.L. Jeyachandran, SaK. Narayandass, D. Mangalaraj, Sol. Energy Mater. Sol. Cells 81 (2004) 1–12, https://doi.org/10.1016/j.solmat.2003.08.008.
[38] K.R. Murali, A. Kalaivanan, S. Perumal, N.N. Pillai, J. Alloys Compd. 503 (2010) 350–353, https://doi.org/10.1016/j.jallcom.2009.11.187.
[39] P.N. Anantharamaiah, S. Mondal, K.S. Manasa, S. Saha, M.M. Pai, Ceram. Int. 46 (2020) 1220–1226, https://doi.org/10.1016/j.ceramint.2019.08.276.
[40] H. Lv, L. Ma, P. Zeng, D. Ke, T. Peng, J. Mater. Chem. 20 (2010) 3665–3672, https://doi.org/10.1039/B919897K.
[41] L. Wang, Q. Zhou, F. Li, 241 (2004) 377–382. https://doi.org/10.1002/pssb.200301923.
[42] M. Suwan, N. Sangwong, S. Supothina, Mater. Sci. Eng. 182 (2017), https://doi.org/10.1088/1757-899X/182/1/012003.
[43] A. Sutka, A. Borisova, J. Kleperis, G. Mezinskis, D. Jakovlevs, I. Juhnevica, J. Aust. Ceram. Soc. 48 (2012) 150–155.
[44] C.S. Xavier, R.A. Candeia, M.I.B. Bernardi, S.J.G. Lima, E. Longo, C.A. Paskocimas, L.E.B. Soledade, A.G. Souza, I.M.G. Santos, J. Therm. Anal. Calorim. 87 (2007) 709–713, https://doi.org/10.1007/s10973-006-7744-6.
[45] L. Yuan, A. Han, M. Ye, X. Chen, C. Ding, L. Yao, Ceram. Int. 43 (2017) 16488–16494, https://doi.org/10.1016/j.ceramint.2017.09.032.
[46] V. James, P.P. Rao, S. Sameera, S. Divya, Ceram. Int. 40 (2014) 2229–2235, https://doi.org/10.1016/j.ceramint.2013.07.141.
[47] Y. Xiao, B. Huang, J. Chen, X. Sun, J. Alloys Compd. 762 (2018) 873–880, https://doi.org/10.1016/j.jallcom.2018.05.233.
[48] Ž. Dohnalová, P. Šulcová, P. Bělina, M. Vlček, N. Gorodylova, Therm. Anal. Calorim. 133 (2018) 421–428, https://doi.org/10.1007/s10973-017-6805-3.
[49] G. Buvaneswari, V. Aswathy, R. Rajakumari, Dyes Pigm. 123 (2015) 413–419, https://doi.org/10.1016/j.dyepig.2015.08.024.
[50] B. Huang, Y. Xiao, C. Huang, J. Chen, X. Sun, Dyes Pigm. 147 (2017) 225–233, https://doi.org/10.1016/j.dyepig.2017.08.004.
[51] S. Radhika, K.J. Sreeram, B.U. Nair, J. Chem. Sci. 126 (2014) 65–73, https://doi.org/10.1007/s12039-013-0559-7.
[52] R. Oka, Y. Shobu, F. Aoyama, T. Tsukimori, T. Masui, RSC Adv. 7 (2017) 55081, https://doi.org/10.1039/C7RA10250J.
[53] E. Asadinia, M. Pakshira, S.E. Hosseini, Prog. Org. Coat. 139 (2020), https://doi.org/10.1016/j.porgcoat.2019.105435.
[54] Z. Mayya, S. Sergey, K. Sergey, Anti-corros. Method. M 67 (2020) 395–405, https://doi.org/10.1108/ACMM-12-2019-2222.
[55] J.F. Moulder, W.F. Stickle, P.E. Sobol, K.D. Bomben, Handbook of Xray Photoelectron Spectroscopy, Perkin-Elemer Corporation, USA, 1993.
[56] G. Deroubaix, P. Marcus, Surf. Interface Anal. 18 (1992) 39–46, https://doi.org/10.1002/sia.740180107.
[57] M.A. Nivin, M.A. Walaa, A.Y. Elham, Pigm. Resin. Technol. 43 (2014) 201–211, https://doi.org/10.1108/PRT-10-2013-0106.
[58] A.A. Mahmoud, M.A. Nivin, A.Y. Elham, J. Coat. Technol. Res. 7 (2010) 703–713, https://doi.org/10.1007/s11998-009-9229-6.
[59] S. Jose, J. Anaswara, S. Laha, S. Natarajan, K.G. Nishanth, M.L.P. Reddy, Dyes Pigm. 124 (2016) 120–129, https://doi.org/10.1016/j.dyepig.2015.09.014.
[60] E. Ghasemi, B. Ramezanzadeh, S. Saket, S. Ashhari, J. Coating Technol. Res. 13 (2016) 97–114, https://doi.org/10.1007/s11998-015-9728-6.